

Viscoelasticity of single biopolymers using Atomic Force Microscopy



Shatruhan Singh Rajput
20143354

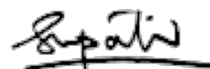
Indian Institute of Science Education and Research, Pune - 411008

A thesis
Submitted in partial fulfillment of the requirements of
the degree of
Doctor of Philosophy

2021

Certificate

Certified that the work incorporated in this thesis entitled 'Viscoelasticity of single biopolymers using Atomic Force Microscopy' submitted by Shatruhan Singh Rajput, was carried out by the candidate, under my supervision. The work presented here or any part of it has not been included in any other thesis submitted previously for the award of any degree or diploma from any other University or institution.



Dr. Shivprasad Patil

Thesis Supervisor

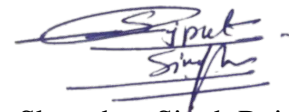
Indian Institute of Science Education and Research

Pune, Maharashtra

Date: 29/10/2021

Declaration

I declare that this thesis is a presentation of my original research work. Wherever contributions of others are involved, every effort is made to indicate this clearly, with due reference to the literature, and acknowledgment of collaborative research and discussions. I also declare that I have adhered to all principles of academic honesty and integrity and have not misrepresented or fabricated or falsified any idea/data/fact/source in my submission. I understand that violation of the above will be cause for disciplinary action by the institute and can also evoke penal action from the sources which have thus not been properly cited or from whom proper permission has not been taken when needed.



Shatruhan Singh Rajput
Enrolment no. - 20143354

Date: 29/Oct/2021

To
Amma, Papa, & Bade Bhaiya

Abstract

Viscoelasticity of single protein molecules is essential to fully understand their dynamic properties and functions. It is also believed that the initial collapse in protein folding is governed by their viscoelasticity. Dynamic atomic force microscopy is recognised as a powerful tool for direct measurement of viscoelasticity in the single molecules. This method had also been vastly applied to understand the dynamic properties of the nano-confined liquids. The estimated viscoelasticity using this method is always debated due to the complex dynamic behaviour of AFM cantilever-beam in liquid environment. In order to resolve this issue, understanding the cantilever dynamics under the influence of interaction force in liquid environment is essential. We have done a comprehensive work to precisely determine the interaction viscoelasticity using amplitude-modulation atomic force microscopy (AM-AFM). Single protein molecule (titin I27₈) has been chosen as a model system for the study. We have applied two types of AFMs- slope detection based (commercial) and displacement detection based (interferometer based home-built) AFM. Two types of cantilever excitation mechanisms have been used- acoustic excitation (cantilever-base is excited using dither piezo) and magnetic excitation (cantilever-tip is excited using the magnetic excitation). Experiments were performed at truly off-resonance regime to avoid the complexities arising at on-resonance operation. Data has been analyzed using two mathematical models- continuous-beam (CB) and point-mass (PM) model. The experiments performed using different AFMs and using different cantilever excitation schemes and data analyzed using different models have been compared and an unified understanding have been tried building up to understand the AM-AFM measurements and its outcomes. We found that there are various sources which can introduce errors/artefacts in final results such as offset in the cantilever initial phase, inappropriate choice of operation frequency and mathematical model for data analysis etc. We propose methodology to perform AM-AFM measurements in order to get accurate results. We also propose the validity limit of widely used point-mass (PM) model. Our work is not only applicable for single protein molecule measurements but all the *biopolymers* and *nano-scale systems* which viscoelasticity can be probed using dynamic atomic force microscopy technique.

Acknowledgements

I would first like to acknowledge my supervisor Dr. Shivprasad Patil for his guidance and liberal behaviour. He gave me a free hand to learn and explore the instruments and resources available in the lab. He always listen my research ideas with patience and guided me appropriately. During my PhD, he provided me many opportunities which was helpful for me to improve my present work and choose future research career.

I acknowledge my research committee members Dr. Apratim Chatterji and Dr. Shouvik Datta for evaluating my work and their fruitful inputs. Their critical view over my work helped me in deeply understanding and interpreting the data.

I would like to acknowledge Dr. A.S.R. Koti (TIFR, Mumbai) for providing protein plasmid, Dr. Thomas Pucadyil (IISER, Pune) and Dr. Amrita Hazra (IISER, Pune) for providing protein extraction and purification facility. Special thanks to Sukrut Kamerkar, Jyoti Yadav, and Yashwant Kumar for helping me out in protein extraction and purification.

I acknowledge my lab seniors, Dr. A.V.R. Murthy and Dr. Amandeep Sekhon for providing me a friendly environment when I newly joined the lab. They helped me in learning the instruments and develop basic understanding of the research.

I would like to acknowledge my current and past lab members: Ajith, Jyoti, Viplove, Vikhyaat, Surya, Saurabh, Aadarsh, Mayank, Rhishabh, Dr. Arpita, Dr. Monika for keeping the lab environment joyful. Special thanks to Ajith, surya, and Saurabh. Ajith wrote all the Labview programs which I have used for experiments, Surya helped me in building the magnetic-excitation setup, and Saurabh played a crucial role in building the home-built setup (interferometer-based AFM). All my labmates were always available as a colleague and a friend for professional as well as personal discussions. I can never forget the fun during tea time 11:00 am and 4:00 pm.

I acknowledge all the staffs: technical, academic, teaching, non-teaching, hostel, house-keeping for helping me out, directly or indirectly, to make my academic and non-academic life better.

My journey would not have been possible without my family and friends. I do not have words how to thank them. I can never forget the time I have spent with Chandan (Singh Sahab), Madan (Lal), Kamal (Pandit ji), Vinay (Lal), Ashok (Lal), Sanjit (Garib), Ajay

(Sharma ji), Bappa (Lutera), Farsaram (Kaviraj), Yashwant bhaiya, Avirup Bhaiya, Neetu (Kumari), Deepak (Barua Ji), Amreen (Madam Ji), Sumit (Faradiya), Anju (Anamika Ji), Chhaya Madam, Sanjay Sir, Umesh Sir, Tripti di, Chitrakant, Rinkesh, Sandeep and all my friends. I had very sweet and sour time with them. I will always miss trekking, cooking at hostel, celebrating birthdays etc. I always feel vibrant with my friends. My father, mother and elder brother supported me unconditionally and took me up to here.

Table of contents

List of figures	xvii
Nomenclature	xxvii
1 Introduction	1
1.1 Proteins	2
1.1.1 Structure of Proteins	2
1.1.2 Classification of Proteins	4
1.1.3 Functions of Proteins	5
1.2 Protein unfolding studies	7
1.2.1 Bulk studies:	8
1.2.2 Single-molecule studies:	11
1.3 Atomic force microscope (AFM)	16
1.3.1 Static mode measurements:	18
1.3.2 Dynamic mode measurements:	21
1.4 Amplitude-modulation atomic force microscopy (AM-AFM):	21
1.5 Specific to my research:	23
1.5.1 Titin I27 protein:	23
1.5.2 Unfolding studies on I27 protein:	25
1.5.3 Motivation of the thesis:	26
1.5.4 Significance of the work:	28
1.6 Plan of the thesis:	30
1.6.1 Chapter 2	31
1.6.2 Chapter 3	31
1.6.3 Chapter 4	31
1.6.4 Chapter 5	32
1.6.5 Chapter 6	32
1.6.6 Chapter 7	33

1.7	Future possibilities:	33
2	Materials and methods	35
2.1	Introduction	35
2.2	Atomic Force Microscope (AFM)	35
2.3	Commercial AFM (<i>slope-detection</i>)	36
2.3.1	Optical beam deflection detection	36
2.3.2	Alignment of detection system	37
2.3.3	Detector sensitivity calibration	38
2.3.4	Cantilever force constant calibration	39
2.3.5	Sample-cell and tip-sample motion	41
2.4	Home-built AFM (<i>displacement-detection</i>)	41
2.4.1	Interferometric detection	42
2.4.2	Optical-fibre: <i>a partial reflective mirror</i>	44
2.4.3	Nano-positioner	44
2.4.4	Detection Sensitivity	44
2.4.5	Sample cell	45
2.4.6	Sample-stage movement	46
2.5	Lock-in amplifier	46
2.5.1	Phase-sensitive detection	46
2.6	Magnetic excitation setup	48
2.6.1	Magnetic cantilever preparation	49
2.6.2	Electro-magnet	50
2.7	Sample preparation	51
2.8	Cantilever	52
3	Theory: Amplitude-modulation atomic force microscopy	53
3.1	Introduction	53
3.2	Equation of motion	54
3.2.1	Point-mass model	55
3.2.2	Continuous-beam model	60
3.3	Discussion	66
3.3.1	Experiment, theoretical model, initial phase offset, and artefact . . .	67
3.3.2	Off-resonance operation	67
3.3.3	Excitation scheme, detection system, and true off-resonance operation	67
3.3.4	Validity of point-mass model	68
3.4	Conclusion	69

4	The nano-scale viscoelasticity using base-excited atomic force microscopy in liquid environment	71
4.1	Introduction	71
4.2	Materials and methods	73
4.2.1	AFM	73
4.2.2	Protein	74
4.3	Theory	74
4.3.1	Cantilever excited at base without interaction ($\bar{\gamma}_i = 0$ and $k_i = 0$)	76
4.3.2	Cantilever excited at base in presence of interaction ($\bar{\gamma}_i \neq 0$ and $k_i \neq 0$)	77
4.3.3	Cantilever excited at base and tip in non-deformable contact	78
4.4	Results and Discussion	78
4.4.1	Measurements performed using two detection methods	78
4.4.2	Quantification of Stiffness	81
4.4.3	The effect of extraneous phase	83
4.4.4	Minimum detectable dissipation coefficient	88
4.4.5	Dissipation in single macromolecules	89
4.5	Conclusions	90
5	Validity of point-mass model in off-resonance dynamic atomic force microscopy	93
5.1	Introduction	93
5.2	Theory	95
5.2.1	Continuous-beam (CB) model	96
5.2.2	Point-mass model	100
5.3	Materials and Methods	103
5.3.1	Magnetic excitation setup	103
5.3.2	Sample Preparation	106
5.4	Experiments	106
5.4.1	Atomic Force Microscopy	106
5.5	Discussion	110
5.6	Conclusion	112
6	Probing the folded protein domain response in dynamic atomic force microscopy	115
6.1	Introduction	115
6.2	Materials and Methods	116
6.3	Discussion	116
6.3.1	Base-excited, displacement measurement	116
6.3.2	High frequency and high amplitude measurement	121

6.4	Conclusion	122
7	Conclusion and future possibilities	125
7.1	Conclusion	125
7.2	Future possibilities:	127
	References	129
	Appendix A Chapter-4 - Supplementary Information	141
A.1	Theory	141
A.2	Discussion	143
A.2.1	Validity of Eq. 11	143
A.2.2	Quantification of Stiffness	143
A.2.3	The effect of extraneous phase	144
A.2.4	Sources of extraneous phase θ_e	144
A.2.5	Off-resonance operation:	147
A.2.6	Minimum detectable dissipation	149
	Appendix B Comparison of estimated stiffness using different methods	153

List of figures

1.1	Structure of amino-acid containing a central carbon atom covalently connected with an amine group (NH_2), a carboxylic group ($COOH$), a hydrogen (H), and a side group (R). Side group (R) makes difference between 20 naturally abundant amino-acids which contribute in protein synthesis. . . .	2
1.2	Graphical representation of (di)peptide formation. Two amino-acids combine to form a dipeptide and a water molecule is being released. Similarly, multiple amino-acids combine and form polypeptide which is primary structure (primary sequence) of protein.	3
1.3	Schematic representation of slope-detection based AFM. A laser beam reflects from the back of cantilever and collected at the position-sensitive photo-detector. In undeflected state, it generates some current (or voltage) difference (I_1 , net current on upper quadrant - net current on lower quadrant), however, the current difference changes to I_2 when cantilever deflects. The difference, $I_1 - I_2$, is proportional to change in the slope (dy/dx) of the cantilever which is again proportional to its displacement (y).	17
1.4	Unfolding force profile of I27 ₈ (polyprotein with eight identical copies of I27 molecule covalently attached in series) with relative extension between the substrate and cantilever-base. Experiment is performed using constant-speed pulling method at room temperature with 200 nm/sec pulling speed. The calibrated spring constant of the cantilever is 0.406 N/m. Each peak represents unfolding of one domain and further strain-stiffening profile represents force vs extension behaviour of the unfolded protein chain. Usually, first (large) peak is not considered for analysis as it contains non-specific interaction between tip and substrate.	19
1.5	Structural representation of I27 molecule. It is a β rich globular protein. Image is downloaded from PDB (https://www.rcsb.org/structure/1TIT). . .	24

2.1	Schematic representation of laser-alignment in optical beam deflection detection. A laser beam is allowed to fall on the back of the cantilever through a prism. Beam reflects from the cantilever surface and directed to the photo-detector with the help of an adjustable mirror which can be rotated about the axis perpendicular to the plane of paper. As per the requirement, the position of incident laser beam and photo-detector can be adjusted during the alignment.	37
2.2	Graph in black line represents cantilever bending with cantilever base position and red line represents linear fit. Slope of the fitted line is detector sensitivity. For the used rectangular cantilever (length = $250\ \mu m$, width = $35\ \mu m$, and thickness = $1\ \mu m$), it is $34.75\ nm/V$.	38
2.3	Graph in black line represents the calculated PSD for a rectangular cantilever and red line represents the Lorentzian fit. Resonance frequency ($f_0 = 13.54\ kHz$) and quality factor ($Q = 3.3$) are measured as the free parameters. Cantilever force constant ($k_c = 0.84\ N/m$) is estimated using Eq. 2.3.	40
2.4	Schematic representation of our home-built AFM. Alignment of the fibre-end parallel to back of the cantilever is magnified (shown in big circle).	42
2.5	Schematic representation of interferometric detection scheme. Partial reflective end of the optical-fibre is aligned parallel to the back of gold coated cantilever, acts as fully reflective mirror, and this arrangement forms Fabry-perot cavity. Infrared (IR) laser is passed through the optical-fibre which reflects back from two mirrors and interfere. Interfered laser is collected at the photo-detector which is sitting at a fix distance. Change in the distance between two mirrors causes change in photo-detector output current which is utilized to estimate the displacement of the cantilever by keeping the fibre-position fixed using a feedback system.	43
2.6	Picture of sample-cell which we use in home-built setup. (a) Cell is assembled and it is ready for sample drop casting. (b) Different components of the cell.	45
2.7	A thin layer of cobalt (gray colour) is coated at end position of the back of a gold-coated cantilever. Image is captured in 50x optical microscope.	50
2.8	Insulating coated thin copper wire ($\sim 0.15\ mm$ diameter) is wrapped around a ferrite core (diameter $2.5\ mm$ and length $20\ mm$). Electromagnet is mounted on a 3D printed base.	51

3.1	Schematic representation of point-mass approximated cantilever under influence of a linear interaction force. (a) Representing the base-excited point-mass approximation where base is driven by $Ae^{i\omega t}$. (b) Representing the tip-excited point-mass approximation where base is rigidly fixed and tip is excited with force $F_0e^{i\omega t}$	58
3.2	Schematic representation of oscillating cantilever, considered its continuum nature, under influence of a linear interaction force. (a) Representing the base-excited cantilever where base is driven by $Ae^{i\omega t}$. (b) Representing the tip-excited cantilever where base is rigidly fixed and tip is excited with force $F_0e^{i\omega t}$	61
4.1	(a) The schematic of the deflection detection set-up. The laser reflecting from the back of the cantilever falls on the position sensitive four quadrant detector. The outputs I_1 and I_2 correspond to the two positions of the laser spot on the detector. This position depends on the bending dy/dx of the cantilever at $x = L$. The signal from the detector reads the local cantilever bending. (b) In interferometer-based detection, the cantilever acts as one the mirrors in Fabry-Perot etalon. The displacement of the cantilever produces a proportional signal in the photo-diode. The signal from photo-diode measures displacement (y) of the cantilever end. In both schematics the cantilever bending and the displacement are exaggerated.	75
4.2	Frequency-dependent oscillation profile (amplitude-black and phase-cyan) of the cantilever in water. Arrows indicate the operational frequencies (133 Hz and 2.033 kHz) we have used for the measurements. (a) The frequency response in conventional deflection-detection type AFM. The resonance frequency of the cantilever in water is 13.54 kHz. (b) The frequency response in interferometer based displacement-detection type AFM. The resonance frequency of the cantilever in water is 12.74 kHz.	79

- 4.3 Raw data of the measurements performed using a deflection detection type AFM (a) The X and Y components of oscillations in the bending $((dy/dx)_L)$ at the tip end of the cantilever. The measurements are performed at 133 Hz . (b) The amplitude and phase of the oscillations in the bending (dy/dx) of the tip end of the cantilever. The same measurements are repeated at 2.033 kHz in (c) and (d). The Y -component in both measurements is featureless and according to Eq. 4.17 the dissipation in single molecules is immeasurably low. The phase shows clear oscillations in (d), however the corresponding Y -component in (c) does not change as the domains are sequentially unfolded. The use of point-mass model wherein dissipation depends on phase would result in erroneous measurement of dissipation. 80
- 4.4 Raw data of the measurements performed using home-built interferometer based AFM. (a) The X and Y components of the oscillations in the displacement at the tip end $(y(L))$ of the cantilever. (b) The amplitude and phase of oscillations in the displacement. The operational frequency for (a) and (b) is 133 Hz . In (c) and (d) the measurement is repeated for 2.033 kHz . Unlike the phase of the the bending signal in Fig. 4.3(d), the phase of the displacement does not show variations as the protein unfolds. 82
- 4.5 (a) The stiffness estimated from X -component of the cantilever bending at the tip end $((dy/dx)_L)$ using a deflection detection measurement. The peak stiffness is $\approx 20\text{ mN/m}$. This matches well with reports from other measurements and the derivative of the static force-extension curves (see supplementary Fig. S2). (b) The stiffness estimated from the X -component of the cantilever displacement at the tip end $(y(L))$ using the interferometer based AFM. The values of stiffness estimated using both detection schemes are in agreement with each other. 83
- 4.6 Measurements performed at 133 Hz with similar cantilever using a different cantilever holder. The phase of the cantilever bending at the tip end is not 180 degree in deep contact (data not shown). The phase of the free cantilever after immersing in the buffer deviates from the measurement in Fig. 4.3 by the same amount. This is clear case of presence of extraneous phase θ_e . The peaks in Y -signal are identified by arrows. This variation in Y as the protein unfolds is likely to be falsely interpreted as dissipation. 84

- 4.7 Schematics to show how extraneous phase produces artefacts in the measurement. (a) $\theta_e = 0, \bar{\gamma}_i = 0$; The change in k_i affects both phase and amplitude but Y -component remains unchanged. (b) When θ_e is nonzero, The phase and amplitude changes but Y remains unchanged in the co-ordinate system XY wherein $\theta_e = 0$. However in the xy coordinate system, the change in stiffness of the molecule k_i changes the Y -component from y to y' . Using Eq. 4.17 this can be misinterpreted as the dissipation. The change in Y -component is due to change in molecule's stiffness. 86
- 4.8 Measurements performed with 50 % glycerol in the buffer. This increases viscosity of the medium by ~ 8 times. The θ_h is nearly 18 degrees, however $\theta_e = 0$. As the polyprotein is pulled and the domains unfold, the phase changes but the Y -component does not show any variation. This shows that even if the phase is far from zero due to hydrodynamics alone, the Y -component shows no variation indicating again that the dissipation coefficient is immeasurably low. This is in agreement with results in Fig. 4.3 (b) and (d). 87
- 4.9 The dissipation coefficient computed using continuous beam model given by Eqs. 4.19 and the phase and Y -component of the displacement amplitude shown in supplementary Fig. S9. Dissipation shows clear oscillations peaked at separations equal to diameter of water molecules. The variation in phase and Y -component is not seen in case of proteins. 88
- 5.1 Schematic representation of oscillating cantilever under influence of a linear interaction force. In off-resonance operation the medium damping is negligibly small and hence not shown in the schematic. (a) Representing the base-excited cantilever where base is driven by $Ae^{i\omega t}$. (b) Representing the tip-excited cantilever where base is rigidly fixed and tip is excited with force $F_0e^{i\omega t}$ 97
- 5.2 Schematic representation of point-mass approximated cantilever under influence of a linear interaction force. These are devoted to off-resonance operation where medium damping is negligibly small. (a) Representing the base-excited point-mass approximation where base is driven by $Ae^{i\omega t}$. (b) Representing the tip-excited point-mass approximation where base is rigidly fixed and tip is excited with force $F_0e^{i\omega t}$ 101

- 5.3 Schematic for the magnetic excitation setup. An alternative current from the function generator is supplied to the solenoid which creates an alternative magnetic field. A cantilever with cobalt coated at the end is positioned on top of the solenoid. The sinusoidal motion due to the field is detected by the four quadrant photo detector. Photo detector output signal is fed to the lock-in amplifier to determine its amplitude and phase or X and Y signals. Eventually the signals are grabbed by the computer. 104
- 5.4 Frequency response of the cantilever with a thin layer of $Cr - Co$ coating at its end position. It can be observed that the low frequency regime is flat and free from spurious peaks. Also phase is small. The experiments were performed at $133 Hz$ 105
- 5.5 (a) Schematic of interferometer based AFM equipped with base-excitation mechanism. Cantilever is attached with a piezoelectric block which excites its base. Interferometric-detection scheme measures displacement ($y(t)$) of cantilever end. (b) Representing tip-excitation setup equipped with a deflection-detection mechanism. A thin layer of cobalt is coated at the tip-end, which is used to excite cantilever's tip using an electromagnet placed beneath it, base of the cantilever is rigidly fixed. Optical-deflection-detection scheme measures the bending ($dy(t)/dx$) of the cantilever end. A protein with one domain is tethered between the substrate and cantilever-tip. 106
- 5.6 Base-excited unfolding experiment was performed on polyprotein using interferometer based detection scheme wherein cantilever displacement is measured. (a) X -component (solid circle in cyan) and Y -component (solid square in green) of displacement. (b) Amplitude (solid circle in cyan) and $Phase$ (solid square in green) of displacement. 108
- 5.7 Tip-excited unfolding experiment was performed on polyprotein in deflection detection scheme wherein cantilever bending is measured. (a) X -component (solid circle in cyan) and Y -component (solid square in green) of bending. (b) Amplitude (solid circle in cyan) and $Phase$ (solid square in green) of bending. 109
- 5.8 Stiffness calculated using CB model (solid circle in blue color) and PM model (Solid diamond in red color). (a) Represents base-excited displacement measurement. (b) Represents tip-excited bending measurement. 110

5.9	Stiffness of tip-sample contact. interaction regime. Base-excited experiment has been performed in displacement detection system. Blue curve is stiffness estimated using CB model and red curve is using PM model. At low stiffness of the contact, both models yield similar stiffness. However, as the tip is further pressed into high stiffness region, they significantly deviate from each-other. The inset shows zoomed in part of highlighted main curve with dotted square.	111
6.1	Few representative tip-displacement-amplitude vs extension curves at different drive amplitudes. Experiments were performed at small frequency (433 Hz). For higher drives, the fractional change in tip-amplitude during protein extension is lower which indicates reduction in the stiffness.	117
6.2	Peak stiffness with total displacement amplitude (in <i>rms</i>). Stiffness is consistent for the oscillation amplitude upto $\sim 3 \text{ \AA}_{rms}$ and it shows transition afterwards. It reduces further with the oscillation amplitude. We attribute the $\sim 3 \text{ \AA}_{rms}$ as the characteristic length for the I27 ₈ in AM-AFM experiments.	119
6.3	Stiffness estimated by substituting the solution of Eq. 6.2 into Eq. 6.1. Small amplitude oscillation stiffness overlaps with the static stiffness (black circles), whereas a significant deviation can be observed for higher amplitudes. For low stretch, all amplitude results are predicting similar values which is expected as the steepness of the WLC force at lower stretch nearly linear. The lower oscillation amplitude predictions strongly support our experimental observations.	120
6.4	Percentage change in polymer stiffness with drive amplitude. Below 1 \AA drive amplitude, WLC stiffness is reproduce well by estimated stiffness from Eq. 6.1 and above that a significant deviation can be observed.	121
6.5	Representing the peak force (unfolding force) with drive amplitude. Drive amplitude is presented in volts which can be converted into nanometers by calibrating the dither piezo used to drive the cantilever base. Unfolding force of folded domains reduces with increase in the tip amplitude. This indicates softening of folded domains with increase in tip amplitude.	122
6.6	Raw data of unfolding of I27 ₈ molecule at high frequency (2633 Hz) and high amplitude ($\sim 5.4 \text{ \AA}$). (a) <i>X</i> and <i>Y</i> signals in blue solid circle and red solid square respectively. (b) Amplitude and phase signals in blue solid circle and red solid square respectively. Variation in <i>Y</i> and phase signal can be observed corresponding to every unfolding peaks. This signature is more prominent in initial unfolding events.	123

S1	Oscillation profile of base and tip in water for smaller frequency range. Gray and black curves represent the amplitude of the base and tip respectively. Light-cyan and dark-cyan curves represent the base and tip phase respectively. Dotted vertical line represents the range up to which Eq. 11 holds (base and tip amplitudes are approximately same and move in-phase).	144
S2	Directly measured stiffness using deflection detection scheme and the derivative for force simultaneously measured by static deflection of the cantilever.	145
S3	Three unfolding experiments carried out with (a) no added electronic phase (b) by addition -40 degree phase (c) addition of -80 degree. There is no variation in Y without addition of external phase. The variation is seen in Y with addition of external phase and close to -90 degree the there is more variation in Y -component as compared to X -component.	146
S4	Measurements performed when the frequency response is not free from local peaks. The Y -signal shows variation and peaks where the stiffness is maximum. This may wrongly get interpreted as the dissipation signal. . . .	147
S5	(a) Measurements performed at higher frequencies using deflection detection type AFM. The Y -component of the bending oscillations shows variations after 4 kHz . (b) Measurements at higher frequencies using interferometer based AFM. The Y -component of the displacement oscillations shows peaks at extensions where domains unfold. In both measurements, the phase response is not flat. For higher frequencies the phase and the Y -component is not constant when the tip is far from the substrate. In these measurements the electronic phase lag was ensured to be absent by recording phase in the deep contact region (see Fig. S6).	148
S6	Phase at the deep contact at different excitation frequencies are 180 degrees. Free phase increases with increasing excitation frequencies due to increase the hydrodynamic effect in free cantilever	148
S7	Measurements performed in 70% glycerol in the solution using deflection detection scheme. At higher viscosity, the measurement at $\sim 133 Hz$ is not truly off-resonance. The Y as well as phase shows variation as protein is unfolded sequentially.	149
S8	Frequency and phase response in 70% glycerol medium in commercial AFM. It is difficult to find truly off-resonance regime in these curves.	150

-
- S9 The raw data from which dissipation coefficient in Fig. 9 is computed. The measurements are performed with interferometer based AFM. The phase for the cantilever displacement is zero when immersed in liquid and is far from the substrate. The data shows variation in both the phase and Y -component of the displacement signal. 151
- B.1 The peak value of the stiffness were calculated from four independent methods: base of the cantilever was excited using dither piezo and displacement at the end was measured ($n=39$), tip was excited and the slope was measured ($n=45$), and derivative of the static force signal ($n=28$). All these values were matching well with each-other. Error bars represent standard deviation. . . 154

Nomenclature

Acronyms / Abbreviations

\AA - Angstroms

AFM - atomic force microscope

AM-AFM - amplitude-modulation atomic force microscopy

m^* - effective mass

CB - continuous-beam

Hz - Hertz

Cr-Co - chromium-cobalt

DNA - deoxyribonucleic acid

DSF - differential scattering fluorimetry

DSLS - differential static lightscattering

γ_c - cantilever damping coefficient

γ_i - interaction damping coefficient

ω - excitation frequency

A - base displacement

E - Young's modulus

F_i - interaction force

FM-AFM - frequency-modulation atomic force microscopy

FRET - Foster resonance energy transfer

k' - effective stiffness

GdnHCl - guanidine hydrochloride

θ - phase

I - second area moment

k_c - cantilever stiffness

k_i - interaction stiffness

L - cantilever length

R - amplitude

I27 - immunoglobulin27

Ig - immunoglobulin

MD - molecular dynamics

rms - root mean square

MT - magnetic tweezers

nm - nanometer

NMR - nuclear magnetic resonance

OT - optical tweezers

PBS - phosphate-buffered saline

PEG - polyethylene glycol

γ' - effective damping coefficient

pH - potential of hydrogen

PM - point-mass

PSD - power-spectral-density

PSDs - phase-sensitive detectors

RNA - ribonucleic acid

SHO - simple harmonic oscillator

SMFS - single-molecule force spectroscopy

STM - scanning tunneling microscope

T-jump - temperature-jump

UHV - ultra high vacuum

Chapter 1

Introduction

Proteins are essential building blocks of all living creatures of all kingdoms. These are the second most abundant molecule in human body and are necessary to regulate it. They play crucial role in the process from zygote to human body formation. They are the efficient molecular machines involved in various functions in our body such as metabolism [164], inter and intra-cellular communication [1], cell adhesion [4], cell division/degradation [60], DNA transcription/translation [122, 139], protein production [32], protein folding/degradation [113, 121], maintenance of the cell and tissue structure [53], organelle transport inside the cells [67], carriers in the blood stream [149], mechano-transduction [185], immune system [174]. The study of the fundamental properties of proteins will assist to understand different biological processes in human body which will be helpful in curing various diseases. They are naturally abundant molecular motors which can be artificially synthesized once the formation and functions of proteins were understood.

There are variety of proteins which work under forces. Mechanical properties of such proteins are essential to understand their functions [30, 48, 70, 81, 101, 110, 125, 130]. Various techniques have been developed such as Atomic Force Microscope (AFM), Optical Tweezers (OT), and Magnetic Tweezers (MT) to study the mechanical properties of single molecules [103, 108, 111, 127, 148]. These techniques have also been applied to study the thermodynamics and kinetics of the protein folding.

In this chapter, I will introduce the proteins, their structure and formation, and their different applications in human bodies. I will discuss about the various techniques which have been applied in the past to study protein folding/unfolding kinetics and thermodynamics at bulk and single molecule level. The discussion will be focused on the single-molecule techniques, specially on Atomic Force Microscopy, as I have extensively used it for my study.

1.1 Proteins

Proteins are natural polymers, also known as polypeptides. These are made up of monomeric units, called amino-acids. Amino acid is an organic molecule containing a carbon atom covalently connected with an amine group (NH_2), a carboxylic group ($COOH$), a hydrogen (H), and a side group (R) (Fig. 1.1). There are 20 amino-acids which participate in the protein synthesis. The chemical structure of all the 20 amino-acids are same except their side group (R). Depending on the nature of the side group (or side chain), amino-acids can be divided into 6 categories: (i) *polar*: serine (S), threonine (T), glutamine (Q), asparagine (N), (ii) *non-polar*: glycine (G), alanine (A), proline (P), valine (V), leucine (L), isoleucine (I), (iii) *positively charged*: histidine (H), lysine (L), arginine (R), (iv) *negatively charged*: aspartic acid (D), glutamic acid (E), (v) *sulfur containing*: cysteine (C), methionine (M), (vi) *aromatic*: phenylalanine (F), tyrosine (Y), tryptophan (W).

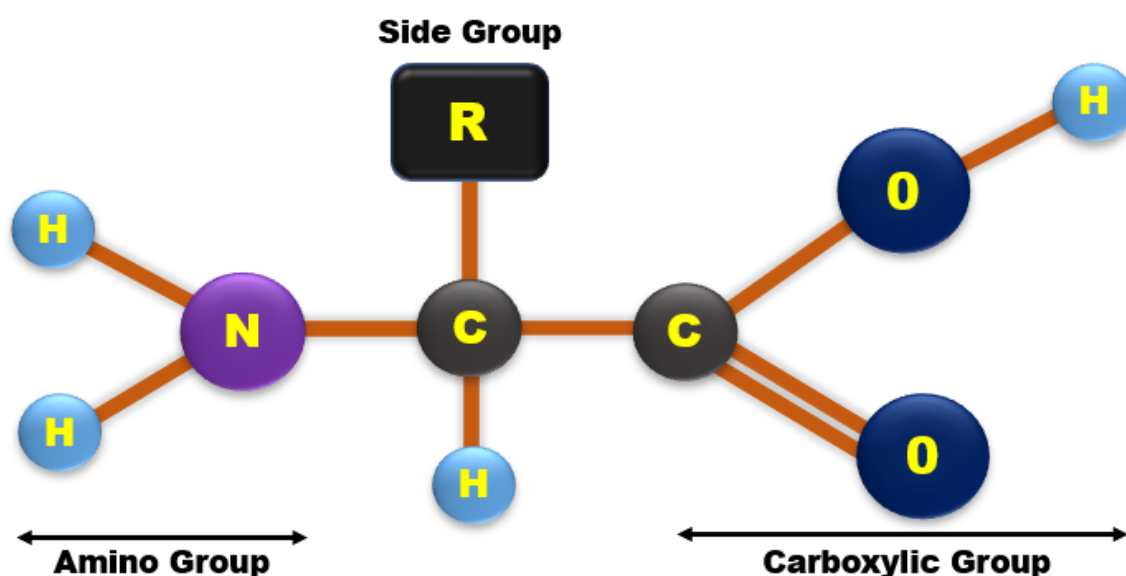


Fig. 1.1 Structure of amino-acid containing a central carbon atom covalently connected with an amine group (NH_2), a carboxylic group ($COOH$), a hydrogen (H), and a side group (R). Side group (R) makes difference between 20 naturally abundant amino-acids which contribute in protein synthesis.

1.1.1 Structure of Proteins

The carboxyl of an amino-acid forms a covalent bond with the amino group of another amino acid by releasing a water molecule (H_2O). Final compound is dipeptide and newly formed bond is known as peptide bond (Fig. 1.2) [71]. By the same process, a linear chain of amino-

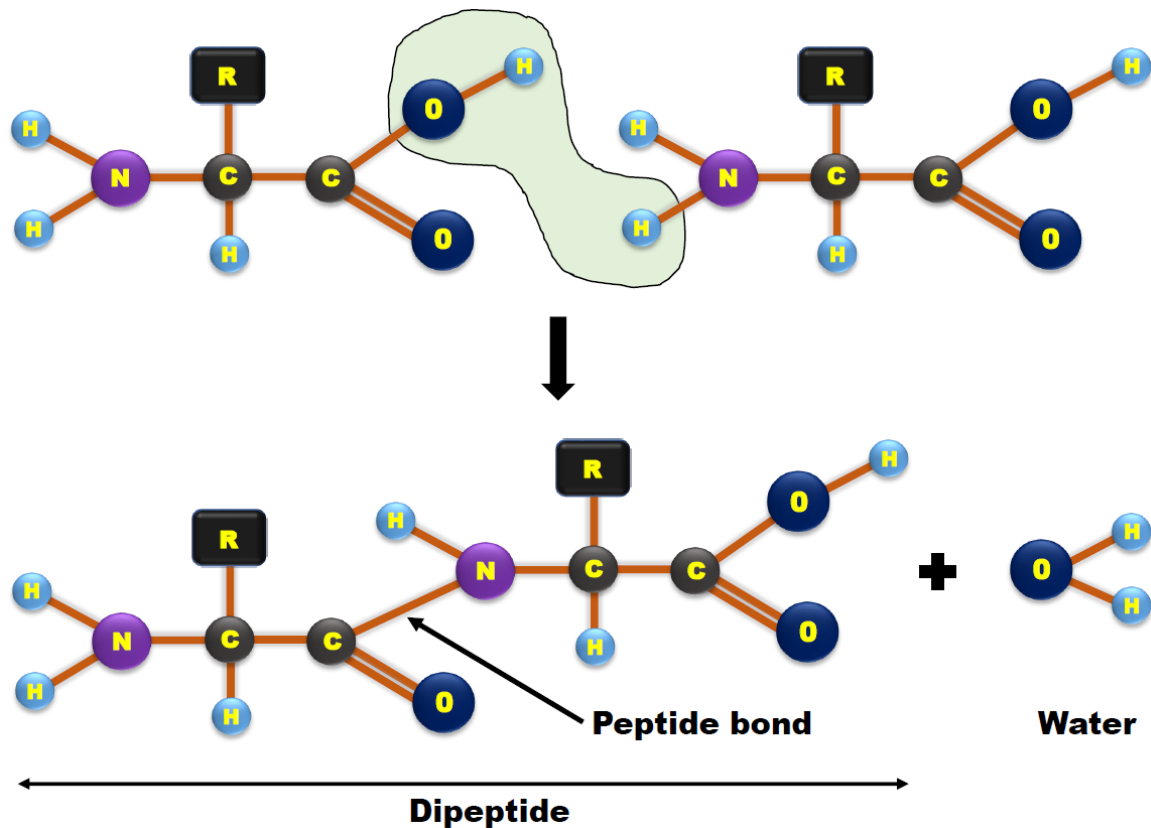


Fig. 1.2 Graphical representation of (di)peptide formation. Two amino-acids combine to form a dipeptide and a water molecule is being released. Similarly, multiple amino-acids combine and form polypeptide which is primary structure (primary sequence) of protein.

acids is formed, where each amino-acid is covalently connected with its adjacent one. This polypeptide chain is known as '*primary structure*' or '*primary sequence*' of a protein. The order and positions of amino-acids in the primary structure determines the native structure that is essential for its function. In an appropriate environmental condition, polypeptide chain collapses into a molten globule state. In this state the amino-acids are in proximity such that they can form non-covalent bonds with each other. These interactions could be of different types in nature: hydrogen bonding (*H-bonding*), hydrophobic, electrostatic, and Van der Waals etc. Before going to the native state, proteins form local structures called '*secondary structure*'. Secondary structure forms due to the interactions (*H-bonding*) between different backbone atoms in the primary sequence, it does not involve side chain interactions. On the basis of their structural arrangements, secondary structures have been categorised into two types: (i) α -helices: the Oxygen from a carboxyl-group of one amino-acid forms H-bond with the Hydrogen of the amino-group of another amino-acid in the chain. Each turn of helix contains 3.6 amino-acids. and (ii) β -sheets: in this structure, the two segments

of the backbone chain lineup in such a way that it appears like a sheet. When the direction of one segment (direction of N to C terminus) is same as the other, it is known as *parallel β -sheet* configuration, however, when they are in opposite, it is known as *anti-parallel β -sheet* configuration. The various interactions between secondary structures form a stable 3D structure, called *tertiary structure*. Depending on the amount of α -helices and β -sheets, the tertiary structure can be classified into three: all α structure, α/β structure, and all β structure. When the protein is made up of only one primary chain (primary sequence), the tertiary structure is the native state. However, many proteins are made up of multiple primary chains and have multiple tertiary structures. In such proteins, different tertiary structures combined to form native state, called *quaternary structure*.

1.1.2 Classification of Proteins

Every protein in our body has a specific function to perform which depends on its unique native structure (shape). In the process of folding, if a protein does not acquire its desired native structure then it is called a misfolded protein. A misfolded protein can not perform the function for which it has been made and sometimes it also prevents the other active proteins to function. So, it is essential for a protein to acquire its desired native structure in order to function. Surrounding medium play a crucial role in protein folding process. On the basis of structure and interaction with the surrounding, proteins can be broadly classified into three classes:

(i) Globular proteins: In globular proteins, the secondary and native states are formed to hide the hydrophobic side groups from the surrounding solvent and eventually acquire a globular shape. Its secondary structures can be all α , all β , or α/β . This class of proteins are water soluble in nature and can move from one place to another in liquid environment. Sometimes these are the elementary units of fibrous proteins. For example muscle protein titin is made up of multiple Ig-like protein domains along with other elements. Immunoglobulin, insulin, myoglobin, globin, histone, albumin, and rubisco etc. are the examples of globular proteins.

(ii) Fibrous proteins: Fibrous proteins are made up of the elongated polypeptide chain(s) which are fibrous or sheet like in structure. Multiple long polypeptide chains with specific shapes can intertwine to form a long fiber like structure which will be having interesting three-dimensional properties to perform specific functions. The native structure of these proteins are fibrous in shape. These are not water soluble. They are often structural proteins and hence mechanically stable and serve as the structural support of the cells and tissues.

Example: keratins, collagens, myosins, elastins etc.

(iii) Membrane proteins: A cell is covered with an outer layer called cell-membrane. A cell membrane is made up of two lipid layers known as lipid bilayer. A lipid bilayer is made up of lipid molecules. Each lipid molecule has a hydrophilic (head) and a hydrophobic (tail). They come close to protect their hydrophobic heads from the surrounding liquid environment and form a two layer structure, called lipid-bilayer. The communication/transportation between the inner and outer part of the cell happens through some channels. These channels are nothing but the proteins embedded in the cell-membrane. These proteins are called membrane proteins. These proteins are embedded in the membrane in such a way that the amino-acids with hydrophobic groups are present inside and hydrophilic groups are outside of the membrane. This can be further classified depending on their structures: α -helices and β -barrel. Former one have multiple α -helices traversing multiple times across the membrane and latter have multiple β -sheets which form a barrel-like structure to provide a channel through the membrane. Example: spectrin, kinase, phospholipases, glucose permease, glycoprotein etc.

1.1.3 Functions of Proteins

Proteins are the molecular machines that perform a diverse range of functions in our body. Each protein is synthesised for a specific function and various diseases can be caused when a specific type of proteins stop working due to misfolding or aggregation [20, 25, 36, 58, 61, 97]. For example: Parkinson's disease, Alzheimer's disease, Creutzfeldt–Jakob disease, Huntington's disease, Gaucher's disease, cystic fibrosis, and many other neurodegenerative and degenerative disorders. To properly regulate the body, all the proteins are required to perform their specific functions. Few important functions of the proteins in human body are following:

(i) Growth and maintenance: Protein synthesis and breakdown process is a regular process in our body. In normal situation, this happens in a steady state manner i.e. the amount of protein breakdown is equal to the amount of synthesis. However, in cases like illness, breastfeeding, injury etc., body needs more protein to be synthesised. Thus the protein intake to the body need to be increased.

(ii) Biochemical reactions: There are various proteins which helps in biochemical reactions to happen in and outside the cells. For example: blood clotting, energy production, digestion, and muscle contraction etc. The enzymes are the proteins which initiate metabolism process by combining with substrates (specific molecules inside the cell). Digestive enzymes are the proteins which function outside the cell. For example, the lactase and sucrase helps in sugar

digestion.

(iii) Messenger proteins: A major class of hormones is protein which helps in communication process between the cells, tissues, and organs. Few examples of the messenger proteins are following: *insulin* indicates the uptake of sugar and glucose in the cells, *human growth hormone (hGH)* stimulates the growth of tissues, *glucagon* indicates the breakdown of the glucose in the liver, *antidiuretic hormone (ADH)*: indicates the kidneys to reabsorb water.

(iv) Structural proteins: Structural proteins are mechanically strong. They provide structure and shape to the cells, tissues, and organs. Keratin, collagen, elastin are few examples of this class of proteins. *Keratin* is a fibrous protein that makes up skin, hair, and nails. *Collagen* is the most abundant protein in human body. It provides structural support to bones, ligaments, skin and tendons. *Elastin* is responsible to provide the flexibility to the organs (such as uterus, lungs, and arteries), so that they restore their initial state after stretch/contraction.

(v) Maintain pH: The pH level decides the amount of H^+ and OH^- . In our body, different organs function at their optimal pH level. The alteration in pH values can cause serious disorder. Proteins work as a buffer to maintain the pH levels. For example: hemoglobin helps to maintain the pH in the blood.

(vi) Nutrients transport and storage: The intake nutrients (vitamins, minerals, cholesterol, oxygen etc) has to be transported to different organs in the body. This is done by various proteins such as hemoglobin which transports oxygen from lungs to different tissues and lipoprotein which transports cholesterol and other fats in the blood. Many proteins work as the storage of nutrients. Ferritin stores iron which fulfils the iron requirement in the blood.

(vii) Energy buffer: The primary sources of energy in our body are carbs and fat. Protein is a secondary source which is being used in case of low carbs/fat storage. In order to generate the energy, proteins are broken down to the amino-acids. For example: during fasting, energy is generated by breaking down the skeletal muscles.

(viii) Immune system: The deficiency of the proteins/amino-acids impairs the immune system. Unknowingly, we intake the harmful foreign elements like bacteria and viruses which affect our immune system. These cause serious diseases. The antibodies are proteins

which fight with these harmful elements and protect our body.

Proteins are naturally abundant molecular machines. In a cell, proteins interact with other biomolecules, such as DNA, and perform various jobs which are essential to regulate our body. So, the study of the fundamental properties of proteins, such as folding, mechanical stability, interaction with other molecules etc., is of great interest to research. A complete understanding of protein folding process will provide a recipe of constructing the nano-machines which can perform various jobs very efficiently at the nano-scale level. The understanding of fundamental properties and functions of various proteins will help in advancement in the field of medical research. For example, various diseases like Alzheimer's, Parkinson's etc. happen due to misfolding of proteins. Misfolded proteins are unable to function and prevent the underlying physiological process resulting in serious diseases. Knowing the cause and mechanism of protein misfolding is helpful in curing the associated diseases. Many research labs, across the world, are dedicated to study the fundamental properties of proteins.

1.2 Protein unfolding studies

The type of constituent amino-acids and their positions in primary structure determine a unique 3D (native) structure for each protein. The native structure is essential for a protein to function. How the primary sequence of amino-acids attains a unique 3D structure, has been still unanswered? This is known as *protein folding problem*. In order to fully understand the protein folding, following three questions have to be answered: (i) *thermodynamics*: how does a primary structure attains its unique 3D structure? (ii) *kinetics*: how does a protein go from its primary structure to the native structure in a biologically relevant timescale? (iii) *misfolding*: how does it avoid the misfolding?

In past few decades, the protein unfolding experiments were performed to understand the protein folding problem. In a typical unfolding experiments, a protein is denatured using a specific method and the observable parameter is recorded with change in an appropriate reaction coordinate. The method of denaturation, observable parameter, and reaction coordinate are different in different unfolding measurements [104]. The studies on protein unfolding can be classified into two categories: bulk and single-molecule studies.

1.2.1 Bulk studies:

In bulk unfolding studies, an ensemble of protein molecules is simultaneously observed and the average behaviour of molecules can be determined. The denaturation can be caused using various ways such as introducing the chemical denaturation agent (urea, guanidine hydrochloride) in the protein solution, increasing the temperature, applying high pressure, altering the pH value of the protein solution etc. There are various physical properties which change when protein changes its confirmation from folded to unfolded state. By observing the change in one of these parameters, the denaturation process can be monitored. For example: in globular proteins, the residues with hydrophobic side chains are hidden at its core when it is folded. However, upon denaturation, these side chains are exposed to the surrounding aqueous medium. This change can be monitored by introducing a environment sensitive dye into the protein solution. In aqueous environment, the florescence is quenched, however, the dyes are highly sensitive to the non-polar environment such as the hydrophobic sides of the unfolded protein chain. Few bulk unfolding measurements are briefly discussed below.

1.2.1.1 Chemical denaturation:

In this measurement, protein is unfolded by mixing a chemical denaturant in the protein-buffer solution [8, 46, 124, 169, 177]. Urea and guanidine hydrochloride (*GdnHCl*) has been extensively used as denaturant agents in chemical denaturation based unfolding experiments. Both the molecules are highly soluble and have low molecular weight, such that 6-8 molar concentration will denature any proteins. However, the molecular dynamics (MD) simulation of unfolding of a protein using urea and guanidine hydrochloride revealed that the molecular mechanics of unfolding are different in both cases [138].

In a typical chemical denaturation experiment, the concentration of the denaturant is varied and the change in a physical parameter is observed. There are various physical parameters which change when a protein goes from its native state to denatured state. Hence, there can be various techniques to observe the unfolding. The popular techniques are based on ultraviolet difference spectroscopy [37], optical rotation [184], circular dichroism [184], NMR [182] and fluorescence [17]. The sensitivity of a technique is determined by the change in the physical parameter when proteins unfold. More change in the physical parameter represents better the technique is or the technique is more sensitive. The fluorescence based technique is recognised as more sensitive one.

In fluorescence based denaturation measurements, unfolding is observed by a plot between fluorescent-intensity vs denaturant concentration- known as *denaturation curve*. Usu-

ally, an appropriate wavelength, which shows more intensity change with change in protein conformation, is selected for measurement. All the experiments are done at equilibrium. Following equation can be used to extract conformational stability (ΔG_D) at different denaturant concentrations:

$$\exp(-\Delta G_D/RT) = \frac{y - y_N}{y_D - y} \quad (1.1)$$

Where R and T are molar gas constant and absolute temperature respectively. y - fluorescence intensity (it can also be other observed parameter). y_N and y_D are the characteristic parameters at native and denatured state respectively. These characteristic parameters can be estimated by linear extrapolation of low and high concentration regions of the denaturation-curve [46, 136]. The conformational stability at zero denaturant concentration ($\Delta G_D^{H_2O}$) can be estimated by fitting the following equation to the ΔG_D vs denaturant-concentration data-known as method of linear extrapolation [54]:

$$\Delta G_D = \Delta G_D^{H_2O} - m(\text{denaturant}) \quad (1.2)$$

Where m is referred as m -value. This is characteristic of the individual proteins.

What kind of information can be extracted from chemical denaturation studies? One can largely extract following information from these studies [136]: (i) conformational stability, (ii) folding mechanism, and (iii) structural information. *Conformational stability*- free energy difference ($\Delta G_D^{H_2O}$) between the native and denaturation state - is a measure of resistance to maintain its structure against the external perturbation. Large value of $\Delta G_D^{H_2O}$ specifies more stable conformation i.e. it can maintain its native structure in presence of higher external perturbations. A comparative studies of conformational stabilities of various proteins can be made using this method. These experiments suggest the nature of unfolding - whether it is a two-state unfolding or not. This information can be used to predict the behaviour of *folding mechanism*. The *structural information* can be drawn from the denaturation curves. The presence of more than one step in denaturation curve indicates the presence of multiple domains in the protein.

The downside of chemical denaturation experiments is the mixing time while changing the solution. For example, in kinetic experiments of protein folding, rapidly diluting the sample to prompt refolding is a technical challenge. The data analysis is based on consideration of the sample in equilibrium. However, during the mixing/dilution (called dead-times), the sample is not in equilibrium and also the measurements cannot be made during the dead-time. In conventional stop-flow mixers, this time is 1-5 ms that is determined by the turbulence induced in the mixing process. The duration of the dead-time has been reduced to $\sim 30 \mu s$

by using smaller turbulence mixer [11, 86]. The development of laminar mixer has further reduced the dead-time to 2-4 μs [63, 64].

1.2.1.2 Temperature denaturation:

In this method, the protein is unfolded by increasing the temperature of the protein-solution [33, 104, 128, 158, 161]. Increase in the temperature causes the destabilization of the native contacts which results in the denaturation of the native protein. The fluorescence based techniques such as differential scattering fluorimetry (DSF) and differential static light scattering (DSLS) had been used to monitor the denaturation process [158, 175].

In DSF, protein is heated with a particular rate and the fluorescence intensity is observed. Typical heating rate is $\sim 1^\circ C/min$ and temperature range is $25^\circ C - 95^\circ C$. The dye used for this measurement is environment sensitive. In aqueous environment, the fluorescence is quenched, however, the dyes are highly sensitive to the non-polar environment such as the hydrophobic sides of the unfolded protein chain. At low temperature, where the majority of proteins are in their native state and hydrophobic sites are not exposed to the surrounding, the low intensity is observed. However, at high temperature proteins denature and hydrophobic side chains are exposed to the dye molecules. This results in the increase of the fluorescent intensity. The intensity vs temperature plot generates a sigmoidal curve which can be described by the two-state transition mechanism [129].

Thermal unfolding of the protein has been described in terms of the change in Gibbs free energy ($\Delta G = \Delta H - T\Delta S$) between the unfolded and native state [104]. As the temperature increases, the difference in the Gibbs free energy (ΔG) reduces resulting in the increase of the unfolding probability/rate. When the $\Delta G = 0$, the unfolding and refolding probability is same and hence the population in folded and unfolded states are same. This temperature is called transition temperature and usually denoted by T_m . At sufficient high temperature, $\Delta G < 0$ and unfolding probability is higher compared to the folding probability and hence the majority of proteins are found at unfolded state.

There are many advantages of the thermal denaturation based studies. The computer simulation for this measurement is relatively easy compared to the other denaturation methods as the heat is inherently accounted for in the molecular-dynamic (MD) simulations. The computer simulation of high temperature experiments ($\sim 225^\circ C$) was possible as it matches with the computation timescale [33]. The development of temperature jump (T-jump) experiment allows the measurement in $ns - \mu s$ timescale [172].

1.2.1.3 Pressure denaturation:

The first observation of pressure denaturation of protein was accidentally observed by P.W. Bridgman [18]. In this method, protein is denatured by applying high pressure to it [57, 72, 104, 150]. Like temperature, this method is also easy to simulate computationally.

Proteins denature under high pressure- 100 - 300 *MPa* [104]. It was observed that the denatured protein acquires low molar volume compared to its folded state i.e. the change in volume is negative ($\Delta V < 0$). This reduction in the volume reduces the free energy difference between the unfolded and folded state such that it become negative ($\Delta G = (\Delta U + p\Delta V - \Delta S) < 0$). Following reasons were proposed for this reduction in the volume: (i) the density difference between bulk water and water associated with the protein, (ii) change in the bulk water structure due to pressure, (iii) loss of internal cavities in the native state. Julien Roche et al. have shown that in staphylococcal nuclease, which contains 10 cavities in its native state, unfolding due to pressure happens because of the cavities present in the native state. These cavities are absent in the unfolded state [150].

Above-discussed methods are based on measurement on an ensemble of proteins. Every method has its own importance and limitations as well. It has been found that the unfolding pathways of protein are different in different methods. Unfolded state is a random state and it has huge number of conformations. Different methods occupy different volumes in its 3D unfolded conformational space i.e. the unfolded state in various methods lies in different volumes in its funnel-like energy landscape. For example, in mechanical unfolding, the denatured molecule's end-to-end distance is much larger than the chemically denatured one leading to fewer possible conformations. In folding measurements, the initial state is different for different methods and hence folding pathways will also be different. All these methods are limited to provide the quantitative information at the individual molecule level as these are bulk measurements.

1.2.2 Single-molecule studies:

In this method(s), a single biomolecule is directly probed to study the folding/unfolding process. A major advantage with single-molecule studies, compared to the bulk studies, is that the local/small features of folding/unfolding process such as the intermediate states can be measured. In the bulk studies, these features are averaged out as the ensemble of molecules ($\sim 10^{14} - 10^{17}$) are observed at a time. In order to have a complete understanding of the process of protein folding, the resolution up to single-molecule level is essential. In the past, a considerable amount of efforts has been made to develop single-molecule measurement

techniques. Single-molecule studies can be classified into two categories: single-molecule fluorescent spectroscopy and single-molecule force spectroscopy.

1.2.2.1 Single-molecule fluorescent spectroscopy:

Fluorescence measurement based techniques have been vastly used to study the change in the conformations in the biomolecules. For example, differential scattering fluorimetry (DSF) is used to monitor the unfolding of the proteins in thermal denaturation method. In DSF, the fluorescent dyes are highly environment sensitive. In aqueous environment, the intensity is quenched, however, it enhances significantly in the proximity of hydrophobic side chains. This allows to monitor the protein unfolding process.

Forster Resonance Energy Transfer (FRET), is a single-molecule fluorescent spectroscopy method which has been extensively used to study the protein folding/unfolding process. This was first proposed by the Foster in 1998 [43]. This is based on measurement of the fluorescent energy transfer rate between two fluorophores which is sensitive to the distance between them. This allows to monitor the change between the distance of two labeled residues during the protein folding [29, 100, 157, 187]. It was proposed that the electronic excitation energy can be transferred between a suitable pair of two fluorophores (donor and acceptor) and the rate of energy transfer (K_T) depends on the distance (r) as $\sim 1/r^6$ [168]. The rate of energy transfer and the efficiency of energy transfer by the donor (E_{ET}) are given by

$$K_T = \frac{K^2 J K_F \times 8.71 \times 10^{23}}{r^6 n^4} \text{sec}^{-1} \quad (1.3)$$

$$E_{ET} = \frac{r^{-6}}{r^{-6} + R_0^{-6}} \quad (1.4)$$

Where J is the spectral overlap integral, K^2 is the orientation factor (defined for a dipole-dipole interaction), K_F is the fluorescence emission rate constant of donor, and n is the refractive index of the medium between the fluorophores. R_0 is distance between the fluorophores at which the efficiency of the energy transfer is 50 %.

In simple single-molecule FRET experiment, the laser is focused on a tiny volume (few femtoleters) of a dilute protein solution. When a double-labeled protein molecule diffuses through the focused volume, the donor fluorophore gets excited and it relaxes to the ground state via transferring the energy to the acceptor when the necessary criterion is fulfilled. Acceptor fluorophore gets excited to its higher electronic state by absorbing the energy transferred by the donor and it relaxes by emitting the photon with different wavelength than the excited laser. The intensity of the emitted photons is related to the efficiency of the

energy transfer which is highly dependent on the distance between the two fluorophores. The measurement is repeated until a meaningful statistics is achieved [16].

There are two major reasons for the success of FRET: its inherent sensitivity, and a steep dependence of the efficiency of energy transfer on the distance between the fluorophores. This method can be used as a spectroscopic ruler to monitor the distance between the fluorophores in the range of $\sim 10 - 60 \text{ \AA}$. There are downsides of this technique. First one is that the efficiency of energy transfer does not depend only on the distance between the donor and acceptor, but also depend on their associated transition moment and angle between the respective dipoles. The other disadvantage is its intrinsic photolability, because of which the single-molecule FRET cannot be used on the protein in which naturally occurring tryptophan are not present [16].

1.2.2.2 Single-molecule force spectroscopy (SMFS):

A SMFS technique allows the investigation of folding/unfolding of a single protein molecule. Various thermodynamic and kinetic properties of protein folding/unfolded have been studied using these techniques [16, 23, 45, 107, 166, 171]. In a typical SMFS unfolding experiment, an external force is applied to a molecule and allowed it to unfold. The unfolding experiments are performed mainly in two ways: (i) constant speed pulling, and (ii) constant force (force-clamp). In constant speed pulling experiments, a molecule is pulled at a constant speed and the force vs extension profile is recorded [148]. The mechanical stability of a single molecule, at a given pulling speed, is directly measured which can be utilized to determine thermodynamic and kinetic parameters such as the barrier height between the native and transition state, the position of the transition state, folding/unfolding rate etc [71, 131]. In a constant force experiments, a molecule is held at a constant force and the extension vs time is recorded. These experiments allows to determine the thermodynamic and kinetic parameters such as position of the transition state, unfolding rate etc [156]. An additional advantage with the SMFS is that it explores the region between the molten globule state to the stretched state in the energy landscape which was unexplored in classical methods [16].

SMFS are different from the classical experiments due to following reasons. (i) This has a well defined reaction coordinate- extension of the molecule along the direction of pulling. This allows us to define the position of the transition state on unfolding energy landscape. (ii) A part of the molecule can be selected for measurement without affecting the other parts. (iii) One can completely avoid the effect of aggregation in the experiment by selecting the data which are having single-molecule fingerprints.

(i) Optical tweezers (OT):

Optical tweezers was invented by the Arthur Ashkin and he received Nobel prize for it in 2018. The working principle of the OT is based on the optical trapping of micro-objects. It was first reported by Arthur Ashkin and coworkers in 1968 [5]. This technique is extensively used to study the protein folding/unfolding [23, 59, 75, 166].

In an OT, a spherical bead is placed at the center of a Gaussian laser beam which is focused through a high numerical aperture lens. Bead is made up of silica or polystyrene. Its size is of the order of the wavelength of LASER (typically $\sim 1\mu m$) and refractive index is more than the medium. When bead is at the center of the beam, it experiences a force along the direction of light propagation due to the reflected light from the bead surface. This force is balanced by the force arising from the forward scattered beam by the bead. So the bead is trapped along the direction of light propagation. Since the refraction is symmetric, it is also trapped along the direction normal to the light propagation. Now consider the case when a small force is applied to the bead along the direction normal to the beam propagation, bead will be displaced from the center of the Gaussian beam resulting a intensity/momentum difference at different points towards the displacement of the bead. This results in a net restoring force on the bead towards the center of beam. This force is called restoring force. If the stiffness of the trap is known then OT can be used to estimate the force on the molecule tethered between bead and substrate [21].

To detect the bead movement, transmitted light is allowed to fall on a position sensing photo-detector. When bead is at the center of the beam, the refracted light is symmetric and transmitted light shows zero deflection. On the other hand, when bead is off-centered, the reflection is asymmetric. In this case, transmitted light shows deflection on the photo-detector. Using an appropriate calibration factor (detector sensitivity), the photo-detector output voltage can be converted to the actual bead movement [21]. Calibration of the detector sensitivity and trap stiffness (k) allow to estimate the force on the molecule ($F = k\Delta x$, Δx is displacement of the bead from the center of the beam). Here it is assumed that the trap potential is harmonic in nature. Trap stiffness can be calibrated using two methods: (i) experimentally applied known force (drag force on the bead - $F_d = 6\pi\eta r v$, r - radius of the bead, v - velocity of the medium liquid), and (ii) equipartition theorem ($k \langle \Delta x^2 \rangle / 2 = k_b T / 2$, K_b - Boltzman constant, T - absolute temperature, and $\langle \Delta x^2 \rangle$ - mean square displacement of the bead).

In typical OT protein unfolding experiment, a force is applied to the protein and the extension is measured. Unfolding landscape can be represented by a 1D free energy barrier, where extension on the molecule is the reaction coordinate. Applied force reduces the energy

difference between the native and unfolding state ($\Delta G(F)$) in linear fashion [21]:

$$\Delta G(F) = \Delta G^0 - F\Delta x - \Delta G_{stretch} \quad (1.5)$$

Where ΔG^0 is standard free energy, F is applied force, Δx is separation of the native and unfolded state at zero applied force, and $\Delta G_{stretch}$ is free energy required to stretch the polymer from unfolded state (molten globule) to a certain value where force on it is F .

OT is sensitive for the lower forces. Its force working range is $0.1 - 100 pN$. This is a powerful technique to mimic the physiological forces which are actually of the order of few piconewtons. OT is vastly used to study the protein folding/unfolding thermodynamic and kinetic properties. Apart from the protein folding/unfolding, it can also be used to study the mechanics of other biomolecules and micro-organisms. Limitations of OT are following. It cannot be used at high force regime ($> 100 pN$). Laser is supposed to be stable, any fluctuation can cause error in the measurement. The sample purity is crucial. Freely floating particles can get trapped and it can disturb the trapping of the bead. OT needs laser source with high intensity which causes local heating and it can alter the sample properties [118].

(ii) Magnetic tweezers (MT):

The first magnetic tweezers (MT) were assembled by Strick et al. in 1996 [167]. They used MT to explore the elasticity of a supercoiled DNA.

The structure of nucleic acids (DNA and RNA) is not static but it changes while performing various functions. DNA and RNA both exist in double-stranded (dsDNA and dsRNA) and single-stranded (ssDNA and ssRNA). Each structure has a specific function. Double-stranded DNA mainly stores the genetic information, however, single-stranded RNA is involved in various processes such as storage of viral genetic information, DNA replication and recombination etc [24, 137]. Single-stranded RNA is involved in many processes, for example: DNA transcription, translation, and gene regulation, however, Double-stranded RNA works as a carrier of genetic information in dsRNA viruses [180, 181]. The different structures of nucleic acids have many other consequences, for example: if a strain is applied to a dsDNA, it forms other structure such as acquiring additional twist, forming loops etc. These structures are known as DNA supercoiling. These additional structures are important in many cellular processes like cell division and cell cycle progression [106]. Different structural forms of nucleic acids possess different mechanical properties. Magnetic tweezers are capable to investigate these properties. MT has been widely used to study the mechanical properties of the nucleic acids [176]. This technique has been vastly used to study protein folding/unfolding [26, 159, 186] and mechanical properties of the cells [6, 160].

In typical MT experiment, sample is prepared on a flow cell where molecule is tethered between the glass surface and a paramagnetic bead. Molecule can also be tethered between a non-magnetic bead which is immobilised on the glass surface and a paramagnetic bead. A pair of two magnets (permanent or electromagnets) is mounted on top of the flow cell which is being used to apply force on the bead and hence on tethered molecule. Magnets pair also allows to apply a torque on the molecule. A light source is placed on top of the microscope and position of the bead is monitored in 3D by taking its image using a charged-coupled device (CCD) camera which is further analyzed by computer. Complementary metal oxide semiconductor (CMOS) camera has also been used. CMOS camera is faster than the CCD which allows to capture the motion at higher frequencies. Changing the distance between the bead and permanent magnet, the force on the bead can be tuned and the real-time measurement can be performed by monitoring the bead position with time [154].

MT allows to perform measurements with low forces (~ 10 fN). However, other single molecule force spectroscopic techniques do not allow measurements with such a low forces. The working range on the force is 0.01 – 100 pN [176]. The downside of MT are following. Detection of the bead is made using a high resolution camera which limits spatial and temporal resolution in the measurement. The measurements, based on the application of torque, is not readily possible because the torque applied on the attached molecule is orders of magnitude weaker than on the bead which is applied by the magnetic field [35].

(iii) Atomic force microscope (AFM):

Atomic force microscope is one of the popular techniques to study mechanics at the single-molecule level. This has been widely used to study mechanical, thermodynamic and kinetic properties of proteins. Since AFM is extensively used in present thesis, the different aspects of atomic force microscope is discussed in the next section in a detail.

1.3 Atomic force microscope (AFM)

Atomic force microscope (AFM) is a member of scanning probe microscope (SPM) family. It was invented by Gerd Binnig, Calvin Quate, and Christoph Gerber in 1986 [13]. Their motivation for this invention to get the morphology of poorly conducting surfaces which was not possible in scanning tunneling microscope (STM) as it only works for the conducting surfaces [14].

In AFM, a microcantilever-tip assembly is used as a force sensor where tip interacts with the sample that causes bending (or displacement) on the cantilever beam. Usually cantilevers are made using silicon based compounds. Bending on the beam can be measured using a

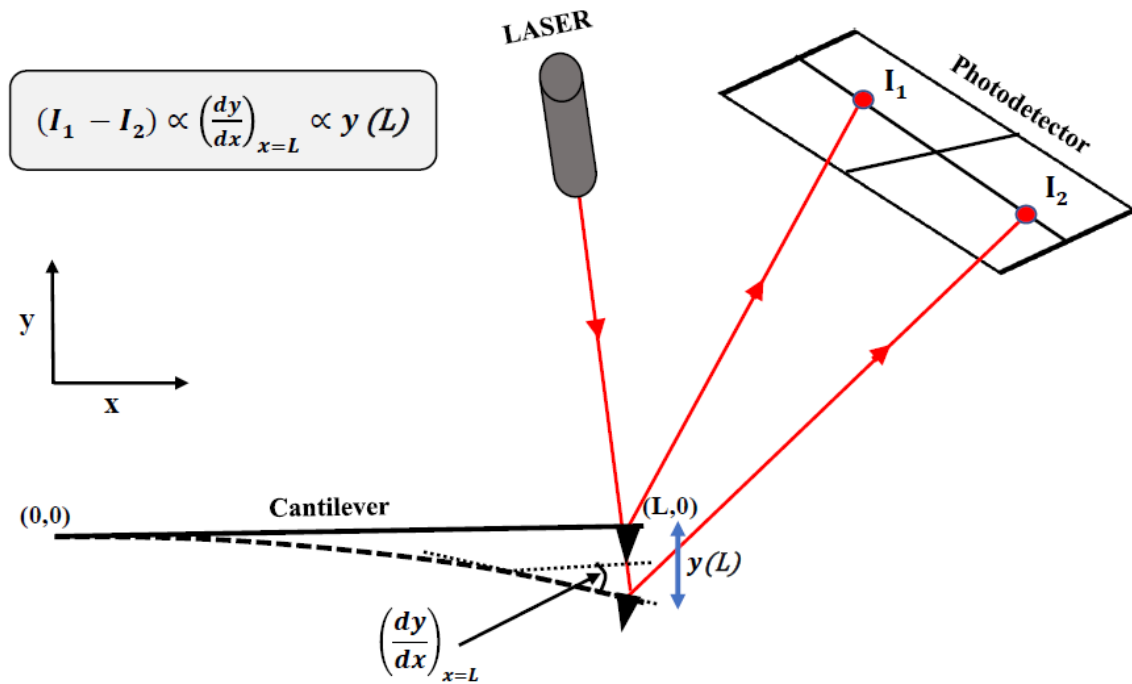


Fig. 1.3 Schematic representation of slope-detection based AFM. A laser beam reflects from the back of cantilever and collected at the position-sensitive photo-detector. In undeflected state, it generates some current (or voltage) difference (I_1 , net current on upper quadrant - net current on lower quadrant), however, the current difference changes to I_2 when cantilever deflects. The difference, $I_1 - I_2$, is proportional to change in the slope (dy/dx) of the cantilever which is again proportional to its displacement (y).

detection scheme (Fig. 1.3). For small bending, force between the tip and sample can be estimated using Hook's law: $F = ky$, where k is the force constant of the cantilever beam and y is bending. The force constant can be independently calibrated using various methods. AFM is capable to measure forces of the order of 10-1000s of piconewtons. The origin of tip-sample forces can be different depending on the experiment. For example: in air medium, when tip is approached to a substrate, it can experience van der Waals interactions, short range repulsive interactions, capillary forces, and adhesion [49]. Whereas, when a single protein molecule, tethered between the tip and substrate, is pulled to unfold it, the origin of the force will be the forces which are responsible to hold the native state of the protein-hydrogen bonds, hydrophobic interactions, and side chain interactions [71]. The capability of measuring such low forces makes AFM a versatile tool and it has been widely used to get surface morphology with atomic/molecular resolution, to quantify the inter-molecular forces between the tip and substrate, to measure forces in the biomolecules.

Further discussion will be mainly focused on the application of the AFM in protein folding/unfolding studies. To perform protein folding/unfolding experiments, AFM can be operated in two modes: static mode, and dynamic mode.

1.3.1 Static mode measurements:

Static mode is also known as the *contact mode*. In this mode, a protein molecule which is tethered between the tip and substrate is either pulled with constant speed and the force vs extension is recorded or it is held at a constant force and the extension vs time is recorded. The former experiment is known as *constant-speed pulling* and the latter is *force-clamp*. In the past, both type of experiments have been used for protein folding/unfolding studies and its mechanical, kinetic and thermodynamic properties have been estimated [9, 42, 45].

In a typical *constant-speed pulling* protein unfolding experiment, a polyprotein is immobilized on a substrate by forming a specific/non-specific bond from its one terminal, however, the other terminal is allowed to attach with the cantilever-tip. The tip-molecule attachment can either be specific or non-specific. Now, the tip-surface gap is changed with a constant speed along the perpendicular direction of the substrate resulting the application of force onto the molecule. Applied force increases with distance and the molecule unfolds when the applied force exceeds a certain value. In this case, cantilever-molecule system can be considered as two springs, with different stiffness, added in series. So, the force on both springs will be same, however, the extensions will be determined by their stiffness. In the experiment, the deflection on the cantilever is measured and the force is estimated by multiplying it with the cantilever force constant which can be calibrated separately. The cantilever is pulled with the help of a piezoelectric element attached at its base. This piezo is calibrated and provides the extension of the cantilever-protein system in the unit of distance (*nm*). Finally, the force vs extension is recorded which is known as *force-curve*. A force-curve can be converted into force vs protein-extension curve. Protein-extension can be determined by subtracting the cantilever deflection from the piezo extension. Unfolding curve of a polyprotein appears as a saw-tooth like pattern (Fig. 1.4).

The static mode in the constant-speed pulling has been extensively used to draw the 1D energy landscape of the protein unfolding. Where the extension on the protein (x) is used as the reaction coordinate. The native state of the protein is maintained by different native interaction which can have different mechanical stabilities along different directions. It basically depends on the orientation of the interactions. For example, the unravelling the hydrogen bonds is easier when they are in zipper-like orientation with respect to the direction of applied force, however, it needs more force when aligned in shear-like orientation [42]. So, the energy barrier that separates the native and unfolded state will be different

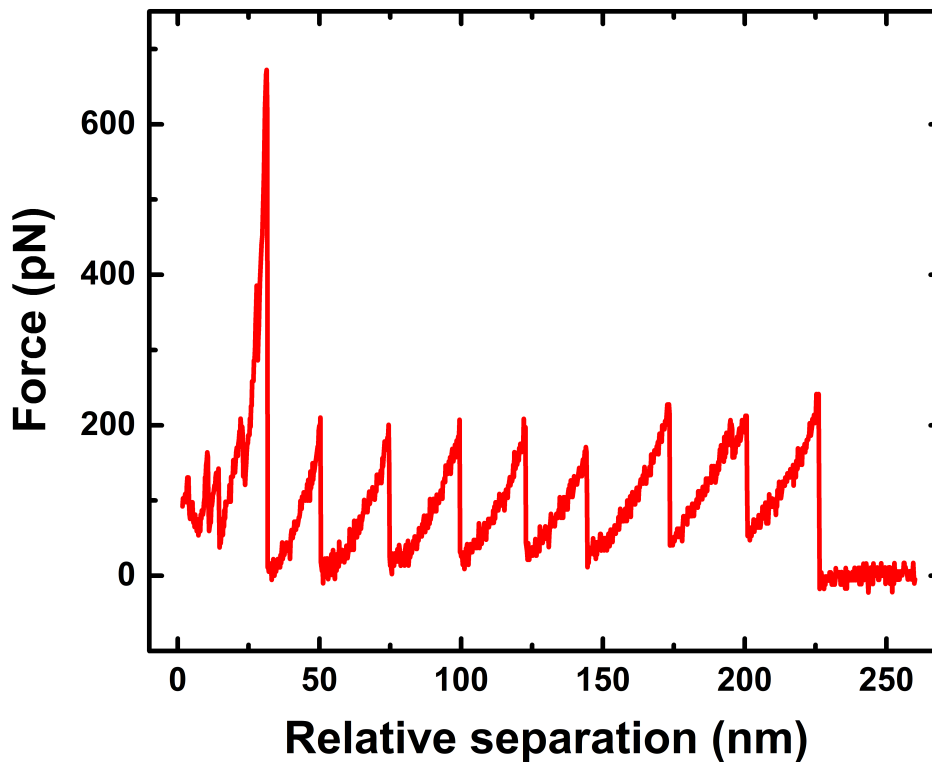


Fig. 1.4 Unfolding force profile of I27₈ (polyprotein with eight identical copies of I27 molecule covalently attached in series) with relative extension between the substrate and cantilever-base. Experiment is performed using constant-speed pulling method at room temperature with 200 nm/sec pulling speed. The calibrated spring constant of the cantilever is 0.406 N/m. Each peak represents unfolding of one domain and further strain-stiffening profile represents force vs extension behaviour of the unfolded protein chain. Usually, first (large) peak is not considered for analysis as it contains non-specific interaction between tip and substrate.

along different directions. The determined energy landscape from a AFM experiment can be thought as a cross-section of the funnel shaped energy landscape. This 1D landscape might be different when the protein is pulled from different directions. There are few proteins which are believed to unfold and refold along a specific direction while performing their function [148]. For example, the different immunoglobulin (*Ig*) domains in the giant muscle protein- titin.

The unfolding of majority of the proteins can be explained by two-state transition, however, few proteins possess meta-stable state(s) between the native and unfolded states. In two-state unfolding energy landscape, the native (*N*) and unfolded (*U*) states are separated

by an energy barrier which is known as the transition state (TS). Unperturbed protein prefer to be in the native state as the Gibbs free energy is less compared to the unfolded state [71]. In other words we can say that the thermodynamic stability, which is determined by the free energy difference between the native and unfolded states ($\Delta G_U^0 = G_N - G_U < 0$), of a protein is more in the native state. The Kramer's rate theory has been used to describe the rate of unfolding of the molecule. According to this theory, the rate of unfolding (k_U^0) depends on following parameters [16]: (i) free energy difference between the native and transition state (ΔG_{TS}^0), (ii) diffusion coefficient (D), and (iii) local curvature of the native and transition states. k_U^0 can be expressed as:

$$k_U^0 = \frac{D(\kappa_N \kappa_{TS})^{1/2}}{2\pi k_B T} \times \exp\left(-\frac{\Delta G_{TS-N}^0}{k_B T}\right) \quad (1.6)$$

Where $D(= k_B T / \gamma)$ is diffusion coefficient, γ is internal friction in the molecule. κ_N and κ_{TS} are local curvatures of the native and transition states respectively. k_B is Boltzmann constant, T is absolute temperature, and ΔG_{TS-N} is free energy difference between native and transition state. Evans and Ritchie proposed an empirical formula based on the Kramer's rate theory to describe the unfolding rate under applied external force (F) [41]. According to this, the applied force tilts the energy landscape and the barrier height linearly decreases with increase in the force:

$$\Delta G_{TS-N}(F) = \Delta G_{TS-N}^0 - F x_U \quad (1.7)$$

Where x_U is extension on the molecule just before unfolding or the distance between the native and transition state. So the rate of unfolding under externally applied force is given by:

$$k_U(F) = \frac{D(\kappa_N \kappa_{TS})^{1/2}}{2\pi k_B T} \times \exp\left(-\frac{(\Delta G_{TS-N}^0 - F x_U)}{k_B T}\right) \quad (1.8)$$

Eq. 1.8 can be written as:

$$k_U(F) = k_U^0 \exp\left(\frac{F x_U}{k_B T}\right) \quad (1.9)$$

Eq. 1.9 suggests that the unfolding rate increases exponentially with force. Prefactor in Eq. 1.9 is difficult to determine experimentally, and therefore assumed to be not affected by the external force. This is an assumption in this model according to which the shapes of native and transition state along with the friction parameter remain unaffected under applied force. Therefore, the kinetics changes due to change in the probability of the barrier crossing [41]. The distribution of the unfolding force (F_U) at a given unfolding rate can be described by the

following relation [40]:

$$P(F_U) = \frac{k_U(0)}{R} \exp\left(\frac{F_U x_U}{k_B T}\right) \exp\left(\frac{k_U(0) k_B T}{R x_U} \left[1 - \frac{F_U x_U}{k_B T}\right]\right) \quad (1.10)$$

Eq. 1.10 can be used to fit the experimental data recorded in AFM unfolding experiments to get $k_U(0)$ and x_U . Barrier height (ΔG_{TS}^0) can be estimated using Eq. 1.6 where prefactor (attempt frequency) is assumed to be an arbitrary value in the ranges $10^6 - 10^9$.

The parameters $k_U(0)$ and x_U can also be determined by the Monte Carlo (MC) simulation. The unfolding of the protein molecule is simulated in MC for different pair of $k_U(0)$ and x_U at different pulling speeds. The pair, which better generates the experimental behaviour, is accepted [19].

1.3.2 Dynamic mode measurements:

In the dynamic mode operation, similar to static mode, the cantilever is pulled with a constant speed along the direction normal to the substrate. The difference here is that the cantilever is sinusoidally oscillated while pulling. In other words, a dynamic perturbation is applied to the tethered molecule- between the cantilever-tip and substrate- while pulling. The change in the oscillation of the the cantilever-tip is recorded which is then further utilized to extract the sample properties. There are mainly two dynamic modes of AFM which are described in the literature: frequency-modulation AFM (FM-AFM) and amplitude-modulation AFM (AM-AFM). In FM-AFM, the cantilever is oscillated with an amplitude which is kept constant with the help of a feedback circuit and the shift in the frequency is measured when the interaction is altered by varying the tip-sample gap. This is further utilized to extract interaction properties [52, 65, 85]. Since the present thesis use the amplitude-modulation AFM, it will be discussed in detail in the next section.

1.4 Amplitude-modulation atomic force microscopy (AM-AFM):

Amplitude-modulation atomic force microscopy (AM-AFM) was first proposed by Y. Martin, C.C. William, and H.K. Wikramsinghe in 1987 [120]. Their aim was to measure the long-range forces between the cantilever-tip and substrate. They observe that when the cantilever is oscillated sinusoidally and approached close to the substrate, the amplitude of the tip reduces. They used the amplitude as a feedback and get the image of the substrate. Further, the theoretical modeling of the cantilever oscillation under external force suggested that the

change in the amplitude can be related with the gradient of the tip-surface interaction force [123].

Over time, it was extensively used to quantify the inter-atomic forces between the cantilever-tip and substrate atoms in UHV [68, 69, 78, 80, 83, 134, 143] and ambient conditions [51]. In the past few decades, the AFM has been recognised as a versatile tool to extract the viscoelastic properties of single-molecules [7, 87, 109, 146]. This method can directly probe the single-molecule viscoelasticity.

In a typical AM-AFM experiment, cantilever is oscillated with a fixed frequency (ω) and the tip is allowed to interact with the sample. The changes in the amplitude (R) and phase (θ) of the cantilever-tip is measured with the tip-sample separation, where θ is the phase difference between drive and tip. The measured parameters are then inserted in an appropriate mathematical model to extract sample's elasticity (k) and damping (γ , measure of viscosity) coefficients. In the past, two types of detection schemes- measurement of slope and displacement at the end of the cantilever, and various cantilever excitation schemes- acoustic, magnetic, and thermal have been used for the experiments. Mainly two mathematical models- continuous-beam and point-mass models have been used to quantify the interaction viscoelasticity. Researchers usually choose one of the two operational frequency regimes for the measurements- on-resonance and off-resonance. In on-resonance, cantilever is oscillated with frequency near (or slightly below) its fundamental resonance, however, it is oscillated far below the resonance in case of off-resonance. The analytical solution of the cantilever dynamics under interaction force is complex for on-resonance case. Whereas, it is straight forward for off-resonance operation but it requires high detection sensitivity of the instrument which could be achieved by implementing the interferometer based detection scheme [140]. The different aspects of the AM-AFM, such as the detection and excitation schemes, and choice of operation frequency and mathematical model for data analysis, will be discussed in detail in the coming chapters.

There are advantages of working with the dynamic mode. Firstly, using this the conservative and dissipative components of the force can separately be measured which is essential to completely understand the mechanical behaviour of the system. The damping behaviour of the biological systems control response time while performing their function. Dynamic mode experiments can directly probe system's damping which allows us to understand their function. Dynamic mode measurements facilitate the study of rheology of the system under investigation. Secondly, the use of phase sensitive detection such as lock-in amplifier makes it sensitive to the gradient of interaction force which increases its sensitivity compared to the static mode where the interaction force is directly measured. Measuring the force needs sufficient deflection on the cantilever which puts a limit on the minimum discernible force.

However, in dynamic mode (AM-AFM), change in amplitude is measured. The minimum detectable force gradient is again limited by the cantilever stiffness but with the help of the phase-sensitive detection it becomes more sensitive compared to the static mode. For example, when the unfolding of a single polyprotein (titin-I27) is studied using the dynamic mode, the known intermediate which appears before the final unfolding event can be clearly observed. However, this is rarely observed in static mode measurements [87, 146].

There are few downsides of this method. The dynamics of the cantilever is complex, particularly when operated in liquid medium, which is necessary to study most of the biological systems [7]. There are various sources of artefacts which may appear in the results such as offset in the initial phase, not being truly off-resonance, inappropriate choice of the cantilever stiffness etc [135, 146].

1.5 Specific to my research:

In this section, I will discuss about the work I have done during my PhD and its place in single-molecule force spectroscopy research. My aim was to quantify the viscoelasticity of the single protein molecule using amplitude-modulation atomic force microscopy (AM-AFM). The amplitude-modulation atomic force microscopy has been used for the entire study. I have used two types of AFMs- slope detection based (commercial) and displacement detection based (interferometer based home-built) AFM. Two types of cantilever excitation mechanisms have been used- acoustic excitation (cantilever-base is excited using dither piezo) and magnetic excitation (cantilever-tip is excited using the magnetic excitation). To quantify protein viscoelasticity, off-resonance frequency operation regime has been chosen. Data has been analyzed using two mathematical models- continuous-beam (CB) and point-mass (PM) model. The experiments performed using different AFMs and using different cantilever excitation schemes and data analyzed using different models have been compared. A unified understanding have been developed to understand the dynamic AFM measurements and its outcomes. This is applicable not only in context of single-molecules but for all the *biopolymers* and *nano-scale systems* where viscoelasticity can be probed using this technique. For my experiments, I have chosen titin I27 protein molecule as a model system.

1.5.1 Titin I27 protein:

Titin is a polyprotein and largest known protein so far (size $\sim 1 \mu\text{m}$, molecular weight $\sim 3 \text{MDa}$). It spans half the length of a sarcomere, connects *Z* to *M* discs, in a muscle cell [102]. Its *I*-band is responsible for the muscle's passive elasticity. The *I*-band is made up of

mainly two tandem immunoglobulin-like (*Ig*) segments along with a small PEVK segment (unstructured). There are ~ 200 *Ig* domains in *I*-band. Most of the *Ig* domains are common in all type of muscles (cardiac, smooth, and skeletal), however, few small sections are present only in the cardiac muscle- known as *unique sequence*.



Fig. 1.5 Structural representation of I27 molecule. It is a β rich globular protein. Image is downloaded from PDB (<https://www.rcsb.org/structure/1TIT>).

I27 is one of the *Ig* domains from the unique sequence in the cardiac muscle. This is a globular protein with 89 amino-acids. It has seven β -strands (Fig. 1.5). In *I*-band, all the *Ig* domains are almost similar in structure and hence, in mechanical properties. So, the I27

is chosen as a representative domain for the single molecule studies and has widely been explored [7, 9, 42, 44, 71, 87, 93, 107, 146, 148]. In AFM unfolding experiments, an I27 with n -identical repeats (homo-polyprotein) is tethered from its N and C terminus and pulled to unfold it. A typical unfolding force-curve appear as a sawtooth-like pattern. Before the final unfolding peak, a small peak appears at lower force which is its intermediate state [44].

1.5.2 Unfolding studies on I27 protein:

In past few decades, I27 protein has been extensively studied, few measurements performed using static mode are cited here [9, 42, 44, 45, 71, 107, 148]. However, in dynamic mode it is not much explored. Literature studies on I27 using dynamic mode (AM-AFM) are discussed below.

1.5.2.1 Literature studies on I27 using dynamic AFM experiments:

In the past, many attempts have been made to measure the viscoelasticity of the single-molecule viscoelasticity using different methods.

H. Janovjak et al. (2005) measured the viscoelasticity of a membrane-protein bacteriorhodopsin using the magnetic excitation based AM-AFM measurements. Cantilever (stiffness = 0.08 N/m) was oscillated at low frequency (3 kHz) compared to its fundamental resonance (7 kHz in liquid) with the amplitude of $6 - 9\text{ nm}$ (peak-to-peak). Simple harmonic oscillator (SHO) model with off-resonance approximation were used for data analysis. The observed stiffness and damping coefficients were attributed to the unfolded chain [77].

M. Kawakami et al. (2006) measured the viscoelasticity of the titin-I27₅ protein where the cantilever-tip was excited at on-resonance (5 kHz) with amplitude of 2 nm using the magnetic excitation scheme. They observed the elasticity and damping coefficient both when the molecule sequentially gets unfolded. They observed that the unfolding force of individual domains was reduced. Simple harmonic oscillator (SHO) model were used for data analysis. They inferred that the observed response could be from the unfolded, partially folded, and folded domains [87].

Khatri et al. (2008) measured the viscoelasticity of titin I27₈ homopolymer using power-spectral-density method in which the thermal fluctuation of the cantilever wherein the tip is tethered with the molecule and held at a fixed force were measured. Point-mass approximation based analytical model has been used for the data analysis. They claim that the observed stiffness and dissipation coefficient are from the unfolded chain and damping was attributed to the internal friction of the unfolded chain [93].

F. Benedetti et al. (2016) performed unfolding experiments titin I27₆ using amplitude-modulation atomic force microscopy. They raised the question in the adequacy of point-mass model and proposed a new mathematical model, abbreviated as the continuous-beam model, for a low excitation-frequency (excited from the base) and small interaction forces. Cantilever was oscillated at low frequency ($\sim 100\text{ Hz}$, first resonance was $1 - 2\text{ kHz}$ in liquid) with peak-to-peak base amplitude ($1 - 2\text{ nm}$, estimated from the deep contact response of the cantilever amplitude). The dissipation coefficient from the molecule was not observed, however, the stiffness signal was observed. They suggested that the X and Y components of the oscillation (X, Y) are the appropriate observable parameters to extract the viscoelasticity of the single-molecule instead of the amplitude and phase (R, θ) [7].

1.5.3 Motivation of the thesis:

For more than two decades, researchers have been using the amplitude-modulation atomic force microscopy to study the viscoelasticity of nano-scale systems in liquid environment. Two systems have been extensively studied: (1) Nano-confined liquids such as water [82, 92], ionic liquids [91], and non-polar liquids [34, 117, 133, 141], and (2) Single biomolecules such as proteins [77, 87], and unstructured polymers [109]. Apart from the AM-AFM there are other studies on nano-scale viscoelasticity using AFM based experiments. For example: power-spectral-density (PSD) based method have been applied to investigate viscoelasticity of confined liquid [82], proteins [93], polysaccharides (dextran) [15, 88], unstructured polymer (polyethelene glycol) [87]. The two fields of research, confined liquids and single-molecule studies, had been growing independently. The common factor in both these fields was that in almost all the above cited works a point-mass approximation based model has been used to extract the system's viscoelasticity.

Recently, F. Benedetti et al. (2016) performed amplitude-modulation atomic force microscopy on the titin I27₆ [7]. They proposed a mathematical model for low excitation-frequency (excited from the base) and small interaction forces. The model takes the continuum nature of the cantilever-beam into account. They claimed that the point-mass model is not adequate to model the cantilever dynamics under interaction force and can lead mis-interpretation of the final results, particularly the phase data. They suggested that instead of the amplitude and phase (R, θ), the X and Y -components of the oscillation (X, Y) are the appropriate observable parameters to extract the viscoelasticity of the single-molecule. This report raises concerns in the accuracy of all the previous measurements where point-mass model (or based on the point-mass approximation of cantilever) had been used to extract sample viscoelastic properties.

Apart from this, the previous estimates of dissipation coefficient of the unfolded protein chain was reported very high ($\sim 5 \times 10^{-6} \text{ kg/s}$) [77, 93]. The dissipation coefficient from a few nanometers size polymer chain lies in the same order of the micrometer size cantilever. Similar values of dissipation coefficient were observed for other polymers when investigated using PSD-based method [15, 87, 88]. In absence of other independent measurements of dissipation in single-molecules these results were accepted by many researchers but not by all. Such a high value of dissipation coefficient from single-molecule was under controversy.

The report by F. Benedetti et al. [7], discussed above, motivated us to review the entire methodology of extracting the nano-scale viscoelasticity using amplitude-modulation based atomic force microscopy. We did a comprehensive study to understand the methodology. In order to do this we followed following strategies:

1. AFM(s) as a tool: We used two types of AFMs for our experiments. The detection system in the two are different and they measure completely different and independent quantities. One is the commercially available AFM which is equipped with LASER reflection based detection system and it measures slope (dy/dx) of the cantilever. Second is the home-built AFM which is equipped with an interferometer based detection system and it measures the displacement (y) of the cantilever. It should be noted that we have applied interferometer based AFM for single-molecule studies for the *first time*, however, in all previous studies, commercial AFM have been used. Whereas for confined liquid experiments, some groups have been used slope-detection based AFM [34, 117] and few groups used interferometer based AFM [82, 92, 141]. Simultaneous study of the same system (I27 protein) using the same experimental conditions in both type of AFMs allows us to compare the results in conclusive way.

2. Cantilever-excitation schemes: In the past, two types of excitation schemes have been extensively used to drive the cantilever. First is base excitation which can be implemented by attaching a dither piezo at the cantilever base and feeding it an alternative current (confined liquid [34, 92, 96, 117], proteins [7]). Second is the magnetic excitation which can be implemented by coating a magnetic material (or attaching a piece of magnetic particle) at the back of the cantilever that can be excited using an electromagnet (confined liquid [133], proteins [77, 87]). We have separately applied both types of excitation schemes to study the one system (I27 protein). In both measurements, the experimental conditions were same. This allows us to make a fair comparison between the results from the two independent experiments.

3. Mathematical models for data analysis: We have used the two mathematical models, point-mass (PM) model and continuous-beam (CB) model, to analyse the data. Analysing

the same data with two different models allows us to compare results and make conclusive comments on it.

1.5.4 Significance of the work:

My research work contributes to single-molecule force spectroscopy mainly in two ways. First, it improves the dynamic atomic force spectroscopy method of extracting the viscoelasticity of the systems at nano-scale and second, the results obtained for I27 molecule contributes in understanding the behaviour of single-molecule under force.

1.5.4.1 Methodology of dynamic atomic force spectroscopy:

As it has been discussed previously in *amplitude-modulation atomic force microscopy* section, in a typical AM-AFM experiments, cantilever is excited at a fixed frequency and the change in the amplitude (R) and phase (θ) of the tip is measured when the interaction force is varied by varying the tip-surface distance. Further, the R and θ were used to extract the interaction viscoelasticity using an appropriate mathematical model.

We have found that extracting the error/artefact-free results from the AM-AFM experiments are not straightforward. There are many factors that are likely to be present in such measurements can introduce significant error or artefacts in the final results. These factors are listed below:

1. Initial phase offset: Initial phase is the phase difference between the drive and cantilever-tip oscillation when the tip is far away from the surface or in absence of tip-sample interaction. We found that a significant offset in the initial phase introduces artefacts in the dissipation measurements. There can be various sources of the offset in initial-phase: electronic phase, presence of spurious peaks in cantilever response near the operation frequency etc.

2. Choice of operation frequency and mathematical model: Depending on the choice of the operation frequency- off-resonance or on-resonance, a mathematical model has to be chosen. The dynamics of the cantilever is complex when it is operated on-resonance and a complicated deconvolution process is required to extract the accurate interaction viscoelasticity. To overcome this issue, many researchers prefer to work at off-resonance regime where the dynamics of the cantilever is straightforward. However, the limit for off-resonance frequency is not clearly defined. Even though, the cantilever is oscillated at a frequency far below its fundamental resonance, sometimes it may not be *truly* off-resonance. In such case, the use of simple analytical model derived for off-resonance can cause significant error/artefact in final result.

3. Choice of cantilever stiffness: In all the existing mathematical models to extract inter-

action viscoelasticity, the solution of the cantilever-tip motion is assumed to be harmonic which requires that the interaction force (or stiffness) should be very small compared to the cantilever force (or stiffness). However, the use of stiff cantilever reduces the measurement sensitivity. To get high measurement sensitivity most of the researchers use soft cantilevers passing over the fact it has been assumed in the mathematical models. When the cantilever stiffness is comparable or less than the sample stiffness, its solution is no more harmonic and the use of the existing mathematical models to analyzed the data will introduce error in the result.

It must be noted that above discussion is not specific to one particular type of experiment but it is general and applicable in all the experiments where AM-AFM are performed to extract sample viscoelasticity.

1.5.4.2 Application of dynamic AFM to single-molecule study:

In our experiments/data analysis, we took care of all the essential factors which can cause error and artefact in the results and studied the viscoelasticity of titin I27 protein molecule. The results have significance in following ways:

1. Protein folding/unfolding: The (ultra)small-amplitude and off-resonance measurements mainly probe the viscoelasticity of the unfolded protein molecule. Local viscoelasticity from the unfolded (molten-globule) to stretched state can directly be estimated. Further, the relaxation time can be determined which is nothing but the ratio of the dissipation and stiffness coefficients. Relaxation time can be a good estimate of the initial collapse time of protein folding. This estimated timescale can directly be compared with the measured time in single-molecule FRET experiments.

2. Probing the the folded protein: We have observed that the folded protein viscoelasticity can be probed when the experiment is performed with amplitudes more than a critical value. This opens up the window for the amplitude-modulation AFM users to extract the information from the folded protein. In our knowledge, there is no report in the literature claiming the measurement of folded protein's viscoelasticity using the AM-AFM method. Although, there are two reports where authors have inferred that the response could be from the folded protein but there was no any theoretical/experimental support were provided to the hypothesis [65, 87].

3. Dynamic properties of the single-molecule: The AM-AFM experiments allow to study the dynamic properties at the single-molecule level. One can perform rheology of the single protein molecule. Depending on the choice of the experimental parameters, one can study the rheology of unfolded polymer chain or the folded protein up to a certain limit.

It is important to note that the above discussion is not limited to a particular protein but can be applicable to all proteins. This can also be used to study the rheology of the other biomolecules: unstructured polymers such as polyethylene glycol (PEG), polysaccharides such as dextran etc.

1.6 Plan of the thesis:

In *chapter-2*, I have discussed all the materials and methods that have been used in my research work such as instruments, new modules made for specific experiment(s), and sample preparation.

The aim of my work was to quantify (error/artefact-free) the viscoelasticity of the nano-scale systems using amplitude-modulation atomic force microscopy, particularly the single protein molecules. In order to do this, I decided first to find out all the possibilities which can introduce error/artefact in the results. In *chapter-3*, the various sources of error/artefacts have been discussed and also suggested the way to address this issue. After this we examine the validity of the widely used point-mass model by comparing it with the continuous-beam model. In *chapter-4*, I have discussed adequacy of point-mass model in extracting viscoelasticity from AM-AFM experiments. We found that the interferometer-based (home-built) AFM is better suited for such studies, mainly when the base excitation based schemes are used. As this AFM is not commercially available, these experiments cannot easily be performed by other research groups. To address this issue, I worked on finding out the methodology using which one can easily perform such experiments on commercial AFMs. Detail of the methodology has been discussed in the same chapter. I have discussed that it can be achieved in commercial AFMs using the magnetic excitation scheme. A method to coat a thin layer of magnetic material at the tip position will be discussed which is essential for this measurement. Interestingly, the point-mass perfectly works in tip-excitation measurements when performed at truly off-resonance regime.

In a separate experiment which is performed in interferometer based AFM, We found that the AM-AFM can probe the properties from the folded protein. We observed reduction in stiffness and also dissipation signal from the molecule when certain experimental parameters are used. Experimental evidences suggest that the viscoelastic response has contribution from folded protein domains connected in series with the unfolded chain. It has been discussed in *chapter-6*. Eventually, I summarise my thesis work in *chapter-7*.

1.6.1 Chapter 2

Materials and methods

In this chapter, the fundamentals of slope-detection (commercial) and displacement-detection (home-built) based AFMs will be discussed. Various calibrations are required for quantitative measurements. In both AFMs, few of the calibrations could be same such as cantilever force constant and few could be different such as detection-sensitivity. Methods for these calibrations will be discussed. A separate module has been developed for magnetic-excitation based experiments where a thin layer of cobalt was deposited near the tip-position and it is excited using an electromagnet. Working principle of lock-in amplifier will be discussed briefly as it was essential for all dynamic AFM experiments. Sample preparation for experiments will be discussed in a separate section.

1.6.2 Chapter 3

Theory: Amplitude-modulation atomic force microscopy

In this chapter, the theoretical aspects of amplitude modulation atomic force microscopy has been discussed. Equation of motion for continuous-beam model and point-mass model were solved and discussed in detail. This discussion is essential to understand my research work.

1.6.3 Chapter 4

The nano-scale viscoelasticity using atomic force microscopy in liquid medium

We applied *base-excitation* scheme to drive the cantilever and used both slope-detection and displacement-detection based AFMs. It was found that artefacts can appear due to various sources. For example: (1) Offset in the initial phase causes artefact. It can occur due to spurious peaks present in cantilever-frequency response near the operation regime, electronic phase offset due to different electronic components used in the circuit, design of the liquid cell, response of the piezoelectric material etc., (2) Inappropriate choice of operation frequency and mathematical model introduces artefacts. Depending on the choice of the operation frequency- off-resonance or on-resonance, a mathematical model has to be chosen. The dynamics of the cantilever is complex when it is operated on-resonance and a complicated deconvolution process is required to extract the accurate interaction viscoelasticity. To overcome this issue, many researchers prefer to work at off-resonance operation regime where the dynamics of the cantilever is straightforward. However, the limit for off-resonance frequency is not clearly defined. Even though, the cantilever is oscillated

at frequency far below its fundamental resonance, it may not be *truly* off-resonance. In such case, the use of simple analytical model derived for off-resonance can cause significant error/artefact in final result.

We propose the ways to perform artefact-free measurements. We found that the displacement-detection is better suited for such experiments. The presence of offset in initial phase can easily be identified and the data analysis is also straightforward compared to slope measurements.

1.6.4 Chapter 5

Validity of point-mass model in off-resonance dynamic atomic force microscopy

The quantitative measurement of viscoelasticity of nano-scale entities is an important goal in nanotechnology research and there is considerable progress with advent of dynamic Atomic Force Microscopy. The hydrodynamics of cantilever, the force sensor in AFM measurements, plays a pivotal role in quantitative estimates of nano-scale viscoelasticity. The point-mass model, wherein the AFM cantilever is approximated as a point mass with massless spring is widely used in dynamic AFM analysis and its validity, particularly in liquid environments, is debated. It is suggested that the cantilever must be treated as a continuous rectangular beam to obtain accurate estimates of nano-scale viscoelasticity of materials it is probing. Here, We have performed off-resonance dynamic atomic force spectroscopy on a single protein molecule to investigate the validity of widely used point-mass model. We performed measurements with AFMs equipped with different cantilever excitation methods, base-excited using dither piezo and tip-excited using magnetic excitation based setup, as well as detection schemes, bending and displacement, to measure cantilever response. The data was analyzed using both, continuous-beam model which accommodates the geometric details of the cantilever beam and the point-mass model which approximates it as a point-mass. We found that both models yield same results when the experiments are performed in truly off-resonance regime with small amplitudes ($\sim 1 - 3 \text{ \AA}$) and the cantilever stiffness is much higher than the interaction stiffness.

1.6.5 Chapter 6

Probing the folded protein domain response using dynamic atomic force microscopy

We observed that the peak unfolding stiffness/force of the individual domains reduces when the oscillation amplitude exceeds from a critical value. We infer that this transition occurs due to contribution of the folded domains whose mechanical properties alter after this transition.

Interestingly, we observed variation in dissipation signal when experiment was performed at high frequency and amplitude exceeded from a critical value where stiffness reduction occurs. Our experimental observation suggests that the amplitude-modulation atomic force microscopy can be used to probe viscoelasticity of single folded protein molecules.

1.6.6 Chapter 7

Conclusion and future possibilities

In this chapter, thesis has been summarized and discussed the future possibilities of my work.

1.7 Future possibilities:

This work can be extended to extract more information of the mechanical properties at the nano-scale in various fields such as the protein-protein interaction, protein-membrane interaction, confined liquids etc.

In the past, the magnetic excitation base method have been used to study the single-molecule viscoelasticity. The experiments were performed using two types of cantilevers. (1) Commercially available cantilevers- the whole cantilever (backside) is coated with magnetic material. In this case, drive force acts on whole cantilever, however, the mathematical models assume the driving force only at the tip position. (2) A piece magnetic particle glued at the tip position (on backside). The particle has a significant mass which can alter the dynamics of the cantilever. In mathematical models, this mass is usually ignored. In our work, we have proposed a way to coat a thin film of magnetic material near the tip position. We achieved enough deflection on the cantilever by coating $\sim 25 - 30 \text{ nm}$ cobalt. The mass of this thin layer is negligibly small compared to the cantilever mass and can be ignored. This fulfills the assumption of ignoring mass of the magnetic material and the existing mathematical models can be used for data analysis. The got high success rate of stable coating for air and water medium, however, it is low for the buffer medium. More effort will improve the success rate.

As we have experimental observations which suggest that the dynamics of folded protein can also be probed using AM-AFM experiments. It can be extended to study the rheology of the folded proteins. Shape (curvature) of the free energy landscape of folded state is directly related to the stiffness. Measuring the stiffness of the folded protein allows us to explore the energy landscape of protein folding/unfolding.

Chapter 2

Materials and methods

2.1 Introduction

In this chapter, the fundamentals of slope-detection (commercial) and displacement-detection (home-built) based AFMs will be discussed. Some calibrations are required for quantitative measurements. In both AFMs, few of calibrations could be same such as cantilever force constant and few could be different such as detection-sensitivity. A separate module has been developed for magnetic-excitation based experiments where a thin layer of cobalt was deposited near the tip-position and it is excited using an electromagnet. Working principle of lock-in amplifier will be discussed briefly as it was essential for all dynamic AFM experiments. Sample preparation for experiments will be discussed in a separate section.

2.2 Atomic Force Microscope (AFM)

Atomic force microscope (AFM) is a member of scanning probe microscope (SPM) family. In an SPM technique, a sharp probe is allowed to interact with the sample which causes change in some observable parameter(s) which is being recorded and utilized to extract sample properties. The probing and detection mechanisms are the crucial factors which distinguish one SPM technique from another.

In AFM, a probe (tip) is attached at the free-end of a micro-cantilever which is fixed from the other end. Cantilever-tip assembly acts as a force sensor. Tip is allowed to interact with the sample that causes deflection (y_c) on the cantilever-beam which is detected by a detection scheme. For small deflection, cantilever behaves as a Hookean-spring. The interaction force experienced by the tip can be estimated using following relation: $F = k y_c$, where k is the force constant of the cantilever which can be independently calibrated using various

methods. This is known as static mode operation. AFM is capable of measuring forces of the order of few piconewtons to several piconewtons. In dynamic measurements, say amplitude-modulation, cantilever is oscillated with a frequency and tip interacts with sample causing change in amplitude (and phase) of deflection. Change in the observable parameters is detected by the detector with the help of which sample properties are extracted.

There are many popular schemes to detect cantilever deflection. One of them is laser-reflection based scheme which detects slope of the cantilever deflection. It is available in the commercial AFMs. The other is interferometer-based scheme which detects net displacement of the cantilever. This is not available in commercial AFMs, but built in few labs and applied for various studies. I have used both types of AFMs for my measurements. The main difference in the two AFMs are the detection systems.

2.3 Commercial AFM (*slope-detection*)

The working mechanism of all commercial AFMs are similar. I have used *JPK Nanowizard II (Berlin, Germany)* for my measurements. A commercial AFM has five major elements: detection system, cantilever-tip assembly, sample/cantilever motion controller, feedback circuit, and data acquisition and display unit. Apart from the detection system, all the other elements are more or less similar in commercial and our home-built AFM. So, my discussion will focused on the detection system, alignment mechanism, and some essential calibrations.

2.3.1 Optical beam deflection detection

In commercial AFMs, *optical beam deflection* method is used to detect deflection on the cantilever. In this method of detection, a narrow laser beam (few micrometers in diameter) fall on the back of the cantilever and reflected light is collected at a position-sensing photo-detector. Typically a photo-detector has four quadrants which can detect vertical as well as lateral motion of the cantilever. In absence of tip-sample interaction, the position of laser spot on the detector is fixed and the detector output voltage is zero or a constant value. When cantilever deflects, due to tip-sample interaction, the position of the laser spot on photo-detector changes resulting in a difference in the output voltage. This difference in detector output voltage is proportional to the change in the *slope* of the cantilever deflection. So, the *optical beam deflection* method detects the change in the *slope* of the cantilever. Schematic representation of optical beam deflection detection (*slope-detection*) has been shown in Fig. 1.3.

2.3.2 Alignment of detection system

Detection system has three units: laser source (red or visible near infrared), mirror and photo-detector. Usually positions of both units are adjustable. Our AFM (*JPK Nanowizard II*) is equipped with an inverted microscope. A light (visible) source, cantilever, sample, and an objective all are positioned along the same axis (y – axis, normal to the sample surface). Cantilever and sample are illuminated with light (visible) source and transmitted light is collected via objective kept below the sample stage.

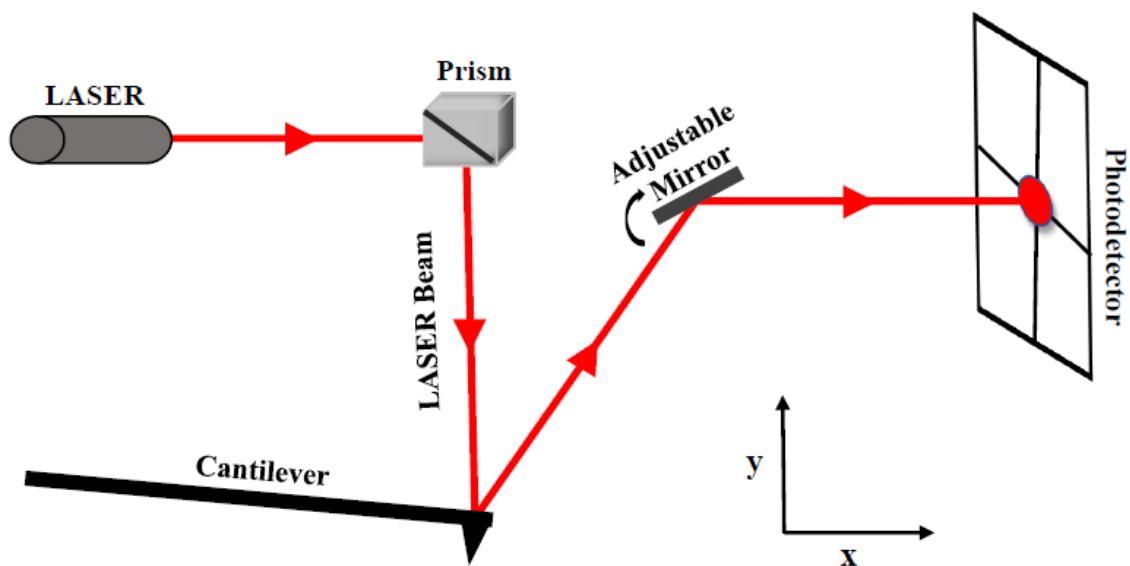


Fig. 2.1 Schematic representation of laser-alignment in optical beam deflection detection. A laser beam is allowed to fall on the back of the cantilever through a prism. Beam reflects from the cantilever surface and directed to the photo-detector with the help of an adjustable mirror which can be rotated about the axis perpendicular to the plane of paper. As per the requirement, the position of incident laser beam and photo-detector can be adjusted during the alignment.

Firstly, to make the cantilever visible on the computer screen, it is focused by adjusting the objective's position along the y – axis. Now the laser filter, an obstacle to block laser to fall on the CCD camera, is removed to see the laser spot on the computer screen. The position of the laser spot is adjusted in such a way that it falls on the back of the cantilever. To guide the reflected light towards photo-detector, a mirror is placed which can be rotated at its position to change the direction of reflected laser. This makes the reflected laser to fall on photo-detector which can be confirmed by maximizing the value of *sum-signal*. Finally, the detector position is adjusted to bring the laser spot at the centre of the detector (Fig. 2.1).

2.3.3 Detector sensitivity calibration

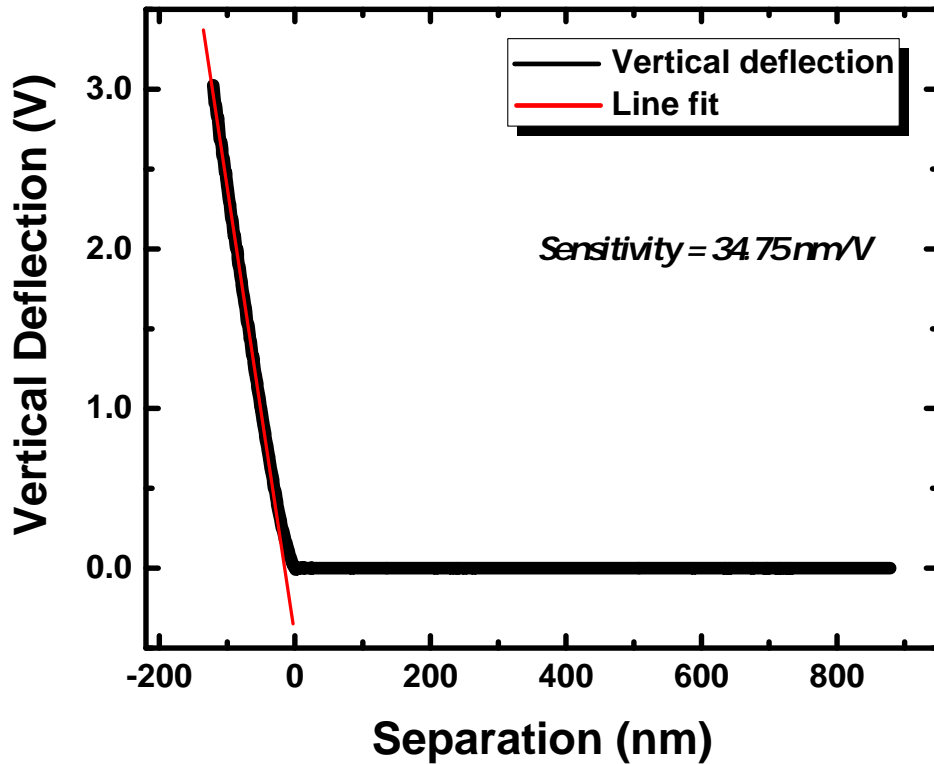


Fig. 2.2 Graph in black line represents cantilever bending with cantilever base position and red line represents linear fit. Slope of the fitted line is detector sensitivity. For the used rectangular cantilever (length = $250 \mu\text{m}$, width = $35 \mu\text{m}$, and thickness = $1 \mu\text{m}$), it is 34.75 nm/V .

The voltage output from the photo-detector can be converted to the cantilever displacement by multiplying it with a conversion factor known as detector sensitivity. Base of the cantilever can be moved along y – axis by the known distance (*extension*) with the help of a well calibrated piezo element which is usually known as scanner piezo. With the help of scanner piezo, cantilever is approached towards a glass surface and tip is pressed against it to take an approach-extension curve (photo-detector output voltage vs cantilever (base)-sample distance) in deep contact region. In deep contact region, cantilever-tip is in contact with the glass surface (repulsive force regime) and hence, cantilever bending increases in upward direction with extension. The tip-glass contact is assumed to be nearly non deformable which can be confirmed by its linear behavior. In this region cantilever bending (detector output in

voltage) is proportional to the extension. Slope of the linear fit to the deep contact region is inverse detector sensitivity. Detector sensitivity is described in unit of nanometers per volt (nm/V).

Fig. 2.2 represents a typical sensitivity calibration curve (black) with a linear fit (red). Slope of the fitted line is the sensitivity. For the used rectangular cantilever (length = 250 μm , width = 35 μm , and thickness = 1 μm), it is 34.75 nm/V .

2.3.4 Cantilever force constant calibration

Cantilever force constant, also known as spring constant or stiffness, is essential for force spectroscopy measurements. In static experiments, interaction force is determined by multiplying the cantilever displacement with force constant, whereas, in dynamic measurements, it is required to subtract cantilever response from the net cantilever-sample response to determine sample properties.

There are various methods to determine cantilever force constant [22, 74, 153]. We use *thermal noise method* in our measurements. This is proposed by Hutter et al. in 1993 [74] and further refined by Butt et al. in 1995 [22]. *Thermal noise method*, is based on the equipartition theorem which states that in thermal equilibrium the average value of each quadratic term in Hamiltonian is equal to $k_B T / 2$. When a cantilever is in equilibrium with its surrounding medium, equipartition relation can be written as:

$$\frac{1}{2} k_c \langle z^2 \rangle = \frac{1}{2} k_B T. \quad (2.1)$$

Where k_c and $\langle z^2 \rangle$ are cantilever force constant (or static force constant) and mean square displacement respectively. k_B is Boltzmann constant and T is absolute temperature. $\langle z^2 \rangle$ ($= \sum_n \langle z_n^2 \rangle$) is superposition of mean square displacements of all possible eigen modes of the cantilever and it can be determined by measuring power spectral density (PSD) over all frequency range. Each eigen mode can be characterized by modal stiffness and frequency and is a separate peak corresponding to each mode in PSD response. Mean square displacement for each eigen mode can be estimated by determining area under the curve for that particular mode. Sum of the area under the curve for all modes determines $\langle z^2 \rangle$. Euler-Bernouli equation for an elastic beam can be solved to get the expression for spring constants of each eigen mode. It was found that the force constant of the fundamental mode (k_1) is almost equal to the static force constant of cantilever:

$$k_1 = 1.030 k_c. \quad (2.2)$$

Eq. 2.2 suggests that the stiffness of fundamental mode can be fairly assumed as the static stiffness of the cantilever. This can be estimated by only calculating the area under the curve for the fundamental mode in PSD:

$$k_c \approx k_1 = \frac{k_B T}{\langle z_1^2 \rangle}. \quad (2.3)$$

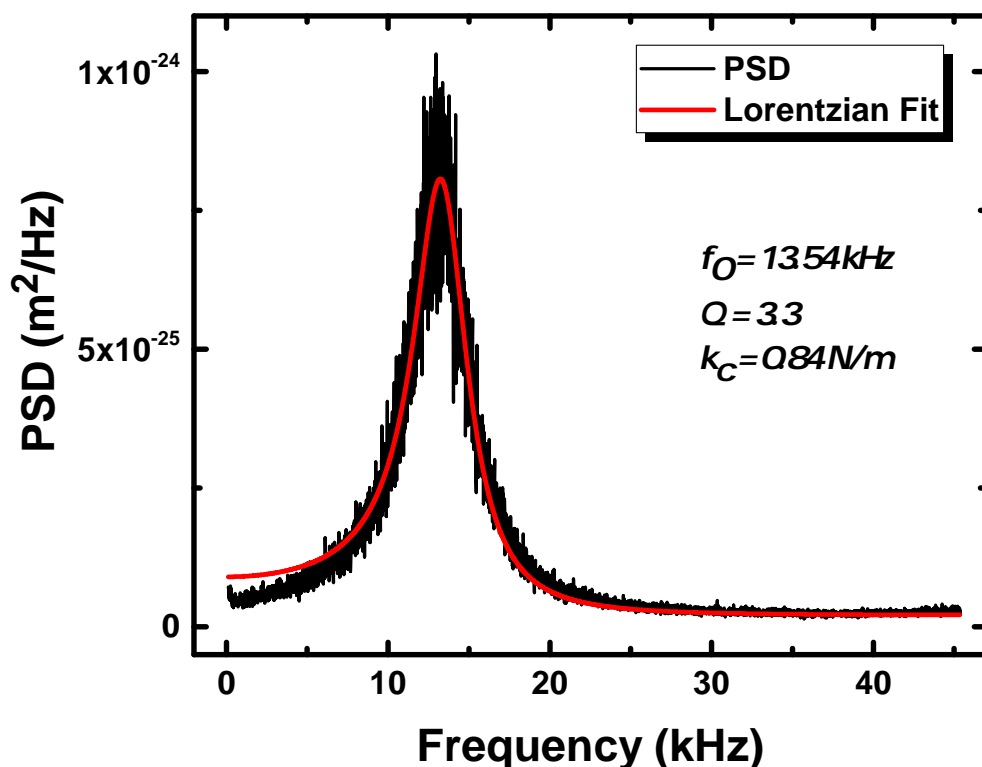


Fig. 2.3 Graph in black line represents the calculated PSD for a rectangular cantilever and red line represents the Lorentzian fit. Resonance frequency ($f_0 = 13.54 \text{ kHz}$) and quality factor ($Q = 3.3$) are measured as the free parameters. Cantilever force constant ($k_c = 0.84 \text{ N/m}$) is estimated using Eq. 2.3.

To estimate $\langle z_1^2 \rangle$, PSD for the fundamental mode (P_d) is calculated and fitted with amplitude-frequency response function of single harmonic oscillator $R(f)$ (Lorentzian function) with an added noise background term (P_b) [49]. This additional background term accounts for the background noise which is not originate from thermal fluctuations.

$$P_d = P_b + R(f). \quad (2.4)$$

Then $R(f)$ is integrated to get area under the curve:

$$\langle z_1^2 \rangle = \int_0^{\infty} R(f) df \quad (2.5)$$

Resonance frequency (f_0) and quality factor (Q) of the cantilever are determined as free parameters. Area under the curve of fitted function (not the real data), which is $\langle z_1^2 \rangle$, is calculated by the software. It is now substituted into Eq. 2.3 to finally get the force constant of the cantilever. Refer [22, 74] for more detail.

Fig. 2.3 represents the PSD (black) calculated for a rectangular cantilever. Red curve represents Lorentzian fit to the PSD. Resonance frequency ($f_0 = 13.54 \text{ kHz}$) and quality factor ($Q = 3.3$) are measured as the free parameters. Cantilever force constant ($k_c = 0.84 \text{ N/m}$) is estimated using Eq. 2.3.

It is important to note that Eq. 2.3 is written for the displacement of the cantilever (z), however, commercial AFMs measure the slope (dz/dx). This discrepancy can be accounted for by multiplying an appropriate conversion factor [22].

2.3.5 Sample-cell and tip-sample motion

We used the commercial sample-cell proved by JPK designated as *life science stage*. It can be moved on $x - z$ plane (parallel to the microscope stage) with micrometers precision with the help of knob provided on the microscope stage. However, its motion along the y -direction is restricted.

Cantilever along with the alignment setup are mounted on a piezo stage which can be moved together along y -direction without perturbing the laser alignment. This allows us to vary tip-sample distance to perform force spectroscopy experiments.

2.4 Home-built AFM (*displacement-detection*)

Our home-built AFM has five major elements like commercial AFM: detection system, cantilever-tip assembly, sample/cantilever motion controller, feedback circuit, and data acquisition and display unit (Fig. 2.4). Apart from the detection system, all the other elements are more or less similar to the commercial AFM. Interferometer-based setup has been used for the cantilever deflection detection. This measures displacement of the cantilever not the slope. Displacement detection has many advantages which will be discussed in coming chapters in detail.

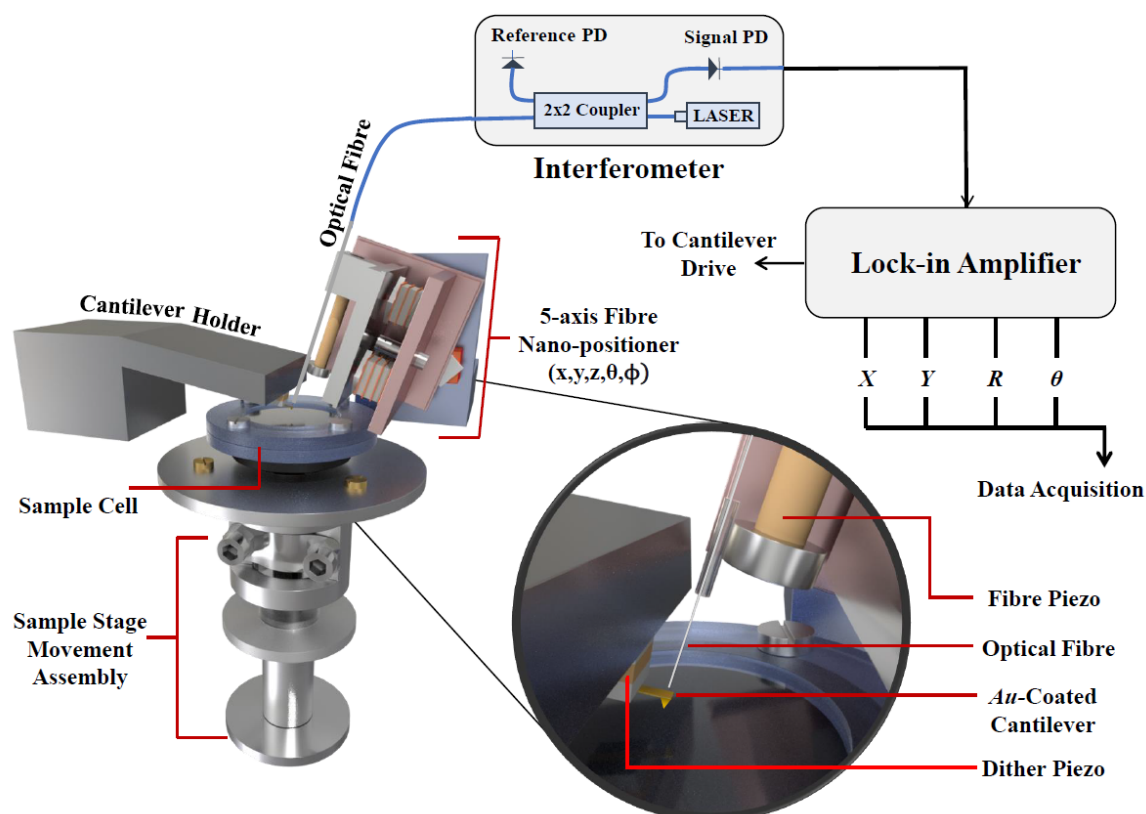


Fig. 2.4 Schematic representation of our home-built AFM. Alignment of the fibre-end parallel to back of the cantilever is magnified (shown in big circle).

2.4.1 Interferometric detection

To detect the cantilever deflection, a Fabri-Perot cavity between cantilever surface and cross-section of an optical fibre which allows us to detect the cantilever displacement. As shown in the Fig. 2.5, back of the cantilever is gold coated which acts as a fully reflective mirror and the end of an optical fibre is cleaved and made it partial reflective by metallic coating which acts as a partial reflective mirror. Fibre end (partial reflective mirror) is aligned parallel to the cantilever back (fully reflective mirror), with the help of a nano-positioner, to form a Fabri-Perot cavity. An infrared laser (*wavelength* = 1310 nm) is passed through optical fibre. Part of the laser reflects back from the end of the fibre depending on its reflectivity and rest of the laser fall on the back of the cantilever which also reflect back to the fibre. The two reflected lights interfere with each-other and it is allowed to fall on a photo-diode, kept at a fixed distance, which produces current. The output current is constant when the distance between mirrors is fixed. The position of the fibre is fixed at the maximum sensitivity

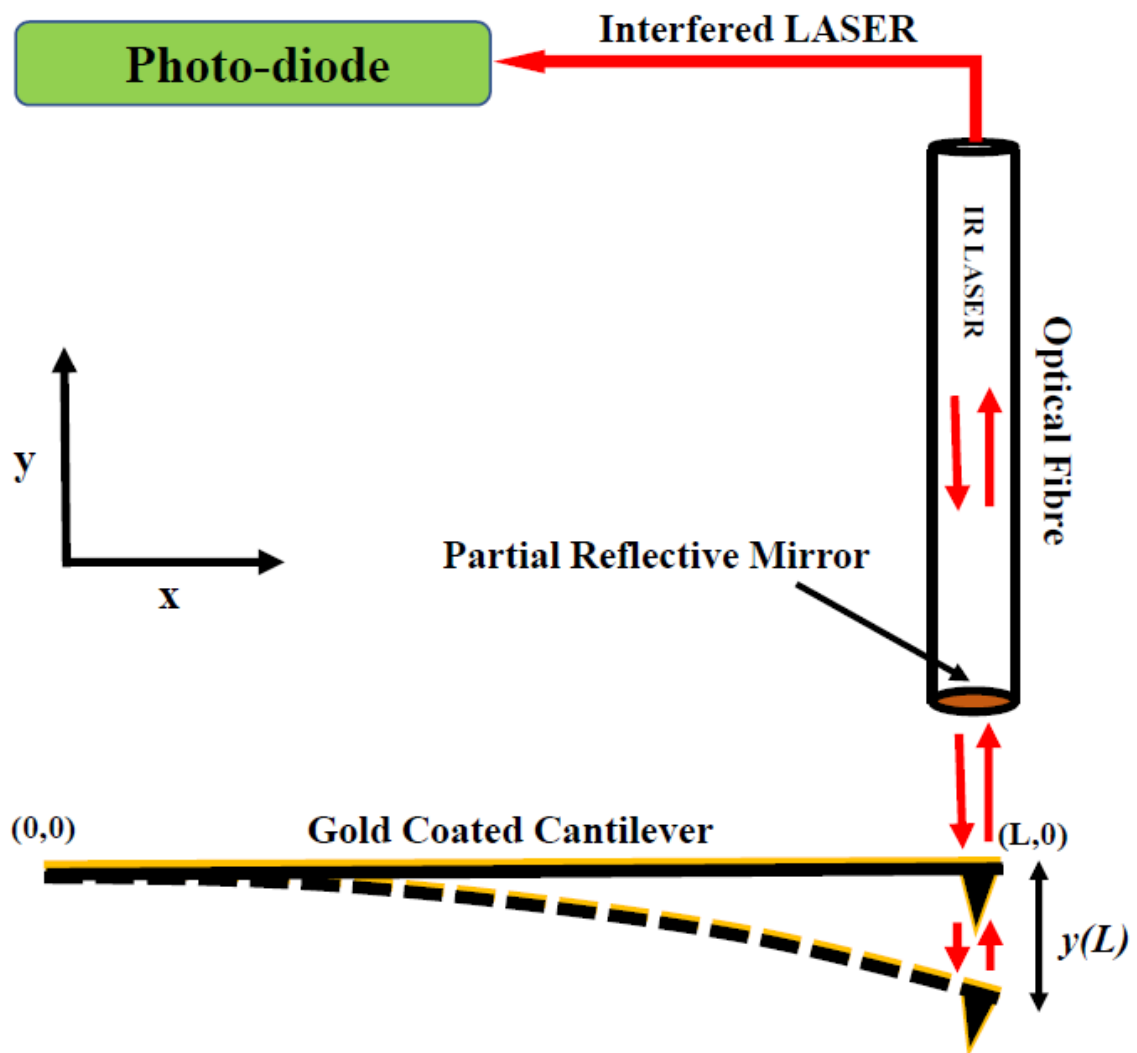


Fig. 2.5 Schematic representation of interferometric detection scheme. Partial reflective end of the optical-fibre is aligned parallel to the back of gold coated cantilever, acts as fully reflective mirror, and this arrangement forms Fabry-perot cavity. Infrared (IR) laser is passed through the optical-fibre which reflects back from two mirrors and interfere. Interfered laser is collected at the photo-detector which is sitting at a fixed distance. Change in the distance between two mirrors causes change in photo-detector output current which is utilized to estimate the displacement of the cantilever by keeping the fibre-position fixed using a feedback system.

which is determined by the software ¹. The deflection on the cantilever due to tip-sample

¹Optical fibre is mounted on a shear piezo (fibre-piezo). Fibre position is moved back and forth with the help of fibre-piezo to get the interference pattern at the photo-diode. Software finds the position at which change in the output current is maximum. This position is known as *quadrature-point*. Slope of the pattern at quadrature point is the sensitivity of the interferometer.

interaction causes the change in distance between the mirrors resulting in change in the output current of the photo-diode. This change in the current is proportional to the displacement of the cantilever. Change in the current (or corresponding voltage) can be converted into the cantilever displacement by dividing it with the detector sensitivity. Refer [140] for more details.

2.4.2 Optical-fibre: a partial reflective mirror

Making fibre end a partial reflective is a crucial part of the interferometric detection system as it is one of the mirrors in the Fabry-Perot etalon. We use an optical fibre with $9\ \mu\text{m}$ diameter core. To make its end flat and partial reflective, we first cleave it with a high precision cleaver. The reflectivity of the cleaved end is $\sim 2 - 3\%$. It is further dipped into a metal-organic precursor which is prepared by dissolving *Titanium-(IV)- ethylhexoxide* in *p-xylene* with 1:2 weight ratio. Now it is flashed into the blue flame of a Butane torch which burns away the organic compound and a uniform thin layer of metallic layer of TiO_2 remain at the end. This enhances the reflectivity of fibre end to $\sim 25\%$. Now, the fibre is glued onto the fibre-piezo for further measurements.

2.4.3 Nano-positioner

The assembly of optical-fibre and fibre-piezo is mounted on the nano-positioner which plays a crucial role in fibre-cantilever alignment. Nano-positioner consists of two plates, each plate has piezo three stacks where each stack contains three shear piezos. These are arranged in such a way that they provide X, Y, Z, θ , and ϕ motions when supplied some logic pulses. Logic pulses are generated using the *hex code* provided in *Nanomagnetic instruments* software. To align the fibre parallel to the cantilever, fibre is manually brought close to the cantilever and then nano-positioner is used for fine movements.

2.4.4 Detection Sensitivity

Detection Sensitivity is a conversion factor which is used to convert the photo-diode output voltage into cantilever displacement. It is defined as the amount of voltage generated per unit displacement of the cantilever.

In order to determine the detection sensitivity, first the fibre is aligned parallel to the cantilever. Now, cantilever is kept unperturbed and a sinusoidal voltage of $100\ \text{V}$ amplitude is supplied to the fibre-piezo. Fibre moves back and forth which generates an interference pattern (constructive and destructive peaks) at the photo-diode. Software plots the output

voltage (or power) vs fibre motion. Slope at each point in the pattern states the sensitivity of the interferometer for the change in distance between fibre and cantilever. We opt '*find quadrature automatically*' option in the software which instructs it to find the maximum slope position. At this position, the sensitivity is maximum and it is known as *quadrature-point*. Once the quadrature-point is found we opt the *lock quadrature* option which fixes the fibre position at quadrature-point. Software displays the slope (detector sensitivity) value which we note down and use for the data analysis. There is a feedback loop whose job is to keep the fibre at maximum sensitivity position (quadrature-point).

2.4.5 Sample cell

We use home-made sample cells. It consists of four components (Fig. 2.6 (b)): upper disc, O-ring, lower disc, and magnetic-disc. Upper disc is hollow, however, lower one is solid. O-ring is placed between the two discs and tightened it using four screws to prevent the liquid leakage. A small circular disc, made up of magnetic material, is attached at the lower surface of the lower-disc. This makes stable contact with the magnets attached on the sample-stage and reduces drift during the experiment. For protein experiments, a gold coated circular glass coverslip is placed between the O-ring and lower disc and screws are tightened properly. Cell is now ready for sample drop casting (Fig. 2.6 (a)). Sample is drop casted on the coverslip and processed further for the measurement.

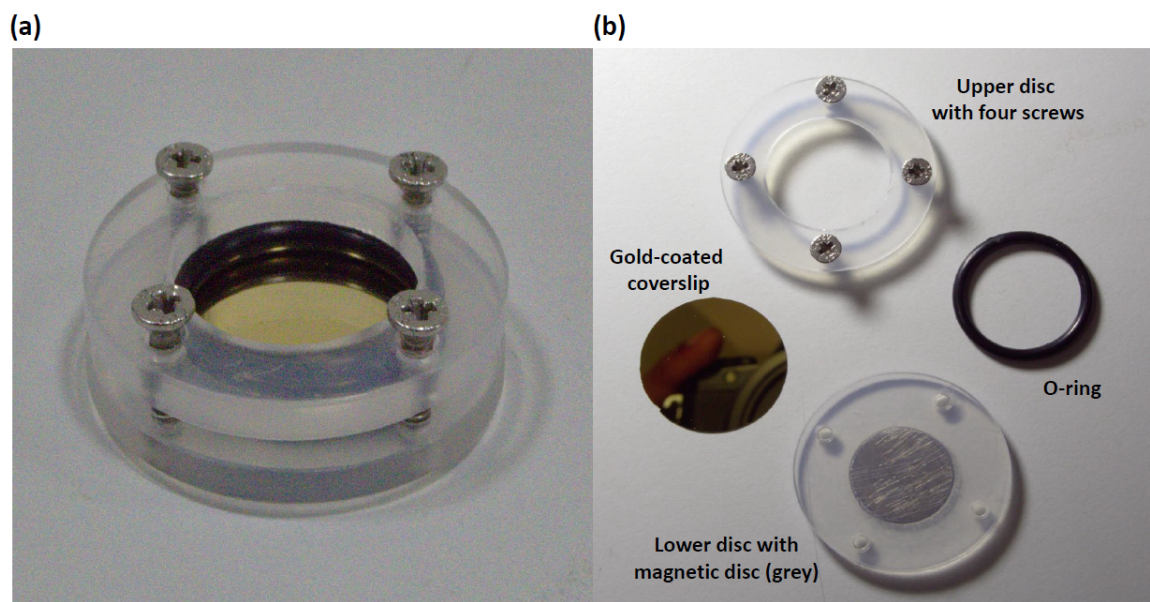


Fig. 2.6 Picture of sample-cell which we use in home-built setup. (a) Cell is assembled and it is ready for sample drop casting. (b) Different components of the cell.

2.4.6 Sample-stage movement

In our home-built setup, cantilever and fiber assembly is stationary during the experiment and tip-sample distance is changed by moving the sample-stage on which sample cell is mounted. Sample stage consists of three components: platform, scanner-piezo, and hammer-piezo. Platform is a flat disc containing three small magnets on the top surface. Sample cell is directly mounted on the platform where magnetic disc on the sample-cell makes stable contact. Scanner piezo is a cylindrical shaped shear piezo. Its outer surface is separated into four quadrants and act as four different electrodes and inner surface acts as another electrode and it is common for all outer electrodes. Sample is moved along X , Y , and Z directions during the experiment by providing pulses to the scanner-piezo. Hammer-piezo is used for coarse movement of the sample-stage to bring the sample close to cantilever. The coarse movement is achieved by supplying sawtooth pulses to it which takes advantage of the inertial effect on the motion. Refer [140] for more details.

2.5 Lock-in amplifier

Lock-in amplifier is essential for amplitude-modulation AFM experiments and it has been used for our all the experiments. We have used digital signal processing SR830 (Stanford, US) for our measurements. In amplitude-modulation AFM experiment, cantilever is sinusoidally excited, either from the base using dither piezo or from the tip using magnetic excitation, with a fixed frequency using the internal oscillator in the lock-in (external sources can also be used). The output from the detector is supplied as input to the lock-in amplifier. It determines the amplitude and phase of the oscillating cantilever at the excitation frequency which are observable parameters in experiment and these are further used to extract the sample properties. Depending on the excitation frequency, an appropriate lock-in time constant is selected. This decides the allowed input frequency bandwidth around the oscillation frequency. The time constant is supposed to be 2-3 times of inverse of excitation frequency such that lock-in generate one output point after averaging at least 2-3 oscillation cycles. The noise signals apart from the excitation frequency (including bandwidth) are blocked which enhances signal to noise ratio. Larger the time constant states lower bandwidth and hence better signal to noise ratio. This mechanism is also known as *phase-sensitive-detection*.

2.5.1 Phase-sensitive detection

Phase-sensitive is a powerful method to measure low signal which is obscured by high noise signal. The basic working principle of phase-sensitive detection is that it multiplies the

signal with a reference signal which allows to select the frequency component of signal which matches with the reference frequency and shows a constant phase difference. Rest of other frequency components are attenuated. Using this method one can make accurate measurement even if the signal is thousands time smaller than noise.

In our measurement, we excite the system (cantilever) with a fixed frequency and measure two parameters- *amplitude* of the system response (cantilever oscillation) and *phase difference* between system response and reference. Two phase-sensitive detectors (PSDs) are required. Consider $V_{sig} = V_s \sin(\omega_s t - \theta_s)$ is signal. For clarity, noise (other frequency components) is ignored as they eventually average out to be zero. Assuming that the form of the reference signal is $V_{ref} = V_r \sin(\omega_r t - \theta_r)$. Multiply the signal with reference:

$$V_{psd1} = V_s V_r \sin(\omega_s t - \theta_s) \sin(\omega_r t - \theta_r).$$

Where V_{psd1} is output of first phase-sensitive detector.

$$V_{psd1} = \frac{V_s V_r}{2} [\cos((\omega_s - \omega_r)t + (\theta_s - \theta_r)) - \cos((\omega_s + \omega_r)t + (\theta_s + \theta_r))]. \quad (2.6)$$

Eq. 2.6 is sum of two AC signals. One is with low frequency $(\omega_s - \omega_r)$ and another is with high frequency $(\omega_s + \omega_r)$. Passing it through a low-pass filter blocks high frequency component. When the signal and reference have same frequency $(\omega_s = \omega_r)$, the final output of first PSD is a DC signal (given that the phase difference between signal and reference remains fixed):

$$V_{psd1} = \frac{V_s V_r}{2} \cos(\theta_s - \theta_r). \quad (2.7)$$

As the reference amplitude is known, the final output of first PSD is just proportional to the amplitude times cosine of phase difference:

$$V_{psd1} \sim V_s \cos\theta. \quad (2.8)$$

Where $\theta = \theta_s - \theta_r$.

In second PSD, signal is multiplied with 90° shifted reference signal:

$$V_{psd2} = V_s V_r \sin(\omega_s t - \theta_s) \sin(\omega_r t - (\theta_r + 90)).$$

Where V_{psd2} is output of second phase-sensitive detector. This results again in sum of two AC signals. Passing this out through the low-pass filter we get final output which is proportional

to the amplitude times sine of phase difference;

$$V_{psd2} \sim V_s \sin\theta. \quad (2.9)$$

Eqs. 2.8 and 2.9 are the outputs from PSD1 and PSD2 respectively. These can be utilized to get amplitude of the signal:

$$V_s = \sqrt{V_{psd1}^2 + V_{psd2}^2} \quad (2.10)$$

and the phase can be computed as:

$$\theta = \tan^{-1}\left(\frac{V_{psd2}}{V_{psd1}}\right) \quad (2.11)$$

It is important to note that the outputs from PSD1 and PSD2 are nothing but the X and Y components of the signal oscillation respectively.

2.6 Magnetic excitation setup

In dynamic AFM experiments, method to extract sample properties is highly dependent on cantilever excitation scheme and the detection system. Usually the base-excitation using dither piezo with the slope-detection system is preferred due to its ease and availability. In AFM community it is well known that off-resonance operation provides a clean way of extracting viscoelasticity. It avoids the coupling of conservative and dissipative signals during the measurement, whereas, there is high probability of such coupling. In a part of our work we have found that *true off-resonance* measurements can only be performed using in displacement-detection system when base excitation scheme is used.

We investigated the possibility of true off-resonance measurements in slope-detection setups. It was found that it is possible when the cantilever-tip is directly excited. In order to do that, we made a module where a thin layer of magnetic material (cobalt) is coated on small-area at the backside of the tip-position. Magnetic excitation schemes have already applied for single molecule measurements in the past [77, 87]. We refined the previously applied methods in our experiment by following ways. (i) In previous experiments, two types of cantilevers have been used: backside fully coated commercial cantilevers and a piece of magnet particle is attached at the cantilever end. In mathematical modeling of cantilever dynamics, force on the cantilever is assumed at the end, not on the whole cantilever, so the use of fully coated commercial cantilevers can introduce error in the result when existing mathematical models are used for data analysis. To address this issue, a small piece of magnet particle is glued and used it for the measurement. But the issue with this cantilever is

significant mass loading due to glued magnet particle which is usually not accounted in the mathematical models.

In our experiment, we have coated the cantilever end position with a thin layer of cobalt ($\sim 30\text{ nm}$). Its mass is negligibly small compared to the cantilever mass, so it can be ignored. Since it is coated at the end position, so the existing mathematical models can also be applied for data analysis. To excite the cantilever-tip, we have made an electro-magnet.

I developed this setup with the help of Surya Pratap Deopa. He is a research fellow in my lab.

2.6.1 Magnetic cantilever preparation

The cantilever preparation was the most challenging part in this experiment. The entire cantilever, except the end position, was masked with photoresistive material using optical lithography technique. Usually, a uniform layer of photoresist is obtained by spin-coating the substrate. This approach did not work for the micro cantilever, due to its low surface area. The cantilever was exposed to ozone-plasma for (~ 30 minutes), which makes the surface adhesive and a uniform layer of photoresist was obtained by simply dipping the cantilever in the photoresist solution. It is then baked for 60 sec . After baking, the photoresist near the cantilever end was exposed to a high intensity laser which burns out the exposed part which is then removed by dipping the cantilever into developer solution. Using thermal evaporation deposition method chromium-cobalt layer ($3 : 30\text{ nm}$) were coated on the masked cantilever. The chromium-cobalt layer was deposited on the form of stacks. A layer of 1 nm was deposited before depositing each cobalt layer of 10 nm . The photoresist was then removed by sonicating (with low intensity) the cantilever in acetone for few seconds. Instead of using the sonicator, it can simply be shaken in the acetone solution. This leads to only the *Cr-Co* film remaining at the end of the cantilever as shown in the Fig. 2.8. It was then sputter coated with thin layer ($\sim 10\text{ nm}$) of gold from all sides to protect it from the buffer in which the experiments were performed. Picture is taken before the gold coating to show the deposited cobalt layer with clarity.

This method of depositing the cobalt layer perfectly works in air and water (milli-Q) medium, however, many times its not stable in buffer medium. The success rate of stable coating in buffer medium was $\sim 30\%$. The reason for such unstable coating is unknown. We perform our experiment using the cantilever with stable coating only.

We also tried coated the *Cr-Co* film at the cantilever-end by physically masking the cantilever (except the end position) using a metal strip. This method bypasses the use of photolithography technique. This method works well but the downside of this technique is the precision of masking.

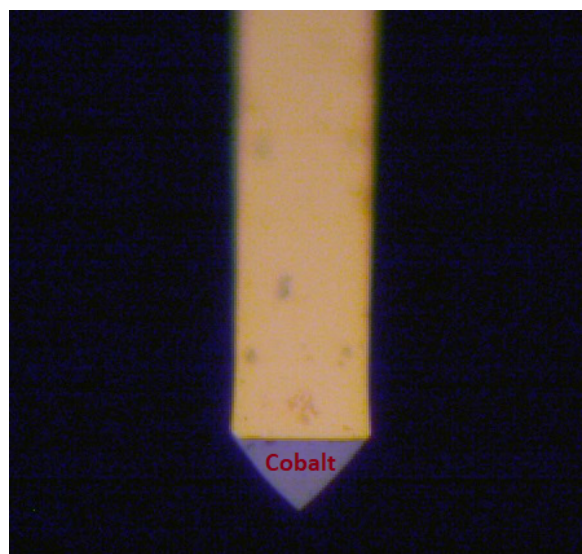


Fig. 2.7 A thin layer of cobalt (gray colour) is coated at end position of the back of a gold-coated cantilever. Image is captured in 50x optical microscope.

2.6.2 Electro-magnet

The AC magnetic field for driving the cantilever was obtained from an alternating current carrying solenoid. A $\sim 0.15\text{ mm}$ insulated copper wire was wound ~ 300 times around a ferrite core of diameter 2.5 mm and length 20 mm . A function generator (Tektronix AFG3252C, Washington, US) with 100 mA as the maximum current output was used as the current source. The solenoid was mounted on a holder that sat on one of the objective lens slots in the inverted microscope (Olympus IX73-check, Denmark). This made it easier to bring the solenoid directly under the cantilever. A maximum of 30 mG was achieved at a distance of $5 - 10\text{ mm}$. The solenoid had an impedance of 12 Ohms and a phase lag of 50 degrees at 133 Hz operation frequency (which we have used for most of our experiments). We observed that the solenoid temperature was increasing due to the Joule heating effect, and may alter the sample temperature. To reduce this heating we increased the number of turns and the wire cross section to use the minimum amount of current. The increased inductance due to higher number of turns did not cause problems since we worked with a constant and low frequency alternating current. The coil had an impedance of 12 Ohms at our operation frequency of 133 Hz .

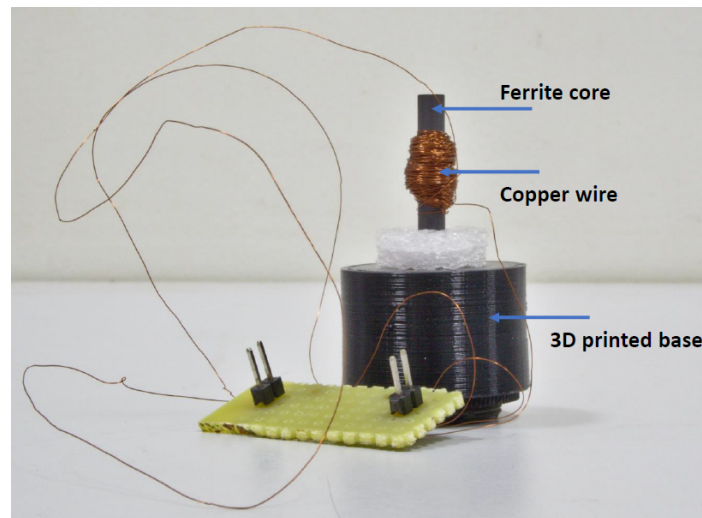


Fig. 2.8 Insulating coated thin copper wire ($\sim 0.15\text{ mm}$ diameter) is wrapped around a ferrite core (diameter 2.5 mm and length 20 mm). Electromagnet is mounted on a 3D printed base.

2.7 Sample preparation

Titin I27₈ polyprotein constructs containing eight identical domains in tandem were constructed from a plasmid similar to described in reference [165]. The plasmid was obtained from Dr. A.S.R. Koti's lab (TIFR, Mumbai). Expression and purification of the protein was done as described before [10] which we did in Dr. Thomas Pucadyil and Dr. Amrita Hazra's lab with the help of Mr. Sukrut Kamerkar and Yashwant Kumar.

The human cardiac muscle protein I27₈ gene was cloned in the pET-23a vector. I27₈ was transformed in BL21(DE3) and induced at 0.6 OD with 1mM IPTG for 6 hours at 37 °C. Cells were pelleted and stored at -40°C. For purification, the frozen bacterial pellet was resuspended in 1XPBS *pH* 7.4 supplemented with protease inhibitor cocktail (Roche). After resuspension, the cells were lysed by sonication in an ice water bath. The lysate was spun down at 18,500 *g* for 30 *minutes* and the supernatant was incubated with His-Pur cobalt resin (Thermo Scientific) for 1 *hour* at 4°C. The supernatant was then poured into the PD-10 column, and the resin was washed with 150 *ml* of 1XPBS *pH* 7.4 to get rid of non-specifically bound proteins. Protein was eluted using 1XPBS with 250 *mM* imidazole. Protein purity was checked using coomassie gel. Purified protein fractions were pooled and dialyzed overnight against 1XPBS *pH* 7.4 buffer to remove imidazole. For short-term storage (about a week), proteins were kept on ice at 4°C. For long-term storage (about 3 *months*) the protein was flash-frozen in liquid nitrogen with the addition of 10% glycerol. Frozen protein was dialyzed overnight against 1XPBS at 4°C to remove glycerol.

The protein sample (100 μL) in PBS with a concentration of 10 mg/mL was adsorbed onto a freshly evaporated gold coated coverslip² assembled in the fluid cell by incubating it on the substrate for 15-30 minutes at room temperature. The sample solution was washed three times with PBS to remove the excess un-adsorbed protein from the working solution.

2.8 Cantilever

We have used rectangular cantilevers, made of silicon nitride, from micromasch (Micromasch, Bulgaria) with stiffness 0.5-1 N/m for the experiments. Typical dimensions of the cantilevers were length $\sim 300 \mu\text{m}$, width $\sim 30 \mu\text{m}$, and thickness $\sim 1 \mu\text{m}$. Typical resonance frequency of the cantilever in water is $\sim 13 \text{kHz}$. Cantilever stiffness is calibrated using thermal fluctuation method available with JPK AFM [74].

²Gold deposition on the coverslips was done using the thermal-vapour deposition and sputtering systems available in the common facility in our institute.

Chapter 3

Theory: Amplitude-modulation atomic force microscopy

3.1 Introduction

Amplitude-modulation atomic force microscopy (AM-AFM) is a dynamic atomic force microscopy (dAFM) method for direct measurement of viscoelasticity of nano-scale systems. AFM cantilever is excited sinusoidally at a fixed frequency and tip is allowed to interact with the sample. Amplitude and phase of the cantilever end alter due to interaction force which is recorded and further utilized to extract interaction (or sample) viscosity and elasticity coefficients using an appropriate set of mathematical expressions. These mathematical expressions were derived from the solution of force equation of oscillating cantilever under influence of tip-sample forces. The force equation is a fourth order partial differential equation and highly non-linear due to the interaction force. Various approximations were imposed to get its analytical solution. The reliability of estimated sample viscoelasticity majorly depends on following two factors: approximations considered during the solution of equation of motion and fulfillment of these approximations in the experiment.

Form of equation, boundary conditions, and hence final solutions are different depending on the nature of experiment- cantilever excitation scheme and detection technique. Final solution is valid for an appropriate set of experimental parameters. So, the selection of suitable set of experimental parameters and a mathematical model are crucial to determine accurate results.

In this chapter, various aspects of solving the dynamics of cantilever under influence of interaction forces were discussed. We analyse our experimental data using these mathematical models which will be discussed in upcoming chapters in detail. All the solutions will be

derived for off-resonance measurements. We will also discuss the applicability of these mathematical models.

3.2 Equation of motion

Bending of a homogeneous rectangular cantilever beam in viscous medium is described by following Euler-Bernoulli equation (internal damping of the cantilever beam has been ignored):

$$-\tilde{\rho}\tilde{S}\frac{\partial^2 y(x,t)}{\partial t^2} - \gamma_c \frac{\partial y(x,t)}{\partial t} = EI \frac{\partial^4 y(x,t)}{\partial x^4} \quad (3.1)$$

Where x is the coordinate along the cantilever length (X -axis) with $x = 0$ at the clamped end and $x = L$ at the free end. y is the displacement along the perpendicular direction of the cantilever length (y -axis). $\tilde{\rho}\tilde{S} = \rho S + m_a$, m_a is hydrodynamic added mass where ρ is mass density of the cantilever material, $S(=bh)$ is area of the cantilever cross-section perpendicular to its length, b and h are width thickness of the cantilever respectively, γ_c is the cantilever drag coefficient per unit length, E is Young's modulus and $I(=bh^2/12)$ is second area moment.

Variable separation method can be applied to solve the Eq. 3.1, where the steady state solution can be assumed as $y(x,t) = y(x)Y(t)$. This allows to write two separate equations in terms of variables x and t . Product of the solutions of these equations determines the complete solution. This method has been applied to derive the *point-mass model*.

Continuous-beam model follows little different approach where the steady state solution of Eq. 3.1 for sinusoidally excited cantilever is assumed as $y(x,t) = y(x)e^{i\omega t}$. This results in following dispersion relation:

$$\tilde{\rho}\tilde{S}\omega^2 - i\omega\gamma_c = EI k^4 \quad (3.2)$$

and

$$\frac{d^4 y(x)}{dx^4} = k^4 y(x) \quad (3.3)$$

Eq. 3.3 is spatial part of Eq. 3.1. Now to get the complete solution of Eq. 3.1, Eq. 3.3 is needed to be solved. This requires a set of four boundary conditions which are nothing but derivatives of $y(x)$ at some values of x . Depending on the external perturbation, excitation mechanism and interaction forces, boundary conditions and hence the solutions

are different. In typical AFM experiments, the interaction force acts at the tip (cantilever-end) and excitation can either be applied at the base or the tip.

A complete analytical solution of Eq. 3.1 could not be derived due to following reasons: (i) Non-linear interaction force, and (ii) inhomogeneous boundary conditions. The interaction force can be assumed as linear in case of *small-oscillation amplitude*.

The analytical solution was derived for some special cases such as small excitation frequency and approximation of homogeneous boundary conditions.

3.2.1 Point-mass model

In point-mass model, variable separation method is applied to solve Eq. 3.1 where two equations, on space and time, are separately solved. To solve space part, boundary conditions were considered as homogeneous which provide a set of independent solutions ($y_n(x)$) for a freely oscillating cantilever. Each solution represents one eigen mode. Now solution ($y(x, t)$) is substituted into Eq. 3.1, multiply with $y_n(x)$ and using the orthogonal property of $y_n(x)$ a set of equations on time-variable is achieved. Each equation is for an eigen mode and are nothing but the damped harmonic oscillator equations- linear second order differential equations. Using the fact that the fundamental mode has most of the contribution in cantilever oscillation, it is considered as the force equation of the freely oscillating cantilever in viscous environment. Excitation force is directly included into the final equation depending on the excitation scheme. The interaction force, which is assumed to be *linear*, is considered as a perturbation on the forced-damped oscillator and included into the final equation. This treatment imposes the assumption of small interaction force compared to the cantilever force or ($k_c \ll k_i$). Now the final equation of motion of oscillating cantilever under influence of interaction force is a simple forced-damped harmonic oscillator equation with an effective mass (m^*), elastic (k') and damping (γ') coefficients. It is important to note that this treatment assumes the cantilever beam as a *point-mass* which is attached with a mass-less spring. That is why the model is known as *point-mass model*.

Lets assume that the solution of Eq. 3.1 is

$$y(x, t) = y(x)Y(t) \quad (3.4)$$

Substituting this into equation Eq. 3.1 and divide entire equation by $y(x)Y(t)$, we get following equations:

$$\frac{1}{y(x)} \frac{d^4 y(x)}{dx^4} = \frac{-\tilde{\rho} \tilde{S}}{EIY(t)} \frac{\partial^2 Y(t)}{\partial t^2} - \frac{\gamma_c}{EIY(t)} \frac{\partial Y(t)}{\partial t} \quad (3.5)$$

Above equation LHS is function of x alone and RHS is function of t alone. These two sides will be equal when each of them will be equal to a constant, say k^4 . This constant is known as the separation constant. So, we can write two separate equations:

$$\frac{d^4 y(x)}{dx^4} = k^4 y(x) \quad (3.6)$$

and

$$\frac{\partial^2 Y(t)}{\partial t^2} + \frac{\gamma_c}{\tilde{\rho}\tilde{S}} \frac{\partial Y(t)}{\partial t} = -\frac{k^4 EI}{\tilde{\rho}\tilde{S}} Y(t) \quad (3.7)$$

Now these two equations can be separately solved and combine to get the final solution (Eq. 3.4).

The general solution of Eq. 3.6 is given as

$$y(x) = a \sin(kx) + b \cos(kx) + c \sinh(kx) + d \cosh(kx) \quad (3.8)$$

Where a , b , c , and d are constants which can be determined using four appropriate boundary conditions. Following homogeneous boundary conditions are applied:

$$\begin{aligned} y(0) &= 0, & y'(0) &= 0, \\ y''(L) &= 0, & y'''(L) &= 0 \end{aligned} \quad (3.9)$$

Solving above set of equations (Eq. 3.9) results in following characteristic equation:

$$1 + \cos(k_n L) \cosh(k_n L) = 0 \quad (3.10)$$

Eq. 3.10 can have n (infinitely large) independent solutions. Each solution represents one flexural mode of the beam. Few solutions are: $k_1 L = 1.8751$, $k_2 L = 4.694$, $k_3 L = 7.8548$, and $k_4 L = 10.996$.

Now the final solution of Eq. 3.1 can be represented as the superposition of all independent solutions:

$$y(x, t) = \sum_n y_n(x) Y_n(t) \quad (3.11)$$

The $y_n(x)$ is defines as follows:

$$y_n(x) = \cos k_n x - \cosh k_n x - \frac{\cos k_n L + \cosh k_n L}{\sin k_n L + \sinh k_n L} [\sin k_n x - \sinh k_n x] \quad (3.12)$$

Where

$$y_n(L) = 2(-1)^n \quad (3.13)$$

Substitute the solution (Eq. 3.11) into Eq. 3.1, multiply entire equation with $y_n(x)$, and integrate it for the limit $[0, L]$. Now use the orthogonality property of $y_n(x)$ and Eq. 3.13, we can write a set of n independent temporal equations for *cantilever-end* ($x = L$):

$$m_c \sum_n \frac{\partial^2 Y_n(t)}{\partial t^2} + \gamma_c L \sum_n \frac{\partial Y_n(t)}{\partial t} + \sum_n k_{c,n} Y_n(t) = 0 \quad (3.14)$$

$m_c = \rho SL$ is actual cantilever mass, $k_{c,n} = k_n^4 EI$ is stiffness of n^{th} mode.

From Eqs. 3.11 and 3.13 we have:

$$y(x, t) = \sum_n y_n(x) Y_n(t) = \sum_n 2(-1)^n Y_n(t) = \sum_n (t) \quad (3.15)$$

So, Eq. 3.14 can be written for $w_n(t)$:

$$m' \sum_n \frac{\partial^2 w_n(t)}{\partial t^2} + \gamma_c L \sum_n \frac{\partial w_n(t)}{\partial t} + \sum_n k_{c,n} w_n(t) = 0 \quad (3.16)$$

Where $m' = 0.25 m_c$.

Using the fact that the fundamental mode dominated over all the other modes as the force constant (k_1) of this mode is almost equivalent to the static force constant (k_s) of the cantilever ($k_1 = 1.030 k_s$). In other words, the fundamental mode has most of the contribution in cantilever oscillation, however, the contribution from higher modes can be neglected. Hence it is assumed that the fundamental mode is adequate to represent the dynamics of the cantilever [49]. The equation of motion for the fundamental mode, which governs the dynamics of the freely oscillating cantilever, is:

$$m^* \frac{\partial^2 w(t)}{\partial t^2} + \gamma_c L \frac{\partial w(t)}{\partial t} + k_c w(t) = 0 \quad (3.17)$$

Where w is displacement of the point-mass (fundamental mode), $m^* (= 0.2425 m_c)$ is effective mass of the cantilever.

The final equation of freely oscillating cantilever (Eq. 3.17) is nothing but an equation of a *damped harmonic oscillator*. Now the contribution of cantilever-excitation and tip-sample interaction force is directly included in Eq. 3.17 and solved for the interaction *stiffness* and *damping* coefficients which are discussed below. It is to note that to derive the final

point-mass model equation, one can include the cantilever-excitation and interaction force into Eq. 3.1 using δ -function as has been done in reference [49].

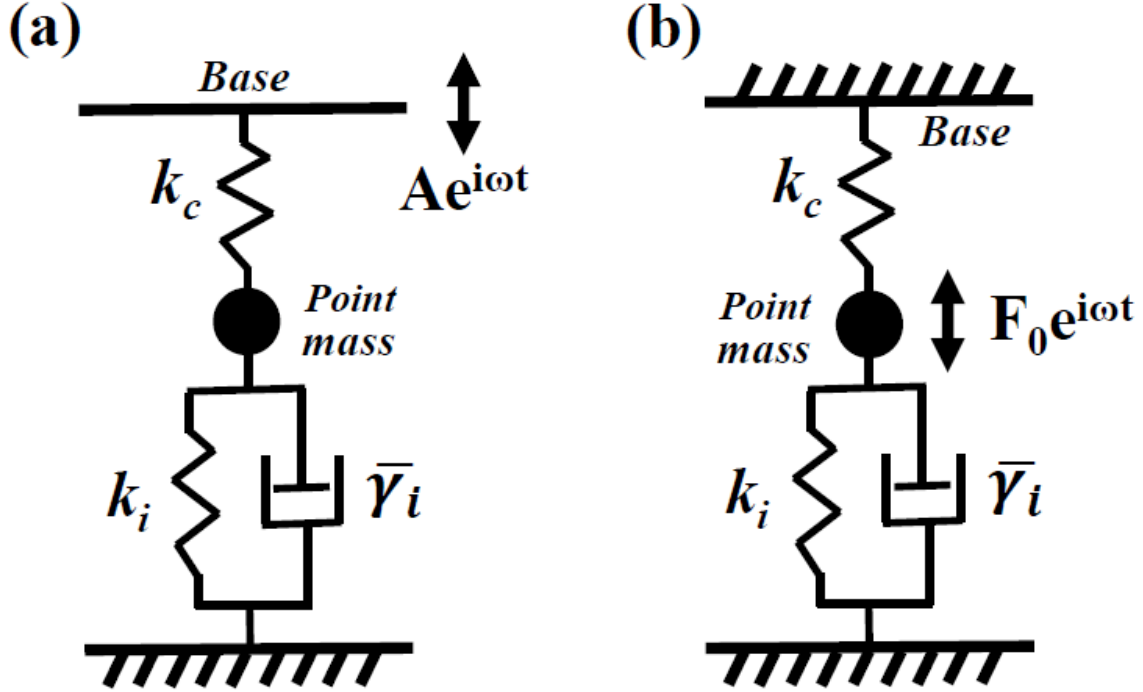


Fig. 3.1 Schematic representation of point-mass approximated cantilever under influence of a linear interaction force. (a) Representing the base-excited point-mass approximation where base is driven by $Ae^{i\omega t}$. (b) Representing the tip-excited point-mass approximation where base is rigidly fixed and tip is excited with force $F_0e^{i\omega t}$.

3.2.1.1 Base-excitation

When an AFM cantilever is excited from the base sinusoidally ($Ae^{i\omega t}$) and tip experiences a *small perturbation* due to a *linear viscoelastic* force ($F_i = k_i w(t) + \bar{\gamma}_i \frac{dw(t)}{dt}$), it is approximated as a point-mass connected to one end of a spring whose other end is driven (see Fig. 3.1 (a)). The Equation of motion for this point-mass can be written as:

$$m^* \frac{\partial^2 w(t)}{\partial t^2} + \gamma_c L \frac{\partial w(t)}{\partial t} + k_c (w(t) - Ae^{i\omega t}) - F_i = 0 \quad (3.18)$$

Where $F_i = k_i w(t) + \bar{\gamma}_i \frac{dw(t)}{dt}$ is the interaction force which is assumed to be *linear viscoelastic*. Other parameters have the same meaning as in the continuous-beam model. Eq. 3.18 can be written as:

$$m^* \frac{\partial^2 w(t)}{\partial t^2} + \gamma' \frac{\partial w(t)}{\partial t} + k' w(t) = k_c A e^{i\omega t} \quad (3.19)$$

Eq. 3.19 is an equation of motion for a forced damped harmonic oscillator with effective stiffness ($k' = k_c + k_i$), effective damping coefficient ($\gamma' = \gamma_c L + \bar{\gamma}_i$), and effective drive force ($k_c A$). The amplitude (R_{pm}) and phase (θ_{pm} , phase difference between drive and tip) of the tip will be given as:

$$R_{pm} = \frac{k_c A}{\sqrt{(k' - m^* \omega^2)^2 + (\omega \gamma')^2}}, \quad \theta_{pm} = \tan^{-1} \left(\frac{\omega \gamma'}{k' - m^* \omega^2} \right) \quad (3.20)$$

Further, Eq. 3.20 can be solved for interaction stiffness and damping coefficient for small excitation frequency ($\omega \ll \omega_0$):

$$k_i = k_c \left(\frac{A \cos \theta_{pm}}{R_{pm}} - 1 \right) \quad (3.21)$$

$$\gamma' = - \frac{k_c A \sin \theta_{pm}}{R_{pm} \omega} \quad (3.22)$$

Again, this solution is valid when stiff cantilever (interaction force (F_i) is considered as the perturbation) is used at off-resonance ($\omega \ll \omega_0$) and small-amplitude ($F_i = k_i w(t) + \bar{\gamma}_i \frac{dw(t)}{dt}$).

3.2.1.2 Tip-excitation

When an AFM cantilever is excited from the tip sinusoidally with excitation force ($F_0 e^{i\omega t}$) and tip experiences a *small perturbation* due to a *linear viscoelastic* force ($F_i = k_i w(t) + \bar{\gamma}_i \frac{dw(t)}{dt}$), it is approximated as a point-mass, connected to a massless spring, which is driven sinusoidally (see Fig. 3.1 (b)). The Equation of motion for this point-mass can be written as:

$$m^* \frac{\partial^2 w(t)}{\partial t^2} + \gamma_c L \frac{\partial w(t)}{\partial t} + k_c w(t) - F_0 e^{i\omega t} - F_i = 0 \quad (3.23)$$

All parameters have the same meaning as described in previous sections. Eq. 3.23 can be written as:

$$m^* \frac{\partial^2 w(t)}{\partial t^2} + \gamma' \frac{\partial w(t)}{\partial t} + k' w(t) = F_0 e^{i\omega t} \quad (3.24)$$

Eq. 3.24 is an equation of motion for a forced damped harmonic oscillator with effective stiffness ($k' = k_c + k_i$), effective damping coefficient ($\gamma' = \gamma_c L + \bar{\gamma}_i$). The amplitude (R_{pm}) and phase (θ_{pm} , phase difference between drive and tip) of the tip will be given as:

$$R_{pm} = \frac{k_c A_0}{\sqrt{(k' - m^* \omega^2)^2 + (\omega \gamma')^2}} \quad (3.25a)$$

$$\theta_{pm} = \tan^{-1} \left(\frac{\omega \gamma'}{k' - m^* \omega^2} \right) \quad (3.25b)$$

Further, Eq. 3.25 can be solved for interaction stiffness and damping coefficient for small excitation frequency ($\omega \ll \omega_0$):

$$k_i = k_c \left(\frac{A_0 \cos \theta_{pm'}}{R_{pm'}} - 1 \right) \quad (3.26)$$

$$\gamma' = - \frac{k_c A_0 \sin \theta_{pm'}}{R_{pm'} \omega} \quad (3.27)$$

Again, this solution is valid when stiff cantilever (interaction force (F_i) is considered as the perturbation) is used and oscillated at off-resonance ($\omega \ll \omega_0$) with small-amplitude ($F_i = k_i w(t) + \bar{\gamma}_i \frac{dw(t)}{dt}$).

3.2.2 Continuous-beam model

In continuous-beam model, continuous-nature of the cantilever beam is considered. Excitation and interaction force are included in the boundary conditions. Interaction force is considered as linear ($F_i = k_i w(t) + \bar{\gamma}_i \frac{dw(t)}{dt}$) and Eq. 3.1 is solved for small interaction force ($g \ll 1$ or $k_i \ll k_c$) and small-oscillation frequency ($z \ll 1$ or $\omega \ll \omega_0$).

3.2.2.1 Base-excitation

When the cantilever is excited from the base, following boundary conditions can be applied to solve Eq. 3.3:

$$\begin{aligned} y(0) - A &= 0, & y'(0) &= 0, \\ y''(L) &= 0, & EIy'''(L) - (k_i + i\omega \bar{\gamma}_i)y(L) &= 0 \end{aligned}$$

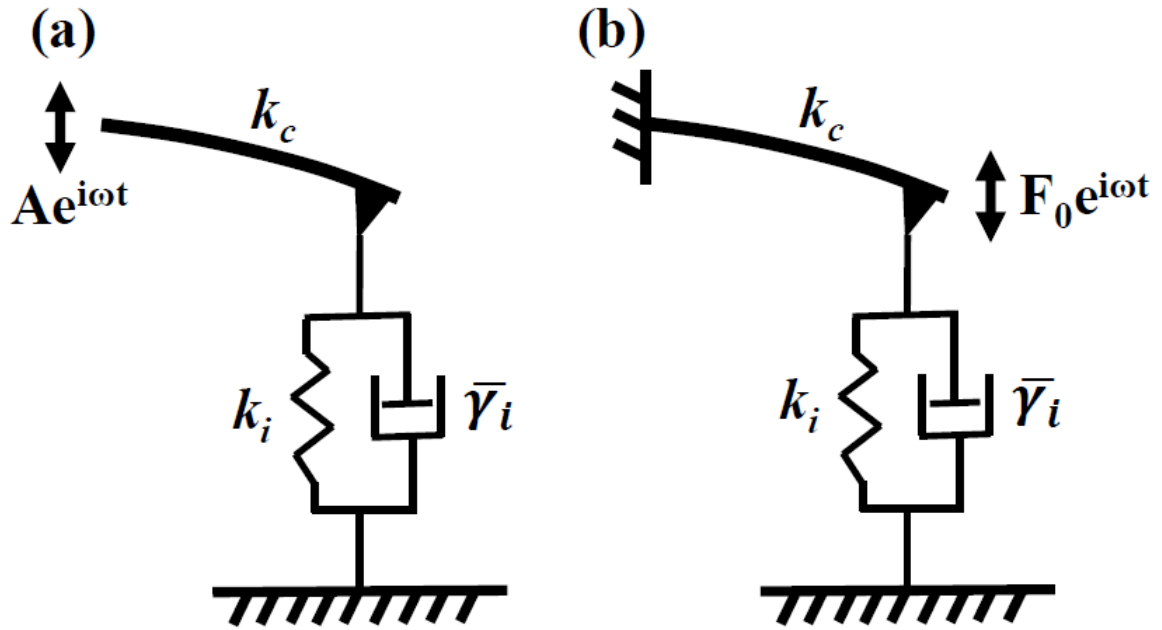


Fig. 3.2 Schematic representation of oscillating cantilever, considered its continuum nature, under influence of a linear interaction force. (a) Representing the base-excited cantilever where base is driven by $Ae^{i\omega t}$. (b) Representing the tip-excited cantilever where base is rigidly fixed and tip is excited with force $F_0e^{i\omega t}$.

Above set of linear equations can be written in matrix form: $MX - N = 0$ and solve for X using matrix method. Where M and N are:

$$M = \begin{bmatrix} 0 & 1 & 0 & 1 \\ k & 0 & k & 0 \\ -k^2 \sin(kL) & -k^2 \cos(kL) & k^2 \sinh(kL) & k^2 \cosh(kL) \\ -\cos(kL) - q \sin(kL) & \sin(kL) - q \cos(kL) & \cosh(kL) - q \sinh(kL) & \sinh(kL) - q \cosh(kL) \end{bmatrix}$$

and

$$N = \begin{bmatrix} -A \\ 0 \\ 0 \\ 0 \end{bmatrix}$$

Where $q = \frac{k_i + i\omega\tilde{\gamma}_i}{EI k^3}$.

Solving the matrix equation $MX - N = 0$, the coefficients (or X) are following:

$$a = \frac{A[\cosh(z)(-2q\cos(z) + \sin(z)) + \cos(z)\sinh(z)]}{2[1 + \cosh(z)(\cos(z) + q\sin(z)) - q\cos(z)\sinh(z)]},$$

$$b = \frac{A[1 + \cosh(z)(\cos(z) + 2q\sin(z)) - \sin(z)\sinh(z)]}{2[1 + \cosh(z)(\cos(z) + q\sin(z)) - q\cos(z)\sinh(z)]},$$

$$c = \frac{-A[\cosh(z)(-2q\cos(z) + \sin(z)) + \cos(z)\sinh(z)]}{2[1 + \cosh(z)(\cos(z) + q\sin(z)) - q\cos(z)\sinh(z)]},$$

$$d = \frac{A[1 + \cos(z)\cosh(z) + (-2q\cos(z) + \sin(z))\sinh(z)]}{2[1 + \cosh(z)(\cos(z) + q\sin(z)) - q\cos(z)\sinh(z)]}$$

Where $z = kL$.

Solution (displacement) at $x = L$ can be written as:

$$y(L) = a \sin(kL) + b \cos(kL) + c \sinh(kL) + d \cosh(kL) \quad (3.28)$$

and slope

$$y'(L) = ak \cos(kL) - bk \sin(kL) + ck \sinh(kL) + dk \cosh(kL) \quad (3.29)$$

Substitute values of a , b , c , and d into Eqs. A.5 and A.6 and assuming following two conditions:

$$z = kL = \left[\frac{3(\tilde{\rho}\tilde{S}\omega^2 L - i\omega\gamma_c L)}{k_c} \right]^{\frac{1}{4}} \ll 1 \quad (3.30a)$$

$$g = \frac{3(k_i + i\omega\tilde{\gamma}_i)}{k_c} \ll 1 \quad (3.30b)$$

we get following relations for slope displacement and slope of the cantilever-end ($x = L$):

$$y(L) = A - \frac{gA}{3} + \frac{Az^4}{8} \quad (3.31)$$

$$y'(L) = \frac{-Ag}{2L} + \frac{Az^4}{6L} \quad (3.32)$$

In Eq. 3.30, the assumption $z \ll 1$ ensures that the excitation frequency is very small compared to the fundamental resonance of the cantilever ($\omega \ll \omega_0$), and $g \ll 1$ ensures that the cantilever stiffness is much larger than the interaction stiffness ($k_i \ll k_c$).

Substituting the values of g and z back into Eqs. 3.31 and 3.32 gives the following expressions for slope and displacement respectively

$$\left. \frac{\partial y(x)}{\partial x} \right|_{x=L} = \frac{A}{2k_c L} (-3k_i + \tilde{\rho} \tilde{S} \omega^2 L) - i \frac{A \omega}{2k_c L} (3\tilde{\gamma}_i + \gamma_c L) \quad (3.33)$$

and

$$y(L) = \frac{A}{k_c} (k_c - k_i) - i \frac{A \omega}{k_c} \tilde{\gamma}_i \quad (3.34)$$

Modulus of Eq. 3.33 gives us the amplitude of the bending (slope) at $x = L$ and the argument gives us the phase lag:

$$R_b = \frac{A}{2k_c L} \sqrt{(-3k_i + \tilde{\rho} \tilde{S} \omega^2 L)^2 + \omega^2 (3\tilde{\gamma}_i + \gamma_c L)^2},$$

$$\theta_b = \arctan \left(-\omega \frac{3\tilde{\gamma}_i + \gamma_c L}{-3k_i + \tilde{\rho} \tilde{S} \omega^2 L} \right) \quad (3.35)$$

Now the real and imaginary components of the bending are

$$X_b = \frac{A}{2k_c L} (-3k_i + \tilde{\rho} \tilde{S} \omega^2 L),$$

$$Y_b = -\frac{A \omega}{2k_c L} (3\tilde{\gamma}_i + \gamma_c L) \quad (3.36)$$

This is identical to the result obtained by Benedetti et al. [7]. Further, the amplitude and phase for the displacement y in the limit $g \ll 1$ and $z \ll 1$ is

$$R_d = \frac{A}{k_c} \sqrt{(k_c - k_i)^2 + (\omega \tilde{\gamma}_i)^2},$$

$$\theta_d = \arctan \left(-\omega \frac{\tilde{\gamma}_i}{k_c - k_i} \right) \quad (3.37)$$

The real and imaginary components of the displacement are

$$X_d = \frac{A}{k_c} (k_c - k_i), \quad Y_d = -\frac{A \omega}{k_c} \tilde{\gamma}_i \quad (3.38)$$

The subscript d stands for displacement.

Finally following set of equations can be used to estimate interaction stiffness and damping coefficients.

(i) For displacement-detection: from

$$k_i = k_c \left(1 - \frac{X_d}{A}\right) \quad (3.39)$$

$$\bar{\gamma}_i = -\frac{k_c Y_d}{A \omega} \quad (3.40)$$

It is important to note that the base amplitude is equal to cantilever's free amplitude ($A \approx A_0$).

(ii) For slope-detection:

$$k_i = \frac{1}{3} \tilde{\rho} \tilde{S} \omega^2 L - \left(\frac{2k_c L}{3A}\right) X_b \quad (3.41)$$

$$\bar{\gamma}_i = \left(\frac{2k_c L}{3A\omega}\right) Y_b - \frac{\gamma_c L}{3} \quad (3.42)$$

3.2.2.2 Tip-excitation

For a cantilever being driven from the tip and the tip experiences a linear viscoelastic force due to tethered macromolecule, the boundary conditions are given by

$$y(0) = 0, \quad y'(0) = 0, \quad y''(L) = 0, \quad EIy'''(L) = (k_i + i\omega\bar{\gamma}_i)y(L) - F_0 \quad (3.43)$$

Where $F_0 = k_c A_0$ is the magnitude of externally applied force at the tip. A_0 is amplitude far away from the surface (free amplitude). The constants are determined by solving the four set of equations (boundary conditions). Rearranging the set of equations (Eqn. 3.43):

$$y(0) = 0, \quad y'(0) = 0, \quad y''(L) = 0, \quad y'''(L) - (k^3 \times q)y(L) - F = 0 \quad (3.44)$$

Where $q = (k_i + i\omega\bar{\gamma}_i)/EIk^3$ and $F = F_0/EI$.

Above set of linear equations can be written in the matrix form: $MX - N = 0$ and solve for X using matrix method. Where M and N are:

$$M = \begin{bmatrix} 0 & 1 & 0 & 1 \\ k & 0 & k & 0 \\ -k^2 \sin(kL) & -k^2 \cos(kL) & k^2 \sinh(kL) & k^2 \cosh(kL) \\ -k^3 \cos(kL) - qk^3 \sin(kL) & k^3 \sin(kL) - qk^3 \cos(kL) & k^3 \cosh(kL) - qk^3 \sinh(kL) & k^3 \sinh(kL) - qk^3 \cosh(kL) \end{bmatrix}$$

and

$$N = \begin{bmatrix} 0 \\ 0 \\ 0 \\ F \end{bmatrix}$$

Solving the matrix equation $MX - N = 0$, the coefficients (orX) are following:

$$\begin{aligned} a &= \frac{F[\cos(z) + \cosh(z)]}{2k^3[1 + \cosh(z)(\cos(z) + q \sin(z)) - q \cos(z) \sinh(z)]} \\ b &= -\frac{F[\sin(z) + \sinh(z)]}{2k^3[1 + \cosh(z)(\cos(z) + q \sin(z)) - q \cos(z) \sinh(z)]} \\ c &= -\frac{F[\cos(z) + \cosh(z)]}{2k^3[1 + \cosh(z)(\cos(z) + q \sin(z)) - q \cos(z) \sinh(z)]} \\ d &= \frac{F[\sin(z) + \sinh(z)]}{2k^3[1 + \cosh(z)(\cos(z) + q \sin(z)) - q \cos(z) \sinh(z)]} \end{aligned} \quad (3.45)$$

Where $z = kL$.

Solution (displacement) at $x = L$ can be written as:

$$y(L) = a \sin(z) + b \cos(z) + c \sinh(z) + d \cosh(z) \quad (3.46)$$

and slope

$$y'(L) = ak \cos(z) - bk \sin(z) + ck(z) + dk \sinh(z) \quad (3.47)$$

Substitute values of a , b , c , and d into Eq. 3.46 and 3.47. We now define dimensionless parameters, g and z given by

$$g = q(kL)^3 = \frac{3(k_i + i\omega\bar{\gamma}_i)}{k_c}, \quad z = \left[\frac{3(\bar{\rho}\bar{\omega}^2L - i\omega\gamma_cL)}{k_c} \right]^{\frac{1}{4}} \quad (3.48)$$

Where k_i and $\bar{\gamma}_i$ are interaction stiffness and damping respectively; $k_c (= \frac{3EI}{L^3})$ is the cantilever stiffness.

Take the Taylor expansion for $z \ll 1$ and $g \ll 1$, displacement and slope are following :

$$y(L) = A_0 \left[1 - \frac{g}{3} \right], \quad y'(L) = \frac{3A_0}{2L} \left[1 - \frac{g}{3} \right] \quad (3.49)$$

Substituting the values of g and z back into the Eq. 3.49 gives the following expressions for slope and displacement respectively

$$\frac{\partial y(x)}{\partial x} \Big|_{x=L} = \frac{3A_0}{2Lk_c} (k_c - k_i) - i\omega \frac{3A_0}{2Lk_c} \bar{\gamma}_i, \quad (3.50)$$

and

$$y(L) = \frac{A_0}{k_c} (k_c - k_i) - i\omega \frac{A_0}{k_c} \bar{\gamma}_i \quad (3.51)$$

Modulus of Eq. 4.14 gives us the amplitude of the bending (slope) at $x = L$:

$$R_b = \frac{3A_0}{2k_c L} \sqrt{(k_c - k_i)^2 + \omega^2 \bar{\gamma}_i^2}, \quad \theta_b = \arctan\left(-\omega \frac{\bar{\gamma}_i}{k_c - k_i}\right) \quad (3.52)$$

Now the real and imaginary components of the bending are

$$X_b = \frac{3A_0}{2k_c L} (k_c - k_i), \quad Y_b = -\frac{3A_0 \omega}{2k_c L} \bar{\gamma}_i \quad (3.53)$$

This is identical to the result obtained by Benedetti et al. [7]. Further, the amplitude and phase for the displacement y in the limit $g \ll 1$ and $z \ll 1$ are

$$R_d = \frac{A_0}{k_c} \sqrt{(k_c - k_i)^2 + (\omega \bar{\gamma}_i)^2}, \quad \theta_d = \arctan\left(-\omega \frac{\bar{\gamma}_i}{k_c - k_i}\right) \quad (3.54)$$

The real and imaginary components of the displacement are

$$X_d = \frac{A_0}{k_c} (k_c - k_i), \quad Y_d = -\frac{A_0 \omega}{k_c} \bar{\gamma}_i \quad (3.55)$$

The subscript d stands for displacement.

Finally following set of equations can be used to estimate interaction stiffness and damping coefficients.

(i) For displacement-detection: from

$$k_i = k_c \left(1 - \frac{X_d}{A}\right) \quad (3.56)$$

$$\bar{\gamma}_i = -\frac{k_c Y_d}{A \omega} \quad (3.57)$$

It is important to note that the base amplitude is equal to cantilever's free amplitude ($A \approx A_0$).

(ii) For slope-detection:

$$k_i = k_c \left(1 - \frac{2L}{3A} X_d\right) \quad (3.58)$$

$$\bar{\gamma}_i = -\frac{2k_c L}{3A \omega} Y_d \quad (3.59)$$

3.3 Discussion

In previous section, we derived the relationships for interaction stiffness and damping coefficient in terms of observable parameters for different excitation schemes and detection systems. These mathematical models were divided into two categories- point-mass model and continuous-beam model. Depending on the experiment, an appropriate mathematical model must be chosen for data analysis. In this section, we will discuss different aspects of these models in order to apply them for

interaction viscoelasticity determination, in brief. This will be elaborately discussed in upcoming chapters.

3.3.1 Experiment, theoretical model, initial phase offset, and artefact

In AM-AFM experiments, cantilever is excited at a fixed frequency and modulation in observable parameters are recorded. There are two methods of excitation: base-excitation and tip-excitation, and it can be excited in two regimes: off-resonance and on-resonance. Two detection systems are used to detect cantilever response: slope-detection and displacement-detection. There are two set of observable parameters which are recorded: (amplitude, phase) and (X, Y) . Finally two mathematical models can be used for data analysis: point-mass model and continuous-beam model.

It is crucial to note that the offset in the initial phase of oscillating cantilever introduces *artefacts* in the final results which is irrespective of the applied excitation scheme, operation frequency regime, detection system, observable parameters, and mathematical models. This will be discussed in *chapter-4* with experimental evidences and its theoretical explanation.

3.3.2 Off-resonance operation

There are many advantages in working *true off-resonance* regime such as the dynamics of the cantilever is linear, probability of presence of spurious peaks in cantilever frequency response is low, effect of hydrodynamics is negligibly small.

Since the effect of hydrodynamics is negligibly small, this allows to oscillate the cantilever-tip in phase with the drive in absence of tip-sample interaction forces i.e. the initial phase is $\sim 0deg$. The priory knowledge of the initial phase helps in identifying the presence of offset in initial phase and allows to perform artefact free measurements. Also the linear cantilever response makes its dynamics easy to model. Different aspects of off-resonance operation will be discussed in almost all upcoming chapters.

3.3.3 Excitation scheme, detection system, and true off-resonance operation

As the importance of true off-resonance operation to perform an artefact free measurement has been briefly discussed in previous section, it is essential to know how it can be implemented in the experiment.

Base excitation scheme with slope-detection system (commercial AFMs) is most popular method of performing AM-AFM experiments due to its ease in implementation and commercial availability. It is important to note that a true off-resonance operation cannot be performed with this setup due to its low sensitivity and low signal-to-noise ratio. It can be achieved in base-excited experiments when displacement-detection system is used. Displacement-detection can be attained by using interferometer

based detection schemes [140]. Displacement-detection based AFMs are not commercially available. A true off-resonance measurement can also be performed in commercial AFMs when the tip-excitation scheme is used. There are two popular methods of tip-excitation: magnetic excitation [79, 84, 170] and photo-thermal excitation [47, 144]. In photo-thermal method, a laser beam is used to excite the cantilever-tip which heats the environment locally. This can damage or change the sample property. Whereas, magnetic excitation does not have heating issue, but a thin layer of magnetic material need to be coated at the cantilever-end. Getting the thin layer at cantilever-end position which is stable in liquid environment (specially in buffer) is not established yet. Also cantilevers with magnetic-material coated only near the tip position are not commercially available. We have proposed a method to get a stable coating of cobalt layer which will be discussed in chapter-5. The true off-resonance measurement using base-excitation scheme in interferometer based displacement-detection system and tip-excitatoin scheme in slope-detection based system will be discussed in *chapter-5*.

3.3.4 Validity of point-mass model

In point-mass model, cantilever-beam is approximated as a point-mass and the interaction force acting on the cantilever-tip is treated as a small perturbation on the moving point-mass. These assumptions make the understanding of cantilever dynamics very simple and its analytical solution becomes straight-forward. This model has been extensively used in the past due to its simplicity. Recent study by Benedetti et al. [7] raises doubt on previous studies that have been done on various nano-scale systems such as single polymer [109] and nano-confined liquids [34, 117] where base-excited experiments were performed in slope-detection based AFMs and PM model were used for data analysis. Their non-observation of dissipation in single protein molecule contradicts with other AFM based measurements [77, 87, 93]. Apart from this, a credible amount work has been done to understand the behaviour of nano-confined liquids using base-excited dynamic measurements in displacement-detection based AFM and PM model have been used for data analysis [82, 90, 92, 141]. Past studies were based on two types of measurements: slope-detection and displacement-detection and PM model have been used for data analysis. So, the reliability of those results depends on the accuracy of the mathematical model, which is point-mass model, that have been used to analysed the data. To resolve the issue associated with the adequacy of point-mass model in order to extract nano-scale viscoelasticity, a detailed study is required. We have investigated the validity of point-mass model. We found that point-mass model predicts same results as the continuous-beam model for base-excited and tip-excited dynamic AFM experiments when they are performed only at truly off-resonance frequency regime using displacement-detection and slope-detection respectively. Small tip-amplitude and stiff cantilevers, essential assumptions in both the models, are also a necessity for this consistency. This will be discussed in *chapter-5*.

3.4 Conclusion

AM-AFM measurements can be performed to quantify the nano-scale viscoelasticity. To perform an artifact free measurement one has to confirm the absence of offset in the initial phase. This can be ensured by choosing a true off-resonance excitation regime where initial phase is known. This can be achieved by using displacement-detection for base-excitation measurements and slope-detection for tip-excitation measurements. We believe that displacement-detection with tip-excitation can also be applied for such experiments. It is important to note that the point-mass model predicts the same results as the continuous-beam model when a *stiff cantilever* is used and it is operated at *truly off-resonance* regime and oscillation amplitude is *small*.

Chapter 4

The nano-scale viscoelasticity using base-excited atomic force microscopy in liquid environment

4.1 Introduction

The viscoelasticity of single proteins and other biologically relevant macromolecules is essential to understand their function in single molecule limit. The single macromolecules such as unfolded proteins bear rubber-like entropic elasticity and internal friction characterized by finite dissipation coefficient. Direct measurement of this viscoelastic response is important since it plays a significant role, both in polymer physics as well as protein folding dynamics. Atomic Force Microscopy is used to measure viscoelasticity of single macromolecules and other nano-scale systems owing to its unprecedented spatial resolution in physiological conditions [7, 34, 73, 77, 82, 87, 92, 96, 117, 132, 141]. However, the viscoelastic response of single polymer chain is difficult to measure and is prone to artefacts owing to the complications of hydrodynamics of macroscopic probe itself in the liquid environment [96, 135, 151].

In a typical AFM experiment, mica or Au substrate is sparsely coated with the biological macromolecule and is placed in the liquid cell. An oscillating sharp probe attached to a cantilever spring is then brought close to a molecule. The protein is allowed to attach to it from either C or N terminus through nonspecific binding. The bending in the cantilever beam as well as the phase and amplitude of cantilever oscillations are measured as the molecule is pulled away from the surface. The cantilever bending provides the amount of force applied on the protein as it is slowly stretched. The amplitude and phase may provide the viscoelastic response of the molecule at different extensions [7, 77, 87].

A solution to an appropriate equation of motion for the cantilever whose tip is tethered with a protein provides a relationship between measured parameters (amplitude and phase) and molecule's viscoelastic properties, namely the stiffness and dissipation coefficient [7, 76]. This approach has been

extremely successful for experiments performed in vacuum or air [3, 31, 50], however quantification of viscoelastic response from observed quantities is not straightforward in liquid medium. This is due to complications in the cantilever dynamics in liquids and the method employed to excite cantilever in a liquid cell. Since the measured cantilever response is a mixture of hydrodynamic forces and forces due to the stretched molecule, the quantification and separation of these two is essential to accurately determine the viscoelasticity of single molecules [7, 34, 39, 62, 132, 183]. It has been recognized that the hydrodynamic forces play a crucial role in determining the phase of the tip motion without the molecule. This phase lag becomes important in determining the viscoelasticity of the molecule [34, 76, 85, 96, 116, 133, 135]. There are theoretical works which provide expressions to predict the phase of a cantilever oscillating in liquid environments [7, 76, 85]. It has also been suggested that the use of phase and amplitude to determine the viscoelastic response of nanoscale systems in liquids leads to artefacts [7]. Moreover, it has been noticed that researchers seldom find the phase lag predicted by theoretical models in experiments. This can be attributed to the phase contributions coming from variety of unknown sources. These sources are responsible for the randomness of experimentally observed phase once the cantilever is immersed in liquid and is yet to be tethered with the molecule. It is extremely difficult to account for such contributions in theoretical models. Therefore it becomes important to make sure there are no contributions from the extraneous sources before the measurement is performed. We refer to phase contributions from such sources as extraneous phase. However, when the cantilever tip is directly driven by magnetic [79, 84, 170] or photo-thermal excitation [47, 144], majority of the problems discussed above -mainly associated with base excitation- can be overcome. However, in this report, we have focused on the widely used base excitation method of driving the cantilever.

In this work, we ensured that extraneous contributions to the phase are not present and performed dynamic, off-resonance force spectroscopy experiments on Titin I27₈ to measure its viscoelasticity. The measurements are performed with both, a conventional deflection-detection type AFM and a fibre-interferometer based home-built AFM. The fibre interferometer AFM measures cantilever displacement while the deflection detection scheme measures the cantilever bending at its free end. The latter is widely used in commercial AFMs. It has been pointed out recently that interpreting phase of the cantilever bending as dissipative signal is inaccurate owing to altered boundary conditions due to molecule's viscoelasticity. Using the solution to Euler-Bernoulli equation of the rectangular cantilever beam, it is proposed that the X and Y components of the oscillations in cantilever bending exclusively determine the stiffness and dissipation coefficient respectively [7]. We show here that even the use of X and Y components to estimate stiffness and dissipation coefficient are not free from artefacts in the presence of extraneous phase and result in cross-talk between the stiffness and dissipation channels. Such artefacts also appeared when the measurements are not strictly off-resonance, a major concern when operating in viscous media.

The theoretical model, in off-resonance regime, predicts negligibly small phase lag (~ 0 degree) due to hydrodynamics for the displacement of the cantilever's free end in viscous medium. Therefore, in interferometer based detection, it is easy to identify presence of extraneous phase due to sources

other than hydrodynamics. Absence of which is essential for ensuring artefact free measurements. This has to be confirmed from the frequency response of the cantilever around the operational frequency. The bending of the cantilever, however has a finite phase lag due to hydrodynamics and hence it is difficult to identify the contribution from the extraneous phase. After ensuring that there are no contributions to the phase from extraneous sources, we compare the stiffness estimates from the displacement and bending measurements of the cantilever tip.

Using both, the interferometer based AFM and the deflection detection type AFM, we found that the dissipation in unfolded Titin I27₈ octomer is immeasurably low. The interferometer based AFM, however clearly shows evidence of dissipation in water layers from the *Y*-component of the displacement oscillations. Since the dissipation is detected in water layers and not in unfolded protein molecule using the same instrument, we conclude that the dissipation in single macromolecules is indeed immeasurably low. The estimated detection limit of our instrument and hence the upper bound on the dissipation in single unfolded protein is 5×10^{-7} kg/s. We compared the stiffness estimated from the experimental data from both detection schemes. They match well and also with the stiffness determined using static method (derivative of force). The stiffness of unfolded I27₈ is in the range of 10 mN/m.

4.2 Materials and methods

4.2.1 AFM

We used two types of AFMs to perform measurements. For deflection detection measurements, we used commercial AFM (JPK Nanowizard II, Berlin, Germany) in which a narrow laser beam incident at the end of the cantilever gets reflected to a four quadrant, position sensitive photo-detector. The position of the reflected beam on the detector corresponds to angle dy/dx due to the bending in the cantilever (see Fig. 4.1(a)). In the home-built AFM, a fibre-based interferometer is used (Fig. 4.1(b)). In brief, a partially coated end of the optical-fibre (partially reflecting mirror) is aligned parallel to the back of a cantilever-end (acting as a fully reflecting mirror) with the help of a nano-positioner. Part of the Laser (1380 nm) is reflected from the end of the fibre. The rest of the light falls on the back of the cantilever and reflects back into the fibre. These two reflected lights interfere to form an interference pattern on a photo-detector. For more details about the instrument see reference [140]. The signal from this photo-detector corresponds to cantilever displacement (y) as opposed to angle (dy/dx) at the free end due to the cantilever bending. This is a crucial difference, since the solution used to quantify stiffness and dissipation is different for angle dy/dx and for displacement y .

Rectangular cantilevers, made of silicon nitride, from micromasch (Micromasch, Bulgaria) with stiffness 0.5-1 N/m were used for the experiments. Typical dimensions of the cantilevers were length ~ 300 μm , width ~ 30 μm , and thickness ~ 1 μm . Typical resonance frequency of the cantilever in water is ~ 13 kHz. Cantilever stiffness is calibrated using thermal fluctuation method available with JPK AFM [74]. Cantilever base is excited using a dither piezo. A sinusoidal signal from internal

oscillator of lock-in amplifier (SRS830, Stanford, California, US) is applied to the piezo and the same signal is used as a reference for the phase sensitive detection. Output signal from the photodetector is supplied to the lock-in amplifier which provides us the amplitude and phase response of the cantilever.

4.2.2 Protein

Titin I27₈ polyprotein constructs containing eight identical domains in tandem were constructed from a plasmid similar to described in reference [165]. Expression and purification of the protein was done as described before [10]. PBS at *pH* 7.4 was used as the standard buffer for all experiments. The protein sample (100 μ L) in PBS with a concentration of 10 *mg/mL* was adsorbed onto a freshly evaporated gold coated coverslip assembled in the fluid cell by incubating it on the substrate for 15-30 minutes at room temperature. The sample solution was washed three times with PBS to remove the excess un-adsorbed protein from the working solution. Experiments are performed at low frequencies (\sim 100-300 *Hz*, for off-resonance measurements) and with small amplitudes (\sim 1-2 \AA). The pulling speed (25 *nm/s*) kept low compared to the conventional protein pulling experiments. These parameters ensure the linearity of the measurements which is essential to use the existing theoretical models for analysis.

4.3 Theory

In order to describe the dynamics of a rectangular cantilever immersed in liquid we begin with Euler-Bernoulli beam equation. The equation is solved for a sinusoidal drive. We derived the solution, in off-resonance regime, for bending and displacement of the cantilever at the tip.

The Euler-Bernoulli equation of motion for a homogeneous rectangular cantilever beam immersed in a liquid is

$$-\tilde{\rho}\tilde{S}\frac{\partial^2 y(x,t)}{\partial t^2} - \gamma_c \frac{\partial y(x,t)}{\partial t} = EI \frac{\partial^4 y(x,t)}{\partial x^4} \quad (4.1)$$

In the model the internal damping of the cantilever has been neglected. The coordinate along the cantilever of length L is x , where the base is at $x = 0$ and $x = L$ is the end/tip-position. Displacement normal to the length at position x and time t is $y(x,t)$. The effective mass per unit length is $\tilde{\rho}\tilde{S} = \rho S + m_a$, where ρ and S are cantilever mass density and cross-section area respectively; m_a is hydrodynamic added mass per unit length; γ_c is the cantilever's hydrodynamic drag coefficient per unit length. E is the Young's modulus of the cantilever and I is the second area moment; $I = \frac{bh^3}{12}$ for a homogeneous rectangular cantilever, where b and h are cantilever's width and thickness respectively; $\tilde{\rho}\tilde{S}$ and γ_c depend on the excitation frequency. To solve the equation, we used variable separation method and assumed the solution to be of the form $y(x,t) = y(x)e^{i\omega t}$; where $y(x)$ is the solution of the space part and ω is the excitation frequency. Substituting the solution into (4.1) gives

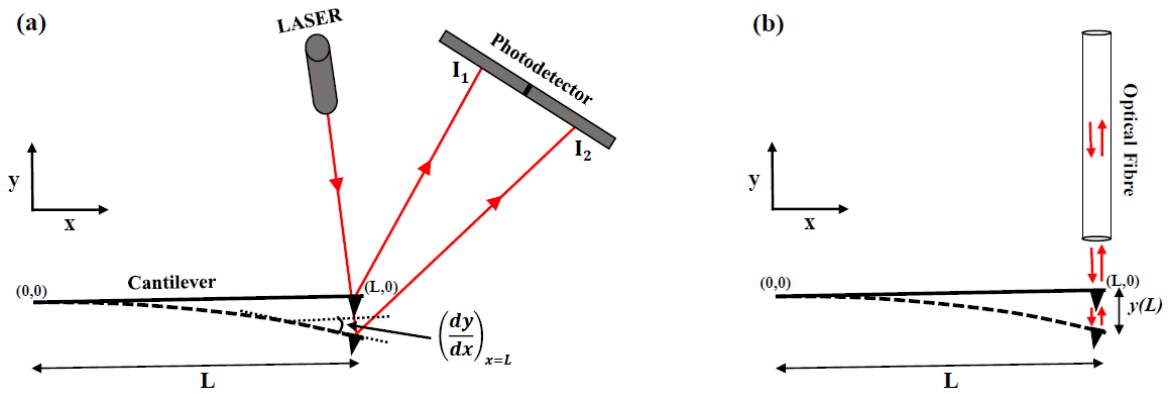


Fig. 4.1 (a) The schematic of the deflection detection set-up. The laser reflecting from the back of the cantilever falls on the position sensitive four quadrant detector. The outputs I_1 and I_2 correspond to the two positions of the laser spot on the detector. This position depends on the bending dy/dx of the cantilever at $x = L$. The signal from the detector reads the local cantilever bending. (b) In interferometer-based detection, the cantilever acts as one the mirrors in Fabry-Perot etalon. The displacement of the cantilever produces a proportional signal in the photo-diode. The signal from photo-diode measures displacement (y) of the cantilever end. In both schematics the cantilever bending and the displacement are exaggerated.

$$\tilde{\rho} \tilde{\omega}^2 - i \omega \gamma_c = E I k^4 \quad (4.2)$$

Where the spatial part of the Eq. 4.1 can be written as

$$\frac{d^4 y(x)}{dx^4} = k^4 y(x) \quad (4.3)$$

General solution of the above equation is given by

$$y(x) = a \sin(kx) + b \cos(kx) + c \sinh(kx) + d \cosh(kx) \quad (4.4)$$

and the slope (cantilever bending) is given by

$$y'(x) = ak \cos(kx) - bk \sin(kx) + ck \cosh(kx) + dk \sinh(kx) \quad (4.5)$$

In general, the coefficients a , b , c , and d are complex numbers and are determined by applying appropriate boundary conditions dictated by the experiments (y - displacement, y' - slope, y'' - internal

moment of force, and y''' - internal shear force).

We now define dimensionless parameters, g and z given by

$$g = \frac{3(k_i + i\omega\bar{\gamma}_i)}{k_c}, z = kL = \left[\frac{3(\tilde{\rho}\tilde{S}\omega^2L - i\omega\gamma_cL)}{k_c} \right]^{\frac{1}{4}} \quad (4.6)$$

Where k_i and $\bar{\gamma}_i$ are interaction stiffness and damping respectively; $k_c (= \frac{3EI}{L^3})$ is the cantilever stiffness. These two parameters will be used for implementing approximations for different experimental situations. For low excitation frequencies $z \ll 1$ and for cantilever having large stiffness $g \ll 1$.

4.3.1 Cantilever excited at base without interaction ($\bar{\gamma}_i = 0$ and $k_i = 0$)

The boundary conditions for cantilever excited from base with amplitude A and in absence of any forces acting on the tip are given by

$$y(0) = A, \quad y'(0) = 0, \quad y''(L) = 0, \quad y'''(L) = 0$$

The constants a, b, c and d in Eqs. 4.4 and 4.5 are determined by using the above boundary conditions. We get the solution for small g and z approximations. (see supplementary section (1) for the full derivation)

$$y'(L) = \frac{Az^4}{6L} \quad (4.7)$$

Substituting the value of z that we had defined earlier (see Eq. 4.6) we get the following solution for the bending of the cantilever at the free end

$$\frac{\partial y(x)}{\partial x} \Big|_{x=L} = \frac{A}{2k_cL} (\tilde{\rho}\tilde{S}\omega^2L) - i \frac{A\omega}{2k_cL} (\gamma_cL) \quad (4.8)$$

Modulus of Eq. 4.8 gives us the amplitude of the cantilever bending and the argument gives the phase difference between drive (or base) and bending at $x = L$

$$R_{b,f} = \frac{A}{2k_cL} \sqrt{(\tilde{\rho}\tilde{S}\omega^2L)^2 + \omega^2(\gamma_cL)^2}, \quad (4.9)$$

$$\theta_{b,f} = \arctan\left(-\omega \frac{\gamma_cL}{\tilde{\rho}\tilde{S}\omega^2L}\right) \quad (4.10)$$

The real and imaginary components are

$$X_{b,f} = \frac{A}{2k_cL} \tilde{\rho}\tilde{S}\omega^2L, \quad Y_{b,f} = -\frac{A\omega}{2k_cL} \gamma_cL \quad (4.11)$$

Where subscript b stands for bending and f for the free cantilever. Constants $\tilde{\rho}\tilde{S}$ and γ_cL can be determined from free X and Y signals using (4.11). Since, $X_{b,f}$ and $Y_{b,f}$ are $R_{b,f} \sin(\theta)$ and $R_{b,f} \cos(\theta)$ it is important to note that an error-free measurement of θ , the phase lag of the tip with respect to

base, is critical to find the exact values of these constants.

The solution for the displacement with $z \ll 1$

$$y(x)\Big|_{x=L} = R_{d,f} = A\left(1 - \frac{z^4}{8}\right) \approx A \quad (4.12)$$

The amplitude of the displacement of the cantilever end ($x = L$) in absence of any interaction is approximately equal to the base amplitude and oscillates in phase with it.

4.3.2 Cantilever excited at base in presence of interaction ($\tilde{\gamma}_i \neq 0$ and $k_i \neq 0$)

For a cantilever which is driven from the base and the tip experiencing a linear viscoelastic force due to tethered macromolecule, the boundary conditions are

$$\begin{aligned} y(0) &= A, & y'(0) &= 0, \\ y''(L) &= 0, & EIy'''(L) &= (k_i + i\omega\tilde{\gamma}_i)y(L) \end{aligned}$$

The constants determined using the boundary conditions are substituted into Eqs. 4.4 and 4.5. Approximations for $z \ll 1$ and $g \ll 1$ are then applied to give us (see supplementary section (1) for the full derivation)

$$y'(L) = -\frac{gA}{2L} + \frac{Az^4}{6L}, \quad y(L) = A - \frac{gA}{3} \quad (4.13)$$

Substituting the values of 'g' and 'z' back into the (4.13) gives the following expressions for slope and displacement respectively

$$\frac{\partial y(x)}{\partial x}\Big|_{x=L} = \frac{A}{2k_c L} (-3k_i + \tilde{\rho}\tilde{S}\omega^2 L) - i\frac{A\omega}{2k_c L} (3\tilde{\gamma}_i + \gamma_c L) \quad (4.14)$$

and

$$y(L) = \frac{A}{k_c} (k_c - k_i) - i\frac{A\omega}{k_c} \tilde{\gamma}_i \quad (4.15)$$

Modulus of Eq. 4.14 gives us the amplitude of the bending (slope) at $x = L$ and the argument gives us the phase lag:

$$\begin{aligned} R_b &= \frac{A}{2k_c L} \sqrt{(-3k_i + \tilde{\rho}\tilde{S}\omega^2 L)^2 + \omega^2 (3\tilde{\gamma}_i + \gamma_c L)^2}, \\ \theta_b &= \arctan\left(-\omega \frac{3\tilde{\gamma}_i + \gamma_c L}{-3k_i + \tilde{\rho}\tilde{S}\omega^2 L}\right) \end{aligned} \quad (4.16)$$

Now the real and imaginary components of the bending are

$$X_b = \frac{A}{2k_c L} (-3k_i + \tilde{\rho}\tilde{S}\omega^2 L),$$

$$Y_b = -\frac{A\omega}{2k_c L}(3\tilde{\gamma}_i + \gamma_c L) \quad (4.17)$$

This is identical to the result obtained by Benedetti et al. [7]. Further, the amplitude and phase for the displacement y in the limit $g \ll 1$ and $z \ll 1$ is

$$R_d = \frac{A}{k_c} \sqrt{(k_c - k_i)^2 + (\omega\tilde{\gamma}_i)^2},$$

$$\theta_d = \arctan\left(-\omega \frac{\tilde{\gamma}_i}{k_c - k_i}\right) \quad (4.18)$$

The real and imaginary components of the displacement are

$$X_d = \frac{A}{k_c}(k_c - k_i), \quad Y_d = -\frac{A\omega}{k_c}\tilde{\gamma}_i \quad (4.19)$$

The subscript d stands for displacement.

Eqs. 4.17 and 4.19 are the main results which can be used to estimate stiffness and dissipation. Eq. 4.17 can be used for experimental data from deflection detection type AFM and Eq. 4.19 can be used for interferometer based AFM.

4.3.3 Cantilever excited at base and tip in non-deformable contact

Cantilever is excited from the base at $x = 0$ with amplitude A and tip is in contact with the substrate. Assuming that both surfaces (tip and substrate) are non-deformable, the boundary conditions are following:

$$y(0) = A, \quad y'(0) = 0, \quad y''(L) = 0, \quad y(L) = 0$$

When the cantilever-tip is pressed against a non-deformable surface, the displacement at the tip is zero however the bending is nonzero. The slope at $x = L$:

$$\left. \frac{\partial y(x)}{\partial x} \right|_{x=L} = -\frac{3A}{2L} \quad (4.20)$$

At deep contact region, cantilever bending at $x = L$ is proportional to the base displacement and moves 180 degree out of phase. (see supplementary section (1) for more details)

4.4 Results and Discussion

4.4.1 Measurements performed using two detection methods

We performed experiments using both a conventional deflection detection type AFM and a home-built interferometer based AFM. These two detection schemes are not only different ways of measuring cantilever oscillations but more importantly measure different quantities. As described in the methods

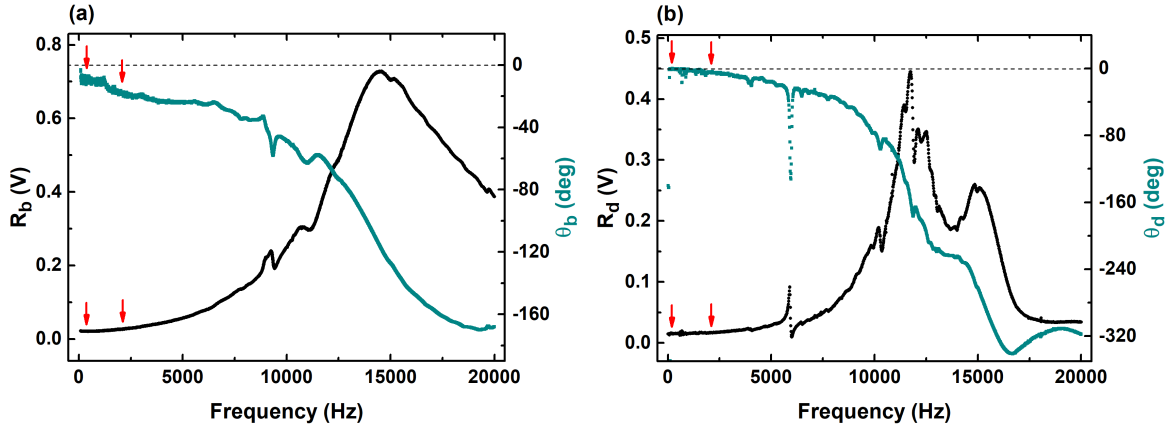


Fig. 4.2 Frequency-dependent oscillation profile (amplitude-black and phase-cyan) of the cantilever in water. Arrows indicate the operational frequencies (133 Hz and 2.033 kHz) we have used for the measurements. (a) The frequency response in conventional deflection-detection type AFM. The resonance frequency of the cantilever in water is 13.54 kHz. (b) The frequency response in interferometer based displacement-detection type AFM. The resonance frequency of the cantilever in water is 12.74 kHz.

section, the former one measures bending (dy/dx) and the later the displacement (y) at the end of the cantilever (see Fig. 4.1). The amplitude (R_d) of measured displacement (y) and its phase (θ_d) are related to the X and Y components of the motion by the following relations: $X_d = R_d \cos \theta_d$ and $Y = R_d \sin \theta_d$. Similarly, amplitude (R_b) of bending (dy/dx) is related to X and Y component by $X_b = R_b \cos \theta_b$ and $Y_b = R_b \sin \theta_b$. The X and Y components can be recorded using lock-in amplifier.

Fig. 4.2 (a) shows the frequency response of the cantilever bending using deflection detection AFM and Fig. 4.2 (b) shows cantilever displacement in the home-built interferometer based AFM. In the figure, the arrows indicate the operational frequencies chosen for the measurements. The region around the operational frequencies is free from spurious peaks. The oscillation profile of the base and tip of the cantilever for a smaller frequency range are shown in supplementary Fig. S1. In Fig. S1, the vertical dotted line (at 1000 Hz) represents the limit up to which the difference between the base and tip amplitudes is less than 0.1 \AA and the observed phase difference is negligibly small ($\sim 1^\circ$). It is fair to assume that the Eq. 4.12 is valid up to 1000 Hz. Kiracofe et al. have observed similar results in another displacement detection based system equipped with a Laser Doppler Vibrometer (LDV) [96].

Fig. 4.3 shows the raw data from measurements using a deflection detection type AFM. The I27 octomer whose one end is attached to the tip and other is fixed to the substrate, is pulled away from the substrate at speed of 25 nm/s . The measurements are repeated at two frequencies of 133 Hz and 2.033 kHz. Fig. 4.3 (a) and (c) is X and Y components of oscillations in the bending dy/dx at 133 Hz and 2.033 kHz respectively. Fig. 4.3 (b) and (d) is amplitude and phase of the bending dy/dx at the tip end. Before measurements were performed we ensured that (i) The cantilever is excited far below resonance and there are no spurious peaks in the region (Fig. 4.2(a)), (ii) The phase lag in deep contact is 180 degrees. These two are important criterion for artefact free measurements of dissipation.

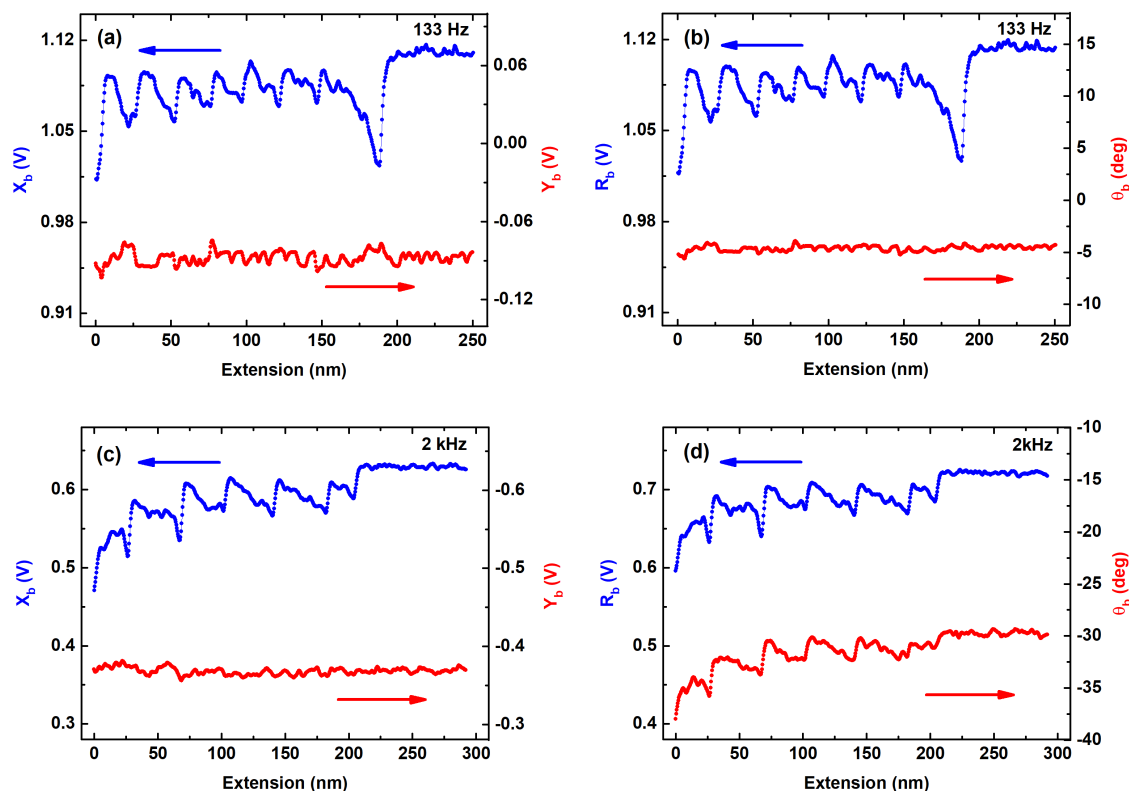


Fig. 4.3 Raw data of the measurements performed using a deflection detection type AFM (a) The X and Y components of oscillations in the bending $((dy/dx)_L)$ at the tip end of the cantilever. The measurements are performed at 133 Hz . (b) The amplitude and phase of the oscillations in the bending (dy/dx) of the tip end of the cantilever. The same measurements are repeated at 2.033 kHz in (c) and (d). The Y -component in both measurements is featureless and according to Eq. 4.17 the dissipation in single molecules is immeasurably low. The phase shows clear oscillations in (d), however the corresponding Y -component in (c) does not change as the domains are sequentially unfolded. The use of point-mass model wherein dissipation depends on phase would result in erroneous measurement of dissipation.

The deep contact response should be recorded when there is no molecule present beneath the tip and with the same cantilever alignment used for the experiment. We observed that for deflection detection type AFM, the cantilever tip oscillates with ~ 6 degree phase lag with respect to the base excitation when immersed in liquid and is freely oscillating. We treat this phase lag as emerging purely from the cantilever hydrodynamics. The Y -component in both these measurements is not varying when the domains are sequentially unfolded. According to Eq. 4.17, this means that the dissipation is immeasurably low when protein unfolds or the unfolded domains are stretched further. However, the measurement performed at 2.033 kHz shows that the phase signal shows clear oscillations. Hence, the

analysis of data in fig. 4.3 (d) using point-mass model shows a measurably high dissipation in single molecule stretching experiments.

Fig. 4.4 shows raw data of the measurements using interferometer based detection system. This detection measures displacement (y) of the cantilever. Fig. 4.4 (a) and (b) show measurements performed at 133 Hz and (c) and (d) show measurement at 2.033 kHz . We clearly see signatures of protein unfolding under force. The typical measurements shown here at both frequencies of 133 Hz and 2.033 kHz show that the Y -component of the signal does not show variation while the octamer is unfolded sequentially. Both the amplitude and X -component show saw-tooth like pattern which is typical of polyprotein unfolding under force. Since the interferometer detection system measures displacement and not the bending in the cantilever, it shows no phase lag (~ 0 degree) when tip is far from the substrate. This is in agreement with result obtained in Eq. 4.12. Interestingly, unlike the measurement of bending performed with deflection detection AFM (Fig. 4.3(d)), the phase of displacement (y) measured using interferometer based AFM does not vary while protein unfolds (Fig. 4.4(d)). At 2.033 kHz the phase lag is $\sim 5^\circ$. To analyze this data, we need to include $(-z^4/8)$ term in Eq. 4.12. Apart from this we also need to measure the base amplitude for analysis since it is different from the freely oscillating tip in the liquid. It is important to note that the range of frequency, up to which the extended form of Eq. 4.12 will be valid, is difficult to define. Although, the results from 2.033 kHz data are similar to 133 Hz (stiffness of the unfolded molecule is ~ 20 mN/m and dissipation is featureless - data not shown), we do not want to stress on the quantification of 2.033 kHz data.

Together, Fig. 4.3 and 4.4 show measurements of X -component, Y -component, the amplitude and phase of both bending ($\frac{dy}{dx}$) as well as displacement (y) signals. These quantities can be used to infer the viscoelastic response of single protein molecules under strain using models describing cantilever hydrodynamics in viscous media - Eqs. 4.17 and 4.19. Clearly, in both measurements the Y -component which is related to the dissipation alone in the molecule is not changing as the unfolded protein domains are pulled with a constant velocity. This indicates that dissipation in the single molecule of titin is immeasurably low. This is in direct contrast with previous claims of measurements performed on single molecules [77, 87, 93].

We estimated the minimum detectable dissipation coefficient from the noise levels in the Y -component signal at our operational parameters to be 5×10^{-7} kg/s (see section 4.4.4 for more details). We conclude that the upper bound on the dissipation coefficient of single unfolded protein is $\sim 5 \times 10^{-7}$ kg/s . This value is smaller than those reported in the literature.

4.4.2 Quantification of Stiffness

To quantify the interaction stiffness from bending measurement data, estimation of the base displacement (A), $\tilde{\rho}\tilde{S}\omega^2L$, and γ_cL is required. Since the base displacement cannot be directly measured in deflection-detection setup, it can be determined from the measured bending amplitude at the deep contact using Eq. 4.20. $\tilde{\rho}\tilde{S}\omega^2L$, and γ_cL can be determined from the free cantilever's $X_{b,f}$ and $Y_{b,f}$

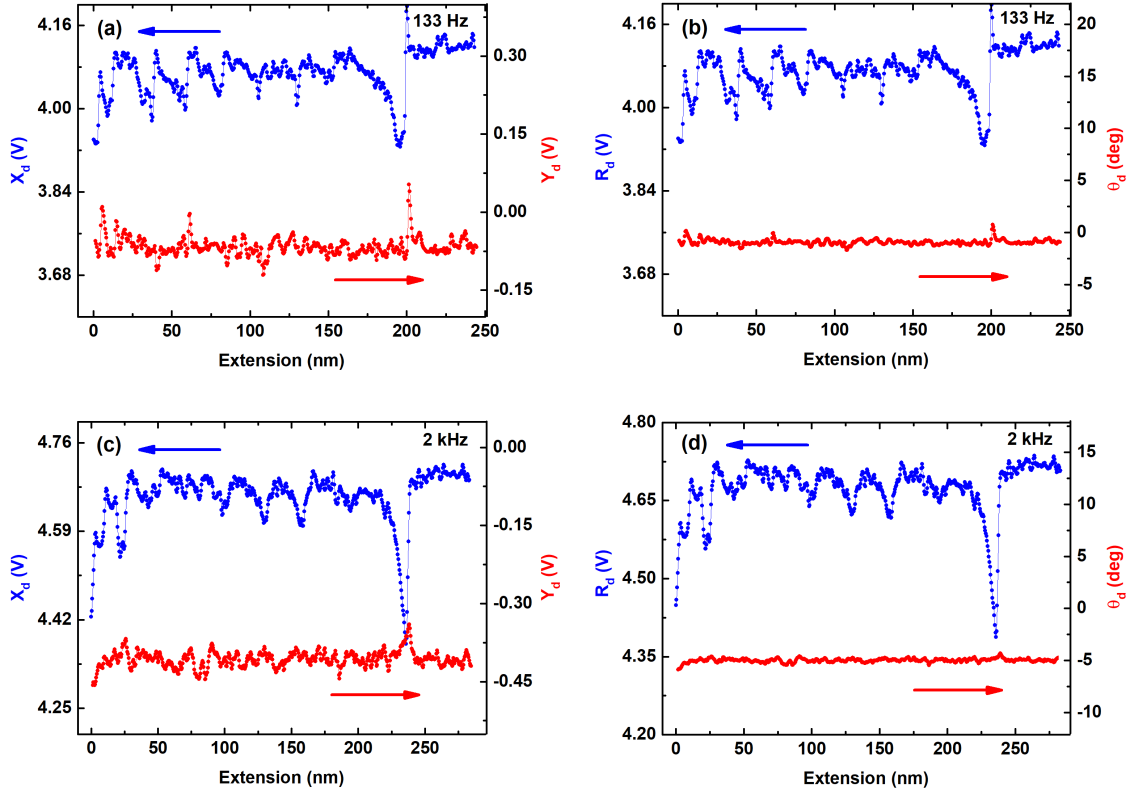


Fig. 4.4 Raw data of the measurements performed using home-built interferometer based AFM. (a) The X and Y components of the oscillations in the displacement at the tip end ($y(L)$) of the cantilever. (b) The amplitude and phase of oscillations in the displacement. The operational frequency for (a) and (b) is 133 Hz . In (c) and (d) the measurement is repeated for 2.033 kHz . Unlike the phase of the the bending signal in Fig. 4.3(d), the phase of the displacement does not show variations as the protein unfolds.

signals respectively (see Eq. 4.11). Finally, for the interaction stiffness and dissipation coefficients, Eq. 4.17 can be written as:

$$k_i = \frac{k_c}{A_{deep}}(X_{b,f} - X_b), \quad \bar{\gamma}_i = \frac{k_c}{\omega A_{deep}}(Y_{b,f} - Y_b) \quad (4.21)$$

Where A_{deep} is the bending amplitude in deep contact and $X_{b,f}$ and $Y_{b,f}$ are the X and Y components of the the free cantilever without any force on it ($k_i = 0$ and $\bar{\gamma}_i = 0$).

Fig. 4.5 (a) shows the stiffness-extension calculated from the data in Fig. 4.3(a) using Eq. 4.17 (or Eq. 4.21). The peak stiffness of the unfolded protein is $\approx 20\text{ mN/m}$. Fig. 4.5 (b) shows stiffness-extension profile calculated from the data in Fig. 4.4 (a) using Eq. 4.19. The stiffness of unfolded protein measured using two detection methods shows good agreement with each other and

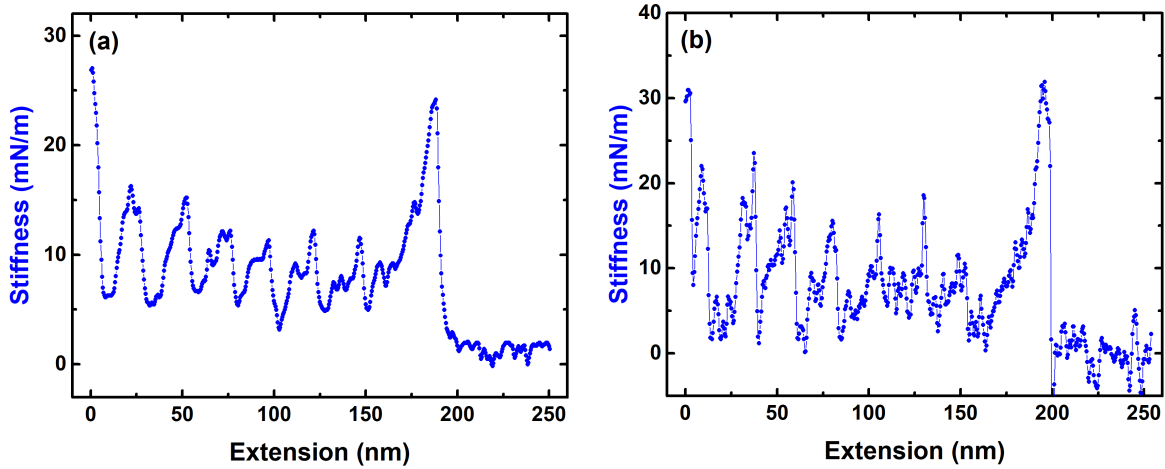


Fig. 4.5 (a) The stiffness estimated from X -component of the cantilever bending at the tip end ($(dy/dx)_L$) using a deflection detection measurement. The peak stiffness is $\approx 20 \text{ mN/m}$. This matches well with reports from other measurements and the derivative of the static force-extension curves (see supplementary Fig. S2). (b) The stiffness estimated from the X -component of the cantilever displacement at the tip end ($y(L)$) using the interferometer based AFM. The values of stiffness estimated using both detection schemes are in agreement with each other.

gives its quantitative estimate for single protein molecule. It is instructive that the stiffness estimated using X -component of the amplitude of bending as well as displacement matches well with the static deflection data - derivative of force (see supplementary Fig. S2). This underlines the robustness of the theoretical modeling used to quantify the stiffness using dynamic AFM having two detection schemes measuring displacement and the bending of the end of the cantilever.

4.4.3 The effect of extraneous phase

For measurements presented in Fig. 4.3 and 4.4, we took care that there is no extraneous contribution to the phase of the free cantilever oscillating in liquid (see Fig. 4.2). This is not an easy task for the deflection detection type AFM, as it has a finite phase lag due to hydrodynamics value of which is not a-priori known. Since there are variety of intractable sources of extraneous phase, it is difficult to identify the contribution from them. For interferometer based AFM, since cantilever displacement is measured, the phase due to hydrodynamics on the freely oscillating cantilever is almost zero. It should be noted that the extraneous phase can also be present in the displacement measurements. However, since we know the phase lag of the displacement at low frequency excitation is nearly zero, we can identify its presence and therefore do not consider those measurements for analysis. Whereas this is not possible in the deflection-detection measurements as the actual hydrodynamic phase contribution is not known. Fig. 4.6 shows a measurement when such extraneous phase is present. The experiment is performed at 133 Hz using the similar cantilever. Typically, the phase of the cantilever bending in

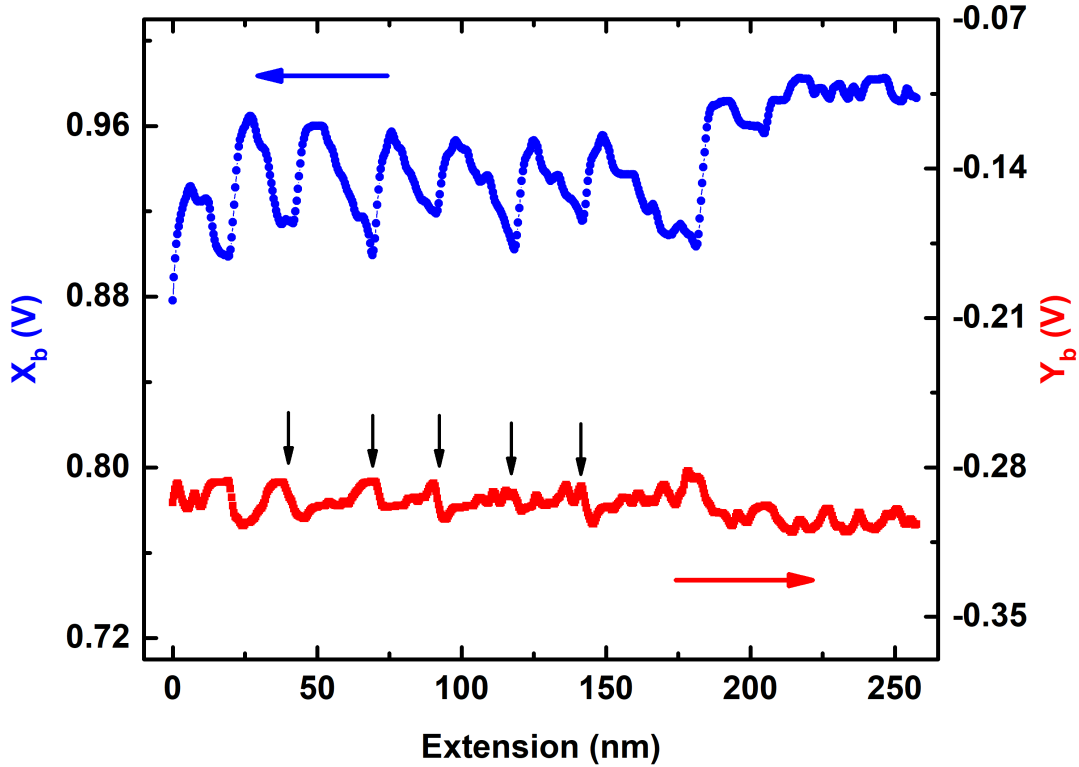


Fig. 4.6 Measurements performed at 133 Hz with similar cantilever using a different cantilever holder. The phase of the cantilever bending at the tip end is not 180 degree in deep contact (data not shown). The phase of the free cantilever after immersing in the buffer deviates from the measurement in Fig. 4.3 by the same amount. This is clear case of presence of extraneous phase θ_e . The peaks in Y -signal are identified by arrows. This variation in Y as the protein unfolds is likely to be falsely interpreted as dissipation.

the deep contact is 180 degrees (see Eq. 4.20). This is not the case for measurements shown in Fig. 4.6. The phase in deep contact is ~ 190 degrees. This produces an extraneous phase contribution of the same amount in phase of the freely oscillating lever in the liquid. The Y -component is clearly showing peaks as protein unfolds, and following Eq. 4.17 one may draw false conclusion about the dissipation in single molecules.

The theoretical models of the cantilever dynamics in the liquid environment, which are presented in the theory section, do not take into account the extraneous phase contributions to oscillating cantilever from variety of sources. In absence of a method to ensure that these contributions are not present, the estimates of stiffness and damping coefficient are not free from errors for the following reason. Let θ_e be the extraneous phase, θ_{h+i} the combined phase lag due to molecule's viscoelasticity (stiffness and dissipation coefficient) and hydrodynamics. θ_{h+i} is accounted for in the models. The

measured phase when the cantilever is immersed in liquid and is far away from the substrate will be having contribution from both θ_h and θ_e . Since θ_h depends on cantilever parameters and viscosity of the medium, it is difficult to estimate the extraneous contribution θ_e to the measured phase lag.

In the following we explain how the presence of extraneous phase leads to changes in Y -component of the amplitude of bending (dy/dx) due to variation in molecule's stiffness alone while it is being stretched.

Here the θ_e is added linearly to the θ_{h+i} . In experimental situations it can not be ensured that the extraneous contribution to the phase adds linearly to the hydrodynamic phase. We have added it linearly to show that such simple linear addition leads to artefacts which are results of stiffness affecting the dissipation measurement. However, the electronic phase can be added in this way. The net phase lag during the molecule's extension will have the contributions from θ_{h+i} and θ_e both and it is given by

$$\theta = \arctan\left(-\omega \frac{3\tilde{\gamma}_i + \gamma_c L}{-3k_i + \tilde{\rho}\tilde{S}\omega^2 L}\right) + \theta_e \quad (4.22)$$

Where the first term is the phase lag in the cantilever deflection due to both the molecular stiffness and the dissipation as well as the cantilever hydrodynamics. For the purpose of understanding how the extraneous phase leads to false interpretation of amplitude and phase as dissipation in single molecules, we assume that molecule being stretched is a purely elastic entity with dissipation $\tilde{\gamma}_i = 0$. Our analysis shows that even in absence of molecular dissipation, the Y -component of cantilever bending signal may show variation when the protein is sequentially unfolded.

Since the molecular stiffness is entropic, it changes with extension. Fig. 4.7 (a) graphically represents Eq. 4.16 and 4.17 in the absence of extraneous phase. The amplitude and phase of the cantilever bending changes due to variation in molecule's stiffness. The net phase lag will have contribution from the molecule's stiffness and the amplitude changes from A to A' . Since the dissipation is assumed to be zero, the Y -component ($\omega\gamma_c L$) does not change. This should only affect the X -component and it reduces from $(\tilde{\rho}\tilde{S}\omega^2 L)$ to $(\tilde{\rho}\tilde{S}\omega^2 L - 3k_i)$.

Consider now a situation wherein there is extraneous phase contribution (θ_e) to phase when the cantilever is far from substrate and is freely oscillating. Fig. 4.7 (b) graphically shows the situation when molecule's dissipation is assumed to be zero and there is extraneous phase θ_e . The xy is the coordinate system wherein the total phase lag is $\theta = \theta_{h+i} + \theta_e$. The coordinate system XY is rotation of coordinate system xy by θ_e . In this co-ordinate system the phase and amplitude changes purely due to the molecule's stiffness in such a way that Y -component does not change. However, in xy coordinate system there is change in Y as shown in the figure due to this additional phase lag θ_e . This change in Y may get wrongly interpreted as the dissipation signal. This arises from having a extraneous phase θ_e which is not considered in the model. It is difficult to theoretically predict the hydrodynamic phase lag of the cantilever. This phase depends on the cantilever stiffness and viscosity of medium and hence is not known *a-priori*. It can not be compensated in order to have phase lag emerging from hydrodynamics alone. In this context, the interferometer based experiments are crucial.

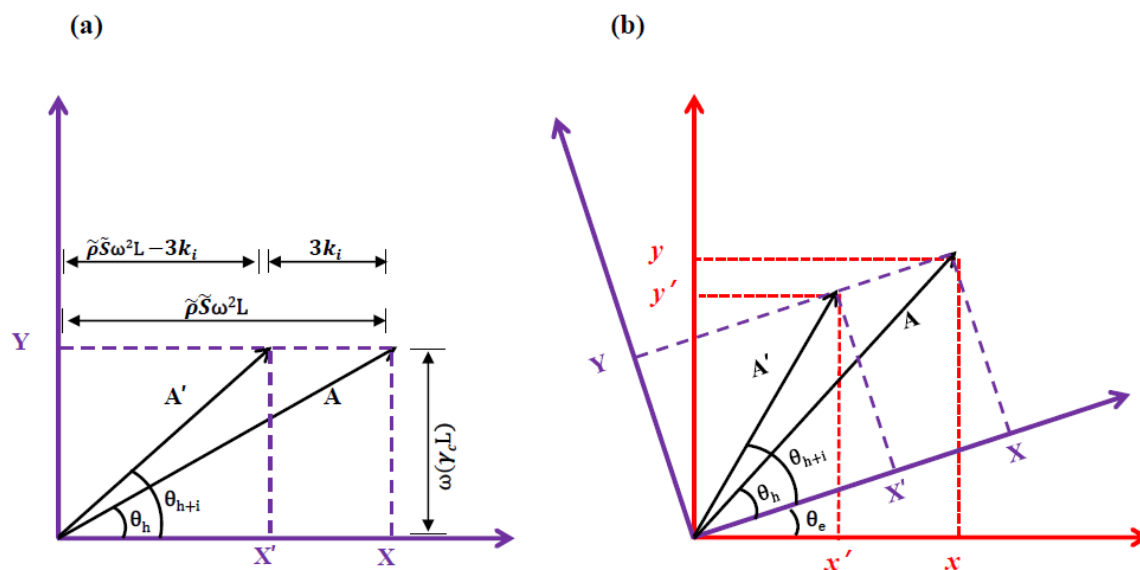


Fig. 4.7 Schematics to show how extraneous phase produces artifacts in the measurement. (a) $\theta_e = 0, \tilde{\gamma}_i = 0$; The change in k_i affects both phase and amplitude but Y-component remains unchanged. (b) When θ_e is nonzero, The phase and amplitude changes but Y remains unchanged in the co-ordinate system XY wherein $\theta_e = 0$. However in the xy coordinate system, the change in stiffness of the molecule k_i changes the Y-component from y to y' . Using Eq. 4.17 this can be misinterpreted as the dissipation. The change in Y-component is due to change in molecule's stiffness.

The theory predicts that the cantilever displacement has nearly zero phase lag with respect to the excitation signal due to hydrodynamics. This has been verified by the experiments. Any additional phase lag due to spurious peaks or other sources can be easily be identified and care can be taken to avoid coupling between the stiffness and dissipation channels.

The above discussion suggests that if there is significant phase lag due to hydrodynamics alone, the phase may have oscillations as the protein unfolds since this large hydrodynamic phase lag makes the numerator inside the arctan bracket large. In such situations the theory predicts that features may appear in phase data even if the dissipation coefficient $\tilde{\gamma}_i = 0$. This is because the stiffness is non-zero and is varying under strain. We performed experiments by keeping all other parameters of the experiment same, except viscosity of the medium. Fig. 4.8 shows a protein pulling experiment after addition of glycerol in the buffer which enhances the medium viscosity. This makes the term $\gamma_c L$ large and thereby the numerator inside the arctan bracket is also large. In this situation, the θ_h is significant (~ 18 degrees). It was ~ 6 degrees for the same cantilever in a much less viscous buffer. As a result, both the phase and Y-components do not change as the protein unfolds. However, after addition of glycerol, the change in molecule's stiffness when it is stretched affects the phase as molecule sequentially unfolds, but the Y-component does not change from its value which was for freely oscillating cantilever.

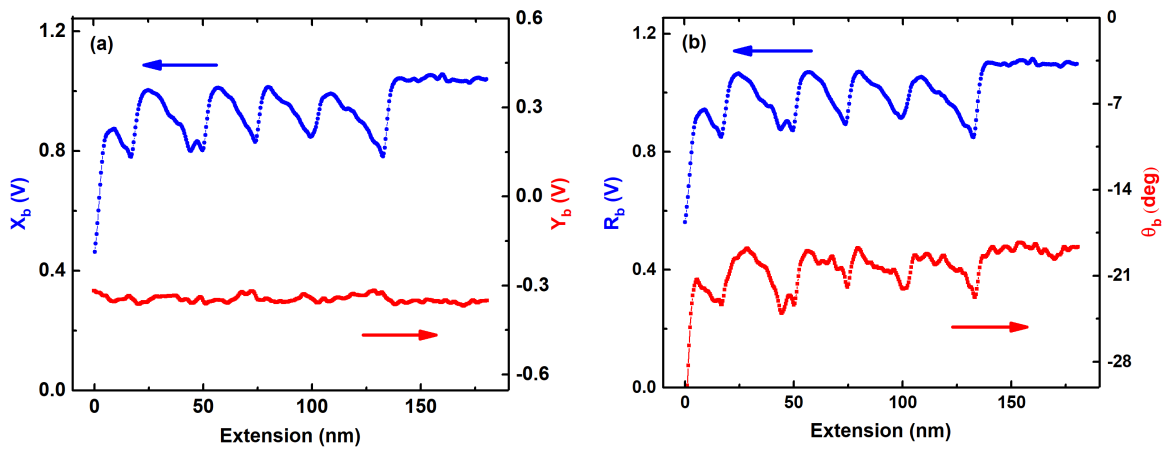


Fig. 4.8 Measurements performed with 50 % glycerol in the buffer. This increases viscosity of the medium by ~ 8 times. The θ_h is nearly 18 degrees, however $\theta_e = 0$. As the polyprotein is pulled and the domains unfold, the phase changes but the Y -component does not show any variation. This shows that even if the phase is far from zero due to hydrodynamics alone, the Y -component shows no variation indicating again that the dissipation coefficient is immeasurably low. This is in agreement with results in Fig. 4.3 (b) and (d).

In a separate set of experiments, we added external phase to the cantilever oscillating in liquid and performed the unfolding experiments. It is seen that Y -component starts to show features corresponding to unfolding events. We performed measurements wherein there is possibility of extraneous phase contributions from electronic or other sources and the Y -component is not free from features (see supplementary section (2.3), Fig. S3).

These experiments clearly show that even if there is a large phase lag due to hydrodynamics when the cantilever is freely oscillating in the liquid, it does not introduce artefacts while interpreting Y -component as a dissipation signal. This is because the models take into account such phase lag due to cantilever hydrodynamics. However, if there is extraneous phase added to the measurement which is not accounted for in the models, one certainly sees variation in the Y -component which is not due to dissipation of the unfolding protein.

Benedetti et al. in their work have warned against the use of point-mass model and interpreting phase signal as dissipation in single molecules. They have shown that the Y -component of the oscillations in deflection (dy/dx) as the signal which contains the information about the dissipative processes. We stress here that even the Y -component is not free from errors as suggested by them, if the extraneous phase is not completely removed from the measurements. The sources of this phase are listed in supplemental materials section (2.3)). Besides θ_e , an experimenter has to safeguard against other sources of artefact. The most important is choice of operational frequency in the off-resonance regime. We ensured that our measurements were *truly* off-resonance. (See supplementary section (2.5))

4.4.4 Minimum detectable dissipation coefficient

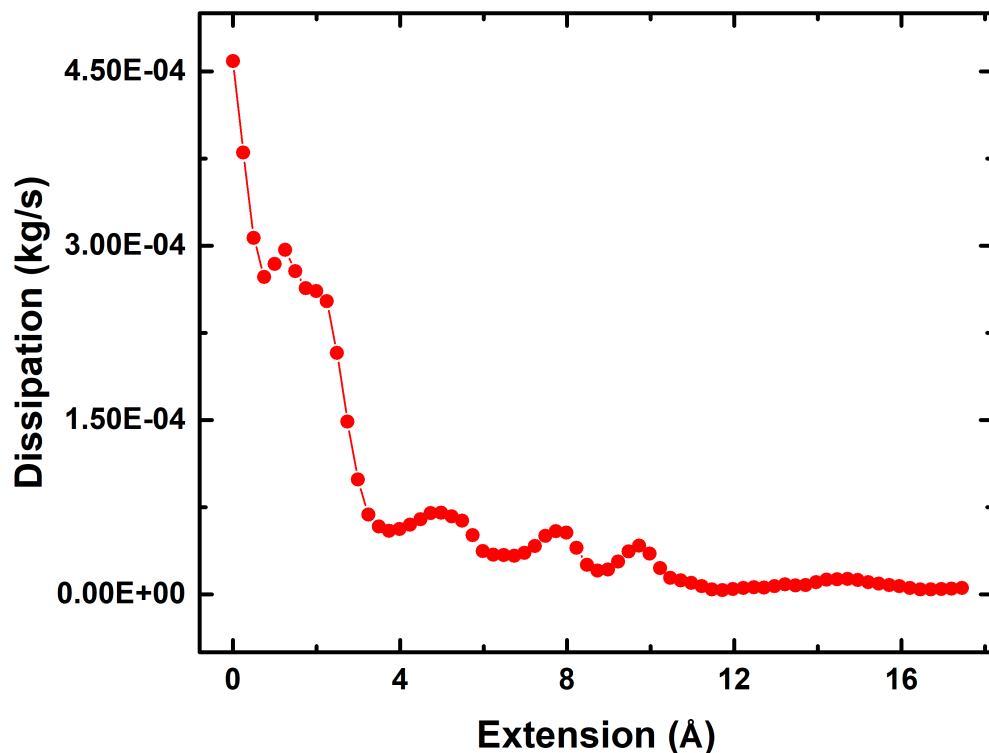


Fig. 4.9 The dissipation coefficient computed using continuous beam model given by Eqs. 4.19 and the phase and Y -component of the displacement amplitude shown in supplementary Fig. S9. Dissipation shows clear oscillations peaked at separations equal to diameter of water molecules. The variation in phase and Y -component is not seen in case of proteins.

Since the protein unfolding experiments did not show any detectable dissipation, we performed similar measurements on water confined to nanoscale. Such nano-confined water shows layering of water molecules parallel to the confining walls. Previous measurements using the interferometer based AFM have revealed that nano-confined water undergoes a dynamic solidification [92]. We repeated the measurements on molecular layers of water using interferometer-based AFM. Clear peaks separated by molecular diameter of water ($\sim 2.5 \text{ \AA}$) in both X -signal (stiffness) and Y -signal (dissipation coefficient) are observed. Fig. 4.9 shows the peaks in dissipation coefficient separated by molecular diameter of water. Experiment is done with 8 \AA/s approach speed and the observed dissipation in two to three layers of water is $\sim 10^{-4} \text{ kg/s}$, which is consistent with the previous report [92]. The raw data is shown in the supplementary (Fig. S9). Such variation in phase signal is not

observed in case of the protein unfolding experiments. The measurements confirm that the dissipation in the single unfolded protein molecule is indeed below the detection limit.

The minimum detectable dissipation coefficient using our interferometer based AFM can be estimated by measuring the noise in the Y -signal when the cantilever is not engaged with the substrate and is oscillating freely in the liquid. We can estimate noise level in the amplitude by recording and analysing the power spectral density of the cantilever displacement. From the noise floor and the lock-in time constant we estimated the noise in the cantilever displacement. Using this value of the noise in Y -component and Eq. 4.19, we obtain the minimum detectable dissipation coefficient to be $5 \times 10^{-7} \text{ kg/s}$. This is the upper bound on the dissipation coefficient of the unfolded single protein molecules.

4.4.5 Dissipation in single macromolecules

In literature there are numerous claims of measurement of viscoelasticity of single molecules using AFM [15, 73, 77, 87–89, 93, 94]. The early reports have shown that the viscoelasticity is dominated by elastic response and the dissipation could not be detected for nucleic acids and Poly Ethylene Glycol [95, 112]. However, there are many other reports of measurement of dissipation coefficient for single molecules of protein, flexible polymers and polysaccharides [77, 87, 109]. A closer look at the experimental details reveal that these measurements were performed at higher frequencies, sometimes very close to resonance, and with much larger amplitudes (2 -10 nm). These measurements are not truly off-resonance. In our opinion, the simple approximation of the cantilever dynamics to a point-mass model is not adequate to interpret the experimental data performed at higher frequencies or close to resonance. We have clearly shown in our experiments that the measurements are prone to artefacts if phase data is used either at water viscosity and higher frequencies (see supplementary Fig. S5), or low frequencies and higher viscosity (see supplementary Fig. S7). Both these situations clearly show features in the dissipation data due to coupling between stiffness and dissipation channels (see supplementary section 2.5). There is no mention in these experiments if the phase is offset by a certain value while performing experiments. If the offset is not accounted for, then the phase data produces artefacts in determining the dissipation coefficient. Moreover, if the phase and amplitude of cantilever *bending* is measured, then the point mass approximation can not be used to analyse the data. This point has been recognized earlier by many [7, 22, 27, 39, 151, 152, 155, 163, 183].

An alternative method of extracting single molecule viscoelasticity using AFM, is the measurement of power spectral density (PSD) of cantilever's thermal fluctuations. The stiffness and dissipation coefficients of single macromolecules have been observed using this method [15, 87, 88, 93, 94]. In these reports, it is important to recognize that point-mass approximation has been used to model the cantilever dynamics. Our findings advise caution while interpreting the constant velocity pulling experiments using such approximation. The analysis of thermal fluctuation data by considering the full details of cantilever's geometry is complicated and future investigations may reveal if this method is actually measuring dissipation in single molecules.

Benedetti et al. have highlighted the issues involved in interpreting the phase signal as dissipation in single molecules [7]. Using a theoretical approach similar to one presented here, they pointed out that use of point-mass approximation leads to erroneous conclusions. They have used experimental data in support of their claim. Our measurements using both, interferometer-based AFM and more conventional deflections detection AFM, reinforces the validity of concerns raised by them. Further, we claim that even the interpretation of Y -component of the cantilever bending, as suggested by them, is not free from errors if extraneous phase contributions are present. In a typical AFM experiment such contributions are not tractable and difficult to include in theoretical models [183]. However, the measurements using interferometer based AFM, wherein displacement of cantilever is measured, the presence of such artifacts can be easily identified which is essential for performing artifact free measurements. We have also provided a method here to quantify the stiffness of single molecules and have shown that it matches with simultaneous static measurements. The static data is collected at extremely low strain rates ($< 1 \text{ s}^{-1}$) compared to the dynamic measurements ($> 100 \text{ s}^{-1}$). It means that the dissipation in the current measurement is indeed immeasurably low. This has also been noted by Liu et al.[112]. Using both types of detection schemes to measure cantilever response we concluded that the dissipation coefficient is immeasurably low. The estimate of minimum detectable dissipation coefficient and stiffness using both methods is useful in determining the upper limit on the value of dissipation coefficient for the unfolded chain of I27₈. This in turn allows for determining a upper bound on Maxwell's relaxation time of the unfolded chain.

As discussed in section 4.4.4, the dissipation in single unfolded titin molecule must be below $5 \times 10^{-7} \text{ kg/s}$. The diffusion coefficient given by $D = KT/\gamma$ must be higher than $\sim 10^4 \text{ nm}^2/\text{s}$. The force spectroscopic measurements have estimated the value of D to be $\sim 10^3 \text{ nm}^2/\text{s}$ [87, 93]. The Fluorescence Resonance Energy Transfer (FRET) have yielded a much faster diffusional dynamics ($10^8 \text{ nm}^2/\text{s}$) [55, 56, 105, 126]. The current measurements suggests that possible reason behind this discrepancy in the literature is the overestimate of dissipation coefficient using AFM methods.

There are reports in the literature which focus on the measurement of viscoelasticity of the folded proteins using microrheology technique. The reported dissipation coefficient of folded protein molecule was higher then our proposed upper limit [178, 179]. It is possible that the damping coefficient of folded protein molecule is much higher compared to the unfolded chain. We do not compare our results with those measurements as we are measuring the viscoelasticity of unfolded molecule.

4.5 Conclusions

In conclusion, we have provided a method to quantify viscoelasticity at nanoscale in liquid environment using both the deflection detection type AFM and interferometer based AFM. It was found that an offset in the initial phase or inappropriate choice of operation frequency can lead to artefacts. We performed measurements of viscoelasticity of single protein (I27₈) using both types of AFM. It was

observed that the dissipation in single macromolecules is immeasurably low for AFM's detection limit. However, it was possible to measure dissipation coefficient in molecular layers of water adjacent to the solid surface. The estimates of stiffness of the macromolecule, using both detection methods is in agreement with each other and also with the static force-extension measurements. The results imply that using phase signal of cantilever bending along with point-mass approximation of the cantilever hydrodynamics may lead to artefacts in the dissipation measurement of single molecules. The results have a strong bearing on the time-scales of initial collapse in folding of I27 domains and it is also important for understanding the passive elasticity of titin in muscles.

Chapter 5

Validity of point-mass model in off-resonance dynamic atomic force microscopy

5.1 Introduction

The atomic force microscope (AFM) is a powerful tool to obtain the surface topography of insulators. Shortly after its invention, it successfully produced images of substrates with atomic resolution [2, 12, 119]. Over time, it has been used to quantify the inter-atomic forces between the cantilever-tip and substrate atoms in UHV [68, 69, 78, 80, 83, 134, 143] and ambient conditions [51]. In the past few decades, the AFM has been recognised as a versatile tool to measure the interaction forces between different biomolecules and forces required to unfold proteins [38, 66, 98, 99, 115, 162]. In addition, many groups have attempted to measure the viscoelastic properties of single-molecules directly via dynamic atomic force spectroscopy [7, 15, 28, 65, 73, 77, 87–89, 93–95, 109, 146].

In a dynamic AFM experiment, an oscillating tip mounted on a cantilever force sensor is allowed to interact with the sample which causes change in the parameters such as amplitude and phase. The dynamic spectroscopy has been used extensively in UHV to study the inter-atomic forces [68, 69, 80]. It is also implemented in viscous medium to study the behaviour of liquids under nano-confinement [34, 82, 85, 90, 92, 117, 133, 141] and single-molecules under force [15, 28, 65, 73, 77, 87–89, 93–95, 109]. In order to extract the mechanical properties of single molecules or the nano-scale system probed by the tip, a mathematical treatment of cantilever dynamics in various media such as Ultra High Vacuum (UHV) or liquid environment is essential. There is a debate among the AFM users about the correctness of various approximations used while trying to describe the cantilever dynamics. In situations wherein the damping provided by the viscous medium to the cantilever is low, such as ambient conditions or UHV, the Point-Mass (PM) model, in which the cantilever is approximated as point-mass attached to a massless spring, has been used successfully for quantitative analysis of the

dynamic AFM data [50, 51]. However, for cantilever hydrodynamics in liquid environment, validity of these approximations in various regimes have been discussed in many works [7, 147, 173, 183].

In another approach to describe the hydrodynamics, the cantilever is modelled as Continuous Beam (CB) [22, 49, 96, 114, 145, 151]. This approach gains importance particularly in liquid environments with significant viscous damping and it works with less number of approximations compared to the PM model. Recently, the CB model is used for base-excited, low frequency measurements of protein pulling performed using AFM [7]. In this work, in order to describe the dithering cantilever-molecule system, the Euler-Bernoulli equation with appropriate boundary conditions was solved. They proposed that the interaction-force alters the boundary conditions of the cantilever-molecule system and were considered explicitly in their calculations. It is argued that ignoring the details of cantilever geometry and not including the interaction in boundary conditions results in ambiguous interpretation of the phase signal as dissipation from the single molecule. It was suggested that the CB model is an appropriate model to extract viscoelasticity of nano-scale interactions and in-phase (X) and out-of-phase (Y) components of the oscillation are the observable parameters which are directly related to stiffness and damping.

In point-mass model, cantilever-beam is approximated as a point-mass and the interaction force acting on the cantilever-tip is treated as a small perturbation on the moving point-mass. These assumptions make the understanding of cantilever dynamics simple and its analytical solution becomes straight-forward. This model has been extensively used in the past due to its simplicity. The use of CB to model the cantilever raises doubt on previous works that have been done on various nano-scale systems such as single polymer [77, 87, 93, 109] and nano-confined liquids [34, 117]. These experiments have used base-excited cantilevers with deflection detection type sensing and PM model was used for data analysis. Apart from this, a large body of work exists to understand the behaviour of nano-confined liquids using base-excited dynamic measurements in interferometer based AFM in which the tip displacement is measured and PM model has been used for data analysis [82, 90, 92, 141]. The reliability of these results depend on the correctness of the mathematical model that has been used to analyse the data. A judicious choice of model which correctly captures cantilever hydrodynamics for a particular experimental strategy is of utmost importance before conclusions about nano-scale dissipation in liquid environments are drawn.

In this chapter, we have treated the cantilever dynamics in liquid environments in two ways, i) the geometric details of the cantilever as a continuous beam are incorporated in Euler-Bernoulli equation of motion and ii) the cantilever is approximated as a point-mass with a mass-less spring whose stiffness is determined by the first eigen mode of the continuous beam. Using these two approaches we derived equations to relate the stiffness and damping coefficient of the nanoscale entity under consideration to the experimentally measured quantities such as phase and amplitude of the oscillating cantilever. We developed solutions for both tip-excited as well as based excited cantilevers. Furthermore, we have investigated the validity of PM model to analyse the dynamic AFM measurements performed in liquid environments. We have solved the equation of motion of the cantilever in both CB as well as PM model. We compare the solutions of these two models within specific experimental

strategies used to excite as well as detect the cantilever response. We have performed two types of measurements. 1) Base-excited cantilever with interferometer based detection scheme wherein cantilever tip displacement is measured 2) Tip-excited cantilever with deflection detection scheme which measures the bending of the cantilever at the tip end. We developed a *magnetic-excitation* setup for tip-excited measurements. The experimental data is analysed using both PM and CB models to check the validity of PM in these measurement schemes. Further, the requirements on experimental scheme in order to use PM model to extract the stiffness and dissipation coefficient of single protein molecules are deduced. We find that PM model is successful in estimating quantitative viscoelastic response of nano-scale entities if care is taken while exciting the cantilever or detecting its response. In general, true off-resonance operation, stiff cantilevers and small amplitudes are key elements in successful quantification of viscoelasticity using PM model in amplitude modulation dynamic AFM.

5.2 Theory

Equation of motion:

Bending of a homogeneous rectangular cantilever beam in a viscous medium is described by Euler-Bernoulli equation. The internal damping of the cantilever beam has been ignored.

$$-\tilde{\rho}S\frac{\partial^2 y(x,t)}{\partial t^2} - \gamma_c \frac{\partial y(x,t)}{\partial t} = EI \frac{\partial^4 y(x,t)}{\partial x^4} \quad (5.1)$$

Where x is the coordinate along the cantilever length with $x = 0$ at the clamped end and $x = L$ at the free end. y is the displacement along the perpendicular direction of the cantilever length. $\tilde{\rho}S = \rho S + m_a$, m_a is hydrodynamic added mass where ρ is mass density of the cantilever material, $S (= bh)$ is area of the cantilever cross-section perpendicular to its length, b and h are width thickness of the cantilever respectively, γ_c is the cantilever drag coefficient per unit length, E is Young's modulus and $I (= bh^2/12)$ is second area moment.

Analytical solution for Eq. 5.1 can be derived for few limiting cases in two ways. One method accounts for the continuous nature of the cantilever-beam in derivation and we refer to it as *continuous-beam (CB) model*. However, another method assumes the cantilever as a point-mass and it is known as *point-mass (PM) model*. In CB model, the solution of Eq. 5.1 is assumed to be $y(x,t) = y(x)e^{i\omega t}$, whereas, to arrive at PM model, method of variable separation is used first where solution is assumed to be of the form $y(x,t) = y(x)Y(t)$. $y(x)$ is the general solution of space part of Eq. 5.1 which is required to be solved in both models. Space part of Eq. 5.1 is,

$$\frac{d^4 y(x)}{dx^4} = k^4 y(x) \quad (5.2)$$

and its general solution is:

$$y(x) = a \sin(kx) + b \cos(kx) + c \sinh(kx) + d \cosh(kx) \quad (5.3)$$

Where a , b , c , and d are constants which can be determined using four appropriate boundary conditions. These Boundary conditions are derivatives of $y(x)$ at some values of x . They are determined by experimental situations such as excitation method as well as the interaction forces experienced by the tip. In typical AFM experiments, interaction force acts at the tip end of the cantilever and excitation can either be applied at the base or the tip.

The two models differ in consideration of boundary conditions. In CB model, cantilever excitation and interaction forces are accounted for in the boundary conditions. Whereas, in PM model, a set of homogeneous boundary conditions are applied and cantilever excitation and interaction force are included in the equation of motion.

5.2.1 Continuous-beam (CB) model

In CB model, continuous-nature of the cantilever beam is considered. Solution of Eq. 5.1 is assumed to be $y(x,t) = y(x) e^{i\omega t}$. Substituting the solution in Eq. 5.1 results in Eq. 5.2 (space-part) and following dispersion relation:

$$\tilde{\rho}\tilde{S}\omega^2 - i\omega\gamma_c = EIk^4 \quad (5.4)$$

To solve Eq. 5.1, cantilever excitation and interaction force are included in boundary conditions. Interaction force is considered as linear ($F_i = k_i y(t) + \tilde{\gamma}_i \frac{dy(t)}{dt}$) and solved for small interaction force ($g \ll 1$ or $k_i \ll k_c$) and small-oscillation frequency ($z \ll 1$ or $\omega \ll \omega_0$). Where g and z are defined as following:

$$z = kL = \left[\frac{3(\tilde{\rho}\tilde{S}\omega^2 L - i\omega\gamma_c L)}{k_c} \right]^{\frac{1}{4}},$$

$$g = \frac{3(k_i + i\omega\tilde{\gamma}_i)}{k_c} \quad (5.5)$$

To get the complete solution of Eq. 5.1 for base and tip excitation, Eq. 5.2 is required to be solved separately.

5.2.1.1 Base-excitation

When the cantilever is excited from the base and a linear interaction force acting on the tip (Fig. 5.1 (a)), following boundary conditions can be applied to solve Eq. 5.2:

$$y(0) = A, \quad y'(0) = 0$$

$$y''(L) = 0, \quad EIy'''(L) = (k_i + i\omega\tilde{\gamma}_i)y(L) \quad (5.6)$$

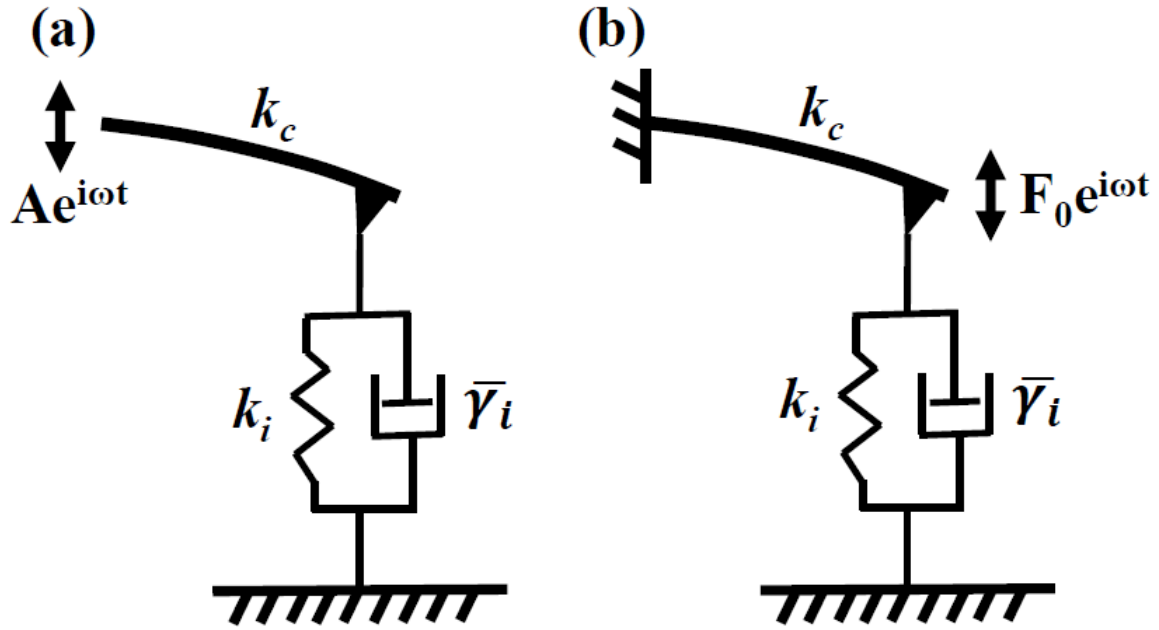


Fig. 5.1 Schematic representation of oscillating cantilever under influence of a linear interaction force. In off-resonance operation the medium damping is negligibly small and hence not shown in the schematic. (a) Representing the base-excited cantilever where base is driven by $Ae^{i\omega t}$. (b) Representing the tip-excited cantilever where base is rigidly fixed and tip is excited with force $F_0e^{i\omega t}$.

Where prime ($'$) denotes the derivative of $y(x)$ with respect to x . k_i and $\bar{\gamma}_i$ are interaction stiffness and damping coefficients respectively. It is important to note that the interaction force is considered as a *linear viscoelastic force*.

Eq. 5.6 were solved to get the constants (a , b , c , and d) and final solution of Eq. 5.2, assuming $g \ll 1$ and $z \ll 1$, are following (see *chapter-3* and [146] for detailed derivation):

Slope (bending):

$$\left. \frac{\partial y(x)}{\partial x} \right|_{x=L} = \frac{A}{2k_c L} (-3k_i + \tilde{\rho} \tilde{S} \omega^2 L) - i \frac{A \omega}{2k_c L} (3\bar{\gamma}_i + \gamma_c L) \quad (5.7)$$

Modulus and argument of Eq. 5.7 gives us the amplitude and phase (difference between drive and tip) of bending at $x = L$:

$$R_b = \frac{A}{2k_c L} \sqrt{(-3k_i + \tilde{\rho} \tilde{S} \omega^2 L)^2 + \omega^2 (3\bar{\gamma}_i + \gamma_c L)^2},$$

$$\theta_b = \arctan \left(-\omega \frac{3\bar{\gamma}_i + \gamma_c L}{-3k_i + \tilde{\rho} \tilde{S} \omega^2 L} \right) \quad (5.8)$$

The real and imaginary components of the bending are:

$$\begin{aligned} X_b &= \frac{A}{2k_c L} (-3k_i + \tilde{\rho} \tilde{S} \omega^2 L), \\ Y_b &= -\frac{A \omega}{2k_c L} (3\tilde{\gamma}_i + \gamma_c L) \end{aligned} \quad (5.9)$$

Rearranging the Eq. 5.9, the expression for interaction stiffness and dissipation coefficient can be written as:

$$\begin{aligned} k_i &= \frac{1}{3} \tilde{\rho} \tilde{S} \omega^2 L - \left(\frac{2k_c L}{3A} \right) X_b, \\ \tilde{\gamma}_i &= \left(\frac{2k_c L}{3A \omega} \right) Y_b - \frac{\gamma_c L}{3} \end{aligned} \quad (5.10)$$

Displacement:

$$y(L) = \frac{A}{k_c} (k_c - k_i) - i \frac{A \omega}{k_c} \tilde{\gamma}_i \quad (5.11)$$

In Eq. 5.11, the amplitude and phase of cantilever-tip displacement are the modulus and argument of $y(L)$ respectively. These can be written as:

$$\begin{aligned} R_d &= \frac{A}{k_c} \sqrt{(k_c - k_i)^2 + (\omega \tilde{\gamma}_i)^2}, \\ \theta_d &= \arctan \left(-\omega \frac{\tilde{\gamma}_i}{k_c - k_i} \right) \end{aligned} \quad (5.12)$$

The real and imaginary components of the displacement are:

$$\begin{aligned} X_d &= \frac{A}{k_c} (k_c - k_i), \\ Y_d &= -\frac{A \omega}{k_c} \tilde{\gamma}_i \end{aligned} \quad (5.13)$$

Eq. 5.13 can be solved for interaction stiffness and damping coefficient:

$$\begin{aligned} k_i &= k_c \left(1 - \frac{X_d}{A} \right), \\ \tilde{\gamma}_i &= -\frac{k_c Y_d}{A \omega} \end{aligned} \quad (5.14)$$

Eq. 5.10 and 5.14 are valid when the stiff cantilever ($g \ll 1$) is used at low operation frequency ($z \ll 1$) and small-amplitude ($EI y'''(L) = (k_i + i \omega \tilde{\gamma}_i) y(L)$). These criterion must be fulfilled when the experiments were performed.

5.2.1.2 Tip-excitation

When the cantilever is excited directly at the tip and also a linear interaction force acting on the tip (Fig. 5.1 (b)), following boundary conditions can be applied to solve Eq. 5.2:

$$\begin{aligned} y(0) &= 0, & y'(0) &= 0, \\ y''(L) &= 0, & EIy'''(L) &= (k_i + i\omega\bar{\gamma}_i)y(L) - F_0 \end{aligned}$$

Where $F_0 = k_c A_0$ is magnitude of excitation force applied at the tip. A_0 is amplitude free amplitude of the cantilever end- when cantilever is far from the surface and interaction force is absent.

We follow similar protocol to solve Eq. 5.2 as has been followed in base-excitation section (see *chapter-3* for detail derivation). The final solutions for assumptions $z \ll 1$ and $g \ll 1$ are following:

Slope (bending):

$$\left. \frac{\partial y(x)}{\partial x} \right|_{x=L} = \frac{3A_0}{2Lk_c} (k_c - k_i) - i\omega \frac{3A_0}{2Lk_c} \bar{\gamma}_i \quad (5.15)$$

Modulus and argument of Eq. 5.15 gives us the amplitude and phase (difference between drive and tip) of bending at $x = L$:

$$\begin{aligned} R_b &= \frac{3A_0}{2k_c L} \sqrt{(k_c - k_i)^2 + \omega^2 \bar{\gamma}_i^2}, \\ \theta_b &= \arctan\left(-\omega \frac{\bar{\gamma}_i}{k_c - k_i}\right) \end{aligned} \quad (5.16)$$

Now the real and imaginary components of the bending are

$$\begin{aligned} X_b &= \frac{3A_0}{2k_c L} (k_c - k_i), \\ Y_b &= -\frac{3A_0 \omega}{2k_c L} \bar{\gamma}_i \end{aligned} \quad (5.17)$$

Eq. 5.17 can be solved for interaction stiffness and damping coefficient:

$$\begin{aligned} k_i &= k_c \left(1 - \frac{2L}{3A_0} X_b\right), \\ \bar{\gamma}_i &= -\frac{2k_c L}{3A_0 \omega} Y_b \end{aligned} \quad (5.18)$$

Displacement:

$$y(L) = \frac{A_0}{k_c}(k_c - k_i) - i\omega \frac{A_0}{k_c} \bar{\gamma}_i \quad (5.19)$$

Modulus and argument of Eq. 5.19 gives us the amplitude and phase (difference between drive and tip) of displacement at $x = L$:

$$R_d = \frac{A_0}{k_c} \sqrt{(k_c - k_i)^2 + (\omega \bar{\gamma}_i)^2},$$

$$\theta_d = \arctan \left(-\omega \frac{\bar{\gamma}_i}{k_c - k_i} \right) \quad (5.20)$$

The real and imaginary components of the displacement are:

$$X_d = \frac{A_0}{k_c}(k_c - k_i),$$

$$Y_d = -\frac{A_0 \omega}{k_c} \bar{\gamma}_i \quad (5.21)$$

Eq. 5.21 can be solved for interaction stiffness and damping coefficient:

$$k_i = k_c \left(1 - \frac{X_d}{A_0} \right),$$

$$\bar{\gamma}_i = -\frac{k_c Y_d}{A_0 \omega} \quad (5.22)$$

Again Eq. 5.18 and 5.22 are valid when the stiff cantilever ($g \ll 1$) is used at low operation frequency ($z \ll 1$) and small-amplitude ($EIy'''(L) = (k_i + i\omega \bar{\gamma}_i)y(L)$). These criterion must be fulfilled when the experiments are performed.

It is important to note here that in most AFM measurements, cantilever is base excited and deflection detection scheme is used which measures cantilever bending. Eq. 5.10 should be used to analyse the data in such experimental situations [7]. In our previous work we have highlighted how these measurements are prone to artefacts owing to the extraneous phase contributions. These phase contributions are difficult to account for in theoretical treatment of cantilever hydrodynamics [146]. It is also noteworthy that displacement solution for base excited cantilever (Eq. 5.14) are similar in form to the bending solution of tip excited cantilever (Eq. 5.18) since $X_d(L) = 2LX_b(L)/3$. The solution for displacement is same for both tip excited or base excited cantilevers See Eq. 5.14 and 5.22 since, for off-resonance operation $A = A_0$.

5.2.2 Point-mass model

In point-mass model, variable separable method is used to solve Eq. 5.1 wherein space and time parts are separately solved. To solve space part, boundary conditions are considered as homogeneous ($y(0) = 0, y'(0) = 0, y''(L) = 0$, and $y'''(L) = 0$). This provides a set of independent solutions ($y_n(x)$)

for a freely oscillating cantilever. Each solution represents an eigen mode. Now solution ($y(x,t)$) is substituted into Eq. 5.1, multiply with $y_n(x)$ and using the orthogonal property of $y_n(x)$ a set of equations on time-variable is achieved. Each equation for an eigen mode is a damped harmonic oscillator equation - a linear second order differential equation. Since the fundamental mode makes up for most of the contribution to cantilever oscillation, it is considered as the force equation of the freely oscillating cantilever in viscous environment. The excitation force is directly included into the final equation of motion depending on the excitation scheme. The interaction force, which is assumed to be *linear*, is considered as a perturbation to the forced-damped oscillator and included into the final equation (or in Eq. 5.1 using δ -function). This treatment imposes the assumption of small interaction force compared to the cantilever force (or $k_c \ll k_i$). Now the final equation of motion of oscillating cantilever under influence of interaction force is a simple forced-damped harmonic oscillator equation with an effective mass (m^*), elasticity (k') and damping (γ') coefficients. It is important to note that this treatment assumes the cantilever beam as a *point-mass* which is attached with a mass-less spring as shown in Fig. 5.2. See *chapter-3* and [49] for detailed derivation.

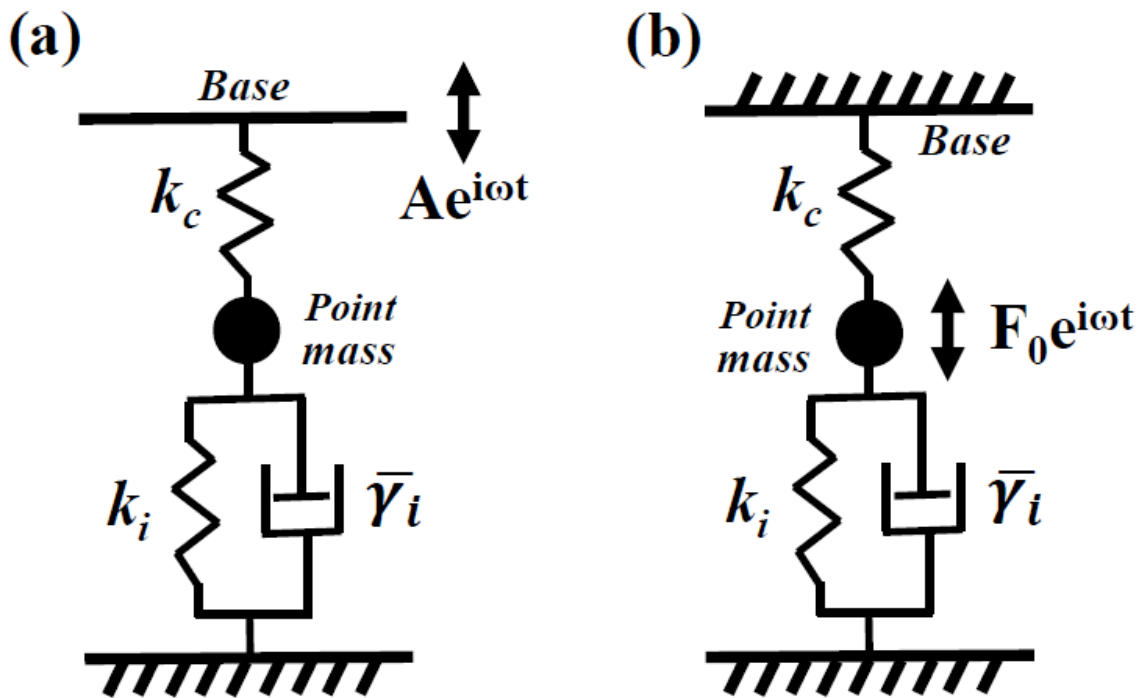


Fig. 5.2 Schematic representation of point-mass approximated cantilever under influence of a linear interaction force. These are devoted to off-resonance operation where medium damping is negligibly small. (a) Representing the base-excited point-mass approximation where base is driven by $Ae^{i\omega t}$. (b) Representing the tip-excited point-mass approximation where base is rigidly fixed and tip is excited with force $F_0e^{i\omega t}$.

5.2.2.1 Base-excitation

When cantilever is excited from the base sinusoidally ($Ae^{i\omega t}$) and tip experiences a *small perturbation* due to a *linear viscoelastic* force (F_i), it is approximated as a point-mass connected to one end of a spring whose other end is driven (Fig. 5.2 (a)). The equation of motion for this point-mass can be written as:

$$m^* \frac{\partial^2 z(t)}{\partial t^2} + \gamma_c L \frac{\partial z(t)}{\partial t} + k_c(z(t) - Ae^{i\omega t}) - F_i = 0 \quad (5.23)$$

Where $m^* = 0.2425 m_c + m_a$ is effective mass, m_c and m_a are the cantilever mass and hydrodynamic added mass respectively. $F_i = k_i z(t) + \bar{\gamma}_i \frac{dz(t)}{dt}$ is the interaction force which is assumed to be *linear viscoelastic*. Other parameters have the same meaning as in the continuous-beam model. Eq. 5.23 can be written as:

$$m^* \frac{\partial^2 z(t)}{\partial t^2} + \gamma' \frac{\partial z(t)}{\partial t} + k' z(t) = k_c A e^{i\omega t} \quad (5.24)$$

Eq. 5.24 is an equation of motion for a forced damped harmonic oscillator with effective stiffness ($k' = k_c + k_i$), effective damping coefficient ($\gamma' = \gamma_c L + \bar{\gamma}_i$), and effective drive force ($k_c A$). The amplitude (R) and phase (θ , phase difference between drive and the oscillator) will be given as:

$$R = \frac{k_c A}{\sqrt{(k' - m^* \omega^2)^2 + (\omega \gamma')^2}},$$

$$\theta = \tan^{-1} \left(\frac{\omega \gamma'}{k' - m^* \omega^2} \right) \quad (5.25)$$

Further, Eq. 5.25 can be solved for interaction stiffness and damping coefficient for ($\omega \ll \omega_0$):

$$k_i = k_c \left(\frac{A \cos \theta}{R} - 1 \right),$$

$$\gamma' = - \frac{k_c A \sin \theta}{R \omega} \quad (5.26)$$

5.2.2.2 Tip-excitation

When an AFM cantilever is excited from the tip sinusoidally with excitation force ($F_0 e^{i\omega t}$) and tip experiences a *small perturbation* due to a *linear viscoelastic* force (F_i), it is approximated as a point-mass connected to a massless spring which is driven sinusoidally (Fig. 5.2 (b)). The Equation of motion for this point-mass can be written as:

$$m^* \frac{\partial^2 z(t)}{\partial t^2} + \gamma_c L \frac{\partial z(t)}{\partial t} + k_c z(t) - F_0 e^{i\omega t} - F_i = 0 \quad (5.27)$$

All parameters have the same meaning as described in previous sections. Eq. 5.27 can be written as:

$$m^* \frac{\partial^2 z(t)}{\partial t^2} + \gamma' \frac{\partial z(t)}{\partial t} + k' z(t) = F_0 e^{i\omega t} \quad (5.28)$$

Eq. 5.28 is an equation of motion for a forced damped harmonic oscillator with effective stiffness ($k' = k_c + k_i$), effective damping coefficient ($\gamma' = \gamma_c L + \bar{\gamma}_i$). The amplitude (R) and phase (θ , phase difference between drive and the oscillator) will be given as:

$$R = \frac{k_c A_0}{\sqrt{(k' - m^* \omega^2)^2 + (\omega \gamma')^2}},$$

$$\theta = \tan^{-1} \left(\frac{\omega \gamma'}{k' - m^* \omega^2} \right) \quad (5.29)$$

Further, Eq. 5.29 can be solved for interaction stiffness and damping coefficient for ($\omega \ll \omega_0$):

$$k_i = k_c \left(\frac{A_0 \cos \theta}{R} - 1 \right),$$

$$\gamma' = - \frac{k_c A_0 \sin \theta}{R \omega} \quad (5.30)$$

As expected, for off-resonance conditions ($A = A_0$) the solutions for tip excited and the based excited cantilever is same. Again, the Eq. 5.26 and 5.30 are valid when stiff cantilever (interaction force (F_i) is considered as the perturbation) is used at off-resonance ($\omega \ll \omega_0$) and small-amplitude ($F_i = k_i z(t) + \bar{\gamma}_i \frac{dz(t)}{dt}$).

5.3 Materials and Methods

5.3.1 Magnetic excitation setup

To perform tip-excited measurements, we developed a method to coat a thin layer of magnetic material at the end of the cantilever. A thin layer of chromium-cobalt (*Cr-Co*) is obtained at the back of the cantilever, near the end position. An electromagnet was prepared to sinusoidally excite the cobalt coated cantilever-tip.

5.3.1.1 Cantilever and electromagnet preparation

Cantilever preparation detail can be found in *chapter-2*. In short, the entire cantilever, except the end position, was masked with photoresistive material using optical lithography technique. The photoresist near the cantilever end was exposed to a high intensity laser and removed using developer. Using thermal evaporation deposition method chromium-cobalt were coated on the masked cantilever. The photoresist was then removed by sonicating the cantilever in acetone for few seconds. This leads to only the Cr-Co film remaining at the end of the cantilever. It was then sputter coated with gold

from all sides to protect it from the buffer in which the experiments were performed. Thin cobalt layer can also be coated using an alternative method where cantilever is carefully masked, except the cantilever end position, using a sheet and it is placed into thermal evaporation deposition chamber to coat Cr-Co film. For this method the use of photoresist for masking is not required.

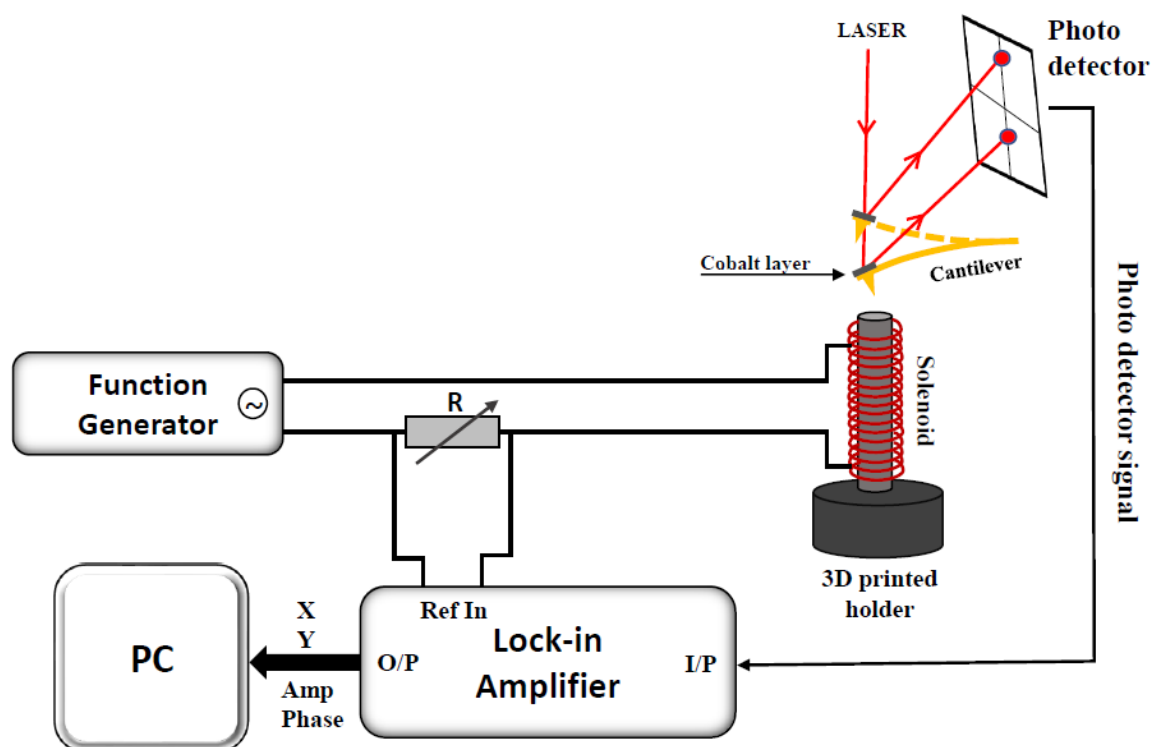


Fig. 5.3 Schematic for the magnetic excitation setup. An alternative current from the function generator is supplied to the solenoid which creates an alternative magnetic field. A cantilever with cobalt coated at the end is positioned on top of the solenoid. The sinusoidal motion due to the field is detected by the four quadrant photo detector. Photo detector output signal is fed to the lock-in amplifier to determine its amplitude and phase or X and Y signals. Eventually the signals are grabbed by the computer.

The magnetic field for driving the cantilever was obtained from an alternating current carrying solenoid. A ~ 0.3 mm insulated copper wire was wound ~ 300 times around a ferrite core of diameter 2.5 mm and length 20 mm. A function generator (Tektronix AFG3252C, Washington, US) with 100 mA as the maximum current output was used as the current source. The solenoid was mounted on a holder that sat on one of the objective lens slots in the inverted microscope (Olympus, Denmark). This made it easier to bring the solenoid directly under the cantilever. A maximum of 30 mGauss was achieved at a distance of 5 - 10 mm. The solenoid had an impedance of 12 Ohms and a phase lag of 50 degrees at 133 Hz operation frequency. We observed that the solenoid temperature was increasing due to the Joule heating effect, and may alter the sample temperature. To reduce this heating we increased the number of turns and the wire cross section to use the minimum amount of current. The increased

inductance due to higher number of turns did not cause problems since we worked with a constant and low frequency alternating current. The coil had an impedance of 12 *Ohms* at our operation frequency of 133 *Hz*.

A schematic representation of magnetically-excited (tip-excited) measurement is shown in Fig. 5.3.

5.3.1.2 Cantilever response in buffer medium

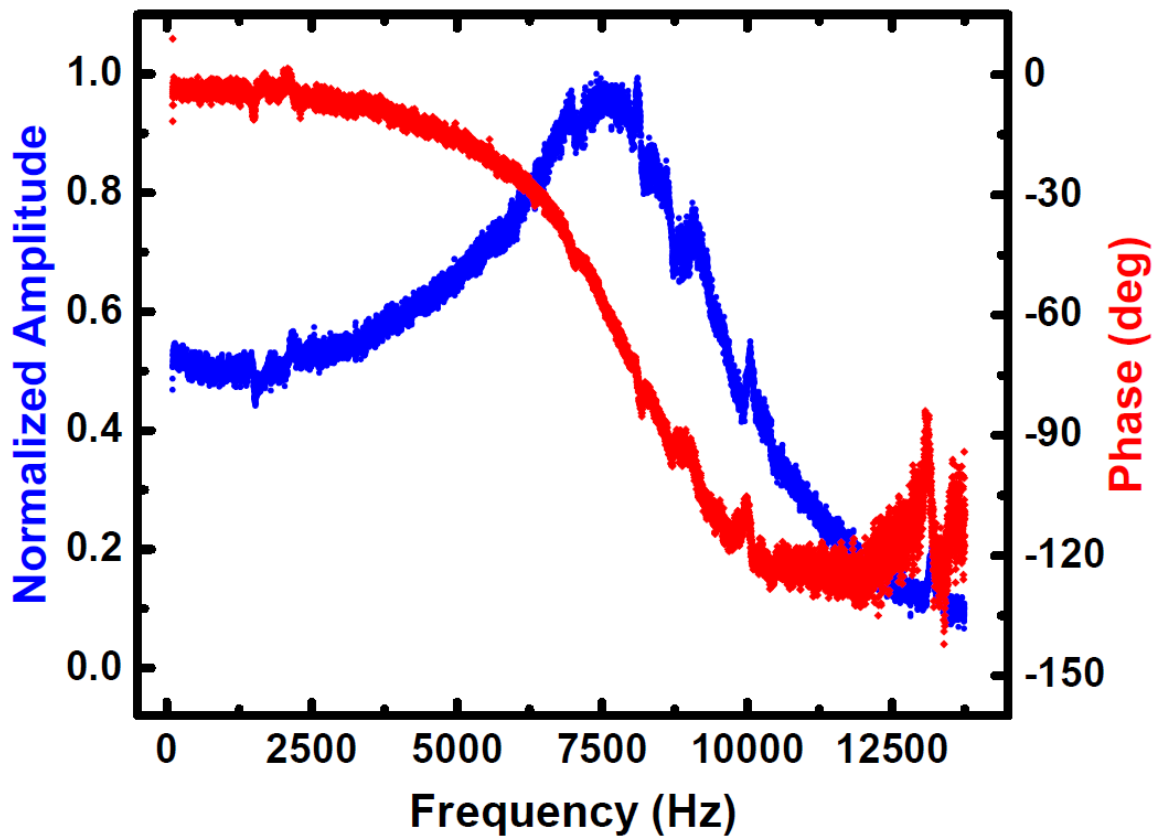


Fig. 5.4 Frequency response of the cantilever with a thin layer of *Cr – Co* coating at its end position. It can be observed that the low frequency regime is flat and free from spurious peaks. Also phase is small. The experiments were performed at 133 *Hz*.

Obtaining a stable magnetic material coating at the end position of the cantilever for buffer medium was the most challenging part in this business. Once the stable coating was obtained, the response of the cantilever in liquid, specially in buffer, was essential to examine as it is crucial to perform an artefact free measurements. A true off-resonance operation can only confirmed by observing the frequency response of the cantilever. The amplitude and phase signals are flat at true off-resonance frequency and also the phase is negligibly small ($\sim 0\text{deg}$) as predicted by Eq. 5.16.

5.3.2 Sample Preparation

Sample preparation is similar to what I have described in *Chapter 2*. A $100\ \mu\text{l}$ protein sample in PBS buffer (pH7.4) with 10mg ml^{-1} was drop casted on a freshly evaporated gold coated coverslip. It is allowed to incubate for 30 minutes along with the cleaning with fresh buffer two-to-three times. Now liquid cell is filled with $600\ \mu\text{l}$ buffer and used it for the measurement.

5.4 Experiments

5.4.1 Atomic Force Microscopy

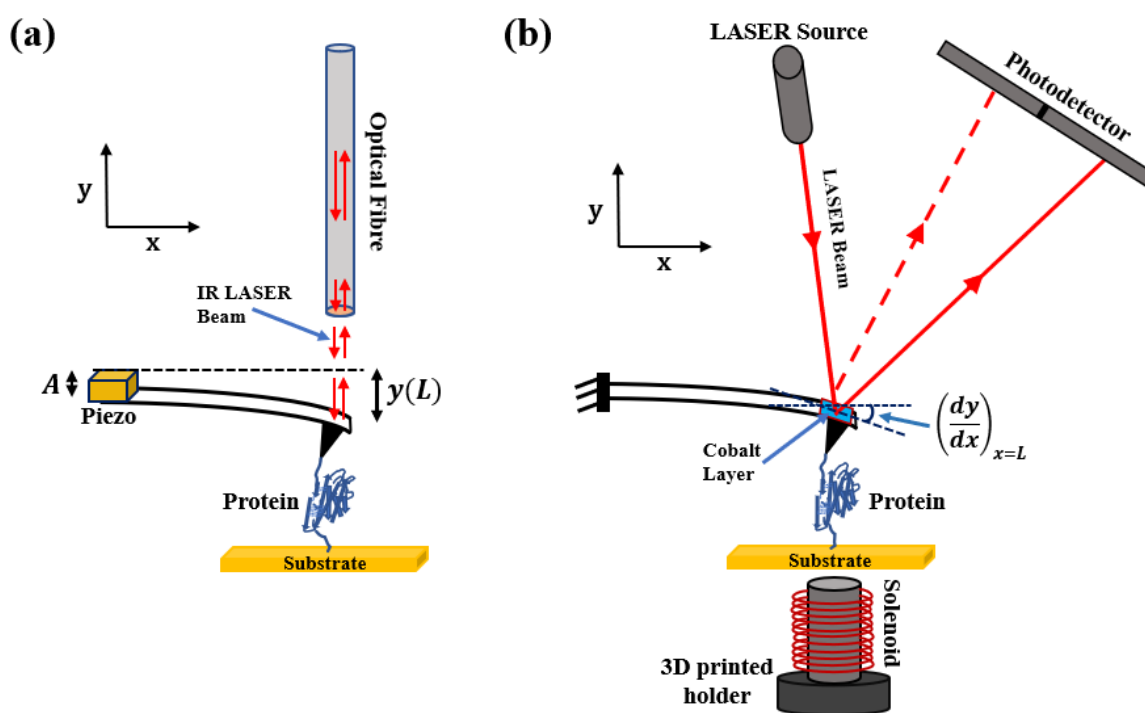


Fig. 5.5 (a) Schematic of interferometer based AFM equipped with base-excitation mechanism. Cantilever is attached with a piezoelectric block which excites its base. Interferometric-detection scheme measures displacement ($y(t)$) of cantilever end. (b) Representing tip-excitation setup equipped with a deflection-detection mechanism. A thin layer of cobalt is coated at the tip-end, which is used to excite cantilever's tip using an electromagnet placed beneath it, base of the cantilever is rigidly fixed. Optical-deflection-detection scheme measures the bending ($dy(t)/dx$) of the cantilever end. A protein with one domain is tethered between the substrate and cantilever-tip.

We performed two types of AFM measurements, i) Base excited cantilever together with interferometer based detection scheme which, as shown in Fig. 5.5 (a), measures cantilever displacement.

The interferometer is home-built with five-axis inertial slider allowing nanopositioning of fiber on the back of the cantilever. It is further aligned exactly perpendicular to the length of the cantilever, so that the end of the fiber and the backside of cantilever form a fabry-perot etalon. This design enhances the sensitivity allowing a thermally limited measurement of the cantilever's displacement [140]. Next, we performed experiments with ii) tip excited cantilever with deflection detection scheme which, as shown in Fig. 5.5 (b), measures cantilever bending at the tip end. The deflection detection type measurement scheme is available in all commercial AFMs and it is preferred due to its relative ease of operation. The deflection detection set-up together with base-excitation is more prone to artefacts in the measurement and quantification of viscoelastic parameters of nanoscale entity under investigation is difficult [146, 147]. Therefore, we avoided exciting the cantilever from base in this case. It is excited at the tip-end. Such excitation requires a magnetic spot at the back of cantilever. This is achieved by coating a spot of Cobalt having $\sim 30\text{ nm}$ thickness on the back of the cantilever, near the tip. A home-built solenoid coil is used to excite the tip sinusoidally. It ensures the tip is preferentially excited compared to the other parts of the cantilever and surrounding liquid.

5.4.1.1 Displacement-detection, Base-excited cantilever

Experiments are performed using a home-built, fibre-interferometer based AFM [140]. Labview programs are used as interface to control the instrument and data acquisition. Rectangular cantilever (HQ:CSC37/Cr-Au, Micromasch, Bulgaria) with stiffness $\sim 1\text{ N/m}$ and dimensions - length = $250\text{ }\mu\text{m}$, width = $35\text{ }\mu\text{m}$, thickness = $1\text{ }\mu\text{m}$ - are used for experiments. Measurements are performed with small-amplitude ($\sim 1\text{ \AA}$) which confirms that the measurements are in linear-regime, and off-resonance frequency (below 500 Hz). The resonance frequency of the cantilever in water was $\sim 14\text{ kHz}$. A low pulling speeds ($\sim 5\text{ nm/s}$) were used. A digital lock-in amplifier (SRS830, Stanford, California, US) was used to get the amplitude and phase during the measurement.

We performed base-excited and displacement-detection AFM unfolding experiment to measure the viscoelastic response on octamers of I27₈ protein. We compare the stiffness estimates after performing analysis on this data using both CB and PM models. Fig. 5.6 (a) shows as collected raw data of the in-phase X -component and out-of-phase Y -component of the cantilever displacement measured using the interferometer. Fig. 5.6 (b) shows the amplitude and phase of the displacement.

While performing these measurements care is taken so that the approximations used to derive Eq. 5.14 and 5.26 are valid. To satisfy the condition $\omega \ll \omega_0$, experiments are performed at low frequency ($f = 133\text{ Hz}$), whereas the fundamental frequency (f_0) of the cantilever in liquid is 14.5 kHz (where $\omega = 2\pi f$). The stiffness of unfolded protein chain is reported to be around 20 mN/m [146]. We used cantilever stiffness $k_c = 1\text{ N/m}$, so that $k_i \ll k_c$.

To get an accurate estimate of stiffness from these linear approximation based models, the experiments must be performed in the linear interaction force regime. This can be achieved by keeping the oscillation amplitude of the cantilever-tip below a certain value so that the potential can

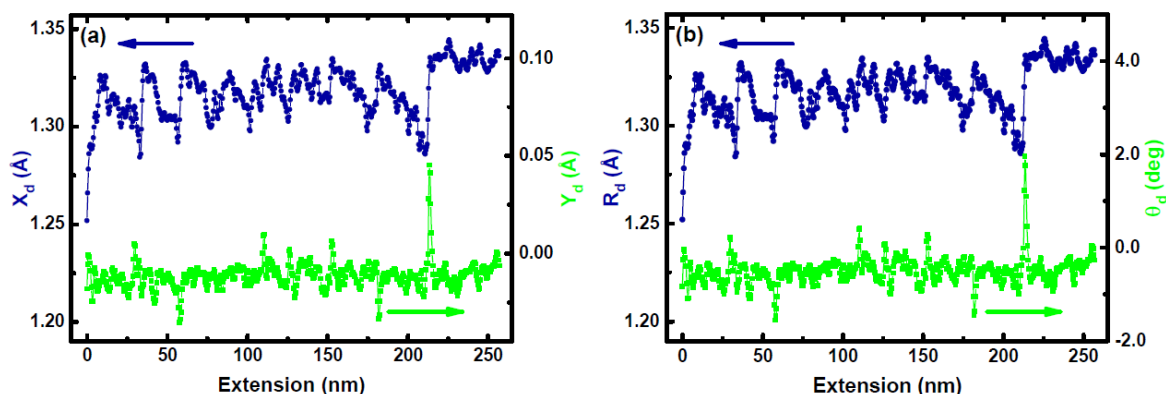


Fig. 5.6 Base-excited unfolding experiment was performed on polyprotein using interferometer based detection scheme wherein cantilever displacement is measured. (a) X -component (solid circle in cyan) and Y -component (solid square in green) of displacement. (b) Amplitude (solid circle in cyan) and $Phase$ (solid square in green) of displacement.

be approximated as linear over the entire oscillation amplitude. The oscillation amplitude for the data shown in Fig. 5.6 were $\sim 1 \text{ \AA}$, which is below the persistence length $\sim 0.4 \text{ nm}$. The data shown in Fig. 5.6 were performed at 133 Hz . These frequency is well below the fundamental resonance of the cantilever in water which is $\sim 14 \text{ kHz}$. At true off-resonance regime, the amplitude and phase response with frequency were flat and phase was $\sim 0 \text{ deg}$ [146], which confirms that the variation in amplitude and phase will occur only due to interaction stiffness and damping forces respectively and not due to resonance frequency shift [69, 142]. The off-resonance operation avoids issues that may arise at resonance operation due to cantilever's complex amplitude and phase response [68, 69, 82, 92]. We have used cantilever with stiffness $\sim 1 \text{ N/m}$ for the measurements shown in Fig. 5.6 which is orders of magnitude more than the peak stiffness of the unfolded I27-molecule ($\sim 0.02 \text{ N/m}$). When the experiments were performed on single I27₈ molecule with above discussed three criterion, the change in amplitude due to molecule stretching is very small ($\sim 0.1 \text{ \AA}$). To detect such a small signal we need a high sensitivity as well as a good signal to noise ratio. In our home-built, interferometer based AFM, we routinely get $\sim 40 \text{ mV/\AA}$ sensitivity and $\sim 5 \text{ pm}$ noise-floor at the measurement bandwidth which allows us to detect such a small signal.

The data in Fig. 5.6(a) and (b) were analyzed using Eq. 5.14 (CB model) and 5.26 (PM model) respectively and the stiffness was plotted in Fig. 5.8 (a). The solid-circle in blue represents the stiffness estimated using CB model and solid-diamond in red estimated using PM model.

We observed that analysis using both models yield same stiffness for the unfolded I27₈ molecule. We obtained consistent results when the measurement was repeated for a range of amplitudes- 0.5 \AA to 3.0 \AA , and frequencies- 100 Hz to 1000 Hz (Data not shown).

5.4.1.2 Deflection-detection, tip-excited cantilever

We performed dynamic AFM experiments on single titin I27₈ protein molecule using deflection-detection wherein the bending of the cantilever at the tip end is measured. For these measurements we used magnetic excitation to drive the cantilever tip. To implement tip-excitation scheme, we coated a thin layer ($\sim 30\text{ nm}$) of cobalt on the backside of the cantilever near the tip-position. The cantilever preparation was the most challenging part in the experiment.

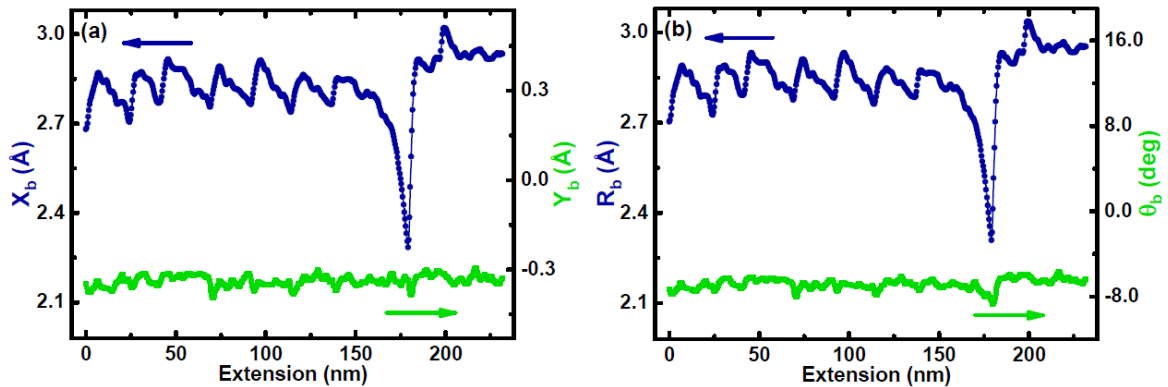


Fig. 5.7 Tip-excited unfolding experiment was performed on polyprotein in deflection detection scheme wherein cantilever bending is measured. (a) X -component (solid circle in cyan) and Y -component (solid square in green) of bending. (b) Amplitude (solid circle in cyan) and $Phase$ (solid square in green) of bending.

Fig. 5.7 shows the raw data of unfolding I27₈ molecule performed in deflection-detection based AFM using the tip-excitation method. Once again care was taken so that the approximations used in the mathematical models are valid. We used cantilever with stiffness - 0.4 N/m and resonance frequency (f_0) in water - 7.5 kHz . Experiments were performed at truly-off resonance regime ($f = 133\text{ Hz}$) and the free amplitude is $\sim 3\text{ \AA}$. In Fig. 5.7, it can be observed that only X -component and the amplitude shows variation when the domain was stretched, whereas the Y -component and phase is featureless. This is consistent with our previous observation that the dissipation coefficient from unfolded chain is immeasurably low [146].

The data in Fig. 5.7 is analyzed using CB and PM models (Eq. 5.18 and 5.30) to calculate the stiffness and it is plotted in Fig. 5.8 (b). The solid-circle in blue represents the stiffness estimated using CB model and solid-diamond in green estimated using PM model. It can be observed that analysis using both models yield same stiffness profiles. We also compare the estimated stiffness using the dynamic methods (base-excited, displacement-detection and tip-excited, slope-detection) with static stiffness. We found a good agreement between results predicted by these three independent methods which ensures the accuracy of the methodology proposed by us (refer *Appendix B*).

5.5 Discussion

Since both PM and CB model yield same results on experimental data collected using two types of measurement schemes, it is important to ask the question- How does a model which accommodates geometric details of the cantilever into its dynamics fares similar to a simplistic point-mass approximation? It must be noted that the interaction force in both models is treated like a perturbation. While using the CB model to derive expressions relating stiffness and damping to experimentally measured quantities such as X and Y components (Eq. 5.14 and 5.18), it is assumed that the interaction stiffness is much smaller than the cantilever stiffness ($g \ll 1$). This implies that the relative change in amplitude due to interaction is minimal ($< 10\%$). The PM model also works with same assumption. The interaction force can be considered as a perturbation on the oscillating cantilever when the entire dynamics is dominated by forces other than the one acting at the tip-end alone. However, when the interaction force is comparable to these forces, the effects of altered boundary condition will be significant. It is important to note that in such a scenario, Eq. 5.14 and 5.18 will have additional terms since the condition $g \ll 1$ is not satisfied. This assumption is crucial while working with both models and is also the reason behind both of them yielding same results on off-resonance measurements.

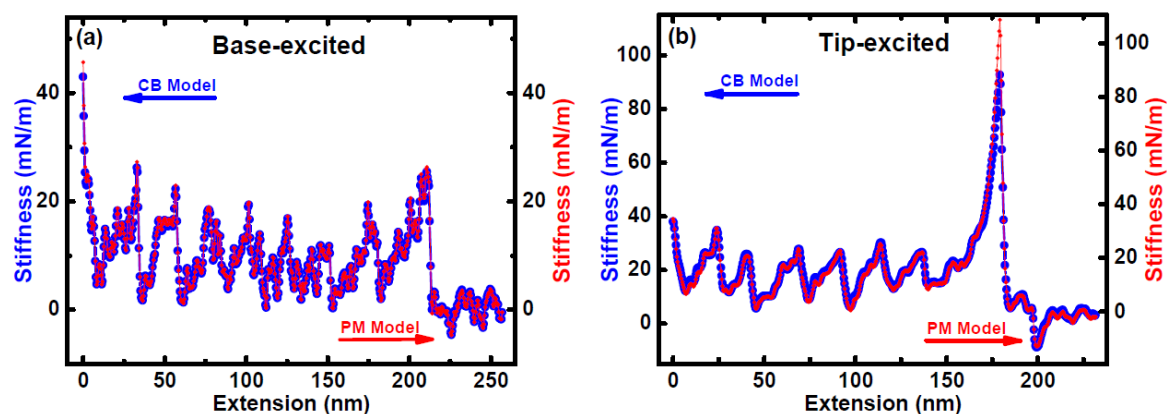


Fig. 5.8 Stiffness calculated using CB model (solid circle in blue color) and PM model (Solid diamond in red color). (a) Represents base-excited displacement measurement. (b) Represents tip-excited bending measurement.

To observe the difference in stiffness estimates using two models at high interaction force in experiment, we analyzed the data when the tip is in strong interaction with substrate resulting in high stiffness compared to stretching of molecules. It is seen that the stiffness estimated using both models coincides up to $k_i \approx 0.1k_c$. Beyond this, the stiffness estimated from PM starts deviating from CB (Fig. 5.9). It has already been stated that beyond $k_i \approx 0.1k_c$ limit, the stiffness estimates using both models will not be reliable. This is because the assumption of $k_i \ll k_c$ in derivation of both models is not valid anymore.

We compare our results with other attempts to measure stiffness of single molecules using dynamic AFM. There are many reports in the literature about measurement of dissipation in single polymer

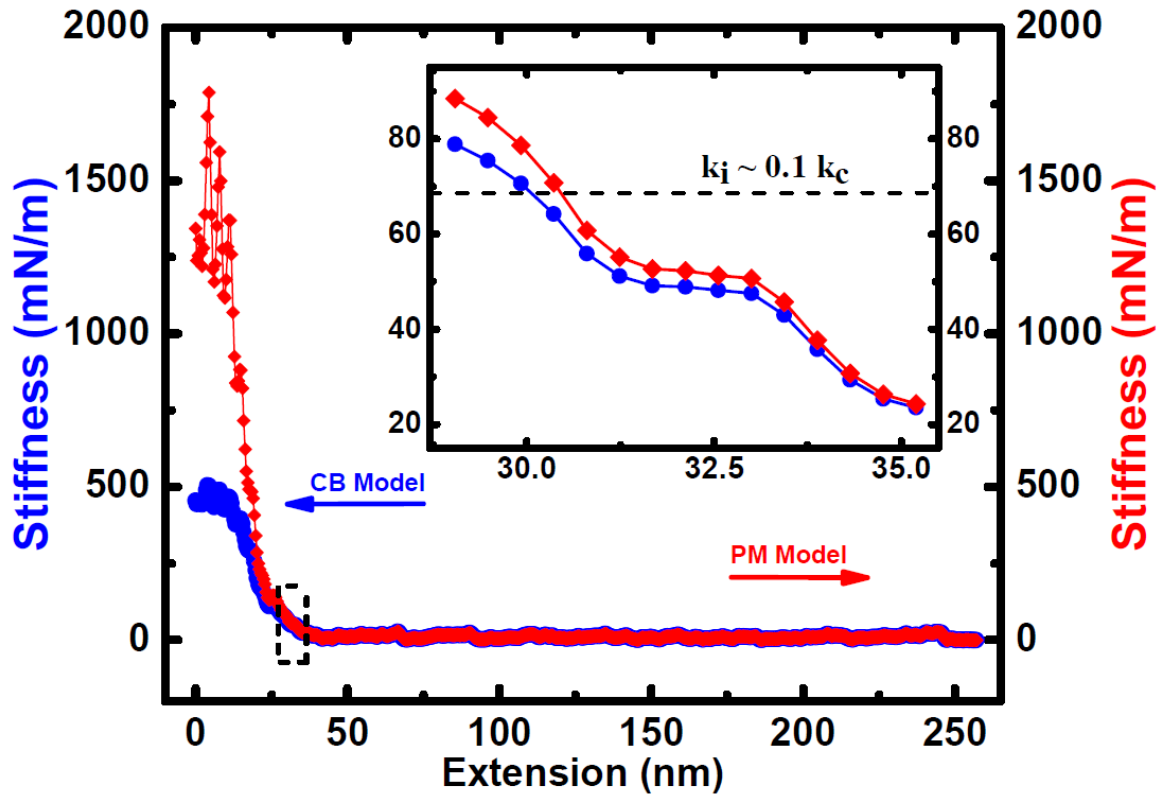


Fig. 5.9 Stiffness of tip-sample contact. interaction regime. Base-excited experiment has been performed in displacement detection system. Blue curve is stiffness estimated using CB model and red curve is using PM model. At low stiffness of the contact, both models yield similar stiffness. However, as the tip is further pressed into high stiffness region, they significantly deviate from each-other. The inset shows zoomed in part of highlighted main curve with dotted square.

chains. They have used PM model to analyse their dynamic AFM data. Recently, Benedetti et al. [7] have proposed a method to estimate viscoelasticity of single proteins using CB model (Eq. 5.10). In our previous work, we have used the same method to analyse our based-excited, deflection detection AFM measurements. It is seen in these experiments that the phase signal contains features as the poly-protein unfolds sequentially, whereas the out-of-phase Y -component of the amplitude is featureless. The use of PM model in such measurements, wherein phase is interpreted as dissipation, certainly produces artefacts. Many groups have used this strategy to report observation of dissipation in single molecules [15, 87, 109]. The phase change actually occurs due to entropic stiffness increase as the unfolded protein is stretched further. Our work has additionally highlighted the effect of extraneous phase contributing to artefacts even to the Y -component when deflection detection scheme is used to measure the cantilever bending at the tip-end. There are many sources of extraneous phase contributions and they are almost intractable in experiments. This clearly indicates that it is extremely

difficult to perform based-excited, deflection detection AFM measurements to estimate error-free viscoelastic response of nano-scale entities in liquid environments.

It is important to note that in a typical commercial AFM the off-resonance measurements are difficult to perform. The cantilever bending at the tip end is negligibly small compared the displacement when the base is excited [49, 140, 146]. In order to perform true off-resonance measurements with based excited cantilevers, one needs to measure displacement which is only possible with interferometer detection schemes set-up for this purpose. As shown in this work, the tip excitation coupled with deflection detection is another strategy to perform true off-resonance AFM measurements with simple PM model to analyse the data.

Furthermore, one may not get such an agreement between application of CB and PM models on base-excited experiments performed with deflection-detection based AFMs, as the base amplitude is not directly measured. One has to rely on indirect ways to estimate this parameter [34, 76]. This may introduce significant errors in final results. One can use the deflection detection based AFMs to perform small-amplitude and off-resonance measurements reliably when the cantilever-tip is directly excited. It can be done in various ways such as magnetic [133] or thermal excitation [47, 144].

In Fig. 5.6, Y and θ signals do not show any change while the molecule stretched. This has already been reported earlier and it has been concluded that the dissipation in single molecule is below the detection limit of AFM [146]. On the other hand, the dissipation in the confined molecular layers of liquid is observed in the past with clear features in the phase signal [92, 141, 146]. The dissipation of confined molecular layers analyzed using both CB and PM models yield the same profiles (data not shown). This implies that PM model is adequate to predict accurate viscoelasticity of nano-scale systems if care is taken while performing the experiments. The measurements performed using small amplitude interferometer-based AFM which are analysed with PM model on nanoconfined molecular layers [92, 141] are accurate estimates of its viscoelasticity.

5.6 Conclusion

We have performed base-excited dynamic atomic force microscopy on a single titin I27₈ molecule using a fiber-interferometer based home-built AFM as well as using a conventional AFM equipped with elaborate tip-excitation scheme. In our experiments, we strictly adhere to fulfilling three important criterion so that approximations used to obtain meaningful expressions using both CB and PM models are valid. These criterion are 1) truly off-resonance operation, 2) small oscillation amplitudes so that the measurements are linear, and 3) cantilevers with many orders of magnitude stiffer than the interaction stiffness. It is shown that when care is taken to fulfill these criterion while performing experiments, both the continuous-beam (CB) and the point-mass (PM) treatment yield same results. It also confirms the past estimates of stiffness and dissipation of molecular layers of liquids using interferometer based AFM are accurate. In conclusion, the PM model is adequate to explain the cantilever-molecule system and can be reliably used to extract the viscoelasticity of

nano-scale interactions given that experiments are performed at truly off-resonance regime and all the assumptions taken in modeling the cantilever dynamics are fulfilled in the experiments.

Chapter 6

Probing the folded protein domain response in dynamic atomic force microscopy

6.1 Introduction

Dynamic atomic force microscopy (dAFM) is recognised as a powerful tool to study viscoelasticity of polymers such as proteins, polyethylene glycol (PEG), polysaccharides [7, 77, 87, 89, 109, 146]. Amplitude-modulation atomic force microscopy (AM-AFM) is one of the popular dAFM technique which have been used to extract elasticity (stiffness) and viscosity (dissipation) of single protein molecules [7, 77, 87, 146].

In typical AM-AFM experiments, a dilute solution of (poly)protein is dropcasted on a freshly gold coated glass coverslip which is fixed in a liquid cell and incubated for 30 minutes which allows proteins to get absorbed on the surface from its one end. It is then rinsed with PBS (pH-7.4) to remove the unbounded or loosely bounded molecules. Liquid cell is filled with sufficient amount of buffer. An oscillating AFM cantilever with a fixed frequency is approached to the surface and cantilever-tip is allowed to attach with the another free end of the protein via a purely nonspecific interaction. Now cantilever is pulled with a constant speed which unfolds the protein domain (one domain at a time) followed by further stretching the unfolded chain and change in observable parameters (amplitude and phase) is recorded. These parameters are utilized to extract protein's elasticity and damping coefficient of the molecule.

Past AM-AFM studies on proteins state that the measured response (change in observable parameters) is mainly due to the unfolded chain and hence, the estimated viscoelasticity is of unfolded chain [7, 77, 146]. Kawakami et al. observed reduction in the unfolding force of folded domains and inferred that the response could be combination of unfolded chain as well as the folded domains, however, they do not provide any experimental/theoretical support to their hypothesis [87].

In this chapter, we will show some preliminary data which indicates that dAFM experiments can be utilized to probe the folded protein's response in certain conditions. We have performed base-excited AM-AFM experiment on single polyprotein titin I27₈ in our home-built (interferometer-based) AFM. Unfolding experiment was repeated at different oscillation amplitudes, however, the excitation frequency was kept fixed. Data were analysed using point-mass (PM) model. We observed that the peak stiffness and local stiffness (when chain is pulled from unfolded to stretched state) values reduce when oscillation amplitude exceeds a critical value. To understand the local stiffness reduction behaviour, we solve the equation of motion of oscillating cantilever under influence of WLC force and the stiffness is estimated using point-mass model which predict increase in the chain stiffness when amplitude is increased. To understand reduction in peak stiffness, we performed unfolding experiment and found that unfolding force reduces with increase in amplitude which indicates the correlation of folded domain mechanical stability and oscillation amplitude. On the basis of experimental observations and numerical solution, we infer that at high oscillation amplitude, measured response (amplitude and phase) and hence the estimated viscoelasticity is combination of both folded domain and unfolded chain.

Interestingly, discernible variation in dissipation signal was observed when single protein molecule was unfolded. This signal appeared when drive amplitude is larger than a critical value and peak stiffness reduces, so the observed dissipation signal can be attributed to the internal friction of the folded protein molecule.

In this chapter, preliminary data has been shown along with the discussion where we have tried establishing the fact that AM-AFM can probe folded protein's viscoelastic response under certain conditions. Further investigation is required to make a concrete claim on our experimental observations.

6.2 Materials and Methods

Sample preparation, experimental conditions, and data analysis were similar to that have been discussed previous chapters. Experiments were performed in our home-built interferometer based AFM.

6.3 Discussion

6.3.1 Base-excited, displacement measurement

We performed base-excited, displacement measurement to at low frequency (433 *Hz*) at different drive amplitudes. It was observed that the peak stiffness reduces when drive amplitude exceeds a certain value. Only the stiffness signal was discernibly observed when the oscillation amplitude was small

and frequency was varied from 100 Hz to 3000 Hz . Interestingly, we observed *dissipation-signal* from the protein molecule at high excitation amplitude ($> 8.5 \text{ \AA}_{p-p}$) and frequency ($> 2000 \text{ Hz}$).

6.3.1.1 Small frequency measurement

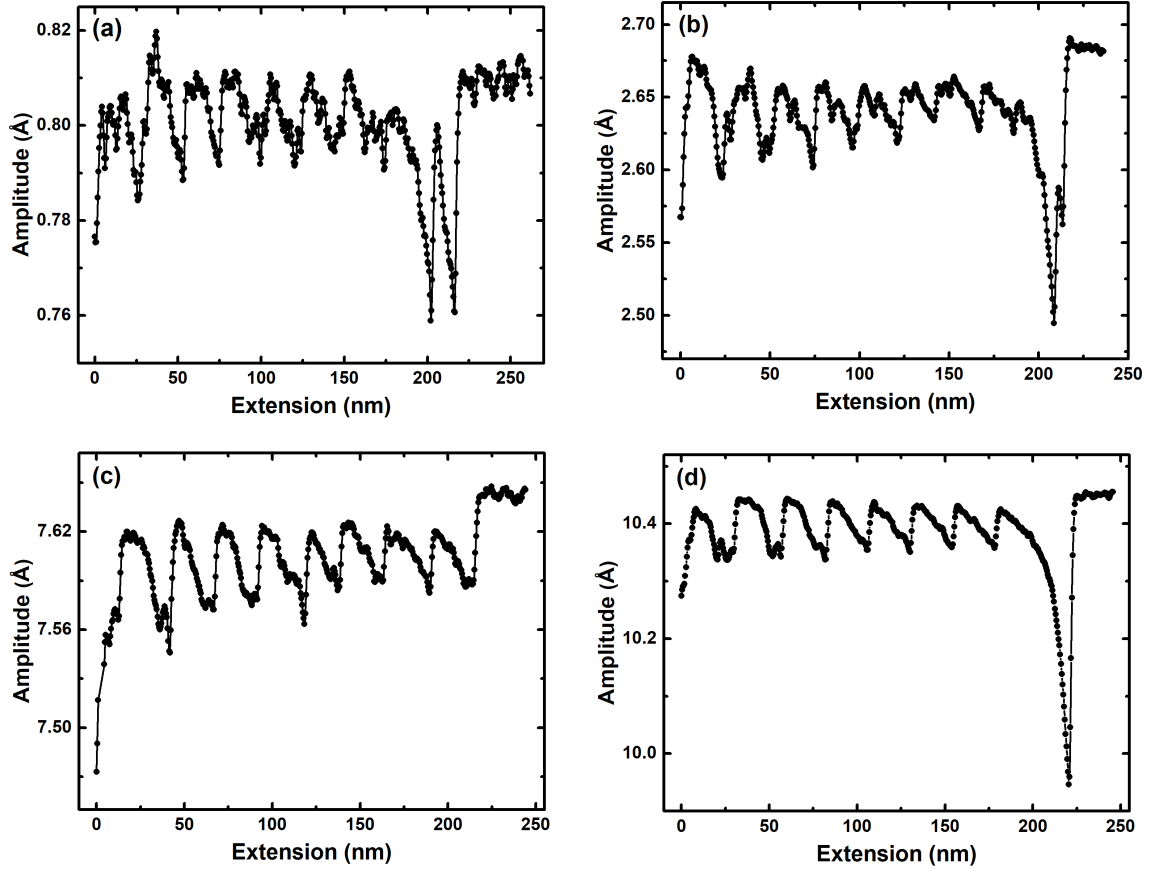


Fig. 6.1 Few representative tip-displacement-amplitude vs extension curves at different drive amplitudes. Experiments were performed at small frequency (433 Hz). For higher drives, the fractional change in tip-amplitude during protein extension is lower which indicates reduction in the stiffness.

We performed small frequency (433 Hz) measurements with varying drive amplitudes. Fig. 6.1 shows few representative amplitude-extension curves at different drive amplitudes. The experiments were performed at a fixed frequency (433 Hz). It is important to ensure that the frequency-response of the cantilever is free from spurious peaks and flat at lower frequency regime. This confirmation avoids the possibilities of presence of artifacts in the measurement [146]. The data in Fig. 6.1 was analysed using SHO model to extract the stiffness-vs-distance profile [92, 141]:

$$k_i = k_c \left(\frac{A \cos \theta}{R} - 1 \right) \quad (6.1)$$

The derivation of Eq. 6.1 assumes the interaction force to be linear over the complete oscillation cycle ($F_i = k_i z$). Where k_i is the stiffness of the molecule and z is the instantaneous position of the cantilever-tip. Here we have focused our discussion only on the elastic interaction forces as the dissipation force contribution from the unfolded chain is negligibly small and the interaction is dominated by the elastic forces [146]. The current discussion will be unaffected even if the dissipation forces will be taken into account. In Eq. 6.1, k_c is cantilever stiffness, A is the amplitude of the cantilever base. For off-resonance operation, it is same as the cantilever-tip amplitude in absence of the interaction [146], θ is the phase difference between the drive signal and cantilever-tip, R is the instantaneous amplitude. For truly off-resonance operation, the phase signal is expected to be ~ 0 deg [146] which we observed in our experiments. In our previous study, we have shown that the phase signal does not vary during the experiment which lead us to conclude that the dissipation in the single unfolded molecule (I27₈) is below the detection limit of AFM. In another piece of work we have shown that at truly off-resonance operation, the continuous-beam model [7, 146] and point-mass model (Eq. 6.1) predict same results when the displacement signal were recorded (refer *chapter-5*). This is true even for the higher amplitude chosen for the current experiments. We have chosen the point-mass model for the analysis and discussion because of its simplicity compared to the continuous-beam model.

Fig. 6.2 shows the peak stiffness with oscillation amplitude which was estimated from the experimental data (few representative data shown in Fig. 6.1). The data is analysed using Eq. 6.1. Each data point is achieved by averaging more than 25 events. The stiffness shows a significant reduction after a critical value of oscillation amplitude which is $\sim 3 \text{ \AA}_{rms}$ (or $\sim 8.5 \text{ \AA}_{p-p}$). This reduction is not only in the peak stiffness but appeared throughout the stretching the molecule from unfolded to stretched state.

6.3.1.2 Numerical solution of cantilever dynamics with experiencing a WLC force

In order to understand the experimentally observed reduction in the stiffness, we numerically solved the equation for the oscillating cantilever-tip experiencing a WLC-force using MATLAB. Since, the force due to unfolded I27₈ is dominated by the elastic contribution, the dissipative contribution has been ignored [146]. The equation can be written as:

$$k_c z = k_c A \cos(\omega t) - F_{WLC} \quad (6.2)$$

Where $F_{WLC} = \frac{K_b T}{l_p} \left[\frac{1}{4} \left(1 - \frac{z}{L_0} \right)^{-2} + \frac{z}{L_0} - \frac{1}{4} \right]$. Eq. 6.2 is solved for cantilever displacement (z). We considered $k_c = 1 \text{ N/m}$, drive frequency = 500 Hz , persistence-length (l_p) = 4 \AA , and contour-length (L_0) = 28 nm . The solutions were substituted into Eq. 6.1 to get the stiffness profiles for different drive-amplitudes.

Fig. 6.3 shows the stiffness-extension, calculated for different oscillation amplitudes, by substituting the solution of Eq. 6.2 into Eq. 6.1. Open circles in black represent the static stiffness (derivative

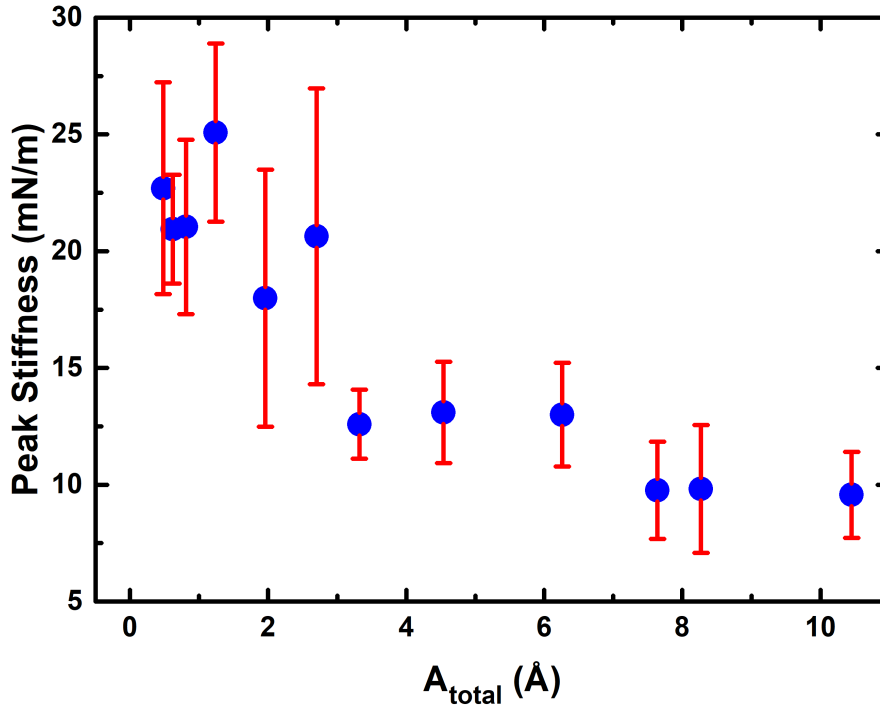


Fig. 6.2 Peak stiffness with total displacement amplitude (in *rms*). Stiffness is consistent for the oscillation amplitude upto $\sim 3 \text{ Å}_{rms}$ and it shows transition afterwards. It reduces further with the oscillation amplitude. We attribute the $\sim 3 \text{ Å}_{rms}$ as the characteristic length for the I27₈ in AM-AFM experiments.

of WLC-force). The stiffness estimated for small oscillation amplitudes reconstructs the static chain stiffness given by WLC model, however the stiffness-extension profiles deviate significantly from the actual WLC behavior for higher amplitudes. In general, the higher drive amplitudes produce an artefact since the extension is not modulated by an amplitude over which the WLC stiffness can not be treated as linear. This is a critical assumption in using Eq. 6.1 for estimating stiffness from experimental data. This artefact tends to overestimate the stiffness of the unfolded chain. See Fig. 6.4. For amplitudes below 1 Å , the stiffness of WLC is accurately reproduced by Eq. 6.1. At 5 Å , there is an overestimate by ~ 300 . This overestimate, as expected is less for smaller extensions where WLC predicts that the force does not change rapidly with extension. The above-mentioned discussion leads us to conclude that the reduction in stiffness at higher drive amplitudes seen in experiment is not an artefact due to violation of linearity condition implicit in deriving Eq. 6.1. It can be safely argued that exciting the the protein mechanically alters its state and affects the data. Since at higher extensions the mechanical perturbation from the cantilever reach the folded domains of the polypeptide, we argue here that it is likely excites certain modes of the folded domains and softens it mechanically. Such

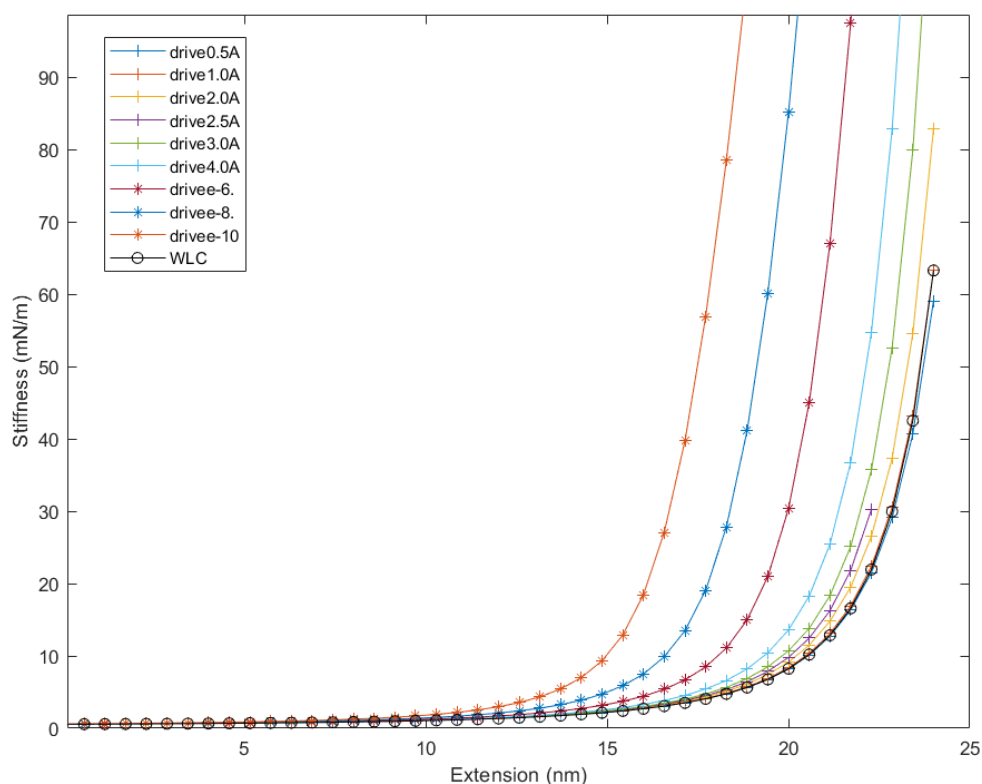


Fig. 6.3 Stiffness estimated by substituting the solution of Eq. 6.2 into Eq. 6.1. Small amplitude oscillation stiffness overlaps with the static stiffness (black circles), whereas a significant deviation can be observed for higher amplitudes. For low stretch, all amplitude results are predicting similar values which is expected as the steepness of the WLC force at lower stretch nearly linear. The lower oscillation amplitude predictions strongly support our experimental observations.

soft domains will now contribute to the measurement and start to affect the cantilever response. To ascertain these claims we perform experiments in which we measure the unfolding forces of domains while the cantilever is excited with similar amplitudes.

This indicates that the lower estimated stiffness in the experiment is not solely due to chain but there is contribution from other element. This element could be the folded protein domain(s) connected in series with the unfolded chain.

6.3.1.3 Unfolding force with drive amplitude

We performed unfolding experiment of I27₈ on commercial (slope-detection) AFM to determine the unfolding force of folded domains when cantilever is oscillated at different amplitudes. Fig. 6.5 shows the average unfolding force reduces with increase in tip amplitude. This is a direct measurement

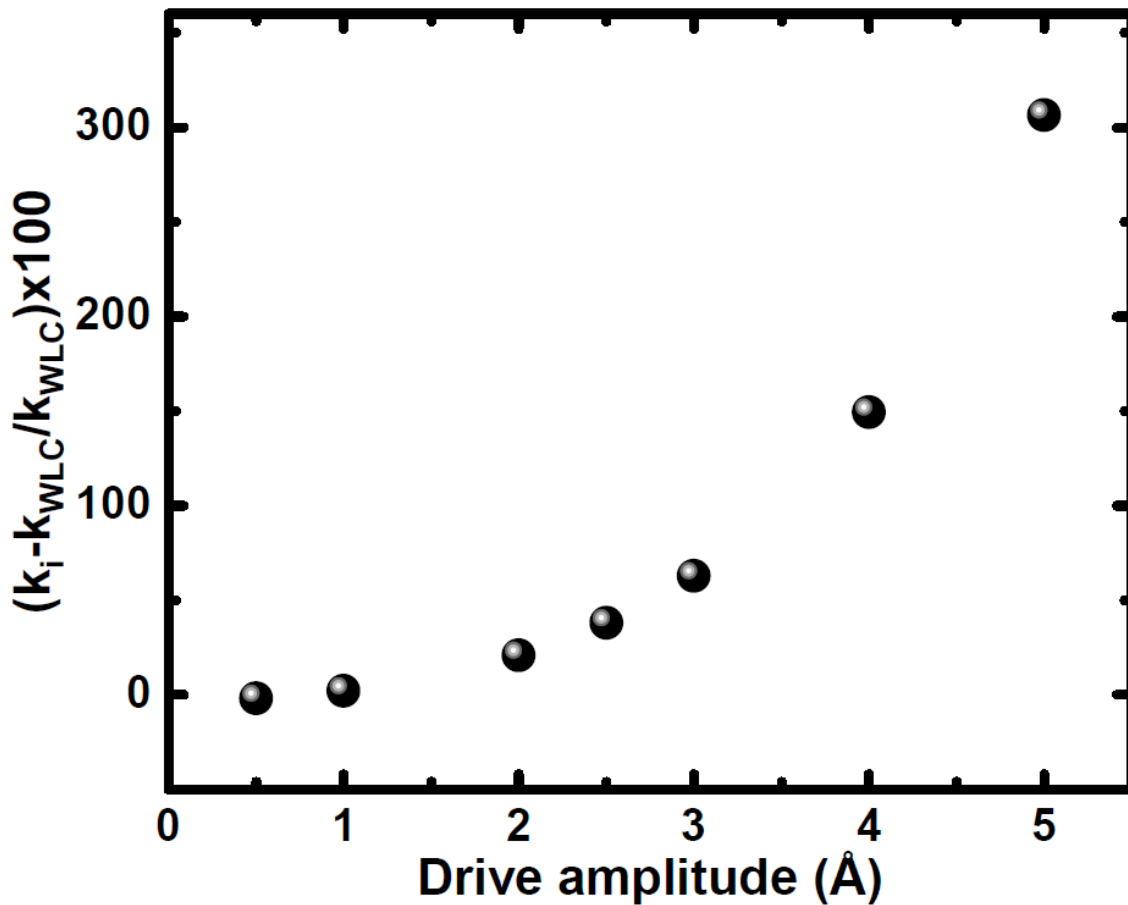


Fig. 6.4 Percentage change in polymer stiffness with drive amplitude. Below 1 Å drive amplitude, WLC stiffness is reproduced well by estimated stiffness from Eq. 6.1 and above that a significant deviation can be observed.

of softening of the folded domains with increase in amplitude. Drive amplitude (tip amplitude) is presented in volts which can be converted in unit of nanometers which needs calibration of piezo used to drive the cantilever base.

6.3.2 High frequency and high amplitude measurement

We performed measurements with high frequency and high amplitude. Interestingly, discernible Y and phase signal were observed when single protein molecule was unfolded. Fig. 6.6 represents raw data of unfolding of single I27₈ molecule. Clear variation in Y signal and phase signal can be observed in Fig. 6.6 (a) and (b) respectively. Since, dissipation signal appears when drive amplitude is larger than a critical value and peak stiffness reduces, the observed dissipation signal can be attributed to the internal friction of the folded protein molecule. Signal to noise ratio can be improved by performing measurements with higher amplitudes, say $\sim 10 \text{ \AA}_p$.

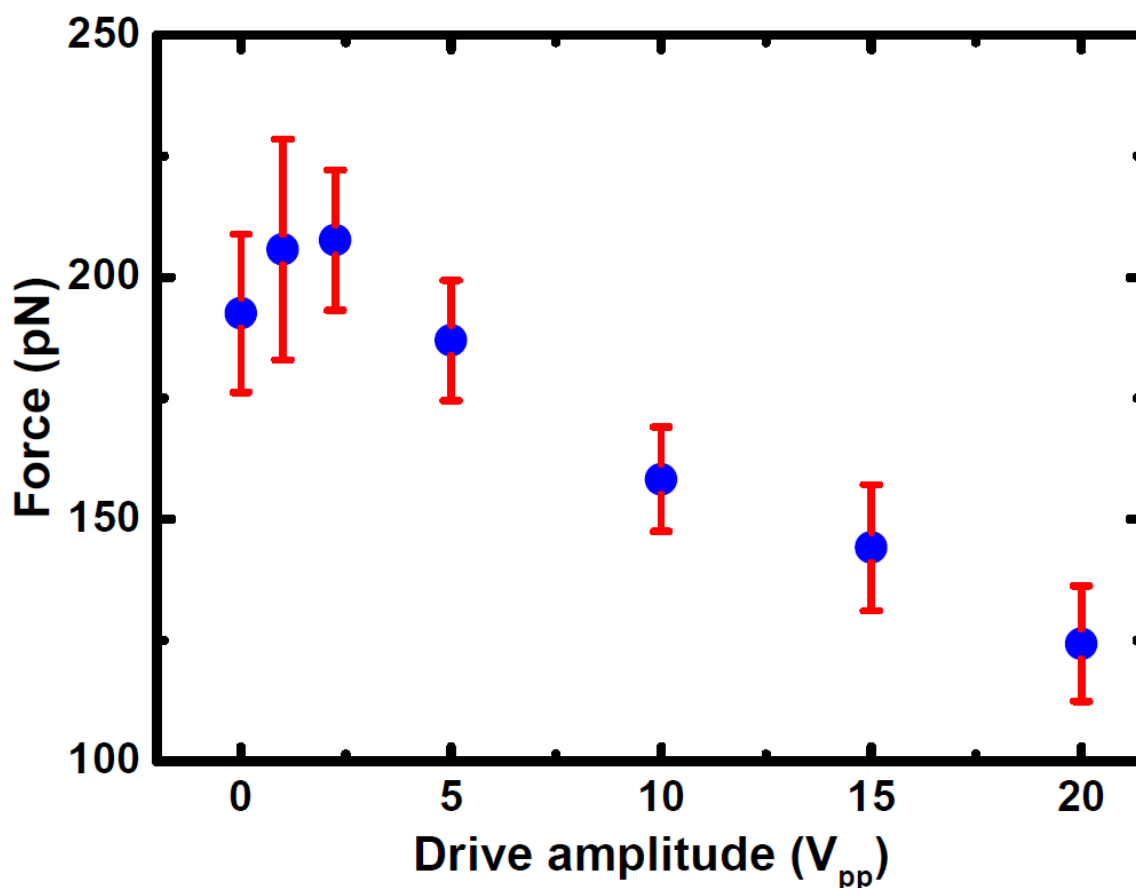


Fig. 6.5 Representing the peak force (unfolding force) with drive amplitude. Drive amplitude is presented in volts which can be converted into nanometers by calibrating the dither piezo used to drive the cantilever base. Unfolding force of folded domains reduces with increase in the tip amplitude. This indicates softening of folded domains with increase in tip amplitude.

6.4 Conclusion

Our experimental observations suggest that the unfolding force is correlated with the tip amplitude in dynamic atomic force spectroscopy experiments. In small frequency measurements, the reduction in local as well as peak stiffness was observed when drive amplitude exceeded a critical value. Estimated stiffness using the numerical solution of oscillating cantilever under influence of WLC force predicts increase in local stiffness with increase in tip amplitude. This prediction is opposite to our experimental observation which suggests that there is additional contribution in estimated stiffness. This could come from the folded domains which are attached in series with the unfolded chain. Reduction in unfolding force with increase in tip amplitude supports our hypothesis. On the basis of experimental observations and numerical solution, we infer that at high oscillation amplitude folded protein domains soften and measured response (amplitude and phase) and hence the estimated viscoelasticity is combination of both folded domain and unfolded chain. Interestingly, clear

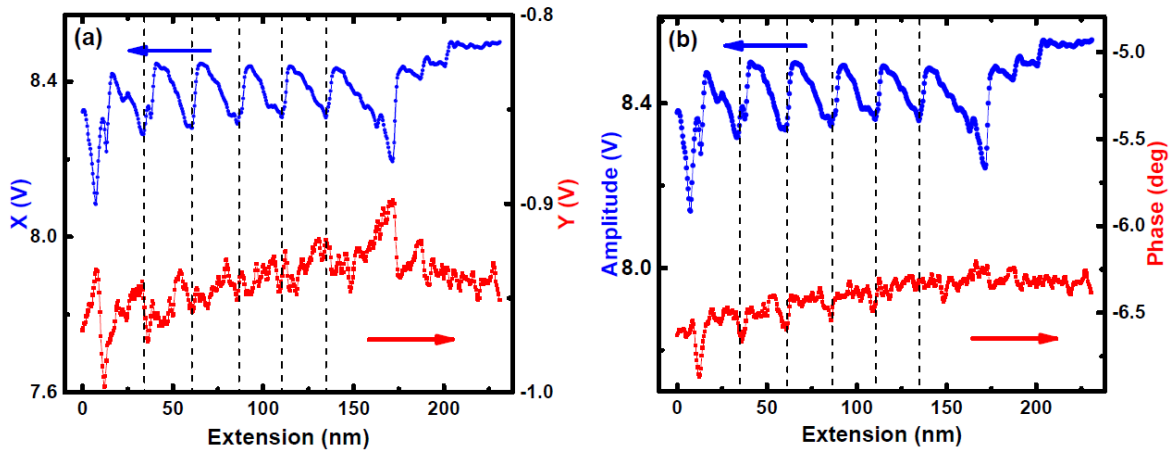


Fig. 6.6 Raw data of unfolding of I27₈ molecule at high frequency (2633 Hz) and high amplitude (~ 5.4 Å). (a) X and Y signals in blue solid circle and red solid square respectively. (b) Amplitude and phase signals in blue solid circle and red solid square respectively. Variation in Y and phase signal can be observed corresponding to every unfolding peaks. This signature is more prominent in initial unfolding events.

dissipation signal was observed when high frequency measurements were performed. The dissipation signal was observed when drive amplitude exceeded from a critical value and peak stiffness reduced which indicates that the observed dissipation is nothing but the internal friction of folded protein domain. We are investigating our observation in detail to make a concrete claim.

Chapter 7

Conclusion and future possibilities

7.1 Conclusion

This thesis is mainly focused to develop a methodology to determine the viscoelasticity of nanoscale systems using the dynamic atomic force microscopy (dAFM). Single biomolecules such as proteins, PEG, and Polysaccharides and nano-confined liquids such as water, ionic liquids, and Octamethylcyclotetrasiloxane (OMCTS) have been extensively studied in the past using dAFM method. We have done a comprehensive study on dAFM (amplitude-modulation atomic force microscopy- AM-AFM) method of extracting viscoelasticity of nanoscale systems and investigated the viscoelasticity of *titin I27₈* protein molecule. We found that, in AM-AFM method, there are various sources which can affect the final results by introducing serious errors and artefacts and these are likely to be present in conventional way of performing these measurements and data analysis. We reported various possibilities of appearing artefact (and errors) and also proposed appropriate methodology to overcome this issue.

For this study, we have used two types of AFMs- slope detection based (commercial) and displacement detection based (interferometer based home-built) AFM. Two types of cantilever excitation mechanisms have been used- acoustic excitation (cantilever-base is excited using dither piezo) and magnetic excitation (cantilever-tip is excited using the magnetic excitation). Experiments were performed using stiff cantilevers excited at truly off-resonance frequency with small-amplitudes. Data has been analyzed using two mathematical models- continuous-beam (CB) and point-mass (PM) model. The experiments performed using different AFMs and using different cantilever excitation schemes and data analyzed using different models have been compared. An unified understanding has been tried building up to understand the dynamic AFM measurements and their outcomes. This is applicable not only in context of single-molecules but for all the nano-scale systems which viscoelasticity can be probed using this technique.

Following conclusions can be drawn from this work:

1. **Quantification of single protein viscoelasticity:** In AM-AFM measurements, a list of factors can

introduce artefacts in final results. First is offset in initial phase which can appear due to various reasons such as presence of spurious peaks in cantilever response near the operation frequency, electronic offset, and design of fluid cell etc. Second reason can be inappropriate choice of operation frequency and analytical model used for data analysis. Offset in the initial phase could be identified by: at off resonance regime, observing 180 deg deep contact response in slope-detection and zero initial phase in displacement detection system. Operation at true off-resonance frequency regime and use of continuous-beam model avoids the probability of artefact arising due to second reason.

Experiments performed on I27₈ by confirming the absence of above discussed reasons of artefact states that the dissipation on the unfolded protein molecule is below the detection limit. The estimated upper bound of unfolded chain damping coefficient is $\sim 5 \times 10^{-7} \text{ kg/s}$. The stiffness of unfolded chain varies from 0 to 20 mN/m when stretched from coiled to extended state. It was also found that displacement-detection is better suited for such measurements when base excitation scheme is used.

2. Validity of point-mass model: In derivation of point-mass (PM) model, the continuum cantilever beam is assumed as a point-mass which makes its derivation simple and the interpretation very easy. Recently, it was proposed that the PM model is not adequate to extract interaction viscoelasticity and a continuous-beam (CB) model was proposed which takes the continuum nature of the beam into account that require to solve a complex Euler-Bernouli equation of motion and it is relatively complicated to understand.

We found that the simple minded point-mass model is adequate to extract accurate viscoelasticity of system under investigation. It predicts same results as the CB model when the cantilever is used and experiment is performed at truly off-resonance regime. These experiments are possible only in displacement-detection and not in slope-detection.

3. Magnetic (or tip)-excited AM-AFM: Coating a thin layer of cobalt near the tip-position allows us to oscillate the cantilever tip directly with the help of an electromagnet. We found that, this mechanism of excitation eliminates major possibilities of appearing artefacts in the measurements. Using this method, one can perform true off-resonance measurements in slope-detection based AFMs. Also the PM model predicts similar results as the continuous-beam model when cantilever is oscillated at truly off-resonance regime. This method is an alternative of the displacement-detection. This method opens up a window for the commercial AFM users interested in measuring the viscoelasticity of the nanoscale interactions in the liquid environment.

4. Probing the folded protein response in AM-AFM measurements: We observed that the stiffness of the unfolded protein (chain) reduces when the oscillation tip amplitude exceeds a critical value which is $\sim 6 \text{ \AA}_{pp}$ for I27. Numerical solution of equation of motion for oscillating cantilever-chain system suggests that the measured response is not just from the unfolded chain but there is additional contributing element. The force measurement showed that the unfolding force of folded domains reduces with increase in oscillation amplitude. This is indication of softening of the folded domains over the oscillatory perturbation which allows it to significantly contribute in measurement. Further investigation is required to make a conclusion.

7.2 Future possibilities:

This work can be extended to extract more information of the mechanical properties at the nano-scale in various fields such as the protein-protein interaction, protein-membrane interaction, confined liquids etc.

In the past, the magnetic excitation based method has been used to study the single-molecule viscoelasticity. The experiments were performed using two types of cantilevers. (1) Commercially available cantilevers- the whole cantilever (backside) is coated with magnetic material. In this case, drive force acts on whole cantilever, however, the mathematical models assume the driving force only at the tip position. (2) A piece magnetic particle glued at the tip position (on backside). The particle has a significant mass which can alter the dynamics of the cantilever. In mathematical models, this mass is usually ignored. In our work, we have proposed a way to coat a thin film of magnetic material near the tip position. We achieved enough deflection on the cantilever by coating $\sim 25 - 30\text{nm}$ cobalt. The mass of this thin layer is negligibly small compared to the cantilever mass and actually can be ignored. This actually fulfills the assumption of ignoring mass of the magnetic material and the existing mathematical models can be used for data analysis. We got high success rate of stable coating for air and water medium, however, it is low for the buffer medium. Further efforts will improve the success rate.

As we have experimental observations which suggest that the dynamics of folded protein can also be probed using AM-AFM experiments. It can be extended to study the rheology of the folded proteins. Shape (curvature) of the free energy landscape of folded state is directly related to the stiffness. Measuring the dynamic response of the folded protein will be helpful in understanding its dynamic behaviour and function. More information of the energy landscape of protein folding/unfolding can be extracted.

References

- [1] Abascal, F. and Zardoya, R. (2012). Lrrc8 proteins share a common ancestor with pannexins, and may form hexameric channels involved in cell-cell communication. *Bioessays*, 34(7):551–560.
- [2] Alexander, S., Hellemans, L., Marti, O., Schneir, J., Elings, V., Hansma, P. K., Longmire, M., and Gurley, J. (1989). An atomic-resolution atomic-force microscope implemented using an optical lever. *Journal of applied physics*, 65(1):164–167.
- [3] Anczykowski, B., Gotsmann, B., Fuchs, H., Cleveland, J., and Elings, V. (1999). How to measure energy dissipation in dynamic mode atomic force microscopy. *Applied Surface Science*, 140(3-4):376–382.
- [4] Arpin, M., Chirivino, D., Naba, A., and Zwaenepoel, I. (2011). Emerging role for erm proteins in cell adhesion and migration. *Cell adhesion & migration*, 5(2):199–206.
- [5] Ashkin, A., Dziedzic, J. M., Bjorkholm, J. E., and Chu, S. (1986). Observation of a single-beam gradient force optical trap for dielectric particles. *Optics letters*, 11(5):288–290.
- [6] Bausch, A. R., Möller, W., and Sackmann, E. (1999). Measurement of local viscoelasticity and forces in living cells by magnetic tweezers. *Biophysical journal*, 76(1):573–579.
- [7] Benedetti, F., Gazizova, Y., Kulik, A. J., Marszalek, P. E., Klinov, D. V., Dietler, G., and Sekatskii, S. K. (2016). Can dissipative properties of single molecules be extracted from a force spectroscopy experiment? *Biophysical journal*, 111(6):1163–1172.
- [8] Bennion, B. J. and Daggett, V. (2003). The molecular basis for the chemical denaturation of proteins by urea. *Proceedings of the National Academy of Sciences*, 100(9):5142–5147.
- [9] Best, R. B., Fowler, S. B., Herrera, J. L. T., Steward, A., Paci, E., and Clarke, J. (2003). Mechanical unfolding of a titin ig domain: structure of transition state revealed by combining atomic force microscopy, protein engineering and molecular dynamics simulations. *Journal of molecular biology*, 330(4):867–877.
- [10] Best, R. B., Li, B., Steward, A., Daggett, V., and Clarke, J. (2001). Can non-mechanical proteins withstand force? stretching barnase by atomic force microscopy and molecular dynamics simulation. *Biophysical journal*, 81(4):2344–2356.
- [11] Bilsel, O., Kayatekin, C., Wallace, L. A., and Matthews, C. R. (2005). A microchannel solution mixer for studying microsecond protein folding reactions. *Review of scientific instruments*, 76(1):014302.
- [12] Binnig, G., Gerber, C., Stoll, E., Albrecht, T., and Quate, C. (1987). Atomic resolution with atomic force microscope. *EPL (Europhysics Letters)*, 3(12):1281.

- [13] Binnig, G., Quate, C. F., and Gerber, C. (1986). Atomic force microscope. *Physical review letters*, 56(9):930.
- [14] Binnig, G., Rohrer, H., Gerber, C., and Weibel, E. (1982). Surface studies by scanning tunneling microscopy. *Physical review letters*, 49(1):57.
- [15] Bippes, C. A., Humphris, A. D., Stark, M., Müller, D. J., and Janovjak, H. (2006). Direct measurement of single-molecule visco-elasticity in atomic force microscope force-extension experiments. *European Biophysics Journal*, 35(3):287–292.
- [16] Borgia, A., Williams, P. M., and Clarke, J. (2008). Single-molecule studies of protein folding. *Annu. Rev. Biochem.*, 77:101–125.
- [17] Brand, L. and Witholt, B. (1967). [87] fluorescence measurements. In *Methods in Enzymology*, volume 11, pages 776–856. Elsevier.
- [18] Bridgman, P. (1914). The coagulation of albumen by pressure. *Journal of Biological Chemistry*, 19(4):511–512.
- [19] Brockwell, D. J., Beddard, G. S., Paci, E., West, D. K., Olmsted, P. D., Smith, D. A., and Radford, S. E. (2005). Mechanically unfolding the small, topologically simple protein I. *Biophysical journal*, 89(1):506–519.
- [20] Bucciantini, M., Giannoni, E., Chiti, F., Baroni, F., Formigli, L., Zurdo, J., Taddei, N., Ramponi, G., Dobson, C. M., and Stefani, M. (2002). Inherent toxicity of aggregates implies a common mechanism for protein misfolding diseases. *nature*, 416(6880):507–511.
- [21] Bustamante, C., Alexander, L., Maciuba, K., and Kaiser, C. M. (2020). Single-molecule studies of protein folding with optical tweezers. *Annual review of biochemistry*, 89:443–470.
- [22] Butt, H.-J. and Jaschke, M. (1995). Calculation of thermal noise in atomic force microscopy. *Nanotechnology*, 6(1):1.
- [23] Cecconi, C., Shank, E. A., Bustamante, C., and Marqusee, S. (2005). Direct observation of the three-state folding of a single protein molecule. *Science*, 309(5743):2057–2060.
- [24] Chase, J. W. and Williams, K. R. (1986). Single-stranded dna binding proteins required for dna replication. *Annual review of biochemistry*, 55(1):103–136.
- [25] Chaudhuri, T. K. and Paul, S. (2006). Protein-misfolding diseases and chaperone-based therapeutic approaches. *The FEBS journal*, 273(7):1331–1349.
- [26] Chen, H., Fu, H., Zhu, X., Cong, P., Nakamura, F., and Yan, J. (2011). Improved high-force magnetic tweezers for stretching and refolding of proteins and short dna. *Biophysical journal*, 100(2):517–523.
- [27] Chon, J. W., Mulvaney, P., and Sader, J. E. (2000). Experimental validation of theoretical models for the frequency response of atomic force microscope cantilever beams immersed in fluids. *Journal of applied physics*, 87(8):3978–3988.
- [28] Chtcheglova, L. A., Shubeita, G. T., Sekatskii, S. K., and Dietler, G. (2004). Force spectroscopy with a small dithering of afm tip: a method of direct and continuous measurement of the spring constant of single molecules and molecular complexes. *Biophysical journal*, 86(2):1177–1184.

- [29] Chung, H. S. and Eaton, W. A. (2018). Protein folding transition path times from single molecule fret. *Current opinion in structural biology*, 48:30–39.
- [30] Chyan, C.-L., Lin, F.-C., Peng, H., Yuan, J.-M., Chang, C.-H., Lin, S.-H., and Yang, G. (2004). Reversible mechanical unfolding of single ubiquitin molecules. *Biophysical journal*, 87(6):3995–4006.
- [31] Cleveland, J., Anczykowski, B., Schmid, A., and Elings, V. (1998). Energy dissipation in tapping-mode atomic force microscopy. *Applied Physics Letters*, 72(20):2613–2615.
- [32] Crick, F. H. (1958). On protein synthesis. In *Symp Soc Exp Biol*, volume 12, page 8.
- [33] Day, R., Bennion, B. J., Ham, S., and Daggett, V. (2002). Increasing temperature accelerates protein unfolding without changing the pathway of unfolding. *Journal of molecular biology*, 322(1):189–203.
- [34] De Beer, S., Van den Ende, D., and Mugele, F. (2010). Dissipation and oscillatory solvation forces in confined liquids studied by small-amplitude atomic force spectroscopy. *Nanotechnology*, 21(32):325703.
- [35] De Vlaminck, I. and Dekker, C. (2012). Recent advances in magnetic tweezers. *Annual review of biophysics*, 41:453–472.
- [36] Dobson, C. M. (2002). Protein-misfolding diseases: Getting out of shape. *Nature*, 418(6899):729–730.
- [37] Donovan, J. W. (1973). [21] ultraviolet difference spectroscopy—new techniques and applications. In *Methods in Enzymology*, volume 27, pages 497–525. Elsevier.
- [38] Duf r ne, Y. F. and Hinterdorfer, P. (2008). Recent progress in afm molecular recognition studies. *Pfl gers Archiv-European Journal of Physiology*, 456(1):237–245.
- [39] Elmer, F.-J. and Dreier, M. (1997). Eigenfrequencies of a rectangular atomic force microscope cantilever in a medium. *Journal of Applied Physics*, 81(12):7709–7714.
- [40] Evans, E. (2001). Probing the relation between force—lifetime—and chemistry in single molecular bonds. *Annual review of biophysics and biomolecular structure*, 30(1):105–128.
- [41] Evans, E. and Ritchie, K. (1997). Dynamic strength of molecular adhesion bonds. *Biophysical journal*, 72(4):1541–1555.
- [42] Fisher, T. E., Oberhauser, A. F., Carrion-Vazquez, M., Marszalek, P. E., and Fernandez, J. M. (1999). The study of protein mechanics with the atomic force microscope. *Trends in biochemical sciences*, 24(10):379–384.
- [43] Forster, T. (1948). Intermolecular energy transfer and fluorescence. *Ann. Phys. Leipzig.*, 2:55–75.
- [44] Fowler, S. B., Best, R. B., Herrera, J. L. T., Rutherford, T. J., Steward, A., Paci, E., Karplus, M., and Clarke, J. (2002). Mechanical unfolding of a titin ig domain: structure of unfolding intermediate revealed by combining afm, molecular dynamics simulations, nmr and protein engineering. *Journal of molecular biology*, 322(4):841–849.
- [45] Fowler, S. B. and Clarke, J. (2001). Mapping the folding pathway of an immunoglobulin domain: structural detail from phi value analysis and movement of the transition state. *Structure*, 9(5):355–366.

- [46] Freire, E., Schön, A., Hutchins, B. M., and Brown, R. K. (2013). Chemical denaturation as a tool in the formulation optimization of biologics. *Drug discovery today*, 18(19-20):1007–1013.
- [47] Fukuma, T. (2009). Wideband low-noise optical beam deflection sensor with photothermal excitation for liquid-environment atomic force microscopy. *Review of Scientific Instruments*, 80(2):023707.
- [48] Gao, M., Craig, D., Lequin, O., Campbell, I. D., Vogel, V., and Schulten, K. (2003). Structure and functional significance of mechanically unfolded fibronectin type iii1 intermediates. *Proceedings of the National Academy of Sciences*, 100(25):14784–14789.
- [49] García, R. (2011). *Amplitude modulation atomic force microscopy*. John Wiley & Sons.
- [50] Garcia, R. and Perez, R. (2002). Dynamic atomic force microscopy methods. *Surface science reports*, 47(6-8):197–301.
- [51] Garcia, R. and San Paulo, A. (1999). Attractive and repulsive tip-sample interaction regimes in tapping-mode atomic force microscopy. *Physical Review B*, 60(7):4961.
- [52] Gießibl, F. J. (2001). A direct method to calculate tip-sample forces from frequency shifts in frequency-modulation atomic force microscopy. *Applied Physics Letters*, 78(1):123–125.
- [53] Goldmann, W. H. and Ingber, D. E. (2002). Intact vinculin protein is required for control of cell shape, cell mechanics, and rac-dependent lamellipodia formation. *Biochemical and biophysical research communications*, 290(2):749–755.
- [54] Greene, R. F. and Pace, C. N. (1974). Urea and guanidine hydrochloride denaturation of ribonuclease, lysozyme, α -chymotrypsin, and β -lactoglobulin. *Journal of Biological Chemistry*, 249(17):5388–5393.
- [55] Haas, E., Katchalski-Katzir, E., and Steinberg, I. Z. (1978). Brownian motion of the ends of oligopeptide chains in solution as estimated by energy transfer between the chain ends. *Biopolymers: Original Research on Biomolecules*, 17(1):11–31.
- [56] Hagen, S. J., Hofrichter, J., Szabo, A., and Eaton, W. A. (1996). Diffusion-limited contact formation in unfolded cytochrome c: estimating the maximum rate of protein folding. *Proceedings of the National Academy of Sciences*, 93(21):11615–11617.
- [57] Harano, Y., Yoshidome, T., and Kinoshita, M. (2008). Molecular mechanism of pressure denaturation of proteins. *The Journal of chemical physics*, 129(14):10B607.
- [58] Hartl, F. U. (2017). Protein misfolding diseases. *Annual review of biochemistry*, 86:21–26.
- [59] He, C., Li, S., Gao, X., Xiao, A., Hu, C., Hu, X., Hu, X., and Li, H. (2019). Direct observation of the fast and robust folding of a slipknotted protein by optical tweezers. *Nanoscale*, 11(9):3945–3951.
- [60] Henley, S. A. and Dick, F. A. (2012). The retinoblastoma family of proteins and their regulatory functions in the mammalian cell division cycle. *Cell division*, 7(1):1–14.
- [61] Herczenik, E. and Gebbink, M. F. (2008). Molecular and cellular aspects of protein misfolding and disease. *The FASEB Journal*, 22(7):2115–2133.
- [62] Herruzo, E. T. and Garcia, R. (2007). Frequency response of an atomic force microscope in liquids and air: Magnetic versus acoustic excitation. *Applied Physics Letters*, 91(14):143113.

- [63] Hertzog, D. E., Ivorra, B., Mohammadi, B., Bakajin, O., and Santiago, J. G. (2006). Optimization of a microfluidic mixer for studying protein folding kinetics. *Analytical chemistry*, 78(13):4299–4306.
- [64] Hertzog, D. E., Michalet, X., Jäger, M., Kong, X., Santiago, J. G., Weiss, S., and Bakajin, O. (2004). Femtomole mixer for microsecond kinetic studies of protein folding. *Analytical chemistry*, 76(24):7169–7178.
- [65] Higgins, M. J., Sader, J. E., and Jarvis, S. P. (2006). Frequency modulation atomic force microscopy reveals individual intermediates associated with each unfolded i27 titin domain. *Biophysical journal*, 90(2):640–647.
- [66] Hinterdorfer, P. and Dufrêne, Y. F. (2006). Detection and localization of single molecular recognition events using atomic force microscopy. *Nature methods*, 3(5):347–355.
- [67] Hirokawa, N. (1998). Kinesin and dynein superfamily proteins and the mechanism of organelle transport. *Science*, 279(5350):519–526.
- [68] Hoffmann, P. M., Jeffery, S., Pethica, J. B., Özer, H. Ö., and Oral, A. (2001a). Energy dissipation in atomic force microscopy and atomic loss processes. *Physical Review Letters*, 87(26):265502.
- [69] Hoffmann, P. M., Oral, A., Grimble, R. A., Özgür Özer, H., Jeffery, S., and Pethica, J. B. (2001b). Direct measurement of interatomic force gradients using an ultra-low-amplitude atomic force microscope. *Proceedings of the Royal Society of London. Series A: Mathematical, Physical and Engineering Sciences*, 457(2009):1161–1174.
- [70] Hossain, M. M., Crish, J. F., Eckert, R. L., Lin, J. J.-C., and Jin, J.-P. (2005). h2-calponin is regulated by mechanical tension and modifies the function of actin cytoskeleton. *Journal of Biological Chemistry*, 280(51):42442–42453.
- [71] Hughes, M. L. and Dougan, L. (2016). The physics of pulling polyproteins: a review of single molecule force spectroscopy using the afm to study protein unfolding. *Reports on Progress in Physics*, 79(7):076601.
- [72] Hummer, G., Garde, S., Garcia, A. E., Paulaitis, M. E., and Pratt, L. R. (1998). The pressure dependence of hydrophobic interactions is consistent with the observed pressure denaturation of proteins. *Proceedings of the National Academy of Sciences*, 95(4):1552–1555.
- [73] Humphris, A., Tamayo, J., and Miles, M. (2000). Active quality factor control in liquids for force spectroscopy. *Langmuir*, 16(21):7891–7894.
- [74] Hutter, J. L. and Bechhoefer, J. (1993). Calibration of atomic-force microscope tips. *Review of scientific instruments*, 64(7):1868–1873.
- [75] Jagannathan, B. and Marqusee, S. (2013). Protein folding and unfolding under force. *Biopolymers*, 99(11):860–869.
- [76] Jai, C., Cohen-Bouhacina, T., and Maali, A. (2007). Analytical description of the motion of an acoustic-driven atomic force microscope cantilever in liquid. *Applied physics letters*, 90(11):113512.
- [77] Janovjak, H., Müller, D. J., and Humphris, A. D. (2005). Molecular force modulation spectroscopy revealing the dynamic response of single bacteriorhodopsins. *Biophysical journal*, 88(2):1423–1431.

- [78] Jarvis, S., Lantz, M., Dürig, U., and Tokumoto, H. (1999). Off resonance ac mode force spectroscopy and imaging with an atomic force microscope. *Applied surface science*, 140(3-4):309–313.
- [79] Jarvis, S., Oral, A., Weihs, T., and Pethica, J. (1993). A novel force microscope and point contact probe. *Review of scientific instruments*, 64(12):3515–3520.
- [80] Jarvis, S., Yamada, H., Yamamoto, S.-I., Tokumoto, H., and Pethica, J. (1996). Direct mechanical measurement of interatomic potentials. *Nature*, 384(6606):247–249.
- [81] Jay, P. Y., Pham, P. A., Wong, S. A., and Elson, E. L. (1995). A mechanical function of myosin ii in cell motility. *Journal of cell science*, 108(1):387–393.
- [82] Jeffery, S., Hoffmann, P. M., Pethica, J. B., Ramanujan, C., Özer, H. Ö., and Oral, A. (2004). Direct measurement of molecular stiffness and damping in confined water layers. *Physical Review B*, 70(5):054114.
- [83] Jeffery, S., Oral, A., and Pethica, J. B. (2000). Quantitative electrostatic force measurement in afm. *Applied surface science*, 157(4):280–284.
- [84] Kageshima, M., Chikamoto, T., Ogawa, T., Hirata, Y., Inoue, T., Naitoh, Y., Li, Y. J., and Sugawara, Y. (2009). Development of atomic force microscope with wide-band magnetic excitation for study of soft matter dynamics. *Review of Scientific Instruments*, 80(2):023705.
- [85] Kaggwa, G., Kilpatrick, J., Sader, J., and Jarvis, S. (2008). Artifact-free dynamic atomic force microscopy reveals monotonic dissipation for a simple confined liquid. *Applied Physics Letters*, 93(1):011909.
- [86] Kathuria, S. V., Guo, L., Graceffa, R., Barrea, R., Nobrega, R. P., Matthews, C. R., Irving, T. C., and Bilsel, O. (2011). Minireview: Structural insights into early folding events using continuous-flow time-resolved small-angle x-ray scattering. *Biopolymers*, 95(8):550–558.
- [87] Kawakami, M., Byrne, K., Brockwell, D. J., Radford, S. E., and Smith, D. A. (2006). Viscoelastic study of the mechanical unfolding of a protein by afm. *Biophysical journal*, 91(2):L16–L18.
- [88] Kawakami, M., Byrne, K., Khatri, B., Mcleish, T. C., Radford, S. E., and Smith, D. A. (2004). Viscoelastic properties of single polysaccharide molecules determined by analysis of thermally driven oscillations of an atomic force microscope cantilever. *Langmuir*, 20(21):9299–9303.
- [89] Kawakami, M., Byrne, K., Khatri, B. S., Mcleish, T. C., Radford, S. E., and Smith, D. A. (2005). Viscoelastic measurements of single molecules on a millisecond time scale by magnetically driven oscillation of an atomic force microscope cantilever. *Langmuir*, 21(10):4765–4772.
- [90] Khan, S. H. and Hoffmann, P. M. (2015). Squeeze-out dynamics of nanoconfined water: A detailed nanomechanical study. *Physical Review E*, 92(4):042403.
- [91] Khan, S. H., Kramkowski, E. L., and Hoffmann, P. M. (2016). NaCl-dependent ordering and dynamic mechanical response in nanoconfined water. *Langmuir*, 32(42):10802–10807.
- [92] Khan, S. H., Matei, G., Patil, S., and Hoffmann, P. M. (2010). Dynamic solidification in nanoconfined water films. *Physical review letters*, 105(10):106101.
- [93] Khatri, B. S., Byrne, K., Kawakami, M., Brockwell, D. J., Smith, D. A., Radford, S. E., and McLeish, T. C. (2008). Internal friction of single polypeptide chains at high stretch. *Faraday discussions*, 139:35–51.

- [94] Khatri, B. S., Kawakami, M., Byrne, K., Smith, D. A., and McLeish, T. C. (2007). Entropy and barrier-controlled fluctuations determine conformational viscoelasticity of single biomolecules. *Biophysical journal*, 92(6):1825–1835.
- [95] Kienberger, F., Pastushenko, V. P., Kada, G., Gruber, H. J., Riener, C., Schindler, H., and Hinterdorfer, P. (2000). Static and dynamical properties of single poly (ethylene glycol) molecules investigated by force spectroscopy. *Single Molecules*, 1(2):123–128.
- [96] Kiracofe, D. and Raman, A. (2011). Quantitative force and dissipation measurements in liquids using piezo-excited atomic force microscopy: a unifying theory. *Nanotechnology*, 22(48):485502.
- [97] Knowles, T. P., Vendruscolo, M., and Dobson, C. M. (2014). The amyloid state and its association with protein misfolding diseases. *Nature reviews Molecular cell biology*, 15(6):384–396.
- [98] Kotamarthi, H. C., Sharma, R., and Ainaravapu, S. R. K. (2013). Single-molecule studies on polysumo proteins reveal their mechanical flexibility. *Biophysical journal*, 104(10):2273–2281.
- [99] Koti Ainaravapu, S. R., Wiita, A. P., Dougan, L., Uggerud, E., and Fernandez, J. M. (2008). Single-molecule force spectroscopy measurements of bond elongation during a bimolecular reaction. *Journal of the American Chemical Society*, 130(20):6479–6487.
- [100] Krainer, G., Keller, S., and Schlierf, M. (2019). Structural dynamics of membrane-protein folding from single-molecule fret. *Current opinion in structural biology*, 58:124–137.
- [101] Krieg, M., Dunn, A. R., and Goodman, M. B. (2014). Mechanical control of the sense of touch by β -spectrin. *Nature cell biology*, 16(3):224–233.
- [102] Labeit, S., Gautel, M., Lakey, A., and Trinick, J. (1992). Towards a molecular understanding of titin. *The EMBO journal*, 11(5):1711–1716.
- [103] Laohakunakorn, N., Otto, O., Sturm, S., Kroy, K., and Keyser, U. F. (2013). Dynamic single-molecule force spectroscopy using optical tweezers and nanopores. In *Optical Trapping and Optical Micromanipulation X*, volume 8810, page 88101F. International Society for Optics and Photonics.
- [104] Lapidus, L. J. (2017). Protein unfolding mechanisms and their effects on folding experiments. *F1000Research*, 6.
- [105] Lapidus, L. J., Steinbach, P. J., Eaton, W. A., Szabo, A., and Hofrichter, J. (2002). Effects of chain stiffness on the dynamics of loop formation in polypeptides. appendix: Testing a 1-dimensional diffusion model for peptide dynamics. *The Journal of Physical Chemistry B*, 106(44):11628–11640.
- [106] Lavelle, C. (2007). Transcription elongation through a chromatin template. *Biochimie*, 89(4):516–527.
- [107] Li, H., Carrion-Vazquez, M., Oberhauser, A. F., Marszalek, P. E., and Fernandez, J. M. (2000). Point mutations alter the mechanical stability of immunoglobulin modules. *Nature structural biology*, 7(12):1117–1120.
- [108] Li, H., Rief, M., Oesterhelt, F., and Gaub, H. E. (1998). Single-molecule force spectroscopy on xanthan by afm. *Advanced Materials*, 10(4):316–319.

- [109] Liang, X. and Nakajima, K. (2019). Investigating the dynamic viscoelasticity of single polymer chains using atomic force microscopy. *Journal of Polymer Science Part B: Polymer Physics*, 57(24):1736–1743.
- [110] Linke, W. A. (2008). Sense and stretchability: the role of titin and titin-associated proteins in myocardial stress-sensing and mechanical dysfunction. *Cardiovascular research*, 77(4):637–648.
- [111] Lipfert, J., Koster, D. A., Vilfan, I. D., Hage, S., and Dekker, N. H. (2009). Single-molecule magnetic tweezers studies of type I topoisomerases. In *DNA Topoisomerases*, pages 71–89. Springer.
- [112] Liu, Y., Leuba, S., and Lindsay, S. (1999). Relationship between stiffness and force in single molecule pulling experiments. *Langmuir*, 15(24):8547–8548.
- [113] Lorimer, G. H. (1996). A quantitative assessment of the role of the chaperonin proteins in protein folding in vivo. *The FASEB journal*, 10(1):5–9.
- [114] Lozano, J. R. and Garcia, R. (2009). Theory of phase spectroscopy in bimodal atomic force microscopy. *Physical Review B*, 79(1):014110.
- [115] Ludwig, M., Rief, M., Schmidt, L., Li, H., Oesterhelt, F., Gautel, M., and Gaub, H. (1999). Afm, a tool for single-molecule experiments. *Applied Physics A*, 68(2):173–176.
- [116] Maali, A. and Cohen-Bouhacina, T. (2006). Comment on "oscillatory dissipation of a simple confined liquid"-reply.
- [117] Maali, A., Cohen-Bouhacina, T., Couturier, G., and Aimé, J.-P. (2006). Oscillatory dissipation of a simple confined liquid. *Physical review letters*, 96(8):086105.
- [118] Mandal, S. S. (2020). Force spectroscopy on single molecules of life. *ACS omega*, 5(20):11271–11278.
- [119] Marti, O., Ribi, H. O., Drake, B., Albrecht, T. R., Quate, C. F., and Hansma, P. K. (1988). Atomic force microscopy of an organic monolayer. *Science*, 239(4835):50–52.
- [120] Martin, Y., Williams, C. C., and Wickramasinghe, H. K. (1987). Atomic force microscope–force mapping and profiling on a sub 100-Å scale. *Journal of applied Physics*, 61(10):4723–4729.
- [121] Martinez-Vicente, M., Sovak, G., and Cuervo, A. M. (2005). Protein degradation and aging. *Experimental gerontology*, 40(8-9):622–633.
- [122] Matsumoto, K. and Wolffe, A. P. (1998). Gene regulation by γ -box proteins: coupling control of transcription and translation. *Trends in cell biology*, 8(8):318–323.
- [123] McClelland, G. M., Erlandsson, R., and Chiang, S. (1987). Atomic force microscopy: General principles and a new implementation. In *Review of Progress in Quantitative Nondestructive Evaluation*, pages 1307–1314. Springer.
- [124] McCrary, B. S., Edmondson, S. P., and Shriver, J. W. (1996). Hyperthermophile protein folding thermodynamics: differential scanning calorimetry and chemical denaturation of sac7d. *Journal of molecular biology*, 264(4):784–805.
- [125] McKittrick, J., Chen, P.-Y., Bodde, S., Yang, W., Novitskaya, E., and Meyers, M. (2012). The structure, functions, and mechanical properties of keratin. *Jom*, 64(4):449–468.

- [126] Möglich, A., Joder, K., and Kiefhaber, T. (2006). End-to-end distance distributions and intrachain diffusion constants in unfolded polypeptide chains indicate intramolecular hydrogen bond formation. *Proceedings of the National Academy of Sciences*, 103(33):12394–12399.
- [127] Neuman, K. C. and Nagy, A. (2008). Single-molecule force spectroscopy: optical tweezers, magnetic tweezers and atomic force microscopy. *Nature methods*, 5(6):491–505.
- [128] Nicoli, D. and Benedek, G. (1976). Study of thermal denaturation of lysozyme and other globular proteins by light-scattering spectroscopy. *Biopolymers: Original Research on Biomolecules*, 15(12):2421–2437.
- [129] Niesen, F. H., Berglund, H., and Vedadi, M. (2007). The use of differential scanning fluorimetry to detect ligand interactions that promote protein stability. *Nature protocols*, 2(9):2212.
- [130] Oberhauser, A. F., Hansma, P. K., Carrion-Vazquez, M., and Fernandez, J. M. (2001). Stepwise unfolding of titin under force-clamp atomic force microscopy. *Proceedings of the National Academy of Sciences*, 98(2):468–472.
- [131] Oberhauser, A. F., Marszalek, P. E., Erickson, H. P., and Fernandez, J. M. (1998). The molecular elasticity of the extracellular matrix protein tenascin. *Nature*, 393(6681):181–185.
- [132] O’shea, S. and Welland, M. (1998). Atomic force microscopy at solid- liquid interfaces. *Langmuir*, 14(15):4186–4197.
- [133] O’shea, S., Welland, M., and Pethica, J. (1994). Atomic force microscopy of local compliance at solid—liquid interfaces. *Chemical Physics Letters*, 223(4):336–340.
- [134] Özer, H. Ö., O’Brien, S. J., and Pethica, J. B. (2007). Local force gradients on si (111) during simultaneous scanning tunneling/atomic force microscopy. *Applied Physics Letters*, 90(13):133110.
- [135] O’Shea, S. (2006). Comment on “oscillatory dissipation of a simple confined liquid”. *Physical review letters*, 97(17):179601.
- [136] Pace, C. (1986). [14] determination and analysis of urea and guanidine hydrochloride denaturation curves. In *Methods in enzymology*, volume 131, pages 266–280. Elsevier.
- [137] Palker, T. (1992). Human t-cell lymphotropic viruses: review and prospects for antiviral therapy. *Antiviral Chemistry and Chemotherapy*, 3(3):127–139.
- [138] Parui, S., Manna, R. N., and Jana, B. (2016). Destabilization of hydrophobic core of chicken villin headpiece in guanidinium chloride induced denaturation: hint of π -cation interaction. *The Journal of Physical Chemistry B*, 120(36):9599–9607.
- [139] Pastor, W. A., Aravind, L., and Rao, A. (2013). Tectonic shift: biological roles of tet proteins in dna demethylation and transcription. *Nature reviews Molecular cell biology*, 14(6):341–356.
- [140] Patil, S., Matei, G., Dong, H., Hoffmann, P. M., Karaköse, M., and Oral, A. (2005). A highly sensitive atomic force microscope for linear measurements of molecular forces in liquids. *Review of Scientific Instruments*, 76(10):103705.
- [141] Patil, S., Matei, G., Oral, A., and Hoffmann, P. M. (2006). Solid or liquid? solidification of a nanoconfined liquid under nonequilibrium conditions. *Langmuir*, 22(15):6485–6488.
- [142] Patil, S. V. and Hoffmann, P. M. (2005). Small-amplitude atomic force microscopy. *Advanced Engineering Materials*, 7(8):707–712.

- [143] Pethica, J. and Oliver, W. (1987). Tip surface interactions in stm and afm. *Physica Scripta*, 1987(T19A):61.
- [144] Pini, V., Tiribilli, B., Gambi, C. M. C., and Vassalli, M. (2010). Dynamical characterization of vibrating afm cantilevers forced by photothermal excitation. *Phys. Rev. B*, 81:054302.
- [145] Rabe, U. (2006). Atomic force acoustic microscopy. In *Applied scanning probe methods II*, pages 37–90. Springer.
- [146] Rajput, S. S., Deopa, S. P. S., Yadav, J., Ahlawat, V., Talele, S., and Patil, S. (2020). The nano-scale viscoelasticity using atomic force microscopy in liquid environment. *Nanotechnology*, 32(8):085103.
- [147] Raman, A., Melcher, J., and Tung, R. (2008). Cantilever dynamics in atomic force microscopy. *Nano Today*, 3(1-2):20–27.
- [148] Rief, M., Oesterhelt, F., Heymann, B., and Gaub, H. E. (1997). Single molecule force spectroscopy on polysaccharides by atomic force microscopy. *Science*, 275(5304):1295–1297.
- [149] Rifkind, J. M., Zhang, L., Heim, J. M., and Levy, A. (1988). The role of hemoglobin in generating oxyradicals. In *Oxygen radicals in biology and medicine*, pages 157–162. Springer.
- [150] Roche, J., Caro, J. A., Norberto, D. R., Barthe, P., Roumestand, C., Schlessman, J. L., Garcia, A. E., Royer, C. A., et al. (2012). Cavities determine the pressure unfolding of proteins. *Proceedings of the National Academy of Sciences*, 109(18):6945–6950.
- [151] Sader, J. E. (1998). Frequency response of cantilever beams immersed in viscous fluids with applications to the atomic force microscope. *Journal of applied physics*, 84(1):64–76.
- [152] Sader, J. E., Larson, I., Mulvaney, P., and White, L. R. (1995). Method for the calibration of atomic force microscope cantilevers. *Review of Scientific Instruments*, 66(7):3789–3798.
- [153] Sader, J. E., Pacifico, J., Green, C. P., and Mulvaney, P. (2005). General scaling law for stiffness measurement of small bodies with applications to the atomic force microscope. *Journal of Applied physics*, 97(12):124903.
- [154] Sarkar, R. and Rybenkov, V. V. (2016). A guide to magnetic tweezers and their applications. *Frontiers in Physics*, 4:48.
- [155] Schäffer, T., Cleveland, J., Ohnesorge, F., Walters, D., and Hansma, P. (1996). Studies of vibrating atomic force microscope cantilevers in liquid. *Journal of applied physics*, 80(7):3622–3627.
- [156] Schlierf, M., Li, H., and Fernandez, J. M. (2004). The unfolding kinetics of ubiquitin captured with single-molecule force-clamp techniques. *Proceedings of the National Academy of Sciences*, 101(19):7299–7304.
- [157] Schuler, B. and Eaton, W. A. (2008). Protein folding studied by single-molecule fret. *Current opinion in structural biology*, 18(1):16–26.
- [158] Senisterra, G., Chau, I., and Vedadi, M. (2012). Thermal denaturation assays in chemical biology. *Assay and drug development technologies*, 10(2):128–136.

- [159] Shang, H. and Lee, G. U. (2007). Magnetic tweezers measurement of the bond lifetime- force behavior of the igg- protein a specific molecular interaction. *Journal of the American Chemical Society*, 129(20):6640–6646.
- [160] Smith, A.-S., Sengupta, K., Goennenwein, S., Seifert, U., and Sackmann, E. (2008). Force-induced growth of adhesion domains is controlled by receptor mobility. *Proceedings of the National Academy of Sciences*, 105(19):6906–6911.
- [161] Somero, G. N. (1995). Proteins and temperature. *Annual review of physiology*, 57(1):43–68.
- [162] Sotomayor, M. and Schulten, K. (2007). Single-molecule experiments in vitro and in silico. *Science*, 316(5828):1144–1148.
- [163] Stark, R. W. and Heckl, W. M. (2000). Fourier transformed atomic force microscopy: tapping mode atomic force microscopy beyond the hookian approximation. *Surface Science*, 457(1-2):219–228.
- [164] Stefan, N. and Häring, H.-U. (2013). The role of hepatokines in metabolism. *Nature Reviews Endocrinology*, 9(3):144–152.
- [165] Steward, A., Toca-Herrera, J. L., and Clarke, J. (2002). Versatile cloning system for construction of multimeric proteins for use in atomic force microscopy. *Protein Science*, 11(9):2179–2183.
- [166] Stigler, J., Ziegler, F., Gieseke, A., Gebhardt, J. C. M., and Rief, M. (2011). The complex folding network of single calmodulin molecules. *Science*, 334(6055):512–516.
- [167] Strick, T. R., Allemand, J.-F., Bensimon, D., Bensimon, A., and Croquette, V. (1996). The elasticity of a single supercoiled dna molecule. *Science*, 271(5257):1835–1837.
- [168] Stryer, L. (1978). Fluorescence energy transfer as a spectroscopic ruler. *Annual review of biochemistry*, 47(1):819–846.
- [169] Swint, L. and Robertson, A. D. (1993). Thermodynamics of unfolding for turkey ovomucoid third domain: thermal and chemical denaturation. *Protein Science*, 2(12):2037–2049.
- [170] Tamayo, J., Humphris, A., Owen, R., and Miles, M. (2001). High-q dynamic force microscopy in liquid and its application to living cells. *Biophysical journal*, 81(1):526–537.
- [171] Tapia-Rojo, R., Eckels, E. C., and Fernández, J. M. (2019). Ephemeral states in protein folding under force captured with a magnetic tweezers design. *Proceedings of the National Academy of Sciences*, 116(16):7873–7878.
- [172] Thompson, P. A., Eaton, W. A., and Hofrichter, J. (1997). Laser temperature jump study of the helix coil kinetics of an alanine peptide interpreted with a ‘kinetic zipper’ model. *Biochemistry*, 36(30):9200–9210.
- [173] Turner, J. A., Hirsekorn, S., Rabe, U., and Arnold, W. (1997). High-frequency response of atomic-force microscope cantilevers. *Journal of Applied Physics*, 82(3):966–979.
- [174] Van Beek, E. M., Cochrane, F., Barclay, A. N., and van den Berg, T. K. (2005). Signal regulatory proteins in the immune system. *The Journal of Immunology*, 175(12):7781–7787.
- [175] Vedadi, M., Niesen, F. H., Allali-Hassani, A., Fedorov, O. Y., Finerty, P. J., Wasney, G. A., Yeung, R., Arrowsmith, C., Ball, L. J., Berglund, H., et al. (2006). Chemical screening methods to identify ligands that promote protein stability, protein crystallization, and structure determination. *Proceedings of the National Academy of Sciences*, 103(43):15835–15840.

- [176] Vilfan, I., Lipfert, J., Koster, D., Lemay, S., and Dekker, N. (2009). Magnetic tweezers for single-molecule experiments. *Handbook of single-molecule biophysics*, pages 371–395.
- [177] Wafer, L., Kloczewiak, M., Polleck, S. M., and Luo, Y. (2017). Isothermal chemical denaturation of large proteins: Path-dependence and irreversibility. *Analytical biochemistry*, 539:60–69.
- [178] Wang, Y. and Zocchi, G. (2010). Elasticity of globular proteins measured from the ac susceptibility. *Physical review letters*, 105(23):238104.
- [179] Wang, Y. and Zocchi, G. (2011). Viscoelastic transition and yield strain of the folded protein. *PLoS One*, 6(12):e28097.
- [180] Wickner, R. B. (1992). Double-stranded and single-stranded rna viruses of *saccharomyces cerevisiae*. *Annual review of microbiology*, 46(1):347–375.
- [181] Wickner, R. B. (1996). Double-stranded rna viruses of *saccharomyces cerevisiae*. *Microbiological reviews*, 60(1):250.
- [182] Wüthrich, K., Wagner, G., Richarz, R., and Braun, W. (1980). Correlations between internal mobility and stability of globular proteins. *Biophysical journal*, 32(1):549–560.
- [183] Xu, X. and Raman, A. (2007). Comparative dynamics of magnetically, acoustically, and brownian motion driven microcantilevers in liquids. *Journal of Applied Physics*, 102(3):034303.
- [184] Yang, J. T., Wu, C.-S. C., and Martinez, H. M. (1986). [11] calculation of protein conformation from circular dichroism. *Methods in enzymology*, 130:208–269.
- [185] Yusko, E. C. and Asbury, C. L. (2014). Force is a signal that cells cannot ignore. *Molecular biology of the cell*, 25(23):3717–3725.
- [186] Zhao, X., Zeng, X., Lu, C., and Yan, J. (2017). Studying the mechanical responses of proteins using magnetic tweezers. *Nanotechnology*, 28(41):414002.
- [187] Ziv, G. and Haran, G. (2009). Protein folding, protein collapse, and tanford’s transfer model: Lessons from single-molecule fret. *Journal of the American Chemical Society*, 131(8):2942–2947.

Appendix A

Chapter-4 - Supplementary Information

A.1 Theory

The Euler-Bernoulli equation of motion for a homogeneous rectangular cantilever beam immersed in a liquid is

$$-\tilde{\rho}\tilde{S}\frac{\partial^2 y(x,t)}{\partial t^2} - \gamma_c \frac{\partial y(x,t)}{\partial t} = EI \frac{\partial^4 y(x,t)}{\partial x^4} \quad (\text{A.1})$$

The spatial part of Eq. A.1 equation can be written as

$$\frac{d^4 y(x)}{dx^4} = k^4 y(x) \quad (\text{A.2})$$

General solution of Eq. A.2 is:

$$y(x) = a \sin(kx) + b \cos(kx) + c \sinh(kx) + d \cosh(kx) \quad (\text{A.3})$$

and slope

$$y'(x) = ak \cos(kx) - bk \sin(kx) + ck \cosh(kx) + dk \sinh(kx) \quad (\text{A.4})$$

A.1.0.1 Base excited and tip-sample interaction is present

Boundary conditions:

$$\begin{aligned} y(0) - A &= 0, & y'(0) &= 0, \\ y''(L) &= 0, & EIy'''(L) - (k_i + i\omega\tilde{\gamma}_i)y(L) &= 0 \end{aligned}$$

Above set of linear equations can be written in matrix form: $MX - N = 0$ and solve for X using matrix method. Where M and N are:

$$M = \begin{bmatrix} 0 & 1 & 0 & 1 \\ k & 0 & k & 0 \\ -k^2 \sin(kL) & -k^2 \cos(kL) & k^2 \sinh(kL) & k^2 \cosh(kL) \\ -\cos(kL) - q \sin(kL) & \sin(kL) - q \cos(kL) & \cosh(kL) - q \sinh(kL) & \sinh(kL) - q \cosh(kL) \end{bmatrix}$$

and

$$N = \begin{bmatrix} -A \\ 0 \\ 0 \\ 0 \end{bmatrix}$$

Where $q = \frac{k_i + i\omega \bar{\gamma}_i}{EI k^3}$.

Solving the matrix equation $MX - N = 0$, the coefficients (or X) are following:

$$a = \frac{A[\cosh(z)(-2q \cos(z) + \sin(z)) + \cos(z) \sinh(z)]}{2[1 + \cosh(z)(\cos(z) + q \sin(z)) - q \cos(z) \sinh(z)]},$$

$$b = \frac{A[1 + \cosh(z)(\cos(z) + 2q \sin(z)) - \sin(z) \sinh(z)]}{2[1 + \cosh(z)(\cos(z) + q \sin(z)) - q \cos(z) \sinh(z)]},$$

$$c = \frac{-A[\cosh(z)(-2q \cos(z) + \sin(z)) + \cos(z) \sinh(z)]}{2[1 + \cosh(z)(\cos(z) + q \sin(z)) - q \cos(z) \sinh(z)]},$$

$$d = \frac{A[1 + \cos(z) \cosh(z) + (-2q \cos(z) + \sin(z)) \sinh(z)]}{2[1 + \cosh(z)(\cos(z) + q \sin(z)) - q \cos(z) \sinh(z)]}$$

Where $z = kL$.

Solution (displacement) at $x = L$ can be written as:

$$y(L) = a \sin(kL) + b \cos(kL) + c \sinh(kL) + d \cosh(kL) \quad (\text{A.5})$$

and slope

$$y'(L) = ak \cos(kL) - bk \sin(kL) + ck(kL) + dk \sinh(kL) \quad (\text{A.6})$$

Substitute values of a , b , c , and d into Eqs. A.5 and A.6. Take the Taylor expansion for small z^4 and g , displacement and slope are following:

$$y(L) = A - \frac{gA}{3} + \frac{Az^4}{8}, \quad y'(L) = \frac{-Ag}{2L} + \frac{Az^4}{6L} \quad (\text{A.7})$$

Whereas, full solution with higher order terms are as following:

$$y(L) = A - \frac{gA}{3} + \frac{Az^4}{8} + \frac{Ag^2}{9} - \frac{19Agz^4}{280} + O[z]^8 \quad (\text{A.8})$$

$$y'(L) = \frac{-Ag}{2L} + \frac{Az^4}{6L} + \frac{Ag^2}{6L} - \frac{71gz^4}{720L} + \frac{71Az^8}{5040L} + O[z]^8 \quad (\text{A.9})$$

Consider first two higher order terms in Eq. A.9:

$$y'(L) = \frac{-Ag}{2L} + \frac{Az^4}{6L} + \frac{Ag^2}{6L} - \frac{71gz^4}{720L}$$

Real and imaginary parts are:

$$\begin{aligned} X_b &= \frac{A}{2k_c} [(-3k_i + \tilde{\rho}\tilde{S}\omega^2L + \frac{3}{k_c}(k_i^2 - \omega\tilde{\gamma}_i^2) - \frac{639}{360k_c}(k_i\tilde{\rho}\tilde{S}\omega^2L + \omega^2\tilde{\gamma}_i\gamma_cL)], \\ Y_b &= \frac{A\omega}{2k_c} [-3\tilde{\gamma}_i - \gamma_cL + \frac{6}{k_c}k_i\tilde{\gamma}_i - \frac{639}{360k_c}(k_i\gamma_cL + \tilde{\gamma}_i\tilde{\rho}\tilde{S}\omega^2L)] \end{aligned} \quad (\text{A.10})$$

In Eq. A.10 Y contains interaction stiffness which could lead variation in the Y -signal due to variation in the interaction stiffness even in absence of dissipation.

Applying the appropriate boundary conditions, similar procedure could be followed to derive the solutions for the freely oscillating cantilever and cantilever is in non-deformable contact with the substrate.

A.2 Discussion

A.2.1 Validity of Eq. 11

At low frequency excitation, the amplitude of the cantilever base and tip displacement is approximately same and move in-phase Eq. 11. Fig. S1 shows the cantilever base and tip amplitude and phase response in displacement detection system in water. Up to 1000 Hz, the difference in amplitude between the cantilever base and tip is less than 1 Å and difference in phase is ~ 0 degree.

A.2.2 Quantification of Stiffness

Fig. S2 shows directly measured stiffness using deflection detection scheme and the derivative of force simultaneously measured by static deflection of the cantilever. The two measurements give identical result. This also indirectly means that the dissipation coefficient is very low.

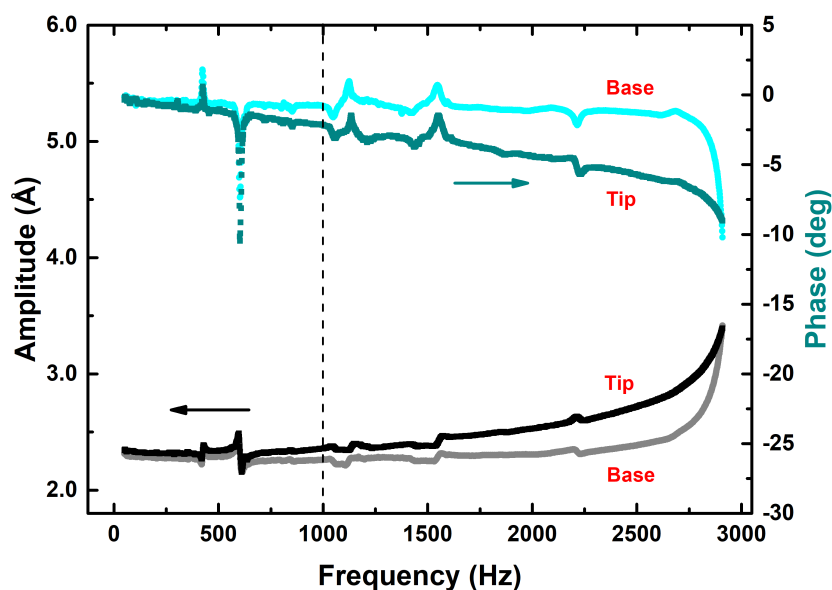


Fig. S1 Oscillation profile of base and tip in water for smaller frequency range. Gray and black curves represent the amplitude of the base and tip respectively. Light-cyan and dark-cyan curves represent the base and tip phase respectively. Dotted vertical line represents the range up to which Eq. 11 holds (base and tip amplitudes are approximately same and move in-phase).

A.2.3 The effect of extraneous phase

Fig. S3 shows the measurement performed by adding phase to the cantilever. Without adding the external phase the cantilever end shows a phase lag of $\theta_h \sim 6$ degrees. This is due to the hydrodynamics and the Y -component is free of any variations as shown in Fig. 3(b). Any addition to this phase externally using phase shifter produces variation in Y -signal as the molecule is stretched and domains unfold one after the other. It is also seen that as the added phase gets close to 90 degrees, the X -signal shows no variation whereas Y shows maximum variation when molecule is stretched. This indicates that for any uncompensated non-zero θ_e , the Y -signal shows a saw-tooth like pattern when the octamer is pulled on and unfolds sequentially. Thus, if the a extraneous phase is not correctly compensated or completely removed from the measurement, one can wrongly interpret the Y -signal as a measurement of dissipation in single molecules when they are stretched.

A.2.4 Sources of extraneous phase θ_e

Following are the sources of extraneous phase when the measurements are performed wherein the base of the cantilever is excited.

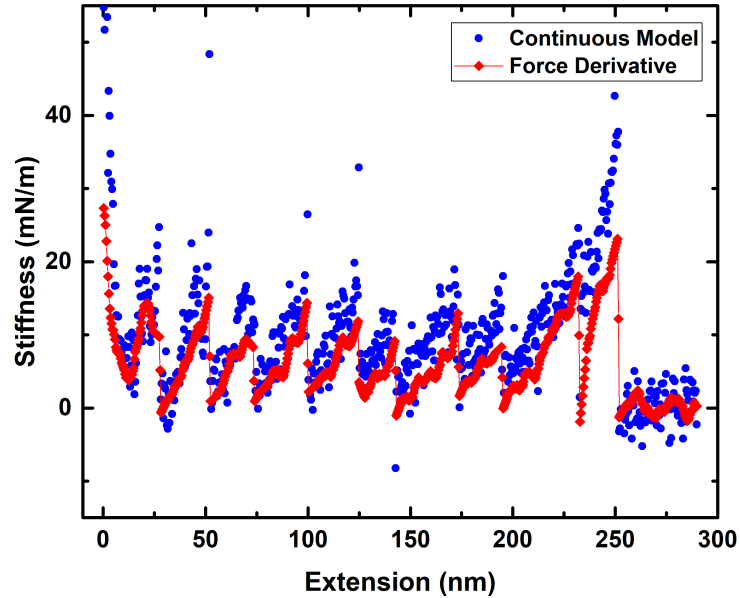


Fig. S2 Directly measured stiffness using deflection detection scheme and the derivative for force simultaneously measured by static deflection of the cantilever.

1. Electronic phase: The cantilever is excited by providing a electrical signal to a piezo excitor on which the base of the cantilever is mounted. The deflection (dy/dx) or the displacement (y) of the cantilever's tip end is measured by optical means. A current to voltage converter is then used to amplify the signal to make it measurably large. Typically a high gain-bandwidth amplifier is used for this purpose and at reasonably low excitation frequencies (0.1 - 1 kHz), there is no delay between input and output of this amplifier. The main source of extraneous phase is then from the electrical connections made to the piezo used for excitation of the base. It is straightforward to measure this phase contribution by recording the phase lag in deep contact. Any deviation from 180 degrees can be attributed to electronic phase contribution.

Furthermore, the absence of electronic phase offset can be confirmed by observing the phase lag in air. It is well known that the cantilever tip has no phase lag when oscillating in air in the off resonance regime (see [49]). We observe zero phase lag in air and 6 degrees phase lag in water. Since in air there is no phase contribution due to electronics, the cantilever immersed in liquid is also devoid of any extraneous phase due to electronics or electrode connections to the piezo-excitor.

2. Local peaks far from the cantilever resonance: Fluid borne excitation: Xu and Raman have investigated different methods of cantilever excitation and have pointed out that cantilever base excitation using a piezo results in tip oscillation having two contributions. The one is structure-borne excitation and the other is fluid-borne excitation. The fluid-borne excitation is due to exciting the local fluid surrounding the cantilever and the base which is roughly thousand times bigger then

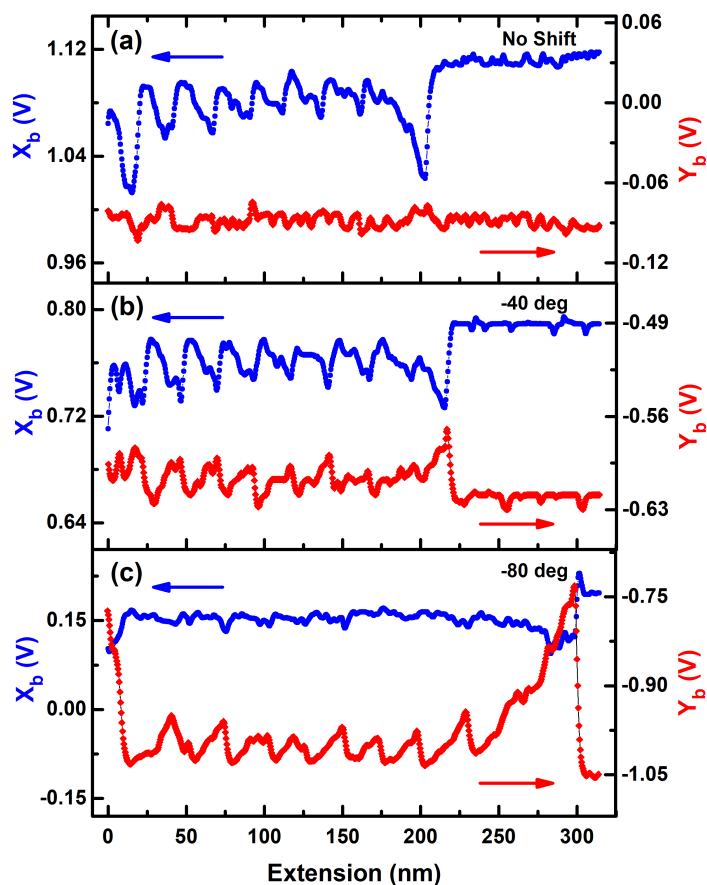


Fig. S3 Three unfolding experiments carried out with (a) no added electronic phase (b) by addition -40 degree phase (c) addition of -80 degree. There is no variation in Y without addition of external phase. The variation is seen in Y with addition of external phase and close to -90 degree there is more variation in Y-component as compared to X-component.

the cantilever itself. These excitations are due to oscillations of the chip on which the cantilever is mounted and strongly depend on the geometry of the liquid cell. This typically results in "forests of peaks" in cantilever excited in liquids. We performed measurements when the frequency sweep is not free from such peaks. Fig. S4 shows result of such a measurement. The arrows point at the peaks in Y-signal which match with unfolding of protein where the stiffness peaks. These peaks are due to variation in the stiffness as shown in the schematic of Fig. 7(b) and not due to dissipation in the molecule.

It should be ensured that for *true* off-resonance there are no local spurious peaks. This adds phase to the end of the cantilever and contributes to θ_e . Fig S4 shows a pulling experiment wherein there is a local peak near the excitation frequency ~ 100 Hz. This spurious peak produces a phase lag that is

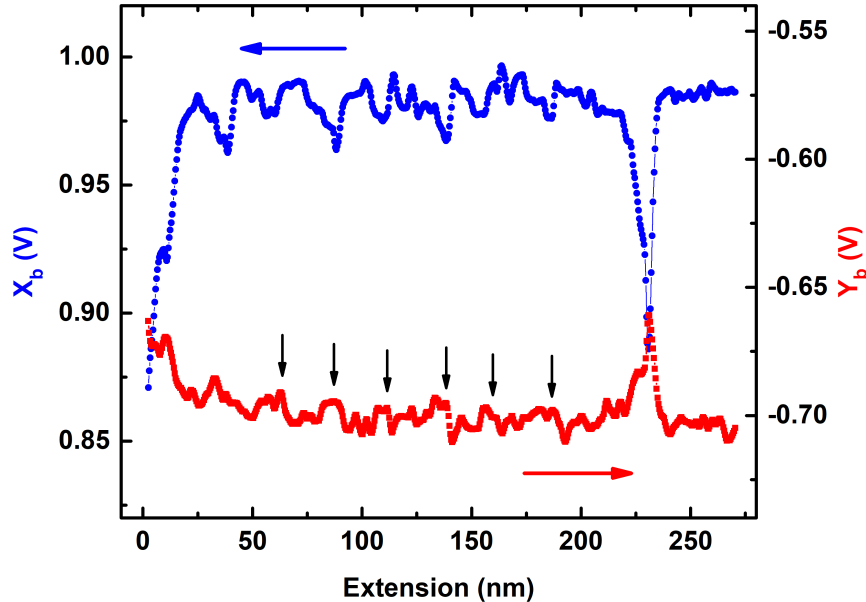


Fig. S4 Measurements performed when the frequency response is not free from local peaks. The Y -signal shows variation and peaks where the stiffness is maximum. This may wrongly get interpreted as the dissipation signal.

not accounted for in the modeling and thus contributes to θ_e . It can be clearly seen that the Y -signal now shows variation while octamer is sequentially unfolded. This is an artefact due to extraneous phase.

A.2.5 Off-resonance operation:

In the following we discuss off-resonance operation and use of Eqs. 16 and 18 to estimate the viscoelasticity of single molecules from the data.

The quality factor of cantilever resonance in air is typically around 100-1000 and in the vacuum environments it is 10,000-100,000. The off-resonance operation is ensured in these situations in a relatively straight-forward manner and nanoscale visco-elastic measurements are free from errors. However, the quality factor in liquids is of the order of 1-5. This poses a serious problem in ensuring that the cantilever is excited at a *truly* off-resonance frequency. Typically, the cantilever can be excited around 100 Hz and can be treated truly off-resonance, if first resonance of the cantilever is around 10 kHz .

We performed experiments to test the range of off-resonance frequencies where one can safely operate and use Eqs. 16 and 18 to quantify viscoelasticity from the experimental data and measurements remain free from artefacts. Using the same cantilever which were used to perform experiments of Fig.

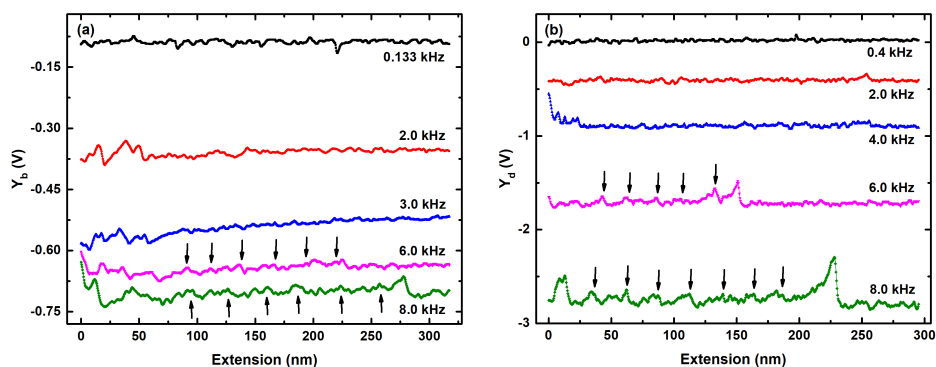


Fig. S5 (a) Measurements performed at higher frequencies using deflection detection type AFM. The Y -component of the bending oscillations shows variations after 4 kHz . (b) Measurements at higher frequencies using interferometer based AFM. The Y -component of the displacement oscillations shows peaks at extensions where domains unfold. In both measurements, the phase response is not flat. For higher frequencies the phase and the Y -component is not constant when the tip is far from the substrate. In these measurements the electronic phase lag was ensured to be absent by recording phase in the deep contact region (see Fig. S6).

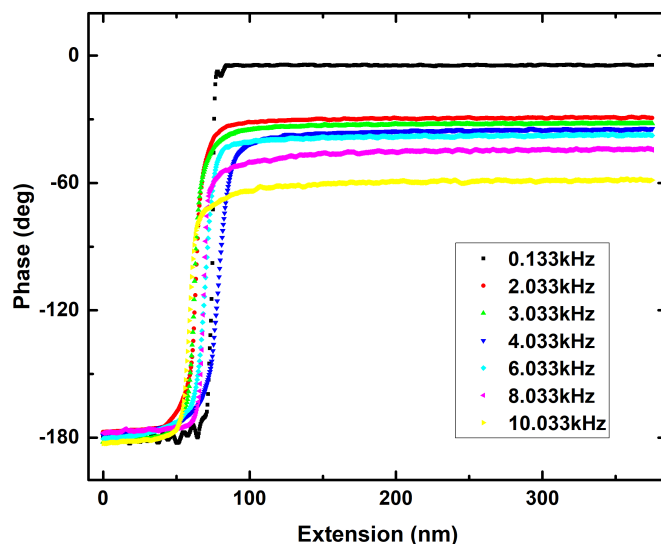


Fig. S6 Phase at the deep contact at different excitation frequencies are 180 degrees. Free phase increases with increasing excitation frequencies due to increase the hydrodynamic effect in free cantilever

3 and 4, we operated at higher frequencies to record X and Y components of the cantilever oscillations in both deflection detection AFM and interferometer based AFM. At relatively high frequencies, the variation is observed not only in phase but also in Y -signal. Fig. S5 shows Y -component recorded using both detection schemes. At 8 kHz , we clearly see variation in the Y -signal as the octamer unfolds.

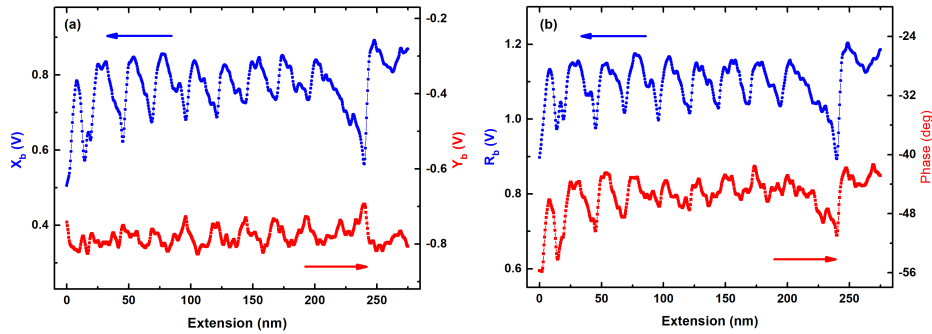


Fig. S7 Measurements performed in 70% glycerol in the solution using deflection detection scheme. At higher viscosity, the measurement at ~ 133 Hz is not truly off-resonance. The Y as well as phase shows variation as protein is unfolded sequentially.

Secondly, we changed the viscosity of the solvent in which the experiments are performed by adding Glycerol (70%) to it. This changes the viscosity of the medium by more than 30 times. We used similar operational parameters used in Fig. 3 and 4. The experiments were performed with similar parameters as was used in low frequency measurement case (frequency = 133 Hz , speed = 25 nm/s , cantilever stiffness = 0.73 N/m). We observed the Y -signal and phase signal when the single molecule is stretched (see Fig. S7). This could be misinterpreted as the dissipation from the stretching molecule. In this highly viscous medium the cantilever quality factor goes down to much less than ~ 1 and the system is overdamped. The drive frequency (133 Hz) is not really off-resonance in this case. The frequency sweep clearly shows no resonance peak and around 133 Hz , the cantilever response is not flat (see Fig. S8).

In both these measurements, the observed variation of Y -signal, which represents the dissipation alone (Eq. 16), is not due to the dissipation but it is result of the cross-talk between stiffness and dissipation. It is seen from Eq. A.10 that molecular stiffness appears in Y if we consider the higher order terms were considered. This clearly shows that at high frequencies but still away from resonance (13 kHz) the X and Y components of the tip oscillations both contain stiffness and dissipation and produces a cross-talk in the measurement. It is of paramount importance that the operation is *truly* off-resonance.

A.2.6 Minimum detectable dissipation

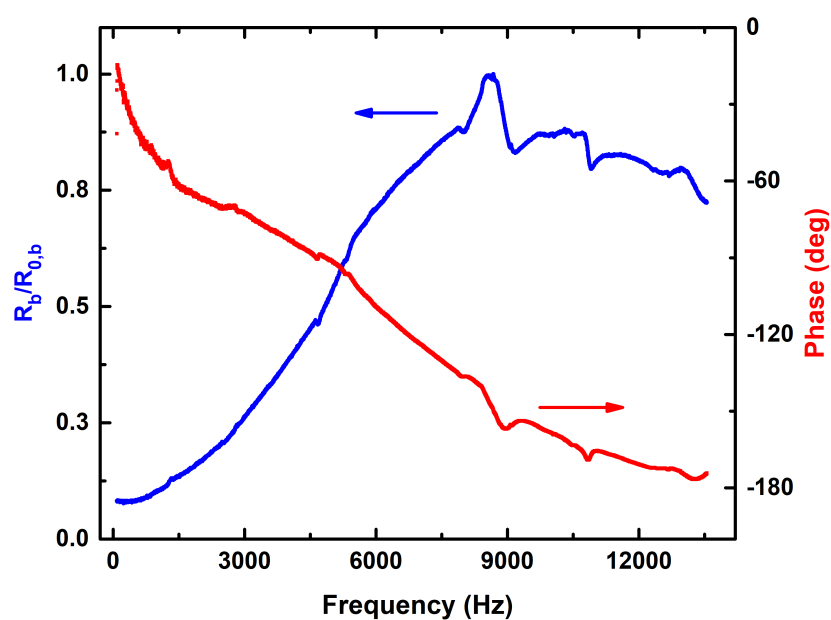


Fig. S8 Frequency and phase response in 70% glycerol medium in commercial AFM. It is difficult to find truly off-resonance regime in these curves.

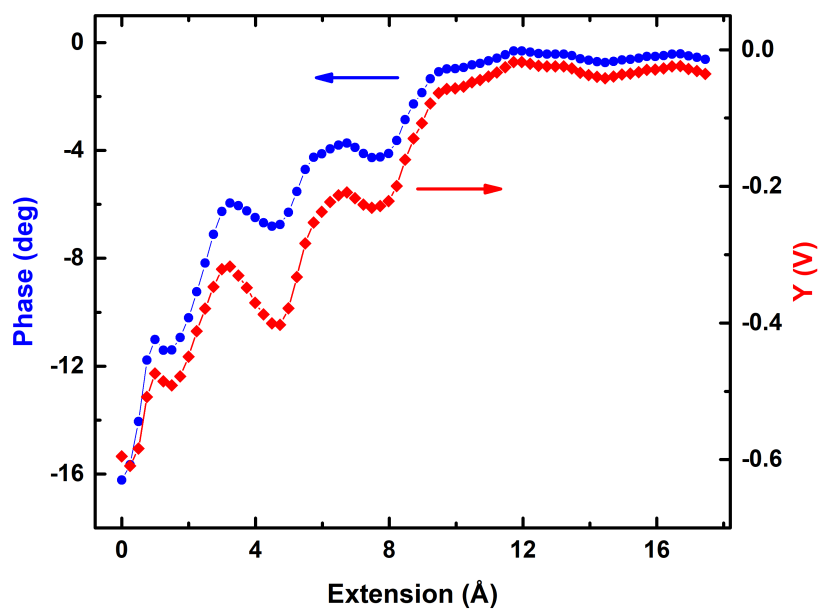


Fig. S9 The raw data from which dissipation coefficient in Fig. 9 is computed. The measurements are performed with interferometer based AFM. The phase for the cantilever displacement is zero when immersed in liquid and is far from the substrate. The data shows variation in both the phase and Y -component of the displacement signal.

Appendix B

Comparison of estimated stiffness using different methods

We compare the estimated peak stiffness of I27₈ molecule using three completely independent methods: (i) The base of the cantilever was excited and the displacement at the end was measured, (ii) The tip of the cantilever was excited and slope at the end was measured (magnetic-excitation), and (iii) The derivative of the static force was calculated. The dynamic measurements ((i) and (ii)) were performed at true off-resonance, using stiff cantilever, and small oscillation amplitudes. The peak values of the stiffness were plotted in Fig. B.1. All these values were matching well with each-other. These observations in completely different and independent methods ensures the accuracy of the methodology proposed by us. It is important to note that the reported peak stiffness of I27 molecule in the literature were not consistent with each-other and also deviate from our result [7, 87, 93]. This inconsistency could be due to the selection of inappropriate experimental parameters which can cause error as well as artefacts in the final results as we have discussed in *chapter-4* [146] and *chapter-5*.

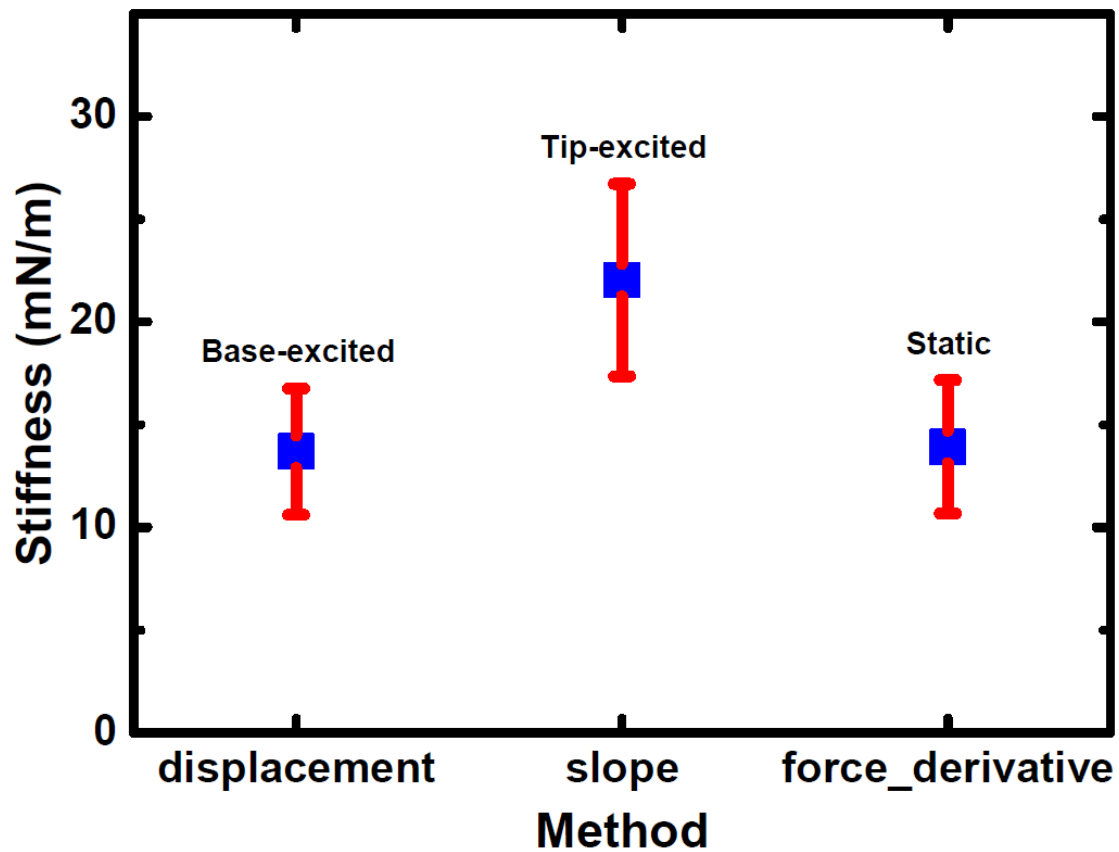


Fig. B.1 The peak value of the stiffness were calculated from four independent methods: base of the cantilever was excited using dither piezo and displacement at the end was measured (n=39), tip was excited and the slope was measured (n=45), and derivative of the static force signal (n=28). All these values were matching well with each-other. Error bars represent standard deviation.